Search for Ultra High Energy Radiation from Astrophysical Sources

Rishi Meyhandan B.Sc. (Hons)

Thesis submitted for the degree of

Doctor of Philosophy

in

The University of Adelaide

(Department of Physics and

Mathematical Physics)

January 1994

FOR MY PARENTS

Summary

This thesis presents results of searches made with the Buckland Park and SUGAR data sets for Ultra High Energy γ-ray emission from certain astrophysical objects. The origin of cosmic radiation at Ultra High Energies remains largely unresolved, and investigations into γ-ray emission from such objects may provide an insight to possible origins of cosmic rays.

The first chapter of the thesis briefly reviews the current status of properties of the cosmic ray flux such as the observed spectrum, composition and anisotropy, followed by a discussion of the field of Ultra High Energy γ-ray astronomy including aspects of possible acceleration mechanisms, attenuation in the interstellar medium and the status of observations from other groups.

The initiation and development of Extensive Air Showers, as well as detection of cosmic ray and γ-ray showers in particular the muon content of Ultra High Energy and Extremely High Energy showers is discussed in Chapter 2.

Chapter 3 describes the Buckland Park Extensive Air Shower Array, the various components of the array as well as the techniques used for analysing data. Included in the discussion are the improvements made by the author to the array and data analysis with emphasis on methods for shower front curvature correction to the data and methods for determining the angular resolution of the array. The improvements to the arrays performance made by the author are shown to be consistent with expectation.

A brief discussion of the SUGAR array parameters is made in Chapter 4. The techniques for the analysis of data in searches for Ultra High Energy emission together with the results are presented in Chapter 5. Included is a summary of observations for each object. The final chapter summaries the results presented in this thesis.

Statement

This work contains no material which has been accepted for the award of any other degree or diploma in any university or other tertiary institution and, to the best of my knowledge and belief, contains no material previously published or written by any other person, except where due reference has been made in the text.

I give consent to this copy of my thesis when deposited in the University Library, being available for loan and photocopying.

DATE.....20/1/94.....

Acknowledgments

During my candidature many people have provided me with help and advice. To those people I have not mentioned - Thank you.

Firstly I would like to thank my supervisors Dr Roger Clay and Dr Bruce Dawson for their guidance and numerous valuable discussions. I would also like to thank Professor Murray Winn for making the SUGAR array data available for analysis in this thesis. Neville Wild is thanked for his patient assistance and discussions on technical matters. I am also greatful to other members of the group and general staff who have all helped me at some stage.

I have shared good times and laughs with many students and staff during my candidature. Particularly I would like to thank Mike, Petar, Gary, Janice, Andrew, Anthony S, Anthony L, Paddy, Terry, Phil and Greg.

Finally I would like to thank my parents for supporting and helping me during my time at University.

Note from the Author

In a project such as this which has involved other students in the development of the Buckland Park array, it is necessary to clarify the contributions made by the author. The author was responsible for:

- Retrieving and partial analysis of data from 1978 – 1982.
- Operating and Maintaining the Buckland Park array from November 1990 to January 1993 (which included improvements made to the array and analysis for UHE-γ-ray astronomy, as discussed in chapter 3).
- Complete analysis of data from May 1990 to January 1993
- Reanalysis of data from 1984 – 1989 for shower front curvature, as discussed in Chapter 3.
- All analysis in the searches for evidence of UHE & EHE neutral emission from several objects using the Buckland Park and SUGAR data sets; except where stated otherwise, as discussed in Chapter 5.

The following nomenclature have been adopted in this thesis. The labeling of γ-ray energies suggested by Weeks (1988)

Very High Energy (VHE) ... $(10^{10} - 10^{14})$eV
Ultra High Energy (UHE) ... $(10^{14} - 10^{17})$eV
Extremely High Energy (EHE) ... $(10^{17} - 10^{20})$eV

GeV ... 10^{9}eV
TeV ... 10^{12}eV
PeV ... 10^{15}eV
EeV ... 10^{18}eV

Contents

Chapter 1

Cosmic rays - An Overview

1.1 Introduction

Cosmic radiation is essentially highly energetic radiation consisting of extraterrestrial (and possibly extragalactic) particles and photons. The observed range of energies begins at around 10^8eV and extends up to 10^{20}eV. Currently it is the only source of high energy particles ($> 10^{15}$eV) available (however the Super-Conducting Super Collider (SSC) would have provided effective target energies above 10^{17}eV). Cosmic rays contribute approximately one-third of the energy density of the interstellar medium and are also responsible for about one-third of the background radiation at sea level (caused by cosmic rays interacting with the earth's atmosphere). Hence they are both astrophysically and practically significant.

Even though cosmic rays have been studied for more than 80 years, there are significant properties of the cosmic ray flux that remain unresolved. In particular, their composition, acceleration and origin. Recently the field of Ultra High Energy (UHE) γ-ray astronomy has hinted at possible sites for the origin and acceleration of cosmic rays but as yet the evidence for this is weak.

This chapter reviews the current knowledge of the properties of cosmic rays and the field of γ-ray astronomy.

1.2 Spectrum

The energy spectrum of cosmic rays has been studied extensively and is shown in Figure 1.1 for the range $10^{12} - 10^{20}$eV. The power law spectrum is, on the whole featureless apart from two small deviation in its slope, occurring at approximately $\sim 3 \times 10^{15}$eV (The Knee) and $\sim 10^{19}$eV (The Ankle). Below the 'knee' the power law index is about -1.6, changing to about -2.1 above 3×10^{15}eV. At lower energies $10^{12} - 10^{14}$eV the spectrum is well known from satellite, balloon and aircraft measurements. However at higher energies due to the rapidly falling flux, the spectrum has to be derived from indirect measurements made at ground level.

The Knee

Measurements in this region are dominated by fluctuations in Extensive Air Shower (EAS) development. In particular, proton-initiated EAS are subject to the largest fluctuations and ground based detectors will have a bias towards downward fluctuated (later developing) showers (Clay 1985). Hence, this bias must be accounted for when deriving the spectrum. Nevertheless the knee is an experimentally well established feature.

The explanations for the existence for the knee vary and none are conclusive. An early interpretation known as the 'Leaky Box Model' (Peters 1961) invoked a change of particle lifetime with energy. Given a population of nuclei all confined in a particular galactic magnetic region, each nucleus will leak out from this confined region depending on its rigidity $R \propto \left(\frac{E}{Z}\right)$ where E is the energy of the nucleus and Z is the atomic number. Cosmic Rays spiral along the magnetic field lines with a radius of curvature proportional to their rigidity. With increasing rigidity this radius (Larmor radius) increases until it approaches the size of the confined region, whereupon the particle escapes. However this model would then suggest a knee for each species of particles, protons lost first at some energy E_r followed by progressivly heavier elements up to iron at $26E_r$.

An alternative explanation was suggested by Karakula et al. (1974). The pulsar

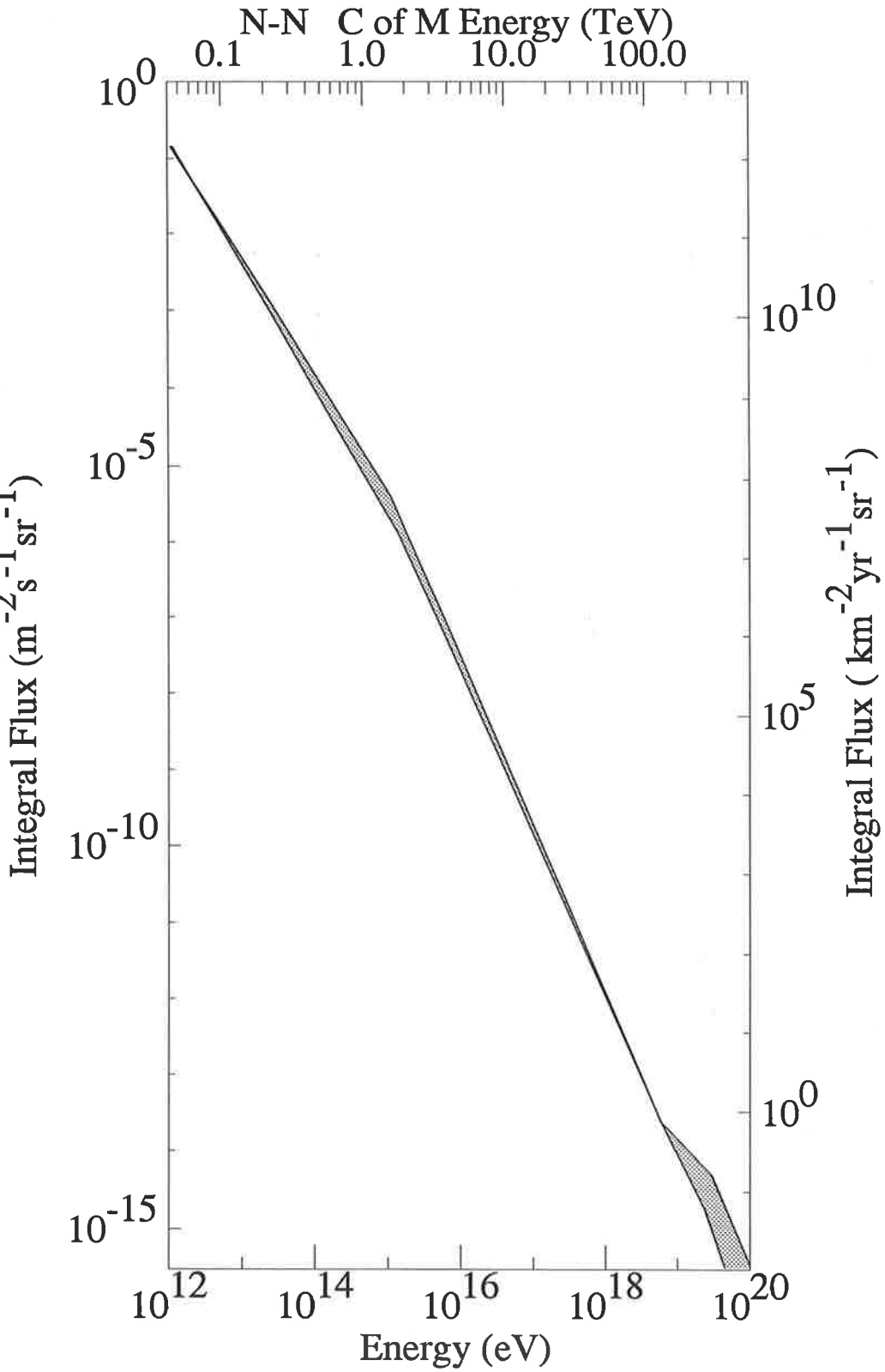

Figure 1.1: The primary (all particle) cosmic ray flux, measured at the top of the atmosphere, shown in integral form. The dotted regions indicate regions of uncertainty. (Adapted from Jones 1985)

model of Ostriker & Gunn (1969) was used together with available experimental data at the time on pulsars, to make a quantitative prediction of the expected primary spectrum at the earth. In this model pulsars accelerate particles up to $\sim 10^{16}$eV with an integral spectral index of -1.5, which results in a dominance of particles from this source in the region of the knee. The analysis reproduced a cosmic ray spectrum which was similar to the observations in the region $10^{14} - 10^{16}$eV.

A model proposed by Hillas (1979) suggested that if acceleration occurred in an environment with a high flux of photons, the onset of photopion production energy losses for protons and photodisintegration for iron nuclei would occur at similar values of energy per particle, and a relatively sharp break could be produced at the knee. Hence there could be an enhanced fraction of protons beyond the knee due to the destruction of nuclei by photodisintegration. A related model was suggested by Protheroe & Szabo (1992) in which a large fraction of the cosmic rays at and above the knee result from the decay of neutrons that escape from Active Galactic Nuclei (AGN) after their parent protons or heavier ions interact with the intense photon field during acceleration.

Between $10^{16} - 10^{19}$eV the region was thought to be featureless with an integral spectral index of -2.1, with good agreement between fluxes of several groups: Akeno (Teshima et al. 1990), Fly's Eye (Cassidy et al 1990), Havarah Park (Lawrence et al. 1991). However recently the Fly Eye group (Bird et al. 1993a) have shown a distinct break in the spectrum, Figure 1.2.

The Ankle

Following the discovery & interpretation of the 3K microwave background (Penzias & Wilson 1965, Dicke et al. 1965), it was suggested by Greisen (1966) and Zatsepin & Kuz'min (1966) that there could be a severe attenuation of the cosmic ray flux above $\sim 5 \times 10^{19}$eV resulting from interactions of cosmic rays with the microwave background (photopion production) if the sources of these particles were at distances of the order of tens of Mpc or greater. Hence the spectral shape in this region puts constraints on the origin and propagation of these extremely high energy particles.

An early report of a steepening of the spectrum above $\sim 10^{19}$eV (Krasilnikov et al. 1983) has not been confirmed by other experiments. A number of groups have claimed that the spectrum actually flattens above $\sim 2 \times 10^{19}$eV to -1.7 (Lawrence et al. 1991, Teshima et al. 1990, Cooper et al. 1990), producing the 'ankle' in the spectrum. Recently the Fly's Eye group published their spectrum above 10^{17}eV which shows a distinct break in the spectrum at $\sim 4 \times 10^{18}$eV. The change in integral spectral index is from -2.4 to -1.7 (Bird et al. 1993a).

Hill and Schramm (1985) investigated the effect of the microwave background on the UHE cosmic ray spectrum as a result of large scale propagation. Photopion production, pair production ($\gamma \rightarrow e^+e^-$), and the red shifting of cosmic ray energies were found to be the dominant effects. These effects result in a spectral enhancement at $\sim 6 \times 10^{19}$eV from the pile-up of energy degraded nucleons, preceded by a dip at $\sim 10^{19}$eV produced by the combined effects of a pile-up and pair production (data from the Haverah Park array were interpreted here).

Subsequent calculations by Hill et al. (1986) using Fly's Eye data suggested that the flattening in the spectrum cannot be interpreted as the recoil proton pile-up. Instead they suggest two possible phenomena: (i) The emergence of a flatter extragalactic component, crossing the steeper, presumably galactic, spectrum or (ii) the pile-up of an arbitrary injection spectrum above E$\sim 10^{20}$eV.

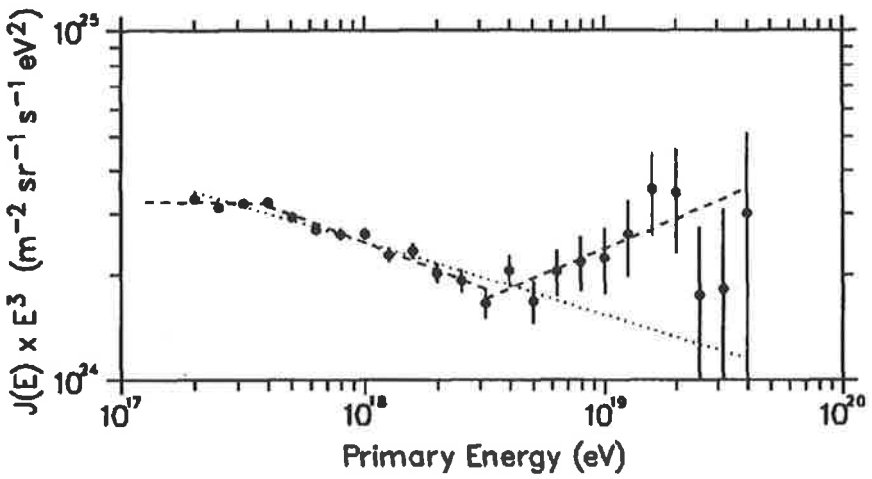

Figure 1.2: The Fly's Eye stereo differential energy spectrum (multiplied by E^{-3}. The dashed line is the best fit in each region, the dotted lined is the best fit below $10^{18.5}$ (from Bird et al. 1993)

1.3 Composition

Below energies of $\sim 10^{13}$eV the composition is well determined by direct (satellite) measurements. The standard low energy composition is shown in Figure 1.3, where a comparison with solar system abundances has been made for Z$\leq$ 28 (nickel). There is an overall agreement except for two obvious places. The cosmic ray hydrogen and helium abundance is less (Meyer 1985), and there is an over-abundance of the light elements Li, Be, B as well as in the region below Fe, namely Sc, Ti, V, Cr, and Mn. It is widely agreed that this relative overabundance is due to spallation of certain primary cosmic ray nuclei (C, N, O, and Fe).

At UHE energies the composition is much less well defined. Information has to be inferred from extensive air showers (EAS), and relies upon models of EAS logitudinal development and lateral parametrization. The composition in the region of the 'knee' in the spectrum is subject to considerable debate. Results from different experiments are subject to inherent problems with selection biases and interpretation (Sokolsky et al. 1987 and references therein). As a result, data from different experiments must be treated carefully.

In the energy range $10^{15} - 10^{16}$eV it has been suggested that the composition is predominately heavy (Yodh et al. 1984, Dawson et al. 1989), becoming lighter above $\sim 10^{16}$eV (Thornton & Clay 1979, Linsley & Watson 1981). However, experiments based on muon multiplicities (Cebula et al. 1990, Chudakov et al. 1991) suggest that in the energy range $\sim 3 \times 10^{13} - 3 \times 10^{15}$ a light composition is favoured, but the reliability of using this technique alone was brought into question by Lloyd-Evans (1991).

At higher energies E $> 10^{17}$eV there is better agreement between experiments. The elongation rate L_E which is defined as the rate of change in the average depth of shower maximum per $\log_{10}$(energy) gives a value of 65 to 70 gcm^{-2} per decade of energy as measured by the Fly's Eye and Havarah Park groups.

Recent results from the Fly's Eye group (Bird et al. 1993c) using only their stereo

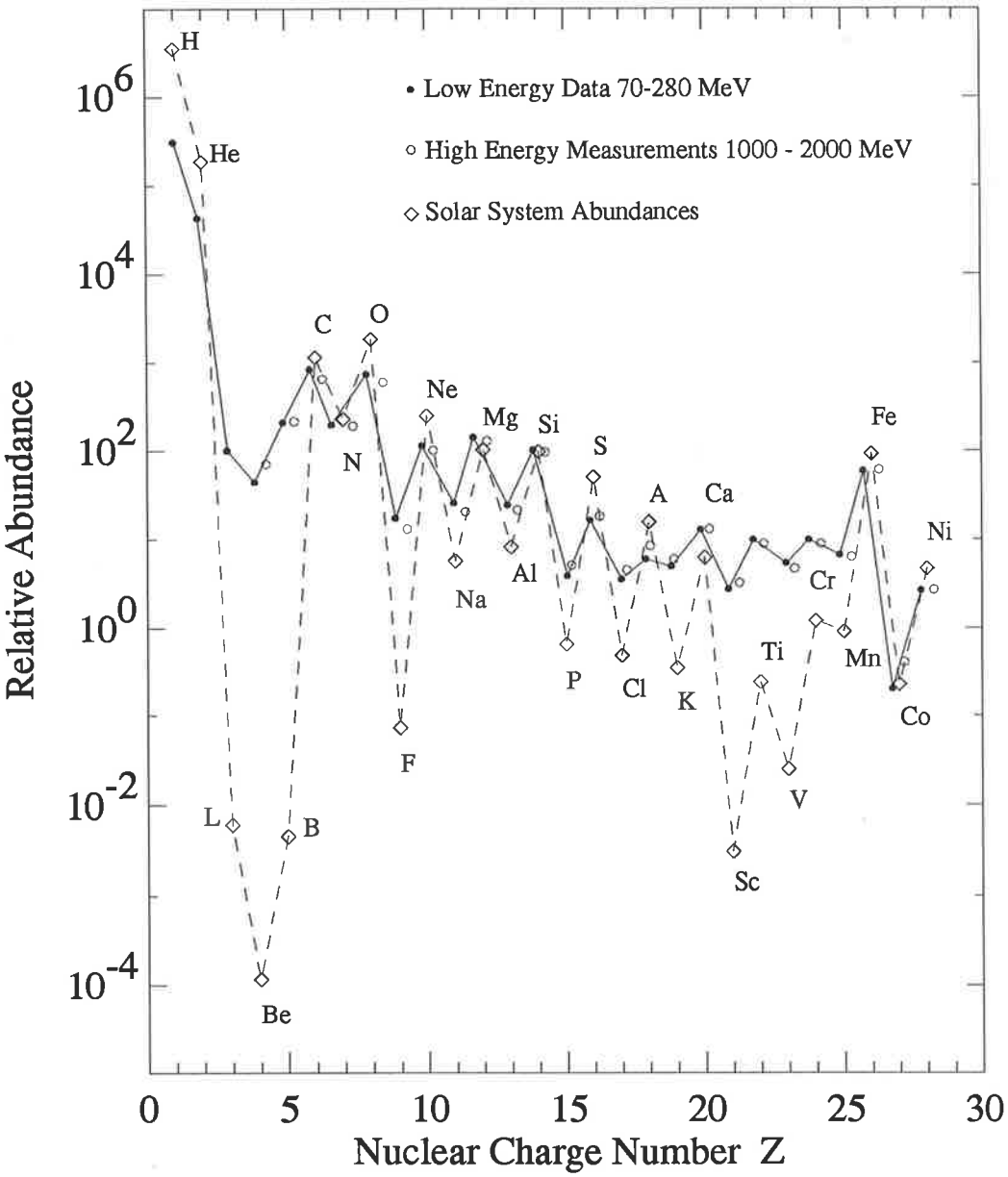

Figure 1.3: The cosmic ray element abundances measured at Earth compared to the solar system abundances, all relative to silicon which is given a value of 100 (Adapted from Simpson 1983)

data and improved statistics suggest that below 3×10^{17}eV the composition is consistent with an unchanging composition, quoting a value of $L_E = 50$ gcm^{-2}. However it appears that above $\sim 3 \times 10^{17}$eV there is a break in the elongation rate, changing to ~ 79 gcm^{-2} at 10^{19} eV. They argue that this increased slope is consistent with a changing composition from a heavy mixture to a predominately light one in the range from $3 \times 10^{17} - 10^{19}$eV.

1.4 Anisotropy

At low energies (< TeV) it is expected that the galactic anisotropy would be substantially determined by the magnetic field topology in a small region ($\sim$ 1pc) around the solar system. Unfortunately this topology is not at all well known. At higher energies, where the large scale structure of the galactic magnetic field is better known, a clear anisotropy may result (Lloyd-Evans 1991). However there does not appear to be any significant broad harmonic anisotropies above 10^{14}eV.

Linsley & Watson (1977) completed a survey of medium energy anisotropy based on experiments from 1951-1965. There were 42 results from 20 independent experiments. Most were air shower counting experiments using atmospheric collimation for directional information. The data were grouped in three decade ranges from ($10^{14} - 10^{17}$)eV and showed an apparent clustering of intensity maxima around 17.5 hours R.A.

More recent measurements have become available from arrays operating from the 1970s onwards, and the recently decommissioned Havarah Park array from 1963 onwards. These data are in general agreement with the previously results. At energies below 10^{15}eV there appears to be a progressive increase in the amplitude of the first harmonic with energy and good agreement in phase. Further up in energy the phase of the first harmonic shows a change from about 18 hours to $\sim$ 5 hours as the energy of observation moves through the knee (Clay 1985).

Clay (1984) has pointed out that there is no reason to expect results from the northern and southern hemispheres to be similar. Most northern observations were obtained at latitudes 20°N to 60°N and most southern observations were made between 15°S to 40°S. Given the limited ranges of of zenith angle of air shower arrays at these energies $\sim 10^{15}$eV, quite separate regions of the sky have been studied.

However, using harmonic analysis (fitting a sine wave to the data), it was noted by Clay (1984) that a minimum in intensity will be interpreted as a maximum intensity 180° away. If there were a general flow of cosmic rays along the spiral arm

(in the direction of the galactic magnetic field), there would appear a maximum in intensity in the direction of the source arm viewed in one hemisphere, and a minimum in intensity away from the source arm viewed in the other hemisphere. Therefore it would be possible to compare both northern and southern observations, one set measuring the inward flow, and the other the outward flow, giving a good agreement in phase.

Clay (1984) and Clay et al. (1993) have suggested that the observed change in phase may be due to a change in the direction of flow just above the knee. Below this energy, the particles would be of galactic origin, streaming outward along the spiral arms, resulting in a maximum in the north and a minimum in the south. Above this energy the particles may be of extragalactic origin streaming inwards, following the arms less as the energy and hence Larmor radius increases.

At higher energies ($E > 10^{17}$eV) results are much less clear. Most contributions come from the northern hemisphere, the most significant from the Havarah Park array (Lawrence et al. 1990b), and others from the Fly's Eye (Cassiday et al 1990a); Akeno (Matsubara et al. 1990); Yakutsk (Efimov 1987); and Volcano Ranch (Cunningham et al. 1977). In the southern hemisphere the SUGAR array has provided the most significant contribution (Horton et al. 1983).

The results are in general only upper limits restricted by statistics. There appears to be an increase of amplitude with energy, but no real phase agreement. Wdowczyk & Wolfendale (1983) had suggested that there could be a contribution to anisotropy around 10^{17}eV from γ-rays due to the different spectral index of γ-rays and cosmic rays at $\sim 10^{8}$eV. However this is not observed.

The significance of medium & high energy ($10^{14} - 10^{19}$eV) anisotropy has been examined by Lloyd-Evans (1982) and in more detail by Clay (1987). It was found by Clay (1987) that while many published results individually suggested quite high confidence levels of real measured anisotropy, the data taken as a whole are less convincing. Although there was some internal phase consistency, it was found from Monte Carlo simulations that this occurred purely randomly 20% of the time, and

therefore an 80% confidence level was placed on the observed phase consistency. The measured phases can be plotted by adding appropriate multiples of 360^o as shown in the figure below.

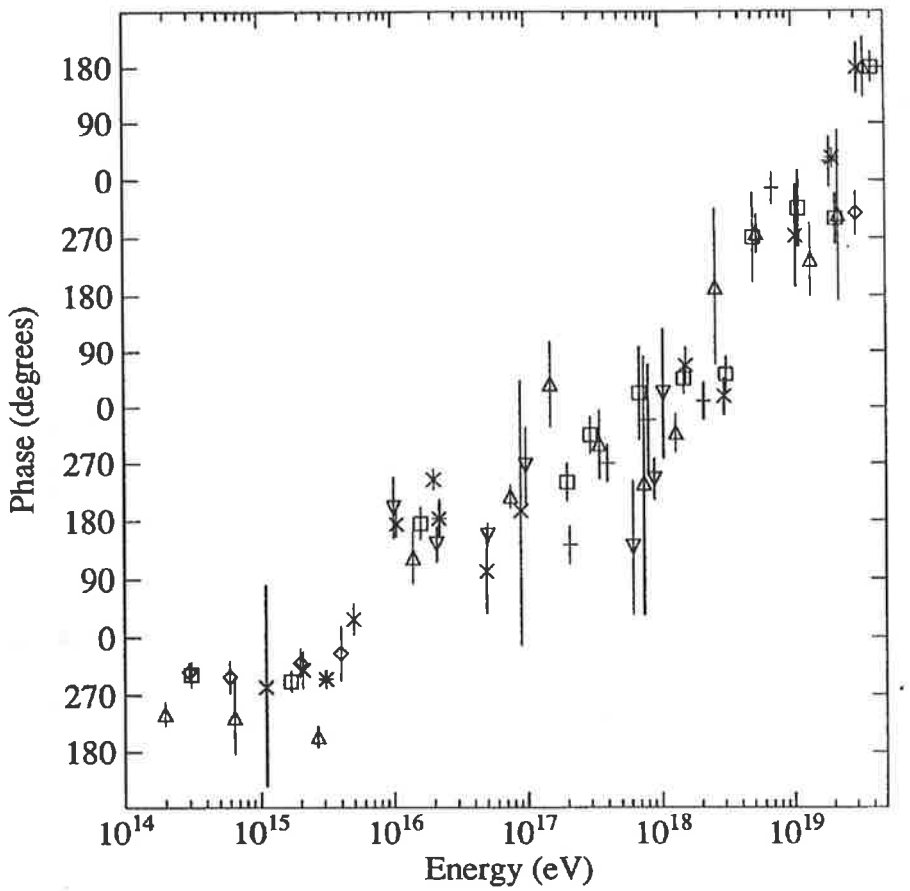

Figure 1.4: A compilation of medium and high energy anisotropy, first harmonic phase measurements (from Bird 1991).

For E $< 10^{17}$eV

◇ Daudin et al. (1956)

△ Delvaille et al. (1962)

× Kifune et al. (1986)

□ Linsley & Watson (1977)

▽ Cranshaw & Galbraith (1954)

∗ Lloyd-Evans (1982)

For E $> 10^{17}$eV

∗ Efimov et al. (1990)

◇ Matsubara et al. (1990)

△ Cassiday et al. (1990)

× Eames et al. (1985)

+ Efimov et al. (1987)

□ Lloyd-Evans (1982)

▽ Kifune et al. (1986)

o Horton et al. (1983)

1.5 UHE γ–Ray Astronomy

The recent motivation for observations of VHE and UHE γ-rays lies in the relationship between possible sites of UHE γ-ray production and cosmic ray origins. The interstellar medium is relatively transparent to γ-rays (see §1.5.3), and they propagate directly from their production region, whereas cosmic rays being charged will deviate in the interstellar magnetic fields. It is believed that γ-rays are produced when cosmic rays interact with interstellar matter or radiation fields. Therefore experimental evidence for UHE γ-rays originating from discrete sources such as X-ray binaries, supernovae, active galaxies etc, with sufficient power and numbers may settle the issue of cosmic ray origin, at least at UHE energies.

It was first suggested by Cocconi (1959) that there was a possibility of detecting primary γ-rays with air shower arrays. Searches for point sources of γ-rays with energy E> 10^{14}eV would be possible with this technique, because at these energies only ground arrays have the necessary acceptance (ie. area $\times$ solid angle $\times$ time). However it was not until Samorski & Stamm (1983) presented evidence for γ-rays above 10^{15}eV from Cygnus X-3 did the field of UHE γ-ray astronomy using ground based arrays seriously begin.

During the intervening period it is not clear whether there was insufficient data from the existing ground arrays, or a lack of knowledge of potential sources for searches to be made. As a consequence of the first observation of UHE γ-rays, many arrays were built in anticipation of detecting sources of γ-rays. These arrays which are currently operating such as CASA (Cronin et al. 1992), Cygnus (Alexandreas et al. 1992) and Tibet ASγ (Amenomori et al. 1993) have characteristics such as energy & angular resolution which are much better than earlier arrays. Despite this, the anticipated confirmation of the Cygnus X-3 result of Samorski & Stamm (1983) and/or the discovery of other γ-ray sources have not occurred. In fact recent results from the northern hemisphere arrays have mostly been upper limits, and in some cases the upper limits have been lower than previous claims of positive results.

One possible explanation for the null observations ($< 3\sigma$) is that binary systems like Cygnus X-3 are variable in their production of γ-rays and that they are currently in a non γ-ray producing state (ie. switched off). Alternatively it is possible the γ-ray spectrum is harder (flatter) than the background cosmic ray spectrum and given the lower threshold of these new arrays ($\sim 10^{14}$eV), they would need to operate for much longer to obtain positive observations

1.5.1 Status of UHE Observations

The flux reported by the Keil array for Cygnus X-3 was 7.4×10^{-14} cm^{-2} s^{-1} above 2×10^{15}eV. Subsequent observations made by several groups in the northern hemisphere reported positive detections. Although none of the observations were highly significant it appeared that there was some consistency in the reported orbital phase of emission, usually $0.2 - 0.3$ or $0.5 - 0.7$ (Protheroe 1987).

However it appears that after approximately 1986, UHE observations of Cygnus X-3 have not shown any positive results, and in fact the flux since the first observation of 1976 to 1980 has shown a steady decline. Typical fluxes in 1985 are a factor ~ 100 lower than those observed around 1976 (Protheroe 1993). The current steady state upper limits from CASA is $< 3 \times 10^{-13}$ cm^{-2} s^{-1} above 1×10^{14}eV (Cronin et al 1992) and from the Cygnus array $< 2 \times 10^{-13}$ cm^{-2} s^{-1} above 4×10^{13}eV (Alexandreas et al 1991).

At higher energies there has been stronger evidence for either γ-ray or neutron emission from Cygnus X-3. The distance to Cygnus X-3 is sufficiently close that at energies $\sim 10^{18}$eV it is possible that neutrons can be detected (Jones 1988). The Fly's Eye group claimed a detection of Cygnus X-3 at a significance of 6×10^{-4} above 5×10^{17}eV by combining all their data from 1981 to 1988 in the form of a contour map of the sky (Cassiday et al. 1990b). The flux was estimated to be 2×10^{-17} cm^{-2} s^{-1}. However subsequent analysis of more recent data (1988 to 1990) did not show an excess, the upper limit (95% CL) was set at 1.4×10^{-17} cm^{-2} s^{-1} (Cooper et al. 1990).

The Akeno group reported a 3.5σ excess from the direction of Cygnus X-3 using data from 1984 to 1986 (Teshima et al 1990). The flux was estimated to be 1.4×10^{-17} cm^{-2} s^{-1} above 5×10^{17}eV essentially confirming the Fly's Eye claim. More recently data taken with AGASA between 1990 and 1991 has shown a 4σ DC excess and they quote a flux of 3.4×10^{-17} cm^{-2} s^{-1} above 3×10^{17}eV (Hayashida et al 1991).

Other northern hemisphere arrays capable of observing Cygnus X-3 at these energies have not reported positive results. The Havarah Park group analysed all their data as well as a subset of data (1982 to 1987) coincident with the original Fly's Eye detection but only report an upper limit (95% CL) of 5×10^{-18} cm^{-2} s^{-1} above 5×10^{17}eV (Lawrence et al 1989). This upper limit is lower than the Fly's Eye and Akeno results. It was noted that the Havarah Park latitude is less favorable for viewing Cygnus X-3 and that it was more responsive to muons and therefore may not trigger efficiently on muon poor γ-ray showers (Sokolsky et al. 1992).

Observations of Hercules X-1 have a similar pattern to that of Cygnus X-3. Many of the early observations have not been confirmed by more recent observations, despite the fact that it is the most extensively observed binary source at TeV and PeV energies. There have been more than 18 reports of individual episodes of emission made by 7 independent experiments, many of which consist of short episodic outbursts at or close to the X-ray period (Weeks 1992).

The most interesting and possibly the most significant observation of episodic emission was the blue shifted observations made in 1986 by three independent groups (Lamb et al. 1988, Resvanis et al. 1988, Dingus et al. 1988). All three observations were blue shifted by the same amount from the neutron star pulsar period of 1.24 seconds.

Recently it appears that Hercules X-1 has not shown any signs of outbursts. The

90% CL upper limits from CASA and Cygnus are $< 6.6 \times 10^{-13}$ cm^{-2} sec^{-1} above 1.1×10^{14}eV (Cronin et al. 1992) and $< 1.6 \times 10^{-13}$ cm^{-2} sec^{-1} above 4×10^{13}eV (Alexandreas et al. 1991) respectively.

Other sources such as those observable from the southern hemisphere have not been studied in such detail, largely due to the lack of air shower arrays operating in the southern hemisphere. A summary of past results is presented at the beginning of the discussion of each of the sources in Chapter 5.

1.5.2 Possible Acceleration Mechanisms

The conventional picture of an accreting X-ray binary star system is one in which a compact object, usually a neutron star is in orbit around a companion star from which it accretes matter. Models have been constructed to explain the likely acceleration methods of charged particles within the environment of the binary star system, however none are conclusive (see Weeks 1988, Nagle Gaisser & Protheroe 1988). The production of UHE γ-rays in all models are thought to result from the decay of neutral pions which are formed when these accelerated particles interact with some target material (beam dump). Three classes of acceleration are discussed below.

Pulsar Dynamo Acceleration

In this model the power for particle acceleration is derived from the rotation of the neutron star. This rotation is expected to give rise to large electric fields which can accelerate particles in the vicinity of the neutron star. It is unlikely that electrons can be accelerated efficiently due to the large synchrotron loss within the magnetic field present, therefore either protons or nuclei constitute the accelerated beam.

In such a model the atmosphere of the companion star may provide sufficient target material in which to convert the beam into UHE γ-rays (Vestrand & Eichler 1982). Figure 1.5a shows a schematic diagram of this type of process. As seen by the observer this condition is met twice, just before and just after eclipse, at orbital phase ~ 0.8 and ~ 0.2 (of course the actual phases would be dependent on the inclination of the binary system as viewed from the earth).

Emission at different phases (0.6 - 0.7) such as those observed at X-ray maximum from Cygnus X-3 is possible by the accretion tail model (Hillas 1987c). This is a variation on this process in which the accelerated beam drives off a lump of material from the atmosphere of the companion star which acts as target material, Figure 1.5b.

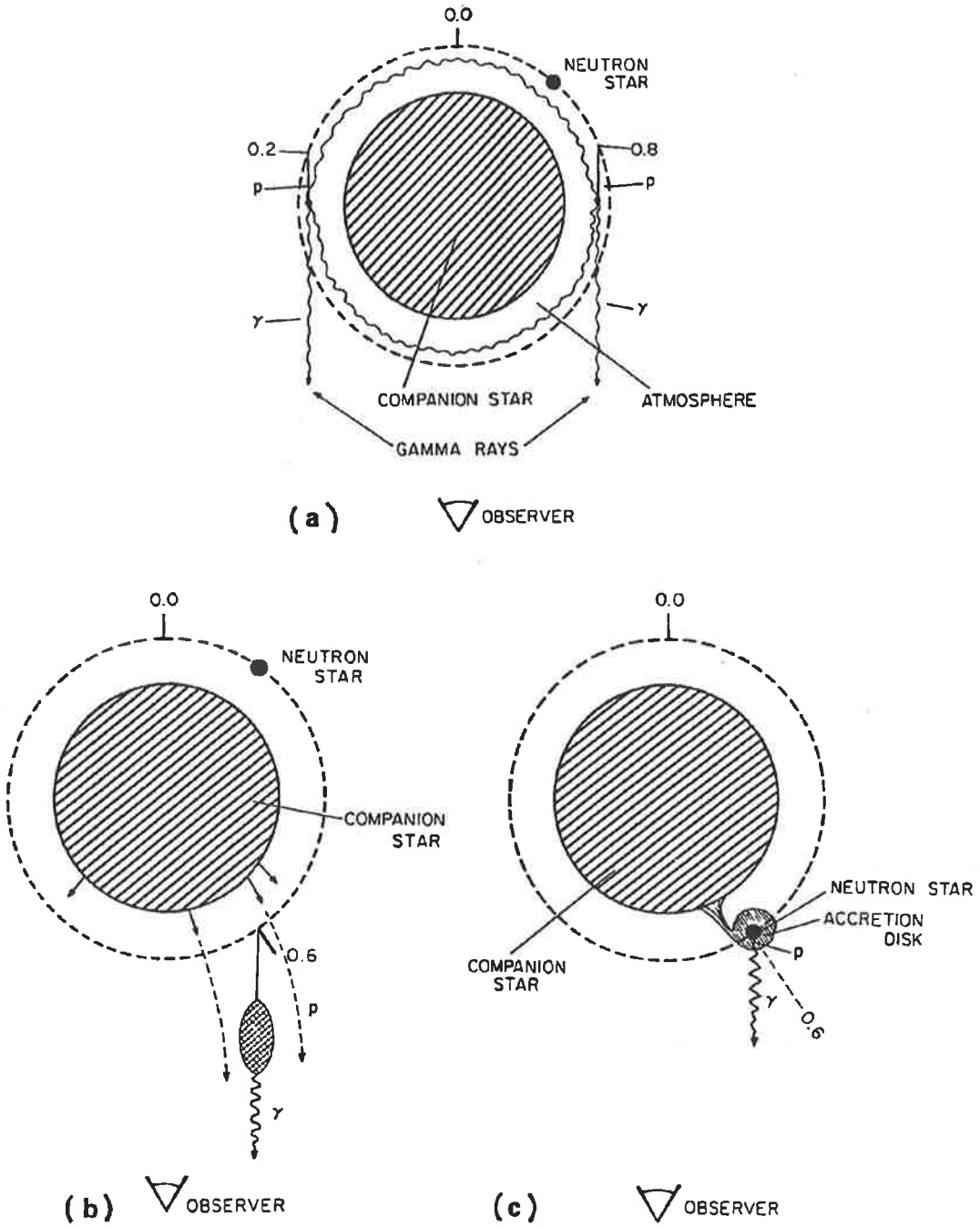

Figure 1.5: The geometry of typical binary star systems showing the possible sites for the production of UHE γ-rays (Weeks 1988). (a) The atmosphere of the companion star serves as a site for conversion of accelerated particles into γ-rays (b) Accelerated beam of particles drives off a lump from the companion stars atmosphere, where particles are converted into γ-rays (c) Acceleration occurs within the accretion surrounding the neutron star. See text for details.

Disk Dynamo Acceleration

Unlike the pulsar dynamo model, this form of acceleration derives its energy from the accretion disk surrounding the neutron star. Matter on the accretion disk which contains its own magnetic field intersects with the magnetic field of the neutron star, and gives rise to a $v \times B$ electric field starting at the inner edge of the accretion disk, where v is the velocity of the accretion particles in the disk and B is the surface magnetic field of the neutron star (Chanmugam & Brecher 1985).

It would be possible to accelerate particles up to $\sim 10^{16}$eV across the accretion disk for neutron stars with relatively small magnetic fields (B$\sim 10^8$ gauss). Again for acceleration up to these energies it is assumed that protons or heavier ions would be involved as electrons would lose energy through synchrotron radiation.

The outer edge of the disk or a bulge within the disk itself may provide a beam dump to convert the accelerated particles into γ-rays, see Figure 1.5c. This method is plausible for systems such as Cygnus X-3 and 1822 -37.1 both of which have sufficiently low neutron star magnetic fields.

Shock Acceleration

Again in this type of acceleration the energy is derived from the accretion disk near the surface of the neutron star. Matter accreting at close to the velocity of light onto the neutron star forms a shock within the accretion flow where there is a pile-up of slower moving matter close to the neutron star. First order Fermi acceleration may occur at this shock. Particles cross back and forth between the two sides of the shock increasing in energy with each crossing (Eichler & Vestrand 1985).

It has been estimated that the maximum energy attainable would be of the order 10^{16}eV per particle (Kazanas & Ellison 1986). In a similar manner to the previous type of acceleration γ-rays may be produced where sufficient target material is found.

There are however problems with the models discussed above. Protheroe (1984) indicated that it was difficult to envisage a mechanism which could accelerate particles to sufficiently high energies ($\sim 10^{16}$eV) within a period shorter than the energy loss time of the environment. Also significant is that the power required to accelerate these particles is a large fraction of the total energy budget for the system, with the luminosity in these particles sometimes exceeding that in the X-rays (Hillas 1987).

Given these difficulties in imagining plausible acceleration methods, some models show promise in describing aspects of UHE observations such as the phase of emission. However no one model address all the problems or could explain emission from all X-ray binaries.

White & Holt (1982) have proposed the accretion disk corona (ADC) model to explain the asymmetrical light curve of the low mass X-ray binary 1822 -37.1. Two bulges on the outer rim of the accretion disk are used to explain the observed X-ray light curve, and this may provide possible target sites for γ-ray production (see §5.2.3). Protheroe & Stanev (1987) have used this model to provide a possible description of the observed time variability in flux and phase of UHE γ-ray emission from Cyg X-3.

Neutrons

It should be noted that apart from the likelihood of UHE γ-ray production, these environments are possible sources for neutrons, which may be produced by collision of high energy protons or nuclei with gas or dust in the vicinity of the pulsar or dissociation of complex nuclei by either sparse gas or dust, or by infrared photons in the vicinity of the pulsar (Jones 1988).

1.5.3 Photon Cascading in the Microwave Background

If the observed air-showers of UHE neutral particles from distant sources are attributed to γ-rays, it may be that these γ-rays would be attenuated by the 3K microwave background. Photons of energy above about 10^{14}eV which traverse large distances are expected to interact with microwave photons producing an electron positron pair ($\gamma + 3\mathrm{K}\gamma \rightarrow \mathrm{e}^{\pm}$). However, further studies showed that this depletion of γ-rays may be partially compensated for by the electrons undergoing inverse Compton scattering subsequently producing γ-rays.

Protheroe (1986) performed a detailed Monte Carlo simulation to investigate the propagation of γ-rays over large distances to see what effect this would have on the observed spectra of extra-galactic sources. His conclusions were that, inverse Compton scattering must occur before electrons lose a significant fraction of their energy by synchrotron emission, hence the magnetic field between galaxies must be sufficiently low ($< 10^{-7}$G). However for electrons of energy $\sim 10^{14}$eV the field has to be even lower ($< 10^{-10}$G) so that the Larmor radius is less than or comparable to the interaction length in the cascade, thereby allowing the secondary UHE γ-rays to retain their directional information.

Sources in the Large Magellanic Cloud, should have energy spectra which exhibit an absorption dip at $10^{14} - 10^{16}$eV together with an excess just below 10^{14}eV from the energy degraded photons in the dip (Figure 1.6a). The shape of the spectrum (if it could be accurately measured) may contain information on the average strength of the magnetic field and distance to the source.

The spectra corresponding to the active galaxy Centaurus A is shown in Figure 1.6c. If $10^{15} - 10^{16}$eV γ-rays were to be observed from Centaurus A then they would be due to primary γ-ray energies of $10^{18} - 10^{19}$eV. The flux would be down a factor $\sim 10^3$ compared to the situation where the microwave background was not present, which appears to be unacceptably high at these energies (Protheroe 1986). So far no strong claims have been made for Centaurus A at energies above 10^{15}eV, however there is some evidence for γ-ray emission at energies up to 10^{14}eV, see §5.2.1.

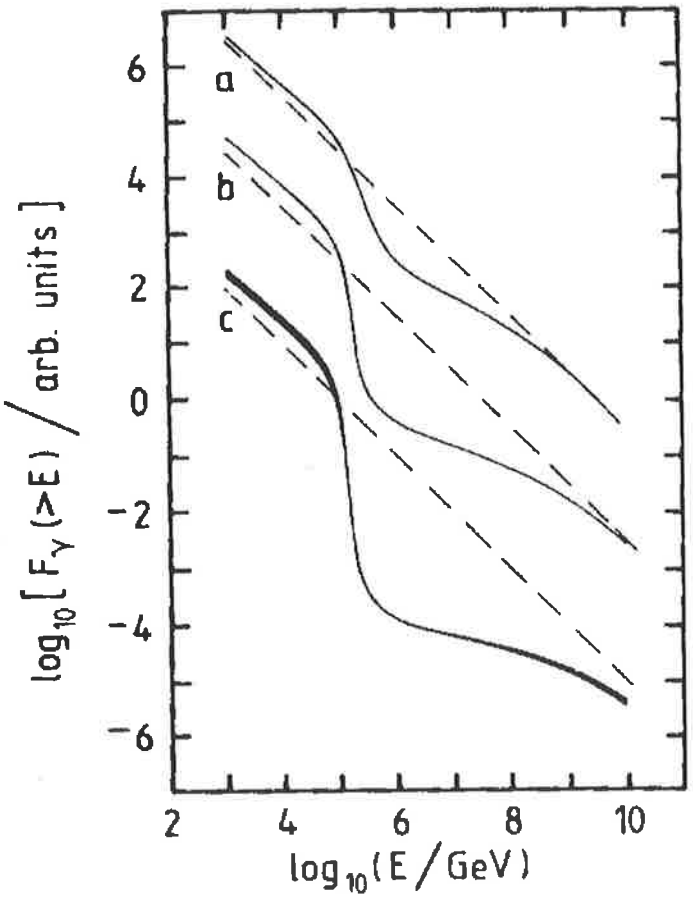

Figure 1.6: Integral energy spectrum of γ-rays after attenuation in the microwave background at distances of (a) 50kpc, (b) 500kpc and (c) 5Mpc from the source (Protheroe 1986).

Chapter 2

Extensive Air Showers

2.1 Introduction

This chapter deals with the interaction of the cosmic radiation with the atmosphere. It examines components and properties of the air shower as a whole which are relevant to its detection and ends with a discussion of γ-ray initiated air showers. There are three components which characterize an air shower, namely the nuclear (hadronic), muon (hard), and electromagnetic (soft) components. The scope of this thesis is largely centered on the detection and interpretation of the electromagnetic component, and to a small extent the muon component. A discussion of these components and their properties follows.

2.2 Nuclear Component

In general, when a high energy cosmic ray particle interacts with an air nucleus (eg N, O), approximately 50% of its energy is lost. The effective size of an incident proton at these energies (10^{15}eV) is much less than the size of a target nucleus, and so the proton can be thought of as a discrete particle that interacts with individual nucleons. The principal products of this interaction are pions ($\pi^+\pi^-\pi^0$). The interaction length for a proton primary is energy dependent and for a proton of

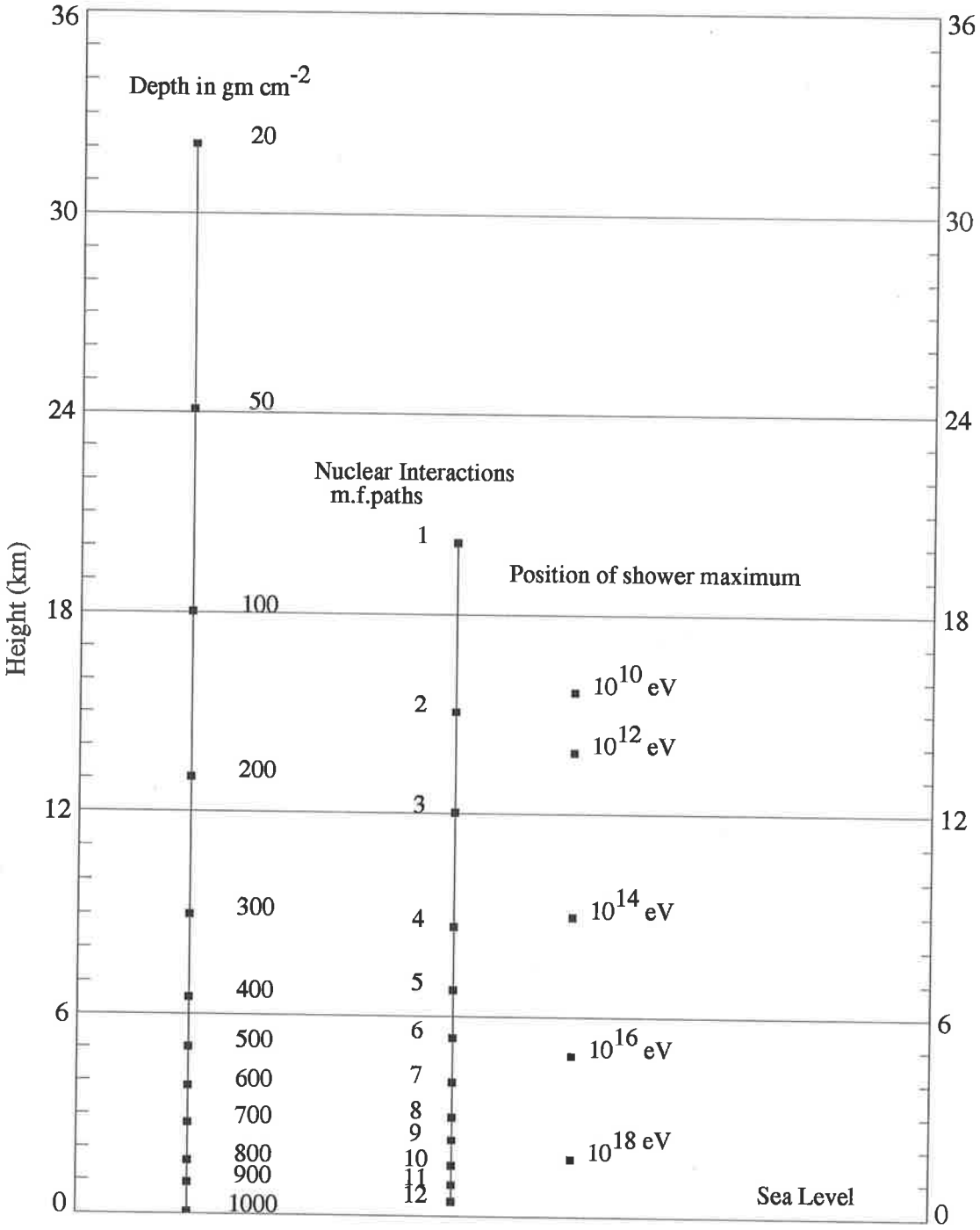

Figure 2.1: Growth of a vertical extensive air shower in the earth's atmosphere (Adapted from Allan 1971)

energy E, can be described by

$$\lambda_p = 67.2 \left(\frac{E(TeV)}{100} \right)^{-0.065} gcm^{-2} \tag{2.1}$$

(Dawson 1985)

In contrast, when a cosmic ray nucleus (eg Fe) interacts head-on with a target air nucleus several pairs of nucleons undergo pion production. However, grazing interactions are much more common, where only a few nucleons interact to produce pions. As with the case of a cosmic ray proton primary the target air nucleus is left in an excited state ejecting nuclear fragments (light nuclei), protons and neutrons. The difference is that the incident nucleus leaves with a stream of relativistic fragments, and these fragments may develop into separate showers. Thus the EAS may have more than one core. The interaction length for an iron primary in the atmosphere is essentially independent of energy, $\lambda_{Fe} \sim$ 13 gcm^{-2}.

Hadronic interactions mostly produce pions and kaons (kaons produced at about 10% of the rate of pions). Three types of pions are produced ($\pi^o\pi^+\pi^-$). The neutral pions decay to a pair of gamma rays ($\pi^o \rightarrow 2\gamma$) which contribute to the electromagnetic (EM) cascade. The charged pions, which have a longer half-life, will either interact or decay depending on the atmospheric density. In the case of decay they produce muons which contribute to the muon component of an EAS.

The kaons are produced in all four species ($K^+K^-K^o\overline{K}^o$). Neutral kaons decay to produce pions, muons and electrons. As in the case of charged pions, charged kaons may interact or decay to pions and muons. Hence the decay products of kaons also contribute to the EM and muon components of an EAS, but to a lesser extent.

The nuclear component of an EAS consists of the leading particle and those secondary hadrons produced in the fragmentation region. Those hadrons which survive to ground level are found within a few meters of the core. This is due to the limited transverse momentum given to the hadrons in the interaction, and the relatively large mass and high energies of these particles which minimize Coulomb scattering.

2.3 Muon Component

The muons in an EAS result from the decay of charged pions and kaons. Smaller contributions are made by pair production, and photoproduction of pions which decay to muons (see §2.5.1). They are often known as the hard component, and have a half-life of 2.2×10^{-6}s. Even though this half-life is small, those which have a Lorentz factor ≥ 20 will reach sea-level before decaying. The dominant energy loss mechanism for muons in the atmosphere is ionization, roughly 2 MeV per gcm^{-2}, so to pass through the entire atmosphere vertically (~ 1000 gcm^{-2}) a muon would need at least 2 GeV of energy. It is thought that those muons, resulting from the decay of pions early in the EAS, give information on the early particle interactions and, possibly, the composition of the primary cosmic ray.

Less energetic muons decay before reaching ground level, and contribute to the electromagnetic component through,

$$\mu^+ \longrightarrow e^+ + \nu_e + \overline{\nu_\mu}$$

$$\mu^- \longrightarrow e^- + \overline{\nu_e} + \nu_\mu$$

Muons in general constitute 10% of the total number of particles in a 10^{15}eV shower at ground level. The average energy of a muon at sea-level is $\sim$ 5GeV with a median energy of $\sim$1GeV (Allan 1971). In contrast, the average energy of a particle in the EM component at ground level is $\sim$20 MeV, so the muon component carries much more energy of the air shower to ground level than the EM component.

At the lower primary energies ($< 10^{14}$eV) the muon component is more likely to survive to ground level than the EM component and, due to the rapidly falling cosmic ray spectrum, these muons make up the bulk of the secondary particles. It is these unaccompanied muons which contribute mainly to the observed secondary flux of 1 particle cm^{-2}min^{-1}.

2.3.1 Muon Lateral distribution

The muon lateral distribution is related to the transverse momentum of the parent pions and kaons and the height of their production. Although the transverse component of the momentum is small, the height is relatively large and so there is a large lateral spread at ground level. Those particles found furthest from the center of the shower generally speaking are produced early in the shower and have the lowest energy (because of the greater distance traveled in the atmosphere). The shape of the distribution is flatter than the corresponding EM component distribution (see below) and is parameterized as

$$\rho\left(N_{\mu}, r\right) \propto r^{-0.75}\left(1+\frac{r}{k}\right)^{-2.5} \tag{2.2}$$

(Greisen 1960)

where k is a function of shower age and zenith angle, ρ is the density of particles at a distance r and N_{μ} is the total number of particles.

Muons are more penetrating than the EM component of an air-shower. Consequently muon detectors are usually covered with a dense material (eg dirt, concrete) which effectively cuts out the EM component. For example the Sydney University Giant Air Shower Recorder (SUGAR) which detected the muon component of air-showers, had detectors buried approximately 1.5 metres under the ground (see Chapter 4). The distribution used to fit the SUGAR data was a modified version of the Greisen muon lateral distribution

$$\rho(\mathrm{r}) = \mathrm{N}_{\mu}\mathrm{k}(\theta)\mathrm{r}^{-0.75}\left(1+\frac{\mathrm{r}}{\mathrm{r_o}}\right)^{-\mathrm{b}} \tag{2.3}$$

where $\mathrm{k}(\theta)$ is a normalization constant

$$\mathrm{k}(\theta) = \frac{\Gamma(\mathrm{b})}{2\pi \mathrm{r_o^2}\Gamma(2-\mathrm{a})\Gamma(\mathrm{a}+\mathrm{b}-2)}$$

Here $r_o = 320\mathrm{m}$

$\mathrm{a} = 0.75$

$\mathrm{b} = 1.5 + 1.86\cos(\theta)$

2.4 Electromagnetic Component

Even though muons dominate the secondary particles at ground level at low energies, above $\sim 10^{14}$eV the electromagnetic component becomes the most numerous containing approximately 90% of the total number of charged particles in an air-shower. Below this energy the EM component is largely absorbed by the atmosphere.

The production mechanism of the EM component is fairly well understood (Rossi & Greisen 1941). Neutral pions produced in the hadronic interactions decay to produce two γ-rays ($\pi^o \rightarrow \gamma\gamma$). These γ-rays may pair produce in the field of atmospheric nuclei producing electron positron pairs ($\gamma \rightarrow e^+e^-$). The electrons emit bremsstrahlung radiation producing further γ-rays. In this way a cascade of particles and photons is produced increasing the number of particles and reducing the individual energies proportionally.

This cascading process develops until the particle number reaches a maximum, at which point the particle loss rate is equal to creation rate. There is a critical energy

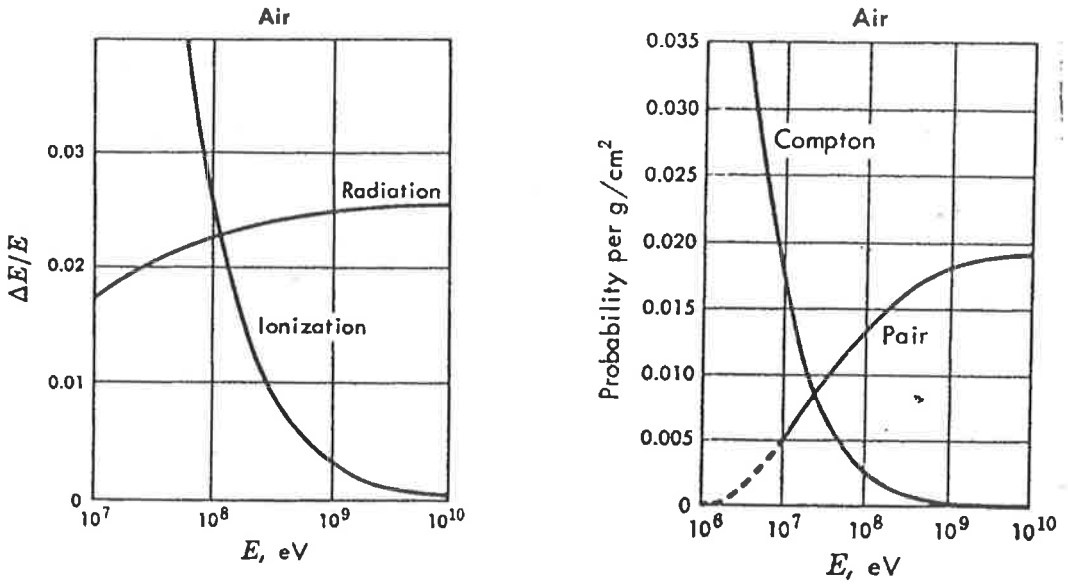

Figure 2.2: Fractional energy loss by ionization and radiation for electrons (left) and the probability that a photon will undergo a Compton collision or pair produce as function of photon energy (right), from Rossi 1964.

where this happens and for electrons it is when the average energy per particle is $E_c^e \sim 84$ MeV below which ionization loss becomes more dominant than the loss by bremsstrahlung radiation (see Figure 2.2). At these lower energies fewer photons are produced and the shower size drops off rapidly. Above this critical energy, electrons have a mean fee path (mfp) between emission of bremsstrahlung radiation of one radiation length $X_o \sim 37 gcm^{-2}$.

For photons the critical energy is $E_c^\gamma \sim 20$ MeV [1]. Energy loss due to Compton scattering and the photo-electric effect become dominant below this energy. The mean free path for pair production above this energy is $\frac{9}{7}X_o$.

2.4.1 Approximation A

A simple model based solely on bremsstralung and pair production processes, known as Approximation A, provides a handle on the EM processes (Rossi 1952). It is assumed that the mean free path of both processes is X_o, and that a γ-ray of energy E_o initiates the cascade with the energy subdivided equally amongst the electrons and photons. Now the distance travelled over which there would be a 50% chance of either process occurring is $X_r = X_o \ln 2$, called the shower unit. Since the number of particles has doubled and the energy halved after each shower unit, there would be 2^n secondary particles after n interactions, with an average energy $E_{ave} = \frac{E_o}{2^n}$.

Shower maximum is reached when the average energy per particle is equal to the critical energy

$$E_{ave} = \frac{E_o}{2^n} = E_c$$

which leads to the number of particles at shower maximum

$$N_{max} = \frac{E_o}{E_c}$$

The position of shower maximum is defined as the number of interactions multiplied

[1] Effectively it is 80MeV for this component as well since any electrons produced below the photon critical energy will lose energy predominately through ionization

by the shower unit (ie nX_r). So combining the equation for the shower unit with the number of particles at shower maximum gives

$$X_{max} = nX_r = X_o ln\frac{E_o}{E_c} \tag{2.4}$$

This estimate for the shower maximum is fairly accurate despite the assumptions made (Allan 1971). The approximation correctly predicts the proportionality of shower size at shower maximum with the initial photon energy E_o, indicated by more detailed shower calculations.

Ionization is a significant although not a dominant factor prior to shower maximum. Approximation B (Rossi 1952) which includes an ionization factor of ~80 MeV per radiation length leads to a relatively accurate description of the longitudinal development of a shower as developed by Greisen (1956). The particle number N_e is described in terms of initial photon energy E_o and atmospheric depth t (in units of radiation lengths)

$$N_e(E_o, t) = \frac{0.31}{\sqrt{t_{max}}}\exp(t[1 - \ln(s)])$$

where $t_{max} = \ln\frac{E_o}{E_c}$ (depth of maximum)

$s = \frac{3t}{t+2t_{max}}$ (shower age)

The shower age parameter (s) describes the state of development of the air-shower. It is defined as 0 at the beginning of the cascade, increasing to 1 at shower maximum, and reaches 2 when there is one particle left. The EM cascade has an attenuation length $\lambda_{EM} \sim 130$ gcm^{-2} past shower maximum.

The EM component of a hadron initiated air-shower can be thought of as a summation of individual cascades initiated by neutral pion decays. The nuclear component influences the overall structure of the EM component as it is the energy source. The sum of all these individual cascades produces an overall cascade which develops gradually in the atmosphere to a maximum number of particles, and then decays. This maximum occurs deeper in the atmosphere with increasing incident energy as expected from the approximations described above.

An estimate of the energy of the initial primary particle can be obtained if the number of particles at shower maximum (N_{max}) is known

$$E_{primary} \sim 3.9 \times 10^{15} \left(\frac{N_{max}}{10^6}\right)^{0.9} eV \tag{2.5}$$

(Gaisser 1990)

In practice this is approximate, limited by the fluctuations in the cascade development.

2.4.2 Electromagnetic lateral distribution

Most air-shower arrays measure the lateral spread of the shower on the ground, not the longitudinal development. So information about the longitudinal development and the initiating particle has to be inferred from these measurements. The main contribution to the spread of the EM shower is Coulomb scattering. The angle of scatter is inversely proportional to the energy of the particle so that lower energy particles are found further from the core of the shower. These particles will tend to lag behind those at the core of the shower because of the longer path length resulting from multiple scatterings.

An EAS can be thought of as a disc of particles moving through the atmosphere at essentially the speed of light. It is approximately 2m thick near the core of the shower and increases in thickness with distance from the core. An EAS initiated by a primary cosmic ray of energy $\sim 10^{15}$eV would develop to maximum high in the atmosphere and, by the time sea-level is reached, would be well past X_{max}. It would have a lateral spread from the core of the shower of $\sim$ 100m. A lateral distribution which describes the density of particles per m^2 as a function of distance from the centre of the shower r, is of the form

$$\rho(N_e, r) = \frac{N_e}{r_o^2} f\left(\frac{r}{r_o}\right) \tag{2.6}$$

where N_e is the total number of electrons. The function $f\left(\frac{r}{r_o}\right)$ is known as the

lateral structure function. A widely used structure function, and one that is used for analysis in this thesis is the Nishimura-Kamata-Greisen (NKG) function

$$f_{NKG}\left(\frac{r}{r_o}\right) = \mathrm{C}(s)\left(\frac{r}{r_o}\right)^{s-2}\left(\frac{r}{r_o}+1\right)^{s-4.5}$$

$$\mathrm{C}(s) = \frac{\Gamma(4.5-s)}{2\pi\Gamma(s)\Gamma(4.5-2s)}$$

The Molière radius r_o is an altitude dependent term, having a value of $\sim$ 80m at sea level (Greisen 1960), and is a measure of the median radius of the shower.

Lately it has been shown that there are deficiencies in the NKG function. Fenyves et al. (1988) have suggested that the EM lateral distribution is narrower than the NKG function, possibly corresponding to a median radius of $\sim 0.5r_o$. Evidence against the NKG function comes mainly from experiments which indicate that the lateral distribution cannot be described by the NKG function with a single age parameter (van der Walt 1988, and references therein). Langutin et al. (1979) suggested the median radius depends on the age parameter as r_m = (0.78 - 0.4s)r_o. van der Walt (1988) suggested a similar dependence but not as steep with r_m = (1.254 - 0.499s)r_o.

2.5 Neutral Particles

So far the discussion of EAS has centered mainly on initiation by charged particles. However, neutral particles are also capable of initiating EAS, two of these which could produce detectable showers are γ-rays and neutrons. A primary neutron would generate an EAS similar in nature to a proton shower. However, a γ-ray initiated EAS would be different.

2.5.1 UHE Gamma Rays

An EAS initiated by a γ-ray is expected to be an electromagnetic cascade as described in §2.4. The absence of a nuclear component which supplies a continual flow of energy into this component should result in a shower with substantially different properties. In particular, the muon content and shower age are expected to differ from an EAS initiated by a massive particle. The muon content is expected to be at least a factor of ten down (Maze and Zawadiski 1960). Muon progenetors (charged pions) can only be created in EM cascades by pair production and photopion production,

$$\gamma + nucleus \longrightarrow hadrons$$

However the cross section for the latter process is the order of 100 times smaller than for muon production by protons at several GeV. The relative probability of photoproduction compared to electron pair production $(\gamma \rightarrow \pi x)/(\gamma \rightarrow e^{\pm})$ is $R_{\gamma} \sim 3 \times 10^{-3}$ for a γ-ray interacting with an air nucleus, thus pair production is more likely. Other potential sources of muons are less than this. The cross section for any pair production process is inversely proportional to the square of the mass of the created particles, hence electrons are $\sim 10^5$ times more likely to be produced than muons.

Early experiments showed evidence for muon-poor showers, and these were attributed to γ-ray primaries (Firkowski et al. 1961, Kamata et al. 1968). It was

later thought that some or all of these showers were due to extreme upward fluctuations in π^o multiplicities in hadron showers leading to a larger than normal electromagnetic component (Maze et al. 1969).

Recent calculations using updated hadronic interaction models essentially confirm the earlier result of $\sim$ 10% muon content for γ-ray initiated EAS at $\sim 10^{15}$eV (Edwards et al. 1985, Stanev et al. 1985, Dumora et al. 1992). It was suggested by Krys et al. (1991) that the number of muons from γ-ray initiated showers is comparable with those from hadron induced showers if a rapid increase in photoproduction cross-section is assumed. They go on to say that, assuming this is true, it is still possible to distinguish γ-ray showers by their considerably wider lateral distribution, and the lower ratio of hadrons to muons.

An argument from Gaisser (1990) provides a good estimate of the number of GeV muons in a photon induced air shower. Once a photoproduction event occurs in an EM cascade, the resulting cascade will be hadronic-like with energy split evenly between hadronic and EM particles. The probability that any branch of the cascade will be hadronic at the GeV level is given by $R_\gamma \times ln\left(\frac{E_o}{2}\right)$ for $nR_\gamma \ll 1$ where E_o is the primary energy and n is the number of splittings in the cascade to reach the GeV level.

For a primary energy of E_o the average energy per particle will be $\sim$GeV after n $\sim \ln\frac{E_o}{GeV}$ interaction lengths. The number of GeV muons in an EM cascade will be

$$N_\mu^\gamma \sim \frac{1}{2} R_\gamma ln E_o \times N_{GeV}$$

where N_{GeV} is the number of branches in the shower at a GeV. The number of GeV muons for the hadronic shower is

$$N_\mu^p \sim \frac{N_{GeV}}{2}$$

So the expected γ-ray to cosmic-ray muon ratio is

$$\frac{N_\mu^\gamma}{N_\mu^p} \sim R_\gamma ln E_o \tag{2.7}$$

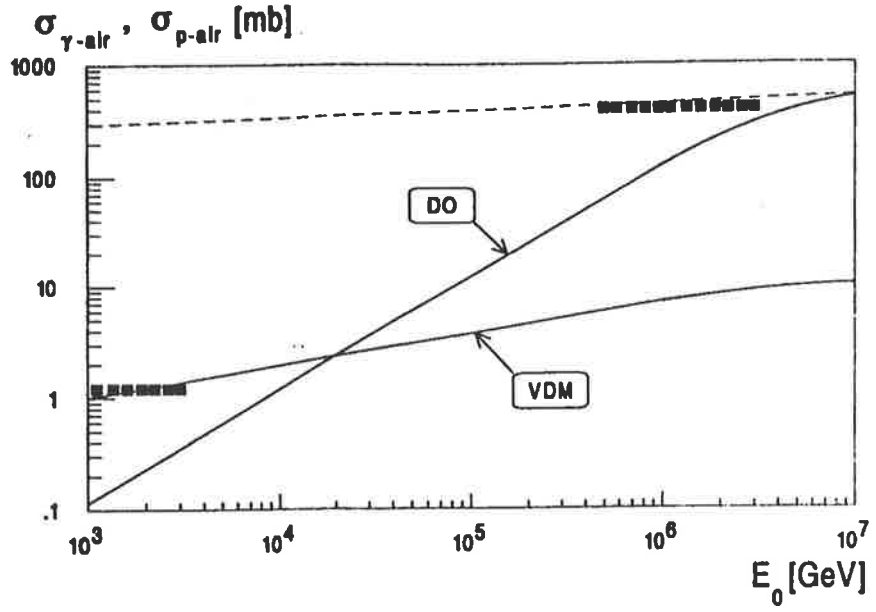

Figure 2.3: The comparison of photonuclear cross section for the production of hadrons as a function of photon interaction energy for the (i) VDM model (Bezrukov and Bugaev) and (ii) DO, the Duke and Owens estimation. The black squares are the gamma-air cross section estimated from the step function used by Wdowczyk and Wolfendale. The dashed line shows the proton-air cross section. (From Dumora et al. 1992)

This predicts that there will be approximately 10 times fewer muons from a γ-ray primary of 10^{15}eV compared to a proton primary of the same energy.

Two estimates for the photoproduction cross section ($\sigma_{\gamma-air}$) for muons as a function of energy are shown in Figure 2.3. Both models suggest an increase in cross section with energy. However the Duke & Owens curve (Dumora et al. 1992) predicts a rapid growth with energy, becoming almost equal to the proton-air cross-section and the photon pair production cross-section at $\sim 10^{16}$eV ($\sigma_{p-air} = 503$mb, $\sigma_{pair} = 520$mb, $\sigma_{DO} = 365$mb). Using this model Krys et al. (1991) have shown that γ showers can produce the same number of GeV muons as a proton shower in the $10^{15} - 10^{16}$eV range. This is however an extreme case, and other models do not predict such an increase in the photoproduction cross-section.

Procureur & Stamenov (1987) have suggested that an increase in the number of

muons may be possible at high altitudes ($700 \mathrm{gcm}^{-2}$) at $\sim 10^{15}$eV from low energy shower γ-rays interacting deep in the atmosphere. These low energy cascade photons, produced in large quantities, compensate for the small photoproduction cross-section at this energy ($\sim 10^{15}$eV) and hence result in an increase in the number of muons. However, the muons are created high in the atmosphere and with sufficiently low energy that they do not survive to ground level.

2.5.2 EHE Gamma Rays

At the highest energies ($10^{18} - 10^{20}$eV) there have been arguments suggesting an increase in the muon content of γ-ray showers. Halzen et al (1988) proposed that the gluon content of high energy photons may increase the number of muons from neutral pion decay. A more plausible argument has been offered by Aharonian et al. (1991). They have suggested that γ-rays and hadronic showers produce the same number of **sub**-GeV muons at sea level ($\sim$ 1000g cm^{-2}, $E_\mu \sim 0.3$ GeV), due to the high penetrability of low energy photons in an extremely high energy (EHE) electromagnetic cascade. They do not assume a rising photoproduction cross-section, or that the character of γ-ray interactions change dramatically at EHE energies. Instead the key elements in their argument are the large depth of observation, the high primary γ-ray energy, and low muon energies.

The number of muons in a γ-induced shower is proportional to the initial γ-ray energy E_o, while in proton showers it is proportional to $E_o^{0.8} - E^{0.9}$ (McComb et al. 1979, Edwards et al. 1985). Therefore at incident particle energies increasing from 10^{15} to 10^{18}eV, the difference in these dependences leads to an increase in the ratio $\frac{N_\mu^\gamma}{N_\mu^p}$ by a factor of $3 - 4$.

The energy range of detected muons is important. The muon energy spectrum is considerably steeper for γ-rays than for hadrons therefore γ-showers remain high energy ($\sim$ 10 GeV) muon poor. The differential muon energy spectrum of a 10^{18}eV shower at sea-level is shown in Figure 2.4. It is steep for γ-ray induced showers, but in the region $\leq$ 1GeV the number of muons is greater than the corresponding spectrum from a proton shower.

Aharonian et al. (1991) show that the effect of approximately equal numbers of sub-GeV muons in γ-ray and proton showers occurs at large depths in the atmosphere where the number of cascade γ-rays with $E_\gamma \sim 0.5$ GeV are able to produce muons with $E_\mu \sim 0.3$ GeV. These low energy γ-rays are produced in sufficient quantities to compensate for the large difference in the cross section of charged pion production by photons and hadrons.

Halzen (1988) estimates the number of low energy muons from an EHE primary γ-ray as follows. In an electron-photon cascade, two thirds of the particles are electrons and the other one third are γ-rays. The mean attenuation length for the cascade particle (electron or photon) is in the following form

$$\langle\lambda\rangle \sim \frac{1}{3} \times \frac{9}{7} X_o + \frac{2}{3}(ln2)X_o \sim 33 gcm^{-2}$$

The number of cascade particles ($e^{\pm}$ & γ_s) initiated by a primary photon with energy E_o at a depth t is 2^n where $n = t/\langle\lambda\rangle$. The number of low energy muons at a given depth is about

$$N_\mu^\gamma \sim 2 R_\gamma N_\gamma \tag{2.8}$$

(Halzen 1988)

where the factor 2 accounts for the contribution of the muons produced at all previous depths and R_γ is the ratio of pion photoproduction to pair production cross sections ($\sim 3 \times 10^{-3}$). At $t \sim t_{max}$ this estimate of the number of muons is relatively correct. The number of photons from a primary γ-ray with energy $E_o = 10^{18}$eV at sea-level ($t_o = 1030$ gcm^{-2}) is approximately

$$N_\gamma = \frac{1}{3} 2^n \sim 7 \times 10^8$$

At this depth the mean cascade γ-ray energy is $\langle E\rangle \sim \frac{E_o}{2^n} \sim 0.5$ GeV, and approximately 60% of this energy is transferred to the muons through the production and decay of charged pions. Substituting these values in equation 2.8 the number of muons with energy $E \geq 0.3$ GeV is $N_\mu^\gamma \sim 5 \times 10^6$. This value is comparable to the analytical value determined by Aharonian et al. (1991) of (4×10^6). The relevant number of low energy muons from a proton-induced shower depends on the model of proton-air interaction (McComb et al. 1979). Using the quark-gluon-string (QGS) model (Dedenko 1987) the value is $N_\mu^p \sim 4.5 \times 10^6$ muons.

Hence there appears to be some alignment in the number of low energy ($E_\mu \leq 1$ GeV) muons at EHE primary energies from proton and photon induced showers without resorting to extreme models of photoproduction cross-sections.

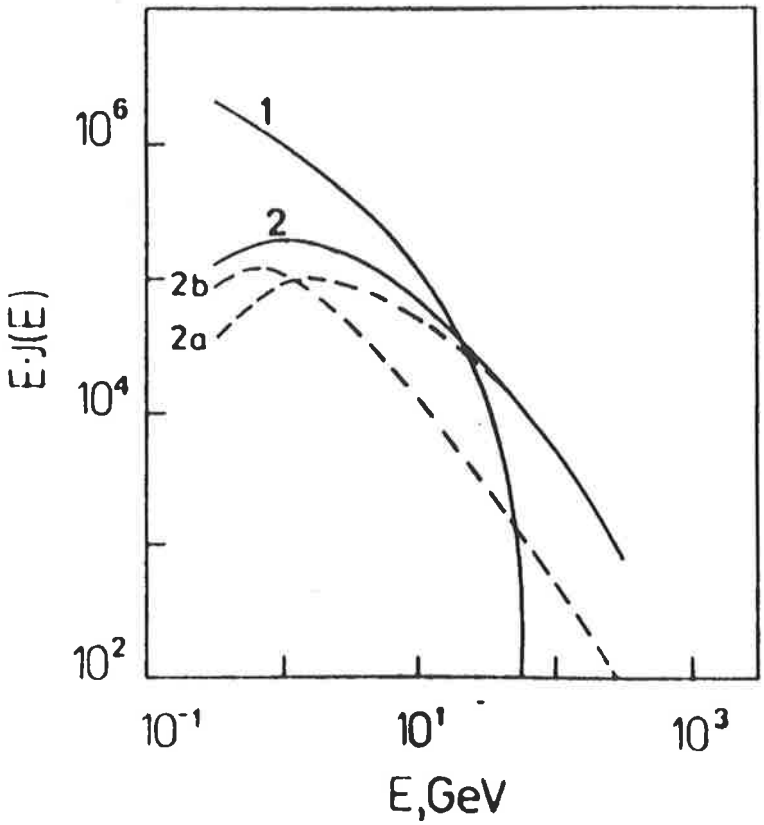

Figure 2.4: The differential muon spectrum (times energy) at sea level from incident gamma-rays (curve 1) and incident protons (curve 2, from McComb et al 1979). As can be seen, the γ-ray spectrum is steeper, and is higher at $E_\mu \leq 1$GeV. (from Aharonian et al. (1991))

Taking the curves from Figure 2.4 and estimating the number of muons (E $\geq$ 1GeV) (a typical SUGAR detector threshold) the values are $N_\mu^\gamma \sim 1.9 \times 10^6$ and $N_\mu^p \sim 2.4 \times 10^6$ (using the QGS model) for a 10^{18} primary.[2] The muon numbers are still comparable. However, it must be noted that the SUGAR array threshold was 2×10^{17}eV and so the expected γ-ray to proton muon ratio would be less (see Chapter 4).

[2]Estimating the γ-ray to proton muon ratio at $E_\mu \geq 10$ GeV gives a value of $\sim 10\%$

Chapter 3

Buckland Park Extensive Air Shower Array

3.1 Introduction

The Buckland Park array is situated approximately 40km north of Adelaide at a latitude of $34^0 38'$ South and longitude $138^0 28'$ East. It is located next to the coast at an atmospheric depth of $\sim 1030 \text{gcm}^{-2}$. The array has undergone many changes since it began operating in 1971, and presently it provides information on Extensive Air Showers in the approximate range $(10^{15} - 10^{16})$eV.

There are 38 scintillation detectors in total covering an area of $\sim 2 \times 10^5 \text{m}^2$ (see Fig 3.4 & 3.7). Most detectors are 1m^2 in area, but there are 5 detectors which cover 2.25m^2. Two types of photomultiplier tubes (PMTs) are used in detectors, 'slow' PMTs which give information on the number of particles passing through the detector, and 'fast' PMTs which allow timing of the shower front across the array. Together these allow one to derive the direction, size and core location of the EAS as well as an estimate of the energy of the initiating primary particle.

3.1.1 The Detectors

The particle detectors at Buckland Park are mainly sensitive to the electromagnetic component of an EAS. They consist of a slab of plastic scintillator which is viewed by either one or two PMTs, all contained in a light-tight box. Detectors with two PMTs give information on both the number of particles and the relative time of the shower front (see Table 3.1). The PMTs typically have $10-15$ stages and their sensitivity is matched to that of the maximum emission of the scintillators $\sim (420 \pm 30)$nm.

The fast PMTs have typical rise times of $\sim$ 2ns or better (eg Philips XP2040), and have gains of $\geq 10^7$ when running at $\sim$2000V. The output pulses from these tubes are carried by high-bandwidth 50Ω cable which minimises the signal loss and helps preserve the pulse shape. The signals are passed through to 'double discriminators'. These discriminators reduce timing uncertainties from pulse jitter. There are 2 channels in the discriminators with a lower and an upper threshold which are delayed with respect to each other. When the upper threshold is triggered the lower threshold pulse is gated through and thus the overall trigger is obtained at a time determined by a point early in the rise of the signal pulse. Typically the lower threshold rate is set 10 times faster than the upper threshold rate which is at the 2 particle level.

The output from the discriminator is passed to a fixed delay ranging from (50-500)ns before triggering the stop on the Time to Digital Converter (TDC).

The intensity of light given off from a scintillator is directly proportional to the number and total path length of charged particles passing through it. A slow PMT whose output pulse is integrated by an on-site (at the detector) charge sensitive preamplifier is used to estimate the number of particles. The output from the preamplifier has an amplitude proportional to the integrated charge, which is in turn proportional to the number of particles. These pulses are passed from the preamplifier along RG8 or RG58 cable to line receivers, and then on to peak-sensing Analogue to Digital Converters (ADC).

3.2 Array Trigger and Recording Event Data

To distinguish real air-showers from unaccompanied muons triggering individual detectors, the lateral spread of the air shower, and coincidences between detectors, provide a means of detection. The shower size threshold for an array depends mainly on the individual detector thresholds and the geometry of the array. Prior to this

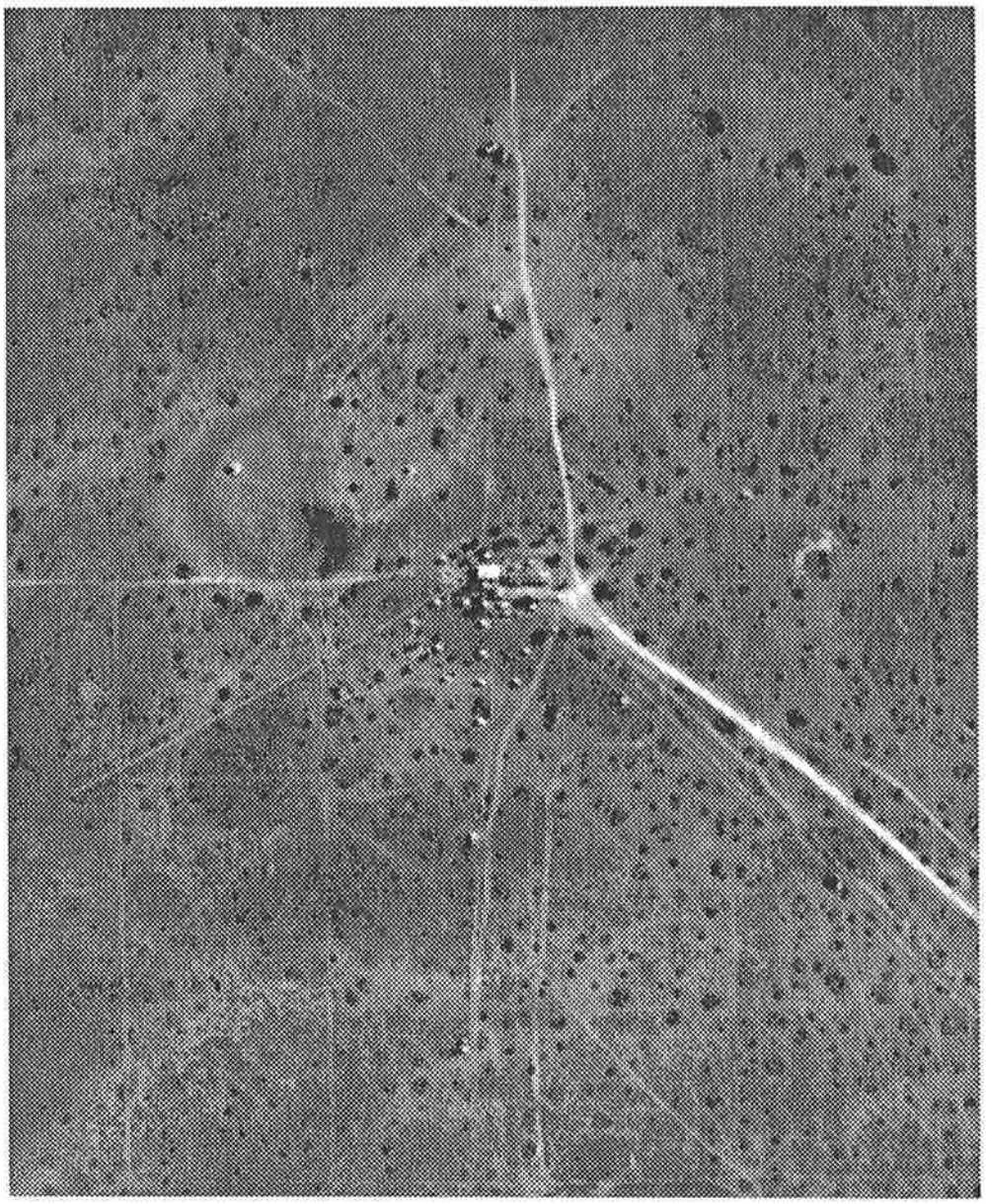

Birds eye view of the Buckland Park Array showing the central electronics hut and the road leading to it, as well as the inner set of detectors

authors cadidature, the Buckland Park array had a size threshold of $\sim 6 \times 10^4$ particles. It was decided to increase the size threshold (see §3.4) to approximately 10^5 particles, similar to its configuration in 1979.

Using simulations, see §3.4.1, it was shown that a coincidence of any 3 out of the 19 slow signals and any 2 out of the 11 fast signals in the trigger was suitable for an increase in the array size threshold to 10^5 particles (see Table 4.1 for detector specifications). This fast coincidence is constrained to occur within 100ns to allow for cable delay and the passage of the shower across the array.

All TDCs, ADCs, scalar and other data are supported by a CAMAC crate, which is interfaced to an Olivetti M24 PC. When an array trigger occurs, through a coincidence, an interrupt is generated by the first TDC in the CAMAC crate, and when this is acknowledged by the PC it proceeds to read the the time, pressure, and temperature followed by the ADC, TDC and scalar data before resetting the crate ready for the next event. The event data are buffered by the PC and then sent to a Motorola MVME 133 computer system, which formats and stores the data onto a hard disk-drive. The MVME 133 multi user computer is based on the VME bus using a Motorola 68020 processor which allows other operations such as access to the power supply voltages and collection of data without interrupting the running of the array. The data from the events are stored in 2 hour files for ease of handling and to minimise loss of data in the event of a power failure.

The system dead-time is $\sim 300\mu$s per event which is more than adequate since the array trigger rate is $\sim 8 \times 10^{-3}$ Hz. The disc drive has 50 Megabytes for data storage, and with approximately 1.5 Megabytes of raw data produced each day it is possible to run for a month before data has to be retrieved. Figure 3.2 shows a schematic of the array control system.

3.3 Data Analysis

Data from the array are transferred to Adelaide University by streamer tape, and are collected approximately every two weeks. The preliminary data processing can be divided into two parts, direction fits and shower size & core estimations. The raw TDC and ADC numbers have to be converted to time in nanoseconds and particle numbers respectively. The TDC conversion is linear and has been found to be stable over time (see Appendix B). However the conversion of ADC numbers is somewhat more complicated.

The ungated single muon spectrum obtained from a detector contains a peak (see Figure below), called a Single Particle Peak (SPP), which is the mode of this

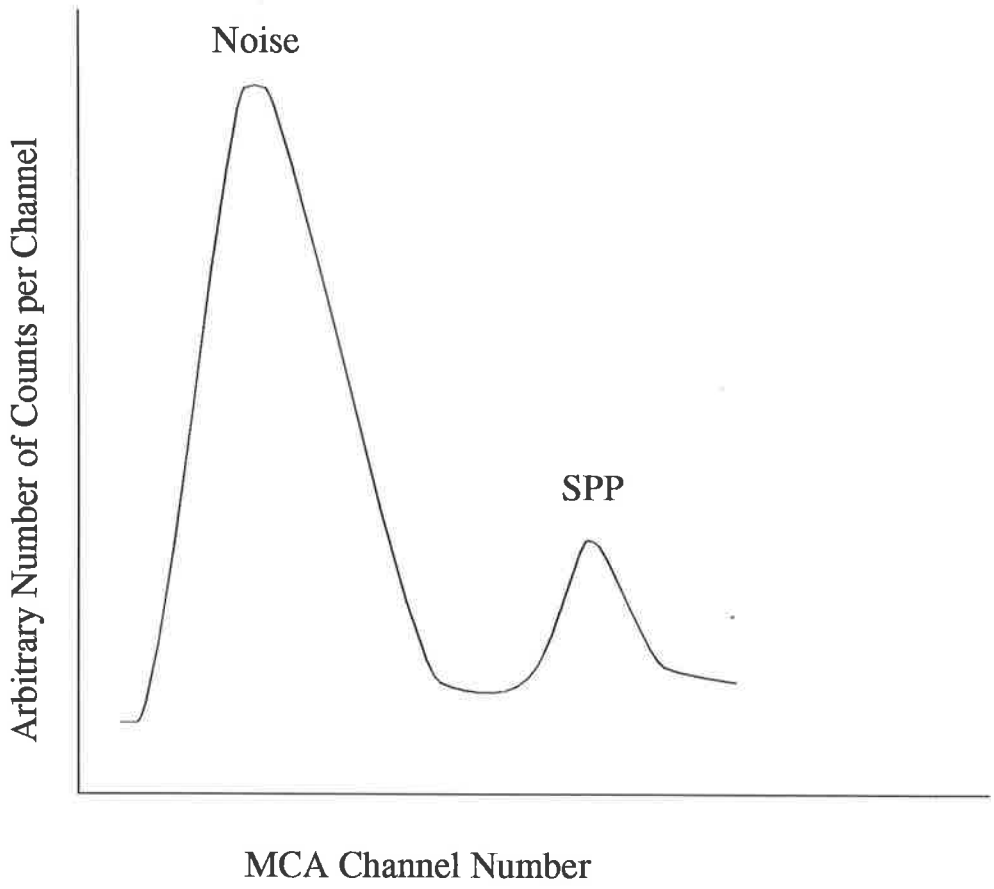

Figure 3.1: A typical pulse height spectrum from detector R, used in calibrating the data for density measurements. This detector was chosen because of its well defined SPP.

spectrum. This spectrum is a good approximate to a Landau distribution. It happens by chance that this SPP is a good approximation to the mean pulse height for vertical single muons. This is true because the ratio of the mean to the mode of a Landau distribution is 1.3, and the SPP of **gated** vertical muons is a factor ~ 1.3 less than the mean for ungated omni-directional muons (Clay & Gregory 1978)

To convert the ADC number to an equivalent single vertical muon a two stage intercalibration is used. A tail-pulse generator is used to simulate the shape of a 'Slow' pulse from a detector, and the ADC is calibrated in terms of this pulse amplitude. A Multi Channel Analyser (MCA) channel number (which is used to measure the SPP) is also calibrated in terms of the pulse amplitude. The conversion is

$$\mathrm{N} = \frac{\mathrm{A} \times (\mathrm{ADC} - \mathrm{Ped})^{\mathrm{B}} \times \mathrm{Slope}}{(\mathrm{SPP} - \mathrm{intercept})} \tag{3.1}$$

(Corani 1986)

where A, B, Slope and intercept are experimentally determined by calibration for each channel of the ADC. Ped is the pedestal for that channel of the ADC and is the number which corresponds to zero pulse height. In practise it is the minimum non-zero value in the data. These calibrations have been found to be stable over time.

3.3.1 Arrival Directions

To calculate the direction of the air-shower in terms of horizontal coordinates (θ, ϕ), the technique of fast-timing is used. To achieve this the relative arrival time of the air-shower at each detector must be known. Inherent in the detectors, cables and electronics are delays which are not all the same and contribute to the measured relative time differences. These delays have to be subtracted from the measured times so that the relative arrival time of the air-shower is obtained. Instead of measuring all these delays explicitly, it is assumed that the average air shower arrival direction is from the zenith. So the mean timing difference between detectors

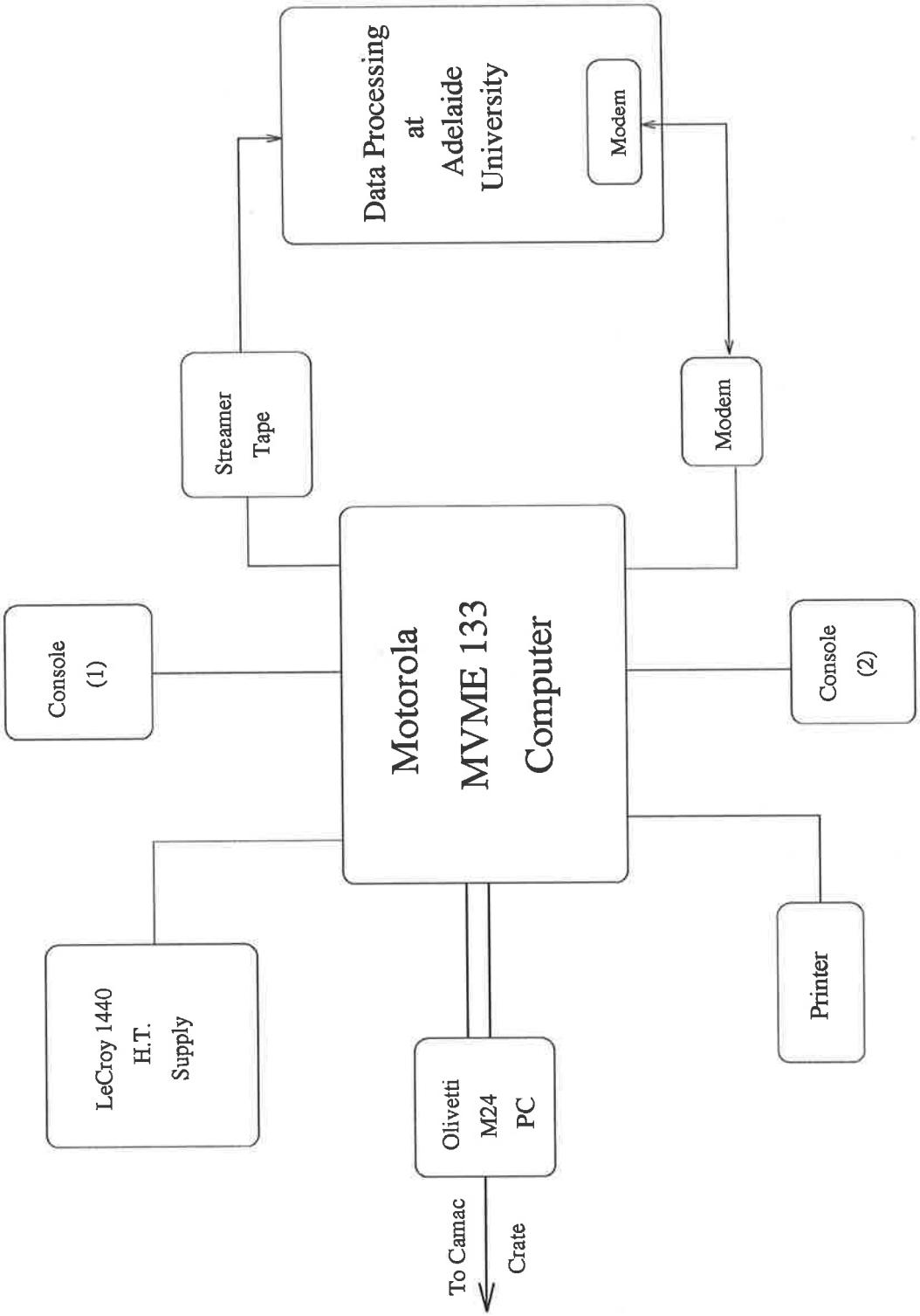

Figure 3.2: Schematic diagram of the array control system at Buckland Park. Data from the Camac crate is sent via a GPIB link to the PC and then via a serial line to the VME computer. The high voltage power to individual detectors can be set and adjusted via the VME. A modem allows a remote check on the operation of the array

sampled over a large enough set of events (typically $10^4 - 10^5$) provides a good estimate of these inherent delays between pairs of detectors. The time difference between the i^{th}&j^{th} detector is defined as

$$\overline{t_{ij}} = \overline{t_i - t_j} = \frac{1}{N}\sum_{k=1}^{N}[t_i(k) - t_j(k)] \tag{3.2}$$

where t_i&t_j are the times of the i^{th}&j^{th} detector and N is the total number of events. It is important when using this method to ensure that false signals from detectors not correlated with an event are not used. A suitable algorithm was developed (see Edwards 1988), and is used in this analysis.

The standard error of these timing differences between the i^{th} & j^{th} detector is given by $S_{ij} = \sigma_{ij}/\sqrt{N}$, where σ_{ij} is the standard deviation of the timing distribution for times between the i^{th} and j^{th} detectors. It is found that to a good approximation σ_{ij} is proportional to the distance between detectors. In order to minimise this error for the larger spaced detectors, better estimates were obtained by 'stepping' between the detectors using intermediate detectors (see Edwards 1988). Deviations between successive difference estimates are found to be $\leq$ 1ns.

For each event, a reference detector is chosen which usually was the first detector in the data with a time available. All other times are made relative to this detector by subtracting the reference detectors time from all times. Assuming that the shower front is planar and propagates across the array at the speed of light c, a fit to the available times is achieved by minimizing the following function and solving for l, m and t_o

$$\Psi^2 = \sum_{i=1}^{N} w_i[c(t_i - t_o) - lx_i - my_i]^2 \tag{3.3}$$

where l and m are direction cosines, t_i and w_i are the time and weight[1] for the i^{th} detector respectively. (see Appendix A for a derivation).

[1]The weight corresponds to whether that detector has a recorded time. It is set to 1 for detectors with recorded times and 0 otherwise.

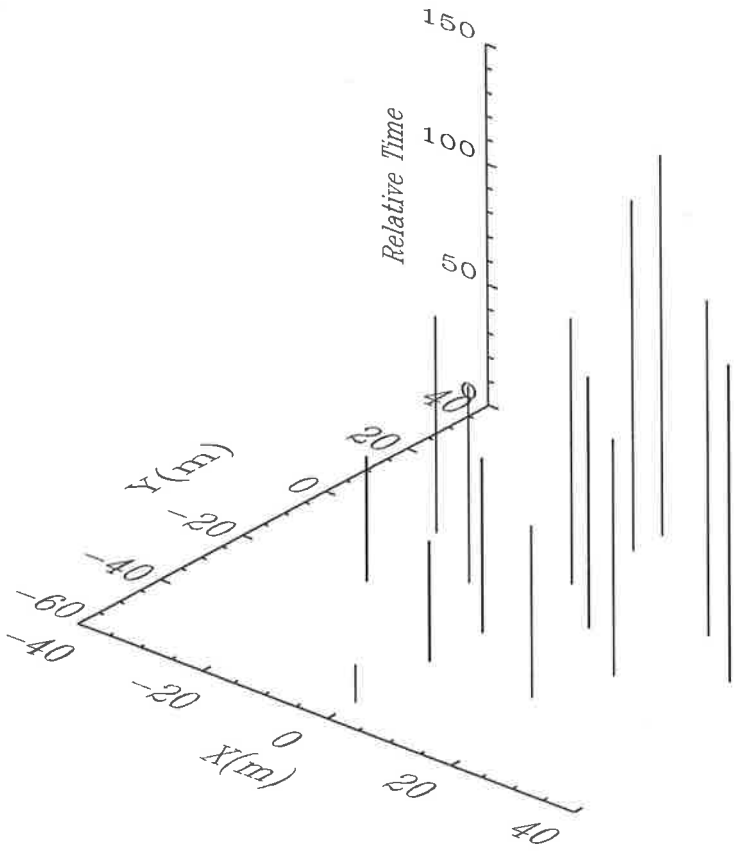

Figure 3.3: Times from an air shower recorded at a number of detectors. The assigned direction is: zenith 41.7°, azimuth: 211.17°

The timing offset t_o is a free parameter so that the fitted shower front is not constrained to pass through the reference detector at time zero.

This fit assumes that all the detectors lie in the same horizontal plane. Variations in the height of detectors is accounted for by correcting the individual arrival times, after an initial estimate of the direction has been made, using the following relationship

$$t_i = t_i - \frac{z_i \cos\theta}{c} \tag{3.4}$$

where z_i is the z-coordinate of the i^{th} detector and θ is the zenith angle. Ψ^2 is

minimized again until the direction converges. In practice at least three detectors which are not co-linear (ie detectors which do not all lie in one line) and which have usable times are needed for a direction fit.

Goodness of fit

A measure of the error in the direction fit to the plane front is given by

$$\sigma = \frac{\sum_{i=1}^{N} w_i[c(t_i - t_o - lx_i - my_i - nz_i]^2}{N_t - 3} \tag{3.5}$$

where N_t is the number of times contributing to the direction fit. As can be seen σ is only meaningful when there are 4 or more times, however only three times are required for a unique fit (assuming they are not co-linear). Of course the assumption that the shower front is planar is inaccurate and will contribute to the overall error. Allowance for this is made once the shower core is determined (see §3.5.2).

3.3.2 Shower parameters

A fit for the other shower parameters can be made once the direction is found, these being the shower size (N_e), core location (X_c,Y_c), and age (s). Once the raw ADC numbers have been converted to particle numbers, the parameters are determined by fitting a NKG lateral distribution function (§2.4 equation 2.6) to the data. This is achieved by using the maximum likelihood (MLH) method, maximizing the following function,

$$\ln P(X_c, Y_c, s) = \sum_{i=1}^{N}[(d_i^o \ln(d_i^c)) - (d_i^c - \ln(d_i^o!))] \tag{3.6}$$

where d_i^o is the observed density and d_i^c is the corresponding calculated density for that detector from the fit and N is the number of detectors contributing to the fit. In practice $-\ln P$ is minimized.

An alternative is to minimise χ^2 where

$$\chi^2 = \sum_{i=1}^{N} \frac{(d_i^o - d_i^c)^2}{\sqrt{d_i^o d_i^c}} \tag{3.7}$$

This fit, unlike the MLH method does not make use of detectors where no particle densities had been recorded (ie where $d_i^o = 0$). So it follows that minimizing χ^2 is not effective in using all available data. Therefore the MLH method is the preferred option especially in situations where there are only a few detectors with available particle densities. A χ^2 is always calculated for the final fit so that there is some handle on the error in the fit.

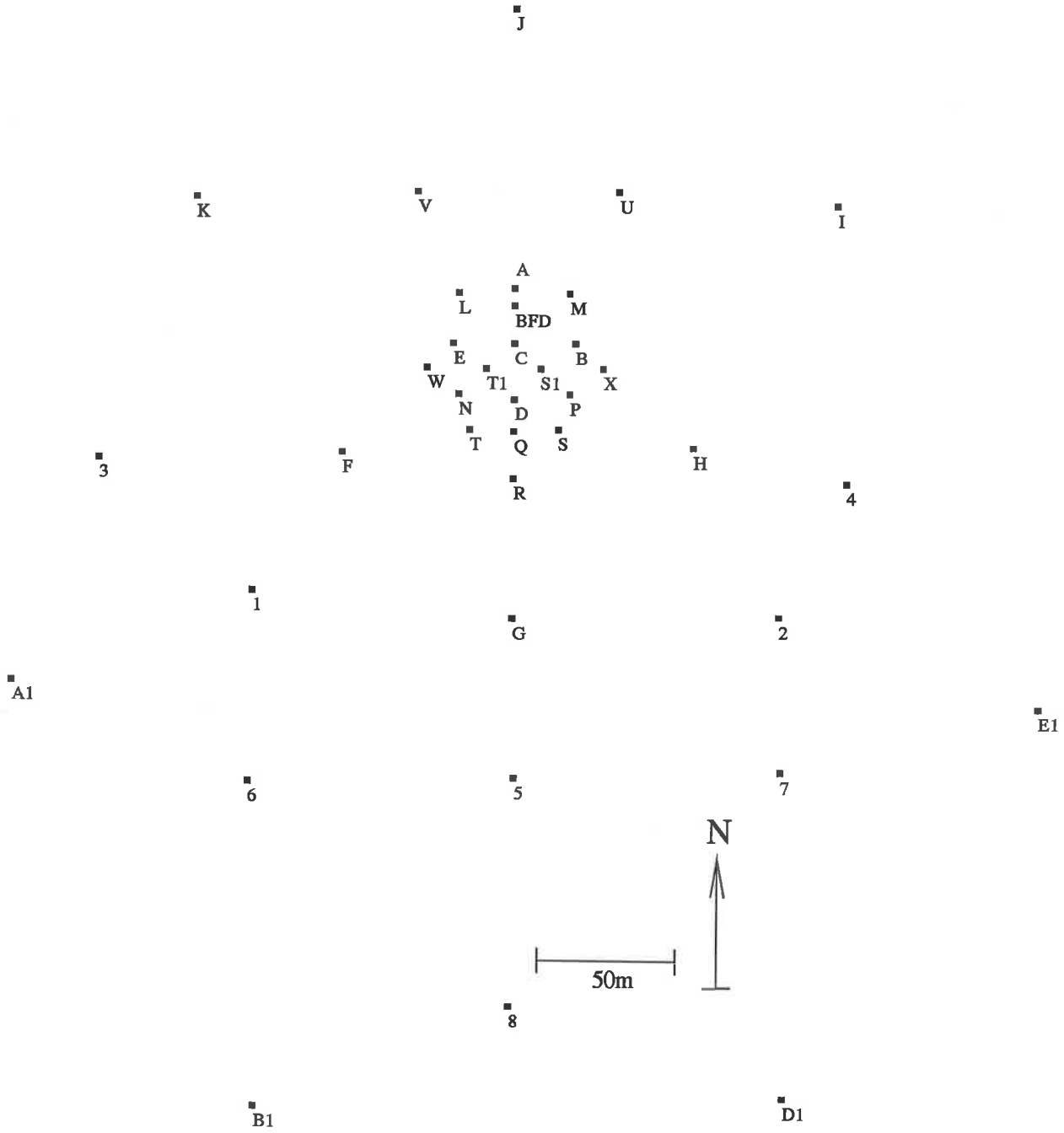

Figure 3.4: Layout of the Buckland Park array. Detector specifications are given in Table 3.1 and Figures 3.5 & 3.6 give the triggering contours for the array. All detectors are $1m^2$ in area except for A1, B1, C, D1, & E1 which are $2.25m^2$ in area.

3.4 Development & Configuration (1991-1992)

The previous alteration to the array during the period 1989-1990 (see D.Bird 1991) had left several problems with its day to day operation. This was mainly due to the relocation of detectors A1,B1,D1,E1 and the addition of eight new detectors to the south of the array ($1-8$, see Figure 3.4). This extended the array and provided a larger collecting area especially for showers $> 10^5$ particles. There were however problems with the high voltage (HV) lines to these detectors. Also 12 channel TDC (made in-house) had been built to provide time measurements for these outer detectors. Unfortunately the original range of 1μs was insufficient, and was extended to 4μs. However, this extension caused problems resulting in the TDC giving poor times (see Table 3.2 later).

It was decided that the present author would raise the array threshold from $\sim 6 \times 10^4$ particles to approximately 10^5 particles (similar to that during the period $1979-1982$) for two reasons. Firstly it would ease the data analysis load resulting from the lower event rate. Secondly, to improve possible detections of UHE point sources, the increased threshold would give a better signal to noise ratio, as it was thought that these sources exhibited a flatter spectrum than the background cosmic rays. In addition to this, the direction fits would be improved which would also improve the signal to noise ratio. These changes are discussed below.

New High Voltage Lines

The original High Voltage (HV) lines to the outer 12 detectors were made up of several smaller lengths of cable. They were laied along the ground and were exposed to the weather and small animals. This resulted in frequent damage to the cables and sometimes detectors. Thus frequent repairs were necessary to maintain the operation of the array.

New lines were installed and sealed. A trench was dug down the 'spine' of the array, from approximately 5m west of detector Q down to detector 8 (see Fig. 3.4). Each of the new HV cables which ran from the power supply and along this trench to

the detectors was continuous (ie without joins). Cables ran from the trench housed in 25mm weather resistant plastic tubing along the ground to the detectors. It was decided not to extend this trench all the way up to the main electronics hut (located 10m north of detector C) due to all the other buried cables in the area. Instead a similar plastic tube 50mm in diameter ran along the ground housing the 14 HV lines from the main hut to the beginning of the trench.

There have been no problems since this change over and the need for repairs has dropped considerably.

Phillips 7186 TDC

As mentioned above the TDC serving the outer 12 detectors was malfunctioning and had to be replaced. A new 16 channel Phillips TDC was purchased. It has a maximum range of $4\mu s$ and a corresponding resolution of 1ns. Each channel was calibrated in terms of conversion of TDC number to time in nanoseconds and checked for linearity (see Appendix B). Channels were found to be stable over an extended period of time. The new conversions replaced the old values for the arrival direction analysis.

Given that these outer 12 detectors had improved TDC times, the discriminators were upgraded to double discriminators. The effect of these changes was to improve the data from the detectors (see Table 3.2).

3.4.1 Simulations for Array Triggering

To determine the array triggering condition and individual detector thresholds it was necessary to perform several simulations. The criteria were, (1) to increase the array threshold to approximately 10^5 particles with the existing detector positions, and (2) that the triggering area for a particular shower size be uniform.

The detectors to the south of the array had been separated by distances of up to 100m, this spacing would accommodate an increase in the array energy threshold. The triggering criteria were changed so that the array threshold would be higher,

closer to a sea-level size of 10^5 particles. The individual detector thresholds, and detectors which are part of the trigger are shown in Table 3.1. Using only those detectors which were part of the slow trigger and fast trigger, it was found that the above conditions were met for an array trigger consisting of a three fold coincidence for the slow trigger and a two fold coincidence for the fast trigger (see Table 3.1).

The positions of the detectors are shown in Figure 3.4. There are 38 detectors in total, 30 of which are used for fast timing. Only vertical showers were considered in the simulation. This leads to an underestimate of the triggering area as the apparent detector spacings in the plane of the shower for inclined showers is smaller. However this affects each simulation similarly, and so comparisons between triggering schemes would not be affected. Shower sizes were set at appropriate values (ie $10^6, 3 \times 10^6$ etc) and the shower age was fixed at 1.3.

The number of particles at each detector was calculated using the NKG formula (equation 2.6), given the core location, zenith angle, size, and age. A random Poisson fluctuation was then applied, to estimate the actual number of particles observed by the scintillator. This number was then compared to the threshold set for each detector in question. If a two fold & three fold coincidence was found for both the 'fast' and 'slow' triggers respectively, an event was recorded. This process was repeated many times with cores on a 1m$\times$ 1m grid centered on the array, the extent of the grid depending on the shower size (eg up to 400m for a 10^7 size shower). The triggering probability P(N_e,x,y) for a particular grid location is the total number of triggers divided by the number of attempts. The total collecting area of the array as a function of shower size A(N_e) was then calculated as

$$A(N_e) = \int\int P(N_e, x, y)dxdy$$

Detectors which were part of the array trigger were chosen so that any selection effects which may bias the data were kept to a minimum. All detectors which were part of the array trigger were within the physical boundary of the array. Large

fluctuations in the detected number of particles were avoided by keeping thresholds of those detectors which were part of the 'slow' trigger high, (see Table 3.1) so that upward fluctuations, especially in the regions where the triggering probability is less than 50%, were minimized. The results are shown in the last column of Table 3.1.

The triggering contours for the chosen triggering scheme are shown in Figures 3.5 & 3.6. The collecting area as a function of sea-level shower size is shown in Fig. 3.7. Also shown is the collecting area for γ-ray showers, where it is assumed that for a γ-ray shower the effective Moiler radius is half its normal value (ie 40m at sea-level, Crewther & Prothroe 1992).

Detector Label	Type (Fast/Slow)	Pos x x(m)	Pos y y(m)	Area (m^2)	Trigger (Fast/Slow)	Threshold (particles)
A	F,S	0	22	1	F,S	8
B	F,S	22	0	1	F,S	8
C	F,S	0	0	2.25	F,S	7
D	F,S	0	-22	1	F,S	8
E	F,S	-22	0	1	F,S	8
F	S	-61.5	-43.2	1	S	6
G	S	0	-107.2	1	S	6
H	S	64.8	-40.7	1	S	6
I	S	116	55	1	-	-
J	S	0	130	1	-	-
K	S	-114	56.6	1	-	-
L	F,S	-20	20	1	S	7
M	F,S	20	20	1	S	7
N	F,S	-20	-20	1	S	7
P	F,S	20	-20	1	S	7
Q	F,S	0	-34.6	1	-	-
R	F,S	0	-53	1	F,S	7
S	F,S	16	-33.8	1	F,S	7
T	F,S	-16	-34	1	F,S	7
U	S	37.6	59.6	1	S	7
V	S	-35.1	59.3	1	S	7
W	F,S	-31.3	-9.6	1	-	-
X	F,S	32	-9.8	1	-	-
S1	F	9.4	-10	1	-	-
T1	F	-10.1	-10	1	-	-
BFD	F	0	15	1	-	-
1	F(S)	-93	-97	1	F,S	6
2	F(S)	96	-106	1	F,S	6
3	F(S)	-148	-46	1	-	-
4	F(S)	120	-54	1	-	-
5	F(S)	1	-170	1	F,S	6
6	F(S)	-94	-172	1	-	-
7	F(S)	97	-167	1	-	-
8	F(S)	0	-258	1	-	-
A1	F,S	-179	-133	2.25	-	-
B1	F,S	-91	-298	2.25	-	-
D1	F,S	99	-293	2.25	-	-
E1	F,S	189	-141	2.25	-	-

Table 3.1: Compilation of the detector names, positions and thresholds. Most detectors are one square meter in area except for detectors C, A1, B1, D1, and E1. Fast type detectors have thresholds set at the two particle level. F(S) signify detectors which only have fast type PMTs and are used to obtain both timing and density information.

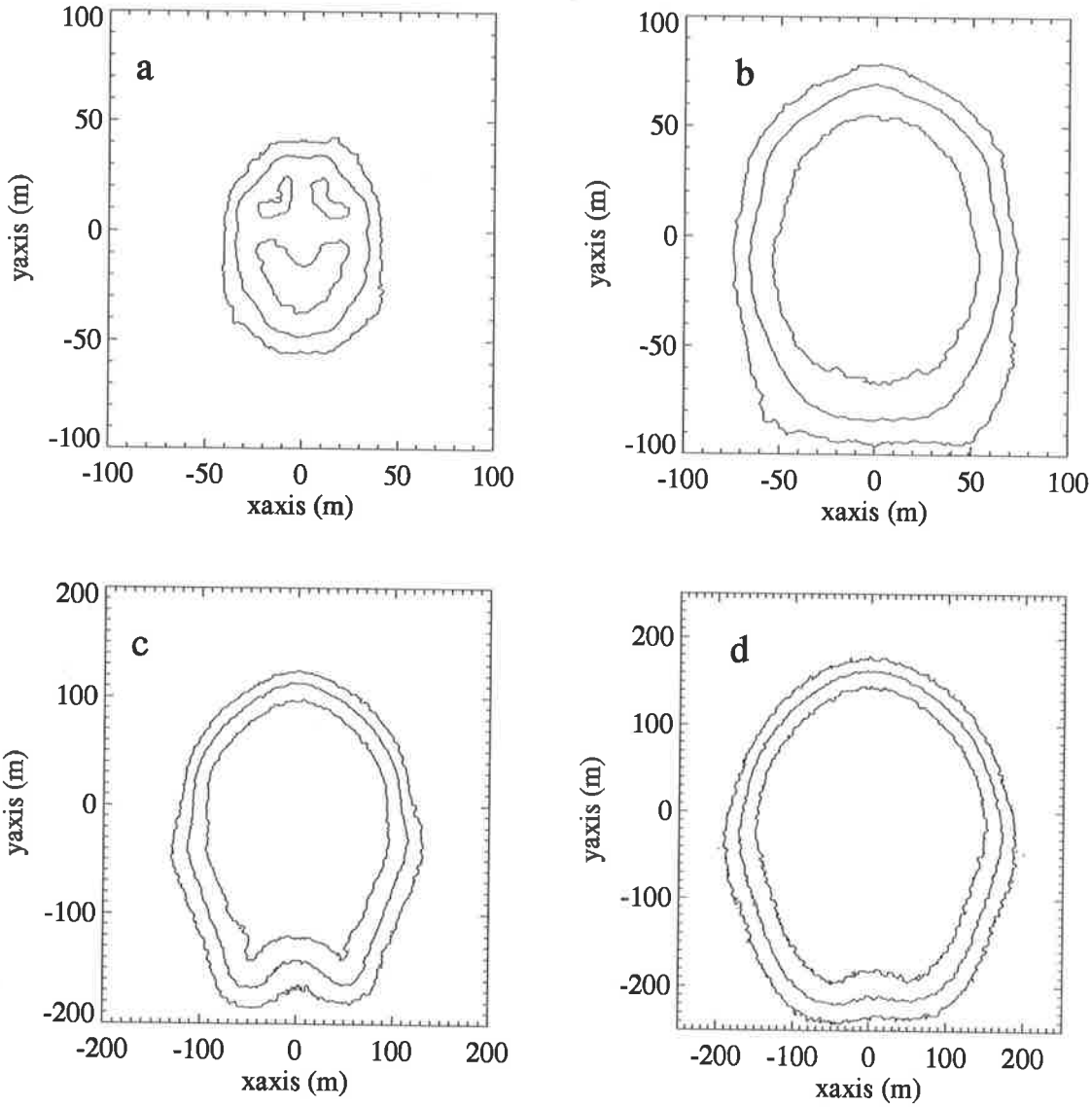

Figure 3.5: Triggering contours for vertical showers falling on the Buckland Park E.A.S Array. Contours shown are 10%, 50% and 100% percentiles corresponding to the following sea level shower sizes.

(a) 10^5 particles
(b) 3×10^5 particles
(c) 10^6 particles
(d) 3×10^6 particles

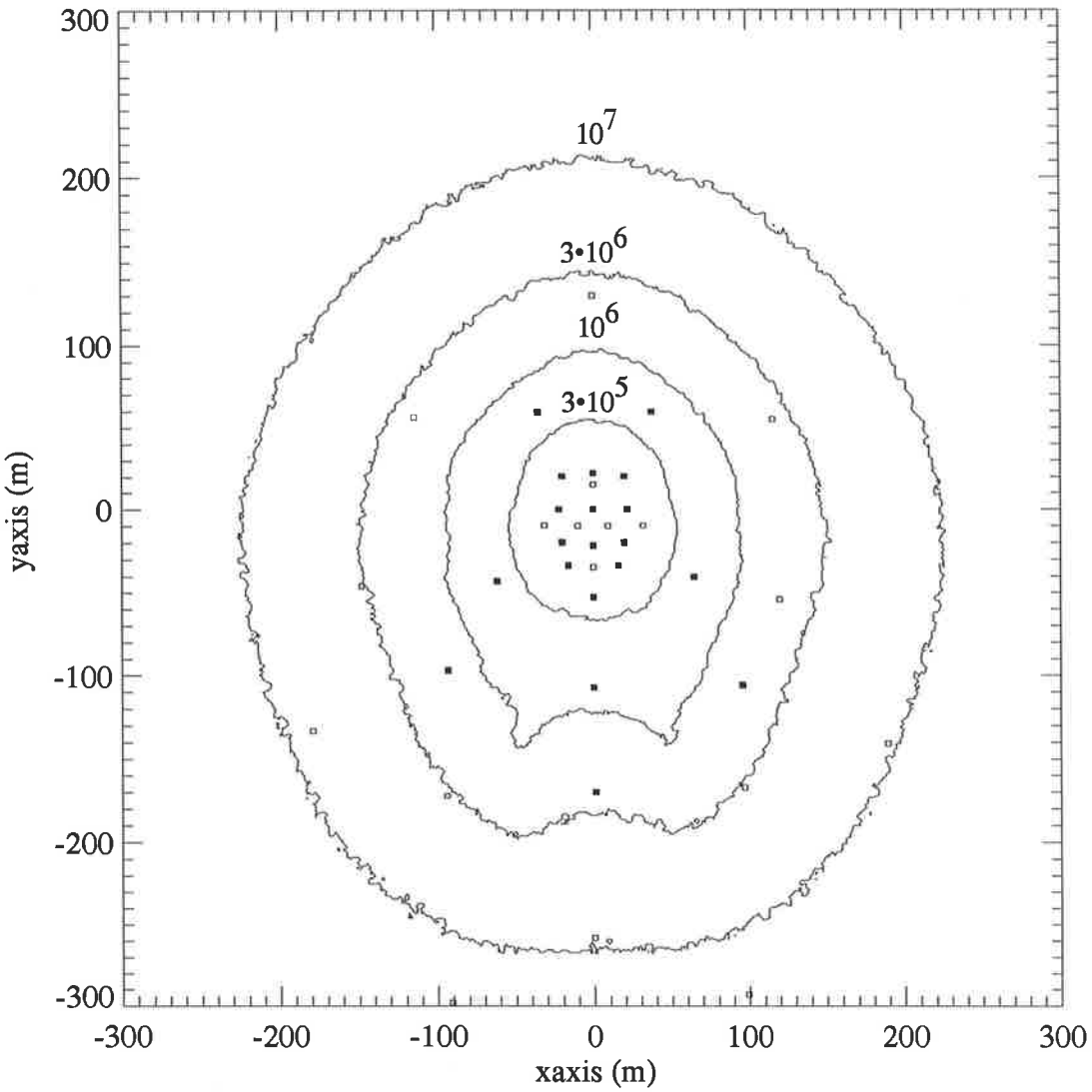

Figure 3.6: 100% triggering contours for Buckland Park shown for various sea level sizes. The position of the array is shown, the black squares are detectors which are part of the slow trigger.

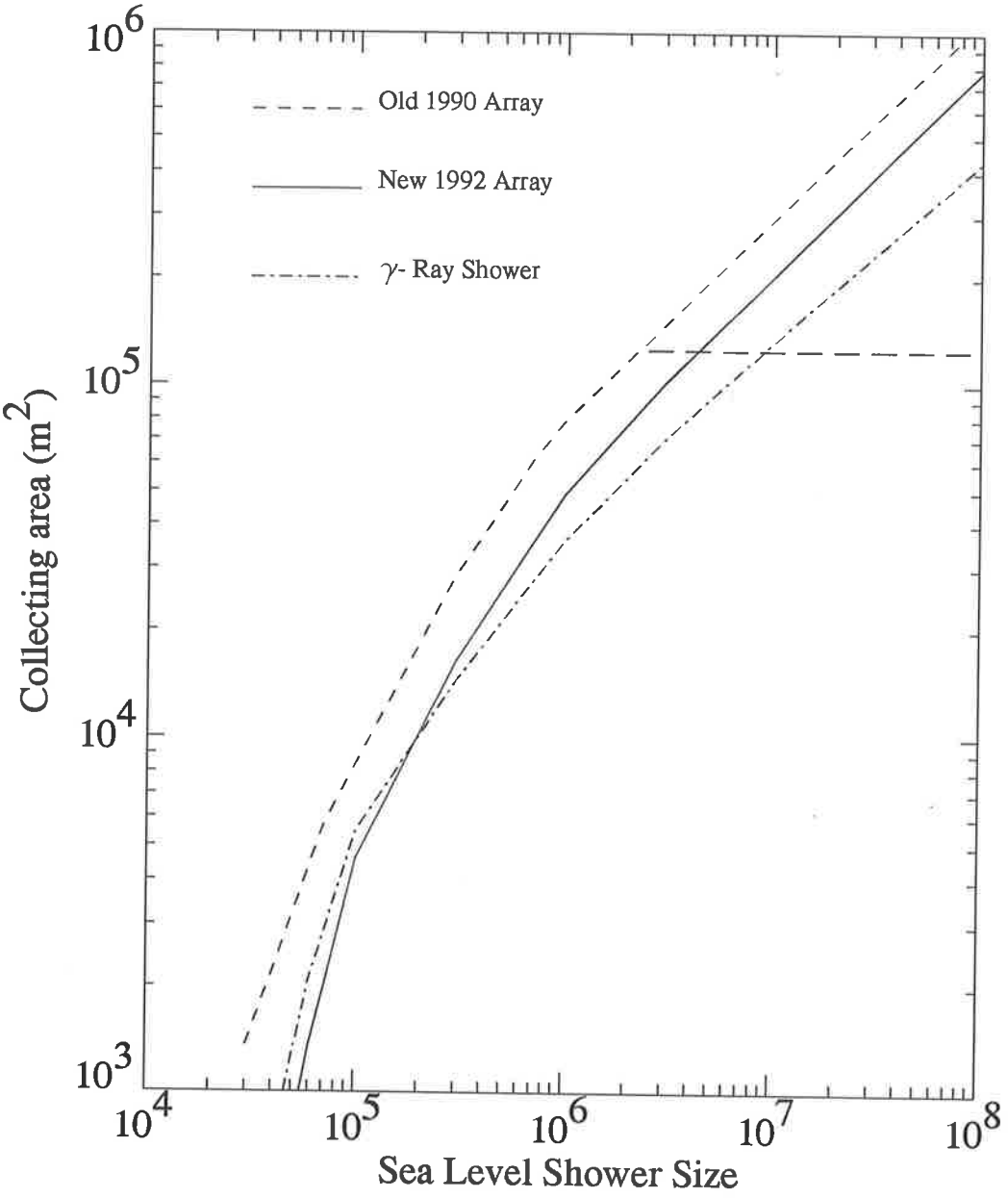

Figure 3.7: Collecting area for the Buckland Park array as a function of energy. The solid curve corresponds to the array in its present state, the dash-dot curve is for γ rays triggering the present array. The horizontal dashed line marks the physical area of the array.

3.5 Shower Front Curvature

It is well known that the shower front of an EAS is curved (Eames et al. 1987). However, the detailed geometry of the curvature is not known, since the relative lag of the curved front with respect to the core of the shower for distances of $\sim$ 100m is of the same order as the timing uncertainty due to the thickness of the shower front.

Linsley (1985) has investigated the average dispersion (shower-front thickness) in the arrival time of air shower particles detected by a scintillator at large core distances and found that it is well described by the following empirical relation:

$$\sigma_t = \sigma_o \left(1 + \frac{r}{r_t}\right)^b$$

where $\sigma_o = 1.6$ns

$r_t = 30$m

$b = 1.5$

The radius of curvature is not well known, but is of the order of 1km for EAS induced by primaries $\geq 10^{14}$eV (Greisen 1960). Taking this value of 1km and estimating the lag in the arrival time at a distance of 100m from the core of the shower, the lag is $\sim$ 20ns. This value is the same order as the value estimated from the equation above of 15ns. So it can be seen that at these core distances it is difficult to determine the true shape of the shower front.

Two methods were used in an attempt to correct for shower front curvature. During the period 1992 – 1993 when the author was responsible for the operation of the array, corrections were made during the routine data analysis. However for the majority of the data 1984 – 1989 where it was not feasible to use raw timing information, an alternate method was employed by the author.

3.5.1 Measurement of Curvature

During the period for which the author was responsible for the operation of the new array (July92 - Jan93) an attempt was made to measure the shower front curvature.

Both timing and density information were available up to $\sim$ 80m from the core of the shower.

Air showers which had core positions within 10m of detector Q and detectors with particle densities greater than 2 particles m^{-2} were used for this investigation. The arrival times measured by the detectors in the region of the air-shower core (D, R, Q, S, and T, see Figure 3.4) were used to calculate the arrival direction under the assumption of a plane shower front. The deviations of the arrival times from the plane-fit as measured by the other detectors were calculated and are shown in Figure 3.8. The best fit (least squares) line to these data, indicates an overall lag of (0.10$\pm$ 0.05)ns m^{-1} behind the plane front. This value is consistent with those obtained from other arrays (Eames et al. 1987, Ciampa 1988, Green 1993).

It is clear from Figure 3.8 that the fluctuations are large which precludes a more accurate determination of the curvature. It should be noted however that the value of curvature obtained is of the same order as that predicted from arguments made above.

3.5.2 Correction for Curvature

A correction for the 'curvature' (for the 1992 data) can be made by adjusting the relative arrival times t_i at each detector to the value expected if the shower front were planar, t_i^P, which would have resulted in an earlier apparent arrival time:

$$t_i^P = (t_i - 0.10 \times r_i)\text{ns}$$

where r_i is the distance of the detector from the core in the plane of the shower. These new times are used to calculate the arrival direction on the assumption of a plane shower front.

However for the bulk of the data (1984 – 1989) it was not feasible to reanalyse the directions by using the raw times as these were not available. Instead a method was developed, which uses the initial directions as a guide for the individual detector

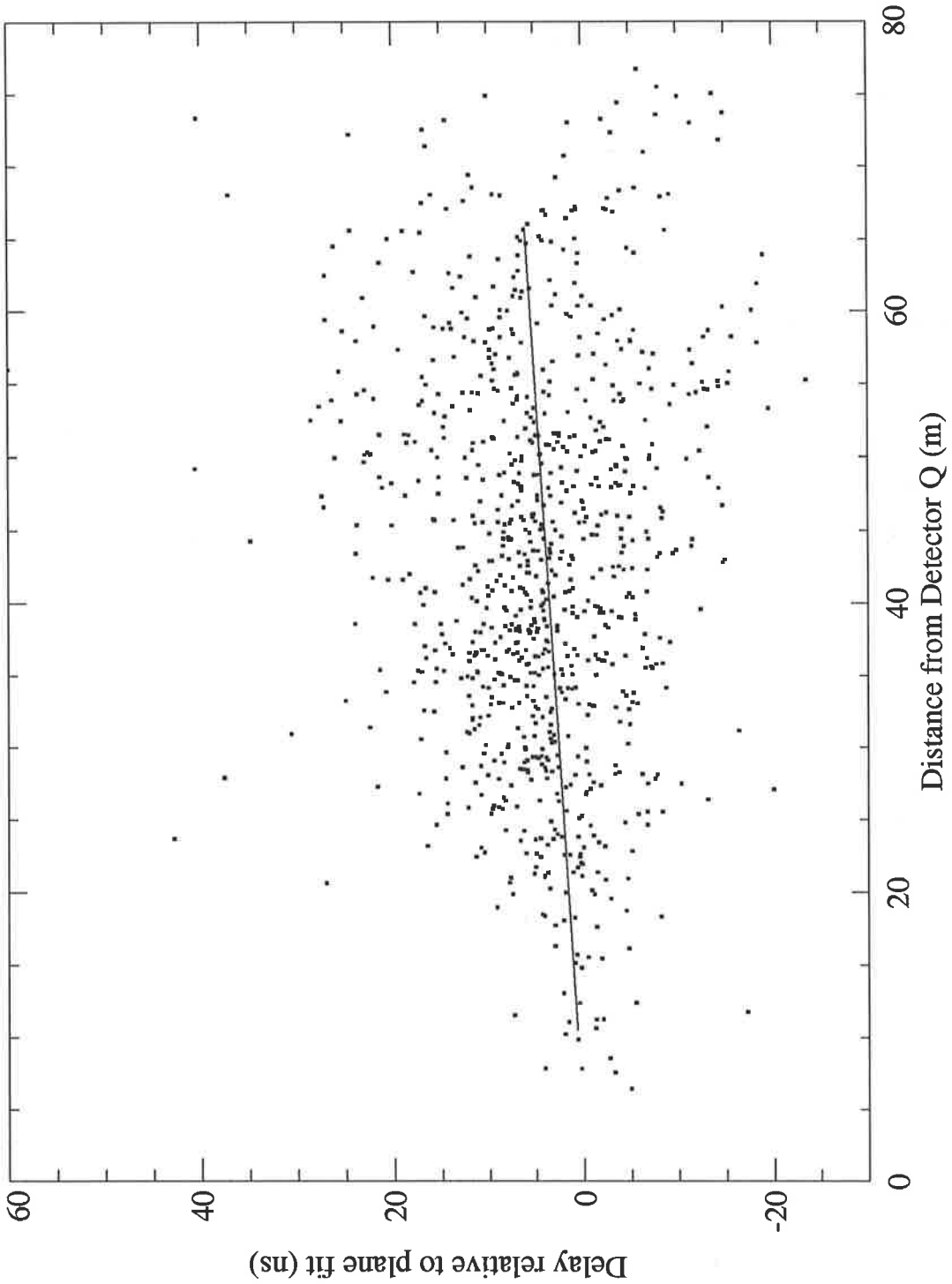

Figure 3.8: The delay in arrival time relative to detector Q as a function of core distance. The solid line is a line of best fit.

times.

Given that the data had already been analysed for directions, size, age and core-location assuming a plane front, a correction for curvature was made as follows. An air shower was simulated to trigger the Buckland Park array using the analysed data as inputs for the shower parameters. The particle densities at the detectors were calculated using the NKG function, given the core-location, shower size, age and direction. Timing detectors which registered a density of 2 particles m^{-2} (the threshold for fast timing detectors) or greater were then assigned artificial 'raw' plane times based on the initial direction of the event. In this way it was possible to estimate which detectors would have triggered for a particular event.

New 'raw' times were then calculated using the distance of the detector from the core in the plane of the shower, assuming a fixed curvature of 0.14 ns m^{-1}, an estimate of the curvature for the different array configuration during this earlier epoch, as calculated by Ciampa (1988).

$$t_i^n = (t_i^o - 0.14 \times r_i)\text{ns}$$

where t_i^n is the new 'raw' time for the i^{th} detector, t_i^o the old assigned 'raw' time, and r_i is the distance of the i^{th} detector from the core of the shower in the plane of the shower.

This has the effect of 'flattening' the curved front into something resembling a plane front. A new direction was calculated from these new 'raw' times assuming a plane front. The change in direction will depend on the number of detectors used in the fit and the location of the core (see Figure 3.9). The largest change will tend to occur for events which land on the edge of the array and which only have a small number of timing detectors triggered. As can be seen from Figure 3.9 the majority of events incur a change in direction of ($\sim$ 2 - 2.5^0). This is expected since the correction for curvature used is $\sim 2.4^0$ (0.14 ns m^{-1}).

This method for curvature correction has the advantage of not requiring the true raw times for the event and is consequently easier to implement. An attempt to be

as accurate as possible was made by using the shower size and core location information. Simulations show that although using the true raw times is preferable it is not significantly better, see below.

3.5.3 Simulated Curvature Correction

A simulation was performed to check for the difference between correcting the true raw times of the detectors and applying the technique described above (Meyhandan et al. 1991). The geometry of the 1986 – 1988 Buckland Park array is shown in Figure 3.10. There are 36 detectors in total of which 24 provided timing information, these are indicated by the filled squares. The trigger condition for the array was set at the 2 particle level for timing channels and the 6 particle level for the channels

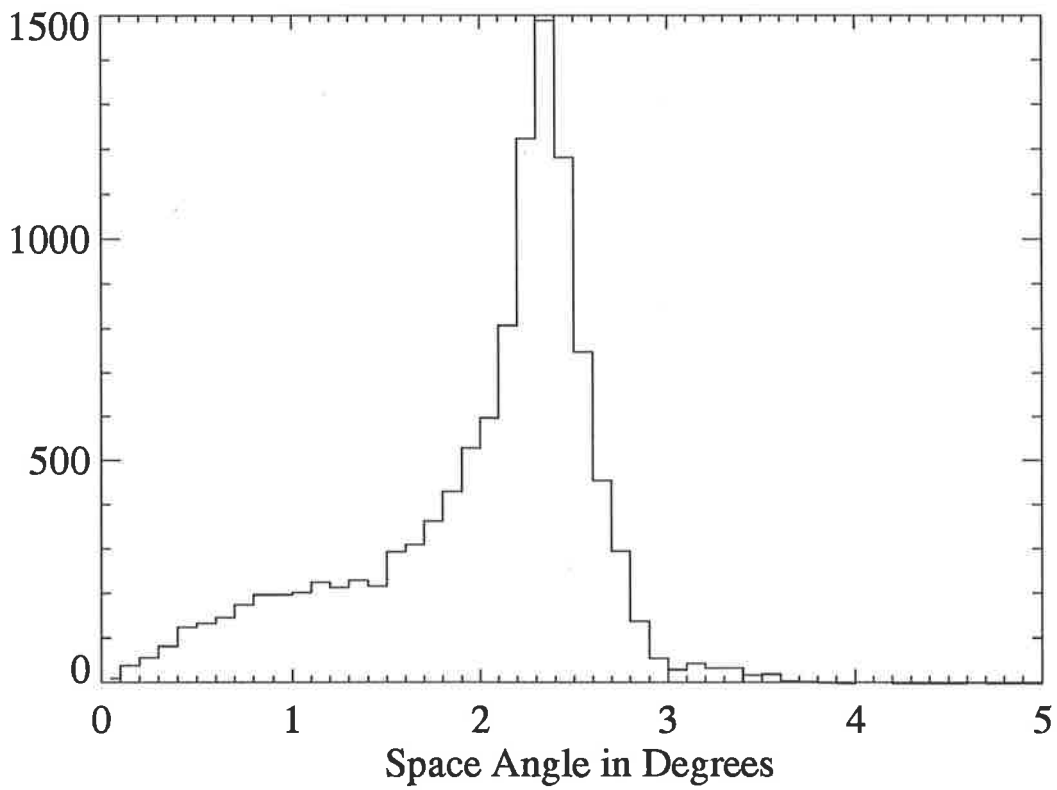

Figure 3.9: Change of arrival direction after curvature correction. The data are for the 26^{th} June 1986.

measuring particle density.

To simulate an event falling on the array, a random core position within 200 metres of the centre was selected along with a random azimuth and zenith angle. Shower sizes were chosen from a standard source spectrum (integral indices of γ = -1.58 for $N_e \leq 3 \times 10^5$ particles, and γ = -2.02 for $N_e > 3 \times 10^5$ particles). The shower size was converted to a sea-level size by accounting for atmospheric attenuation and zenith angle. The particle densities at the detectors were then calculated using the NKG function given the core position and shower size. Once an event satisfied the triggering conditions, raw plane times were assigned to the timing detectors based on the direction of the shower.

Curvature was introduced by adding an amount of time to individual detectors

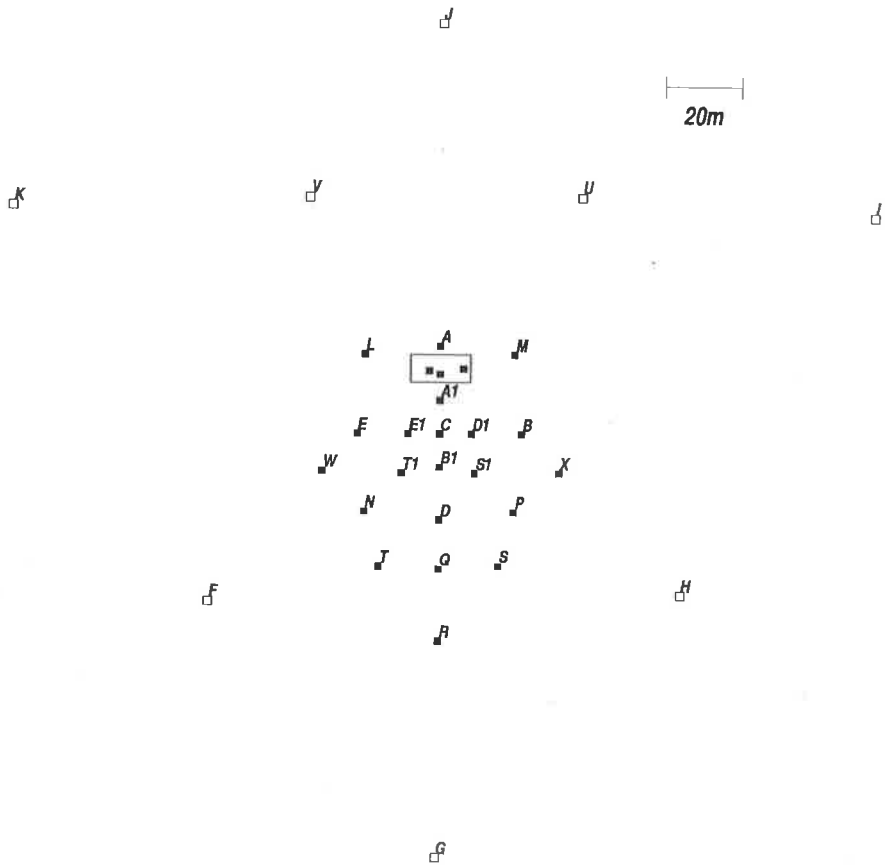

Figure 3.10: The positions of detectors in the Buckland Park array during the period 1984 – 1989. The filled squares represent the timing detectors.

which depended on the distance of the detector from the core in the plane of the shower. This has the effect of producing a shower which looks like a cone falling on the array. The angle of this cone was determined by the measured curvature of 0.14ns m^{-1}, 2.4° (Ciampa 1988). The shower was given finite thickness by applying a random gaussian fluctuating to the particle arrival times at a detector, and the earliest arriving particle determined the trigger time (thus simulating the double discriminators §3.1.1). A timing detector was selected if it has a density greater than 2 particles m^{-2}, so that not all timing detectors were used.

Shower directions were determined in a convential manner by fitting the raw detector times to a plane shower front. The errors in these plane fits are shown in Figure. 3.11. Two other methods of direction fitting were used, with the aim of improving angular resolution.

Method 1: Here it is assumed that the true raw trigger times are unavailable. Artificial 'raw' times are calculated on the basis of a plane fit, and are then corrected using the core distance and a fixed curvature of 0.14 ns m^{-1}. A new plane is the fitted to these corrected times. This is the method described in §3.5.2, for the 1984 – 1989 data.

Method 2: The true raw times are used and the same curvature correction is performed in an inverse manner before a plane is fitted. The distributions of errors for the two methods are shown in Figure 3.11b & c.

It is apparent that both Methods 1 and 2 are an improvement over the traditional plane fit. However there is only a small improvement gained by using Method 2 over Method 1. Figure 3.20d shows a scatter plot of both methods, showing that Method 2 is preferable if the raw data are available.

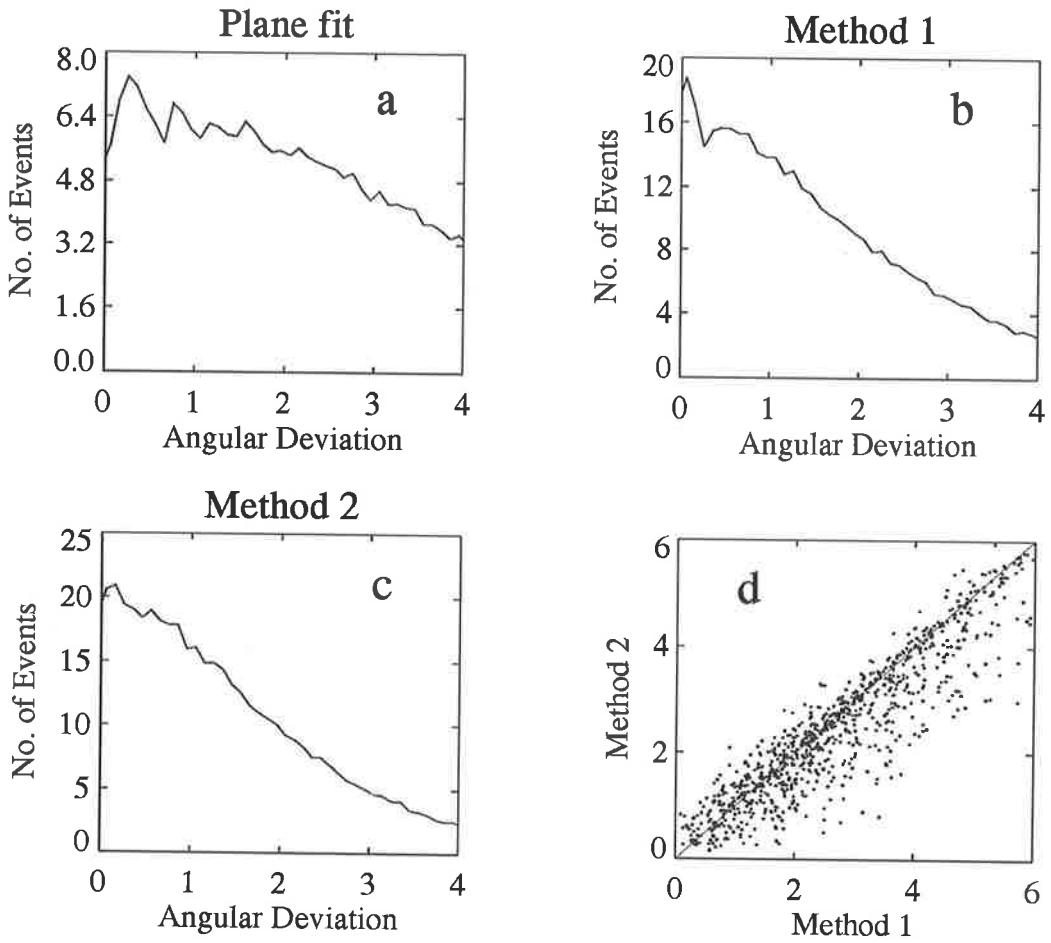

Figure 3.11: Deviation from the true shower direction (in degrees) from simulated data. The y-axes have been divided by 10^3. Results from the plane fit are shown in plot a. Method 1 shown in b and Method 2 in c. A comparison of Methods 1 & 2 (scatter plot) is shown in d.

Summary of Corrections to Data

Shower front curvature corrections were applied to the 1984 – 1989 & the 1992 data. The measurement of curvature is dependent on the array configuration and timing electronics. Therefore different array configurations may give different estimates of the curvature. Since there are no estimates of curvature for the 1978 – 1982 & 1990 data no attempt was made on curvature correction on these data.

3.6 Array Characteristics 1992

The new Buckland Park array began operating on the 23^{rd} July 1992 (JD2448826.6938831). The data presented in this section ends on the 18^{th} of January 1993 (JD2449005.5161034). The array operated continuously during this period with occasional down-time caused by power failures. A total of 112262 events triggered the array with a mean rate of 8×10^{-3} Hz.

Arrival directions were assigned to 109420 events corresponding to 97.5% of the triggered events. Shower sizes, ages, and core locations were then fitted to 107262 events, corresponding to 95.5% of the total triggered events. These values are higher than those of the old (1990) array (95% and 78% respectively). This is primarly due to the increase in array threshold together with the requirement for a minimum of three 'slow' detectors in the array trigger rather than the previous two. A discussion of the 'new' (1992) array characteristics follows.

3.6.1 Zenith & Azimuth Angle Distributions

The zenith angle distribution for the 1992 data is shown in Figure 3.12. This distribution provides information on the development and attenuation of EAS through the atmosphere. The number of events increases intially as the solid angle increases ($\propto \sin\theta$), and reaches a peak typically at 20^o, after which the distribution begins to fall off as atmospheric absorption (dependent upon $\sec\theta$) becomes increasingly important.

By removing the solid angle effect (dividing bin contents by $\sin\theta$) a decreasing distribution with zenith angle is produced. The number of events per steradian is described by

$$\Phi(\theta) = \frac{dN(\theta)}{d\Omega} \propto \cos^{\mathrm{n}}\theta$$

(Hayakawa 1969)

with n in the range $6 - 10$. It is however approximated by a value of 8.3 (Greisen

1956). This value of n leads to a predicted peak in the distribution of $\theta \sim 19^o$, which is in good agreement with the distribution presented in Figure 3.12(a).

An alternative representation of the above equation of may be produced by plotting $Log_{10}\Phi(\theta)$ as a function of $sec(\theta)$ (Kalmykov et al. 1973), that is

$$log_{10}\Phi(\theta) = Csec(\theta) + D$$

The constant C is given at sea-level by $1030(1 - \gamma)/2.3\lambda$, where γ is the index of the cosmic ray differential spectrum, and λ is the shower attenuation length (Ciampa and Clay 1988). Using typical values of γ (2.5 - 3) and λ (185 gcm^{-2}, Clay & Gerhardy (1982)) gives $|C| \sim 3.5$.

Examining the data presented here, the distribution of $Log_{10}\Phi(\theta)$ vs $sec\theta$ is well fitted by a slope of -3.96 (see Fig. 3.12(c)).

The azimuth angle distribution is shown in Fig 3.13. There are no large deviations from a continuous exposure in azimuth.

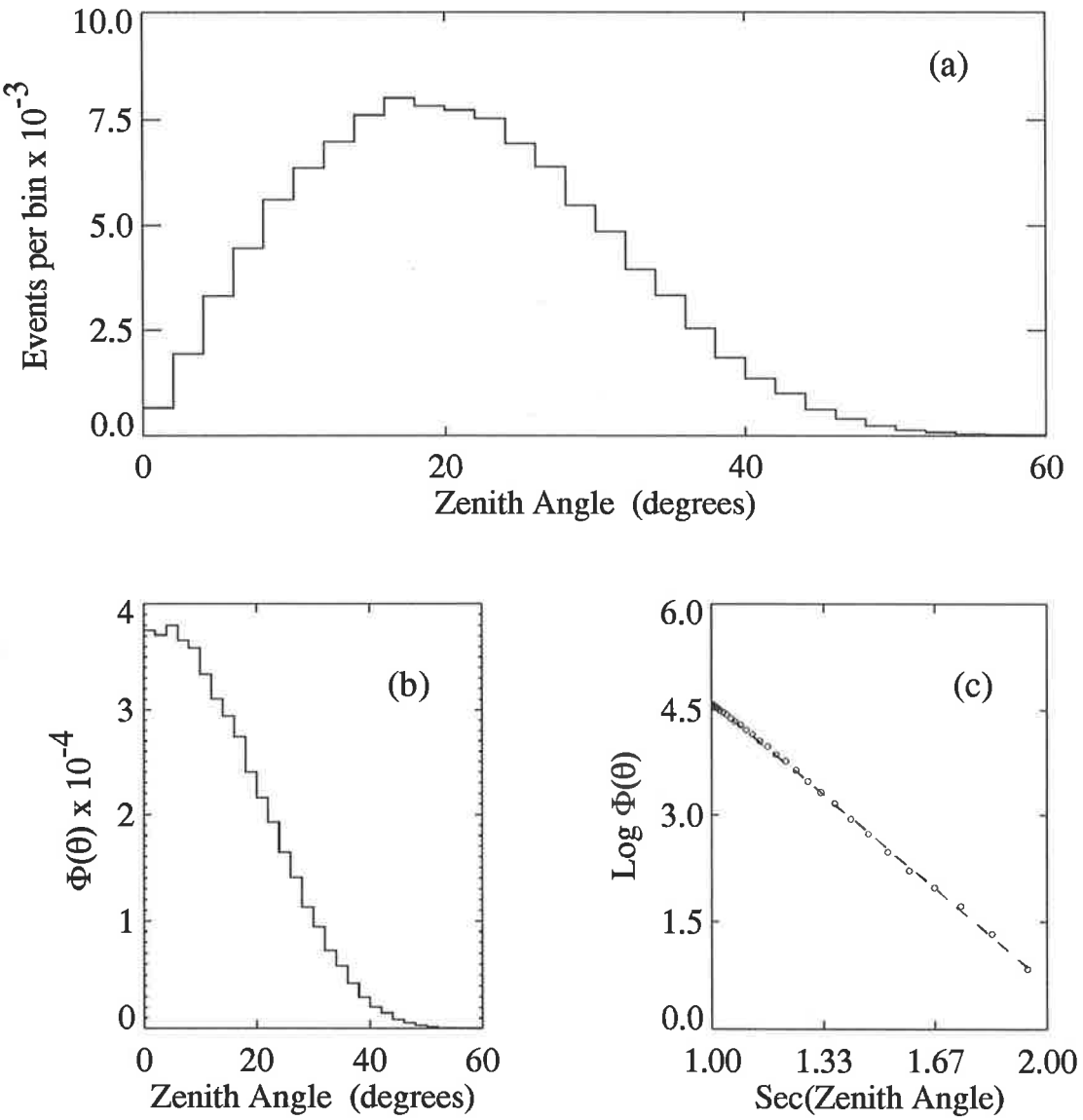

Figure 3.12: The analysed zenith angle distribution from the 1992 data set, presented in three ways as discussed in the text.

(a) The binned data

(b) The zenith angle distribution corrected for solid angle exposure.

(c) The Log $\Phi(\theta)$ versus secθ fit to the data. The dashed line has a slope of $\sim$ -3.96.

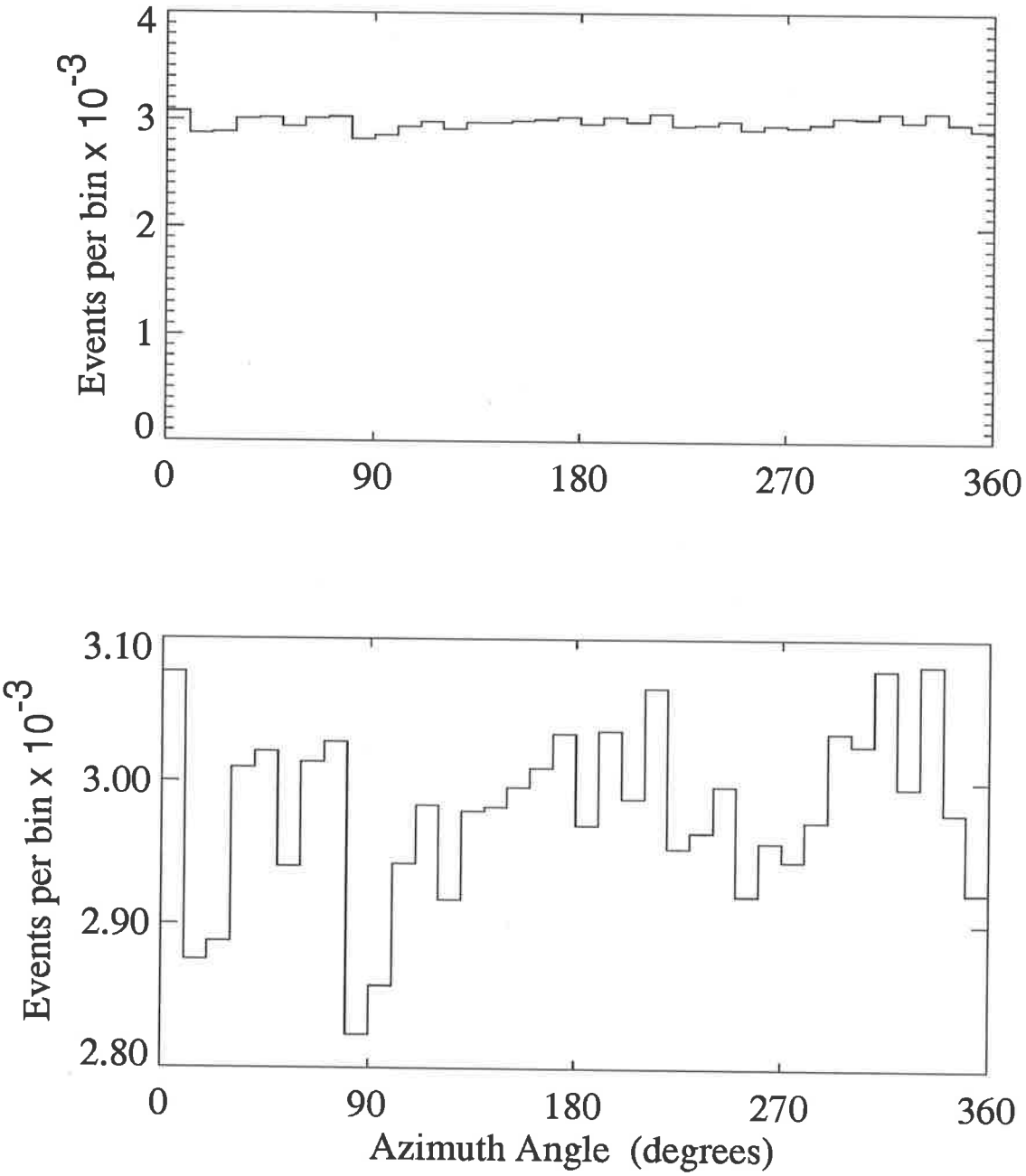

Figure 3.13: The analysed azimuth angle distribution of arrival directions form the 1992 data set, in full & high resolution formats.

3.6.2 Right Ascension & Declination Distributions

The local arrival directions (θ, ϕ) can be converted to equatorial co-ordinates given the event time (in Universal Time) and the array latitude. The right ascension distribution is shown below, and indicates that there has been continuous sky-coverage. When searches are made for a DC excess from a particular source, the background is estimated from the same declination band as the source, but averaged over right ascension regions excluding the source region. Hence it is desirable that this distribution is uniform in order to get a reliable background measurement in a simple way.

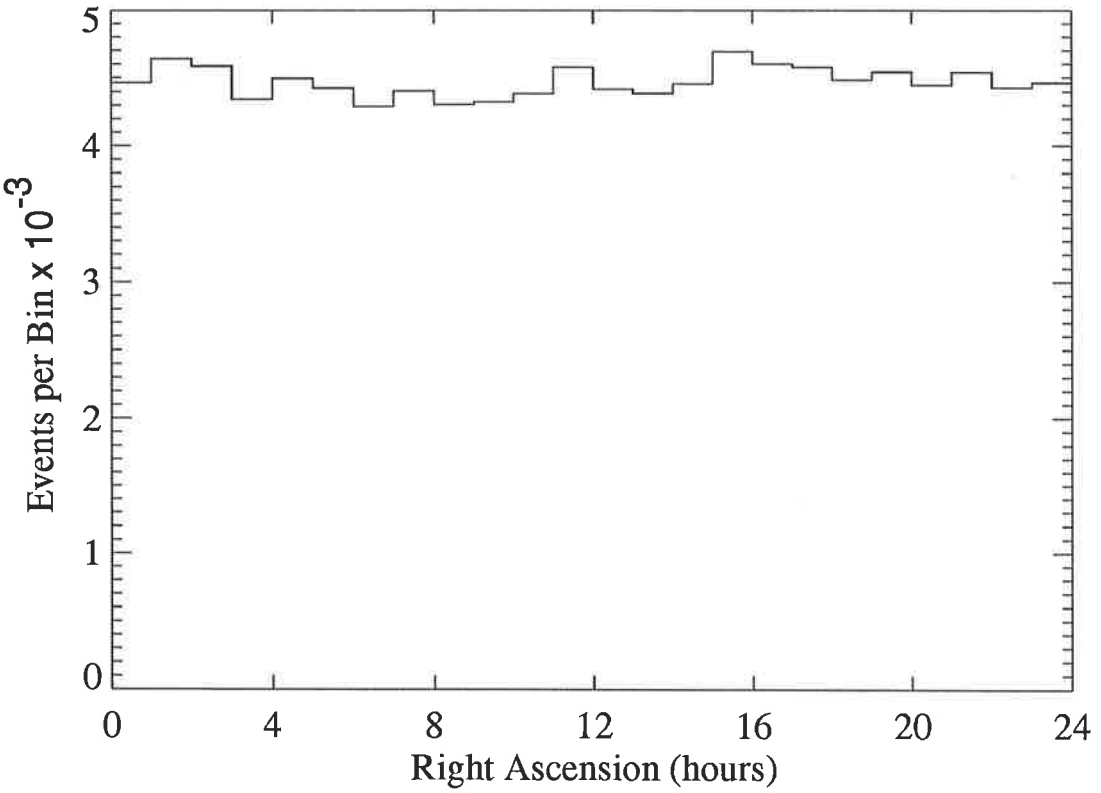

Figure 3.14: The right ascension distribution for events recorded in the 1992 data.

The region of sky over which the array is sensitive is reflected in the declination distribution shown below. The distribution has a peak at approximately the latitude of the array ($\sim 35°$S) and falls off to either side, due to the increase in atmospheric depth with zenith angle. The array is sensitive to declinations in the range $-80^o < \delta < 15^o$.

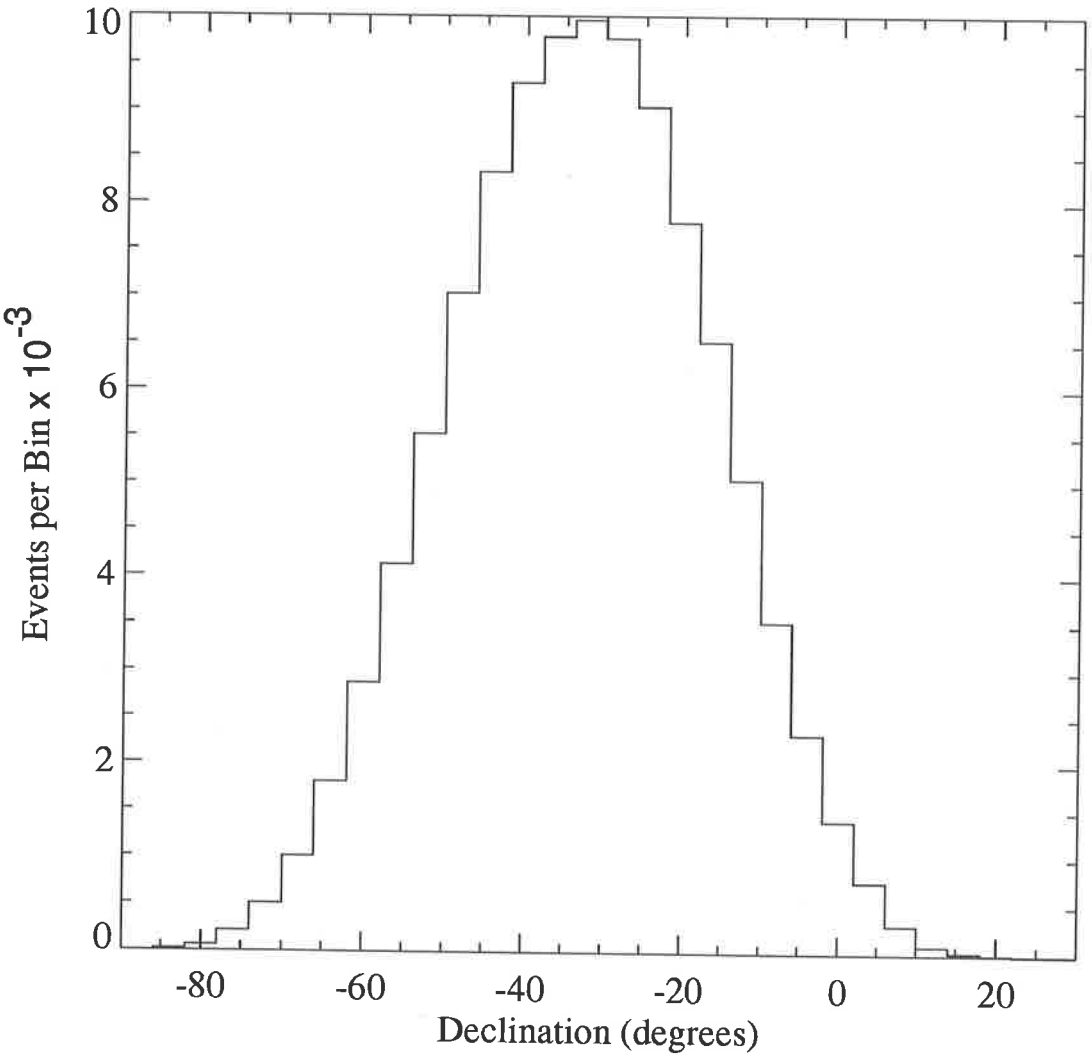

Figure 3.15: The declination distribution of events recorded in the 1992 data, showing the region of sky coverage.

3.6.3 Goodness of fit Distribution

The goodness of fit parameter σ as defined in equation 3.5, reflects how well a direction is fitted to the detector arrival times. The distribution of σ for all analysed arrival directions after correction for shower front curvature is shown below. The mean of the distribution is ~ 2.85 and the mode is ~ 2.35.

The average timing residual for all detectors has been improved, especially for the outer 12 detectors. These outer detectors benefit from the newly installed TDC and the new double discriminators which allow sampling times closer to the leading edge of the shower front. The effect of allowing for shower front curvature is also shown in Table 3.2, where there is a comparison of the average timing residual for the detectors. There has again been an overall improvement in the timing residuals, this time the greatest improvement coming from the inner set of detectors.

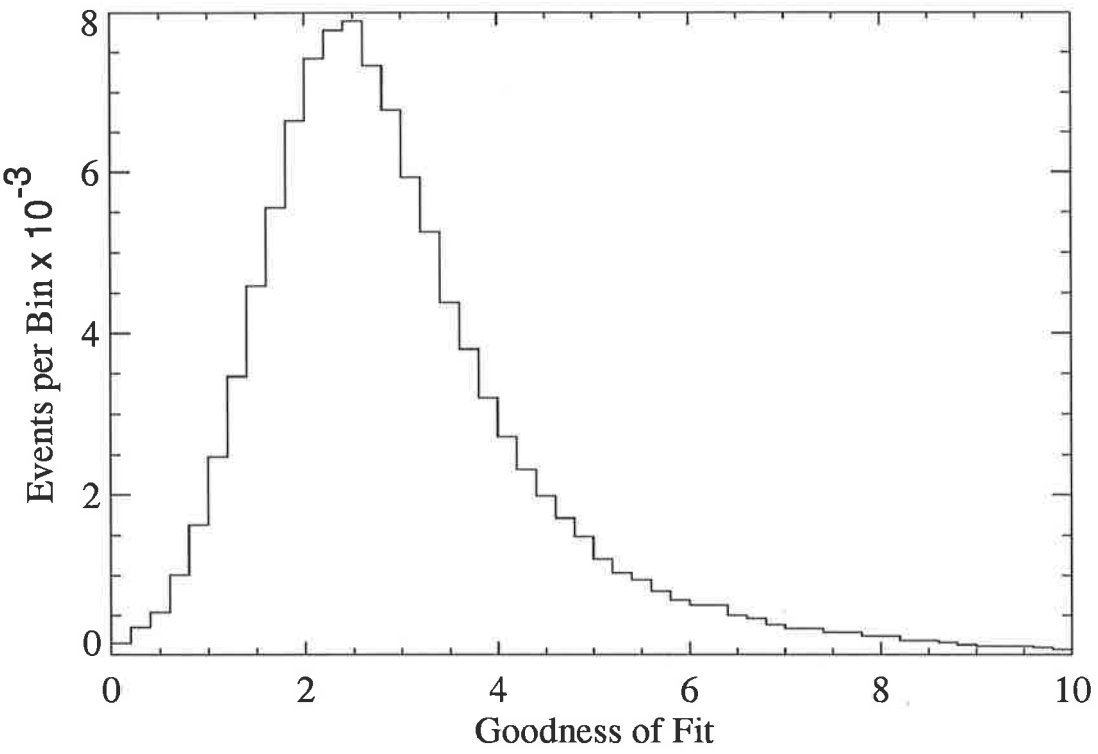

Figure 3.16: The Goodness of fit distribution for the 1992 data after correction for shower front curvature. The mode of the distribution is ~ 2.35.

Overall there has been an improvement after shower front curvature had been included in the analysis. An average of 8% improvement in residuals for the inner set of detectors and ~5% improvement for the outer detectors, which is consistent with fewer leading edge particles at these distances and larger expected fluctuations (see §3.7).

Detector Label	Plane Fit May 1990	Plane Fit July 1992	Curve Fit July 1992	Percentage Improvement
A	4.4	3.4	3.0	12
B	4.1	3.3	3.0	9
C	4.4	3.4	3.1	9
D	4.1	3.3	3.0	9
E	4.2	3.3	3.1	6
S	5.9	3.5	3.2	9
T	5.6	3.5	3.2	9
R	6.1	3.6	3.3	8
S1	4.0	3.4	3.1	9
T1	4.0	3.3	3.1	6
P	4.3	3.2	3.1	3
Q	4.3	3.4	3.3	3
M	3.9	3.3	3.2	3
W	4.2	3.2	3.1	3
BFD	3.8	3.1	3.0	3
N	4.3	3.3	3.1	6
X	3.9	3.3	3.2	3
L	4.1	3.2	3.1	3
1	12.7	5.0	4.7	6
2	11.8	4.7	4.5	4
3	9.9	4.6	4.4	4
4	8.9	4.9	4.8	2
5	15.9	5.1	4.9	4
6	13.3	5.8	5.5	5
7	11.3	5.4	5.2	4
8	11.1	6.6	6.2	6
A1	11.3	5.6	5.2	7
B1	10.1	6.2	5.8	6
E1	9.5	5.7	5.5	4

Table 3.2: The individual average timing residuals in nanoseconds for each detector are shown for the old (1990) array and the new (1992) array. As can be seen there has been an improvement in the overall directions fits, especially for the last 12 detectors which have been connected to the new TDC and double discriminators. The third column are the residual values after shower front curvature has been included in the analysis, and the percentage improvement in the curved fit of July 1992 over the plane fit of July 1992 indicated in the last column.

3.6.4 Triggered Timing detectors Distribution

The distribution of the number of triggered fast-timing detectors N_t is shown below. The distribution reflects features of the array in a similar way to the size distribution (Figure 3.18). Close to the array threshold, those EAS of a given energy which develop deeper in the atmosphere will be preferentially detected by the array (Clay 1985). These showers would have a limited lateral extent and will only trigger a small number of detectors. The number of triggered detectors and collecting area increases with primary particle energy (and shower size). Thus, even though lower energy primaries are more numerous at the top of the atmosphere, only a small fraction will trigger the array compared to higher energy cosmic ray primaries. Given that the cosmic ray spectrum falls steeply with energy, there would be a drop in the number of events triggering higher numbers of detectors. These factors are reflected in the distribution below.

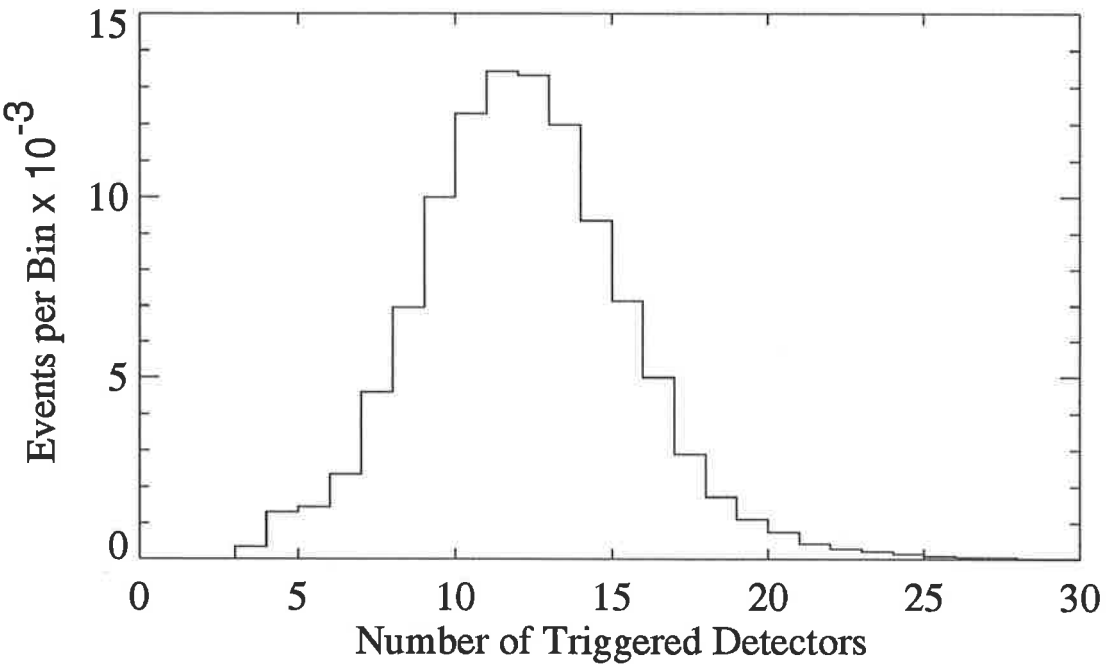

Figure 3.17: The distribution of the number of triggered fast-timing detectors for all analysed events.

3.6.5 Shower Size and Age Distributions

The array threshold was increased form $\sim 2 \times 10^4$ particles to $\sim 10^5$ particles as described in §3.4.1. This resulted in a decrease in the event rate from $\sim 6 \times 10^{-2}$Hz to $\sim 8 \times 10^{-3}$Hz. The fitted shower size distribution is shown below. The shower size was derived by using a maximum likelihood fit of the particle densities to the NKG function (eqn 2.6). The shower core locations (X_c, Y_c) were restricted to lie within (-150 < x < 150) meters and (-250 < y < 150) metres of detector C (the centre of the array).

The size distribution is now comparable with that of the array during the period 1979-1982, with approximately two and a half times the collecting area.

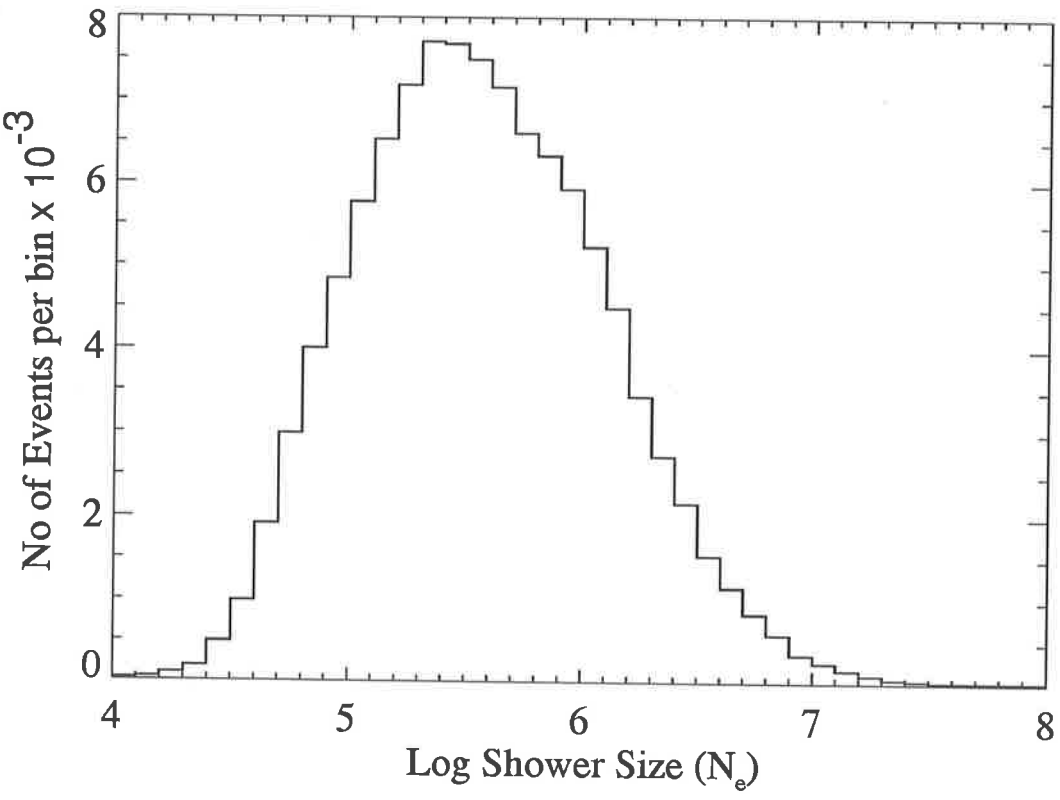

Figure 3.18: The shower size distribution for the 1992 data set.

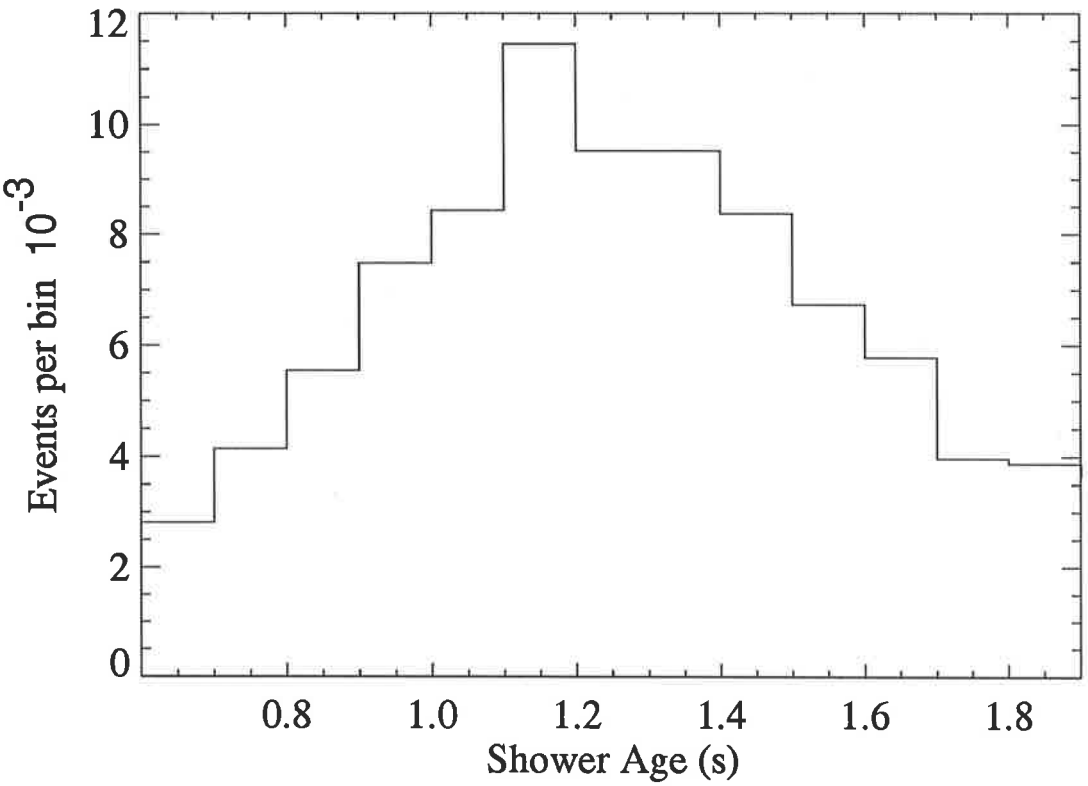

Figure 3.19: The shower age distribution for the 1992 data set. The mean of the distribution is ~ 1.3.

There were only a small percentage of fitted directions which were not analysable due to a failure of the minimization to converge within the limits of the core location and age parameter ($0.5 < s < 2.0$). The mean age of ~ 1.3 is comparable to that of the array during the period $1979 - 1981$. The mode is ~ 1.1 and is lower than the period $1984 - 1990$ which is consistent with the higher size threshold for the array.

3.7 Array Directions 1984 – 1989

The arrival directions for this period (1984–1989) were reanalysed in an attempt to account for shower front curvature as discussed in §3.7.2. There is a total of $\sim 3.4 \times 10^6$ events in the 1984–1986 data set and a total of $\sim 4.2 \times 10^6$ events in the 1986–1989 data set. The configuration of the array during this period (1984 – 1989) is shown in Figure 3.10. The difference between the 1984 – 1986 and 1986 – 1989 configurations are the number of detectors providing timing information. There were 19 and 24 detectors providing timing information for the two epochs respectively. The characteristics of the arrival direction distributions are discussed below.

3.7.1 Zenith Angle Distribution

The Zenith angle distribution for the 1984–1989 data set is presented in Figures 3.21 & 3.22. The conventional distribution shown in Figures 3.22a & 3.23a both show a rise of events with zenith angle and then a fall as atmospheric attenuation becomes increasingly important as discussed in §3.5.1. The peak of both the distributions occurs at $\sim 19^o$ which is consistent with that obtained previously (see Figure 3.12).

Figures 3.22c & 3.23c show the alternative representation in terms of $\log_{10}\Phi(\theta)$ versus $\sec(\theta)$ as discussed in §3.5.1. For the 1984–1986 data set the line of best fit for $\sec(\theta) \leq 1.5$ has a coefficient C = −3.42, and the 1986–1989 data set has a line of best fit for $\sec(\theta) \leq 1.7$ of −3.45. Both values of C are lower than that obtained for the present (1992) array, however it is possible that they are consistent since the 1992 array has a higher threshold and the difference may be due to a change in the triggering efficiency with zenith angle.

3.7.2 Azimuth Angle Distribution

The reanalysed azimuth angle distribution for the 1984–1986 & 1986–1989 data sets are shown in Figure 3.24. There is a prominent feature which shows a preference of events from the south of the array in the 1984–1986 data set, which was also evident

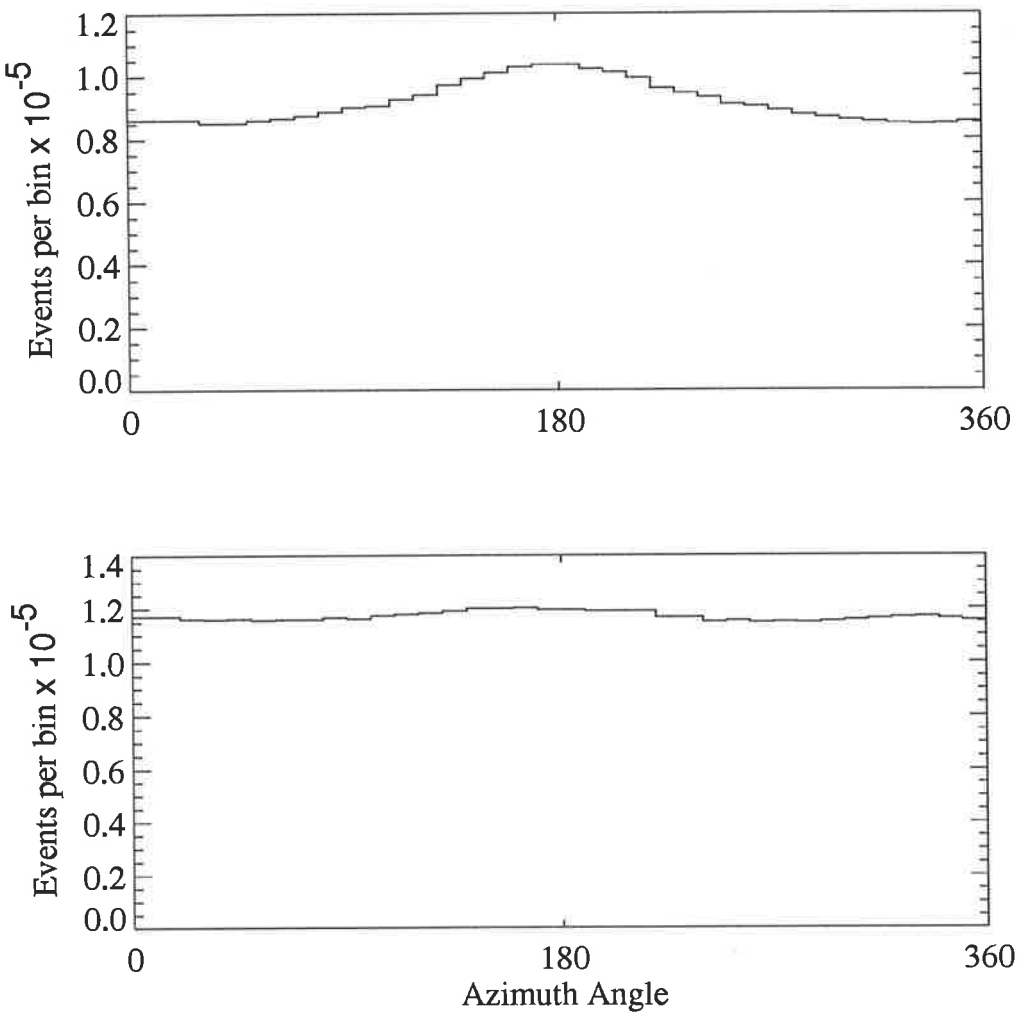

Figure 3.20: The reanalysed azimuth angle distribution of arrival directions for the 1984–86 data (top), and the 1986–89 data (bottom). The non-uniform distribution in the 1984–1986 data set is discussed in the text §3.8.2.

in the plane fit data (see D.Bird 1991). It was suggested by Edwards (1988) that this was the result of the asymmetry of the array during that period especially in the array trigger.

Further development of the array in 1986 (Ciampa 1988) led to a more uniform acceptance of events in azimuth. The reanalysed data for the period 1986–1989 shows a much improved distribution consistent with the plane fit data.

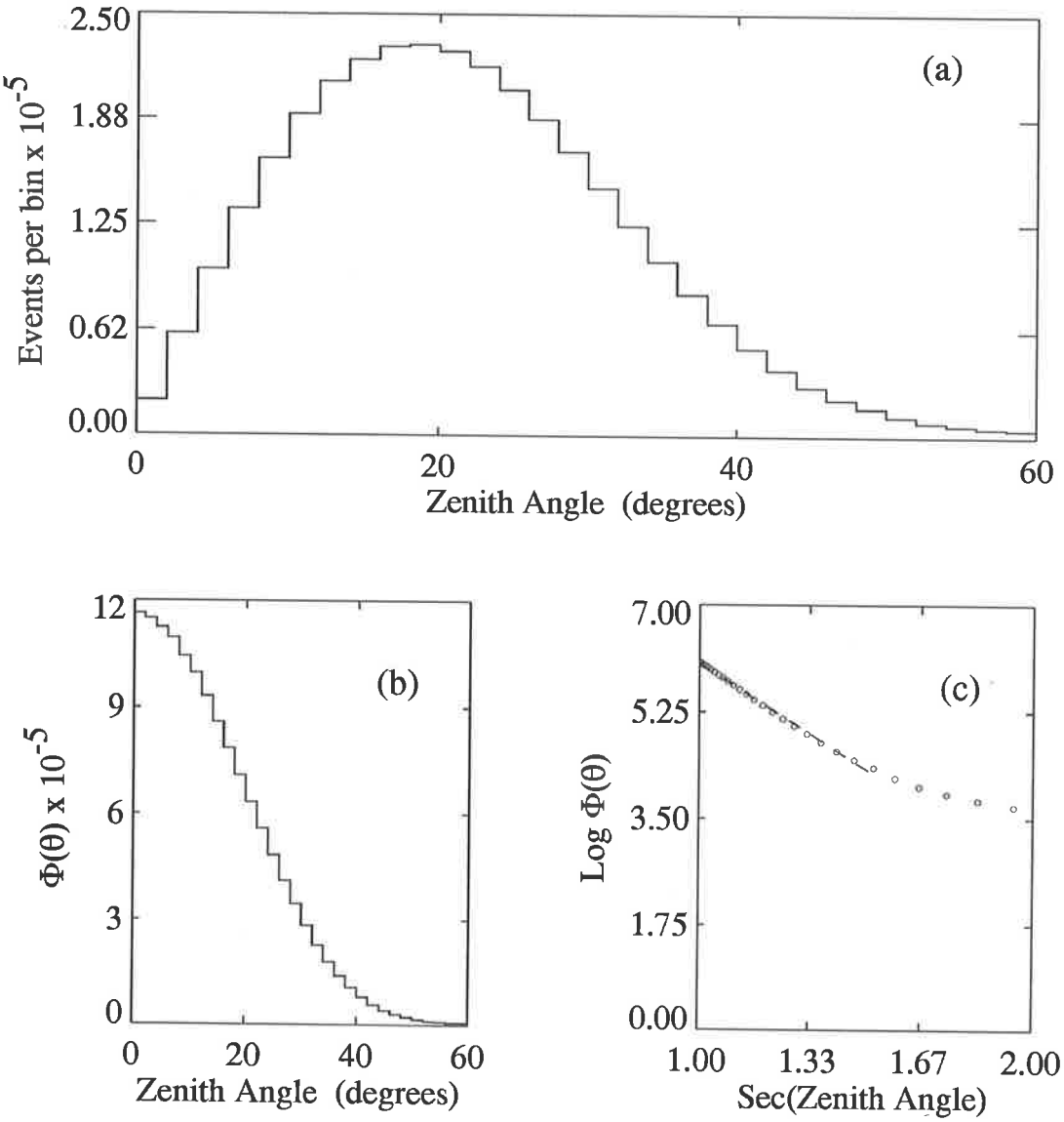

Figure 3.21: The analysed zenith angle distribution from the (1984 – 1986) data set, presented in three ways as discussed in the text.

(a) The conventional zenith angle distribution.

(b) The zenith angle distribution corrected for solid angle exposure.

(c) The Log $\Phi(\theta)$ versus secθ fit to the data, see text. The solid line has a slope of ~ -3.42 for $\sec(\theta) < 1.5$.

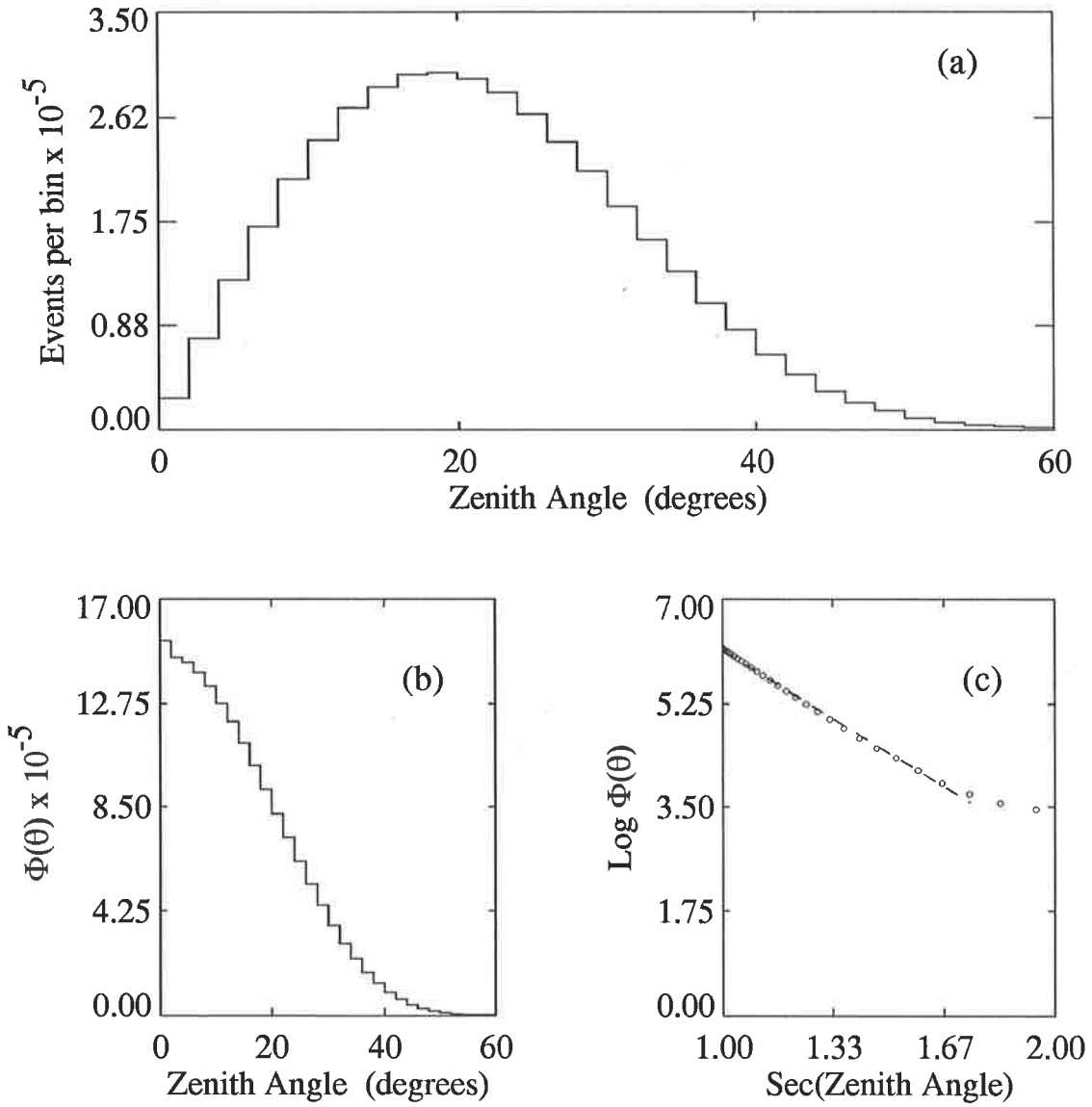

Figure 3.22: The analysed zenith angle distribution from the (1986 – 1989) data set, presented in three ways as discussed in the text.

(a) The conventional zenith angle distribution.

(b) The zenith angle distribution corrected for solid angle exposure.

(c) The Log $\Phi(\theta)$ versus secθ fit to the data, see text. The solid line has a slope of ~ -3.45 for sec$(\theta) < 1.7$.

3.7.3 Right Ascension & Declination Distribution

The declination distribution for the reanalysed 1984−1989 data are shown below. The peak of the distribution is consistent with the latitude of the array (-35^o). The data is sensitive in an effective range $-80^o < \delta < 15^o$.

The Right Ascension distribution is shown in Figure 3.24.

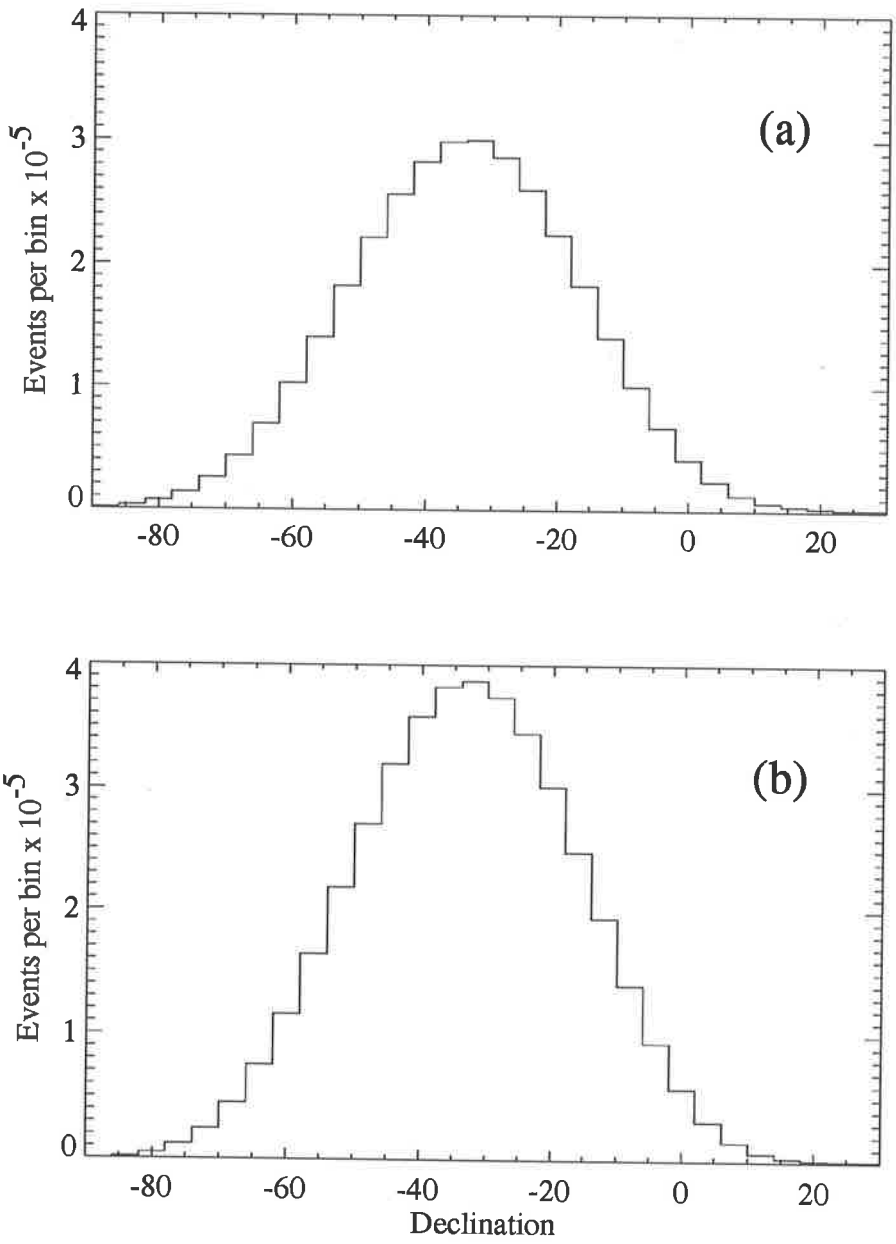

Figure 3.23: The Declination distributions for the reanalysed data sets (a) 1984−1986 and (b) 1986−1989.

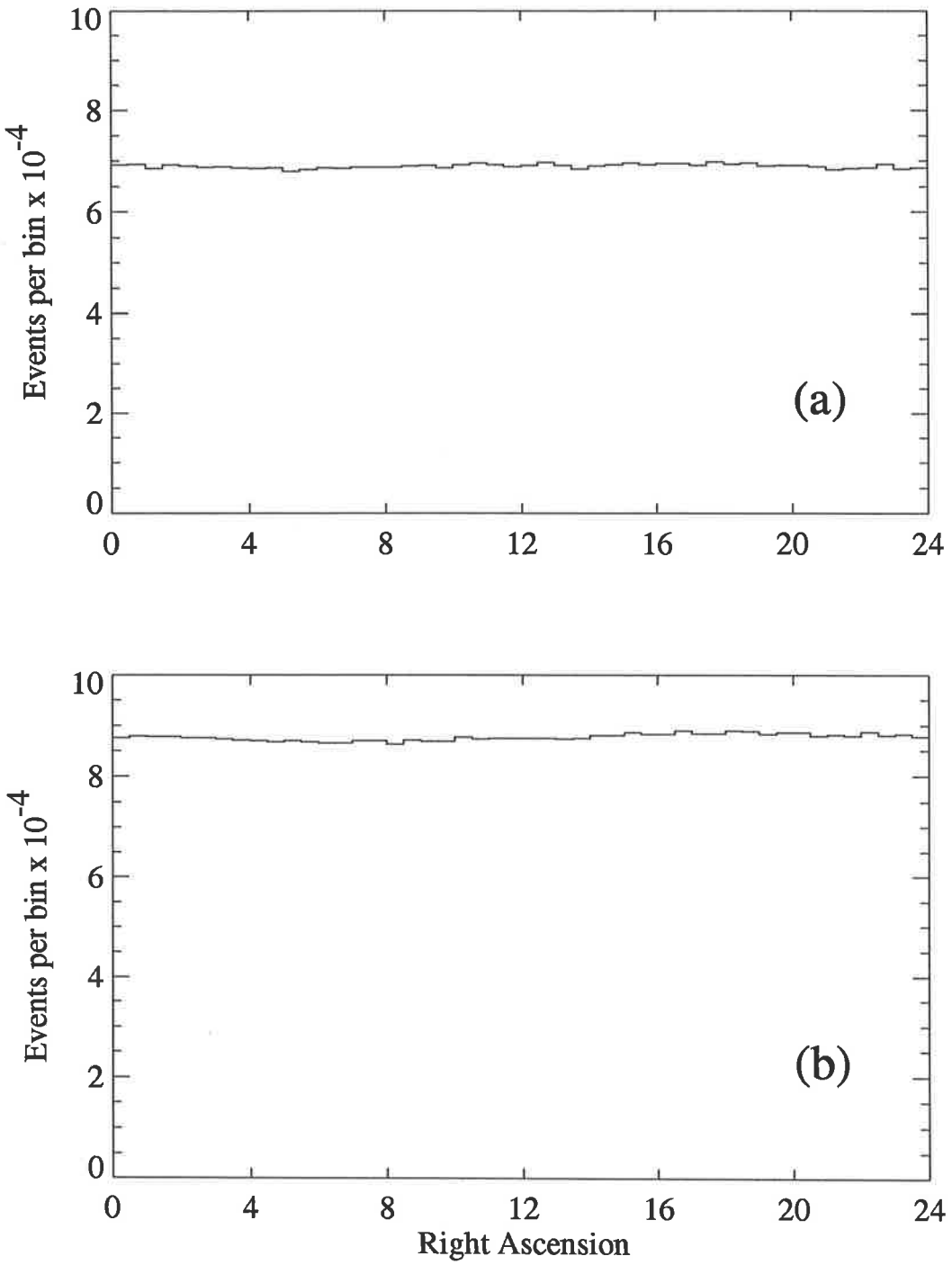

Figure 3.24: The Right Ascension distributions for the reanalysed data sets (a) 1984–1986 and (b) 1986–1989.

3.8 Array Characteristics 1990 - 1991

The array data for the period starting on the 30^{th} of May 1990 and ending on the 19^{th} of March 1991 were analysed for arrival directions $(\theta, \phi, \alpha, \delta)$ and the usual shower parameters (N_e, X_c, Y_c and s as discussed in §1.3.1 & §1.3.2). It was found that for a subset of this data beginning on the 30^{th} of May 1990 and ending on the 1^{st} of November 1990, there were poor arrival directions fitted and incorrect assignment of Julian Days from an earlier analysis of the data. The author was responsible for the operation of the array in the its 1990 configuration from the 11^{th} of September 1990 until the 19^{th} of March 1991 and analysis of the entire $1990 - 1991$ data which included correcting the error in Julian Day and fitting better directions.

There were a total of 9.2×10^5 events which triggered the array. The array had an effective threshold of $\sim 6 \times 10^4$ particles and the mean event rate was $\sim 5.6 \times 10^{-2}$Hz. Directions were assigned to 8.77×10^5 events, corresponding to 95% of the total events. Shower sizes, ages and core positions were assigned to 7.3×10^5 events corresponding to 80% of the total events.

The array characteristics are shown in Figure 3.25.

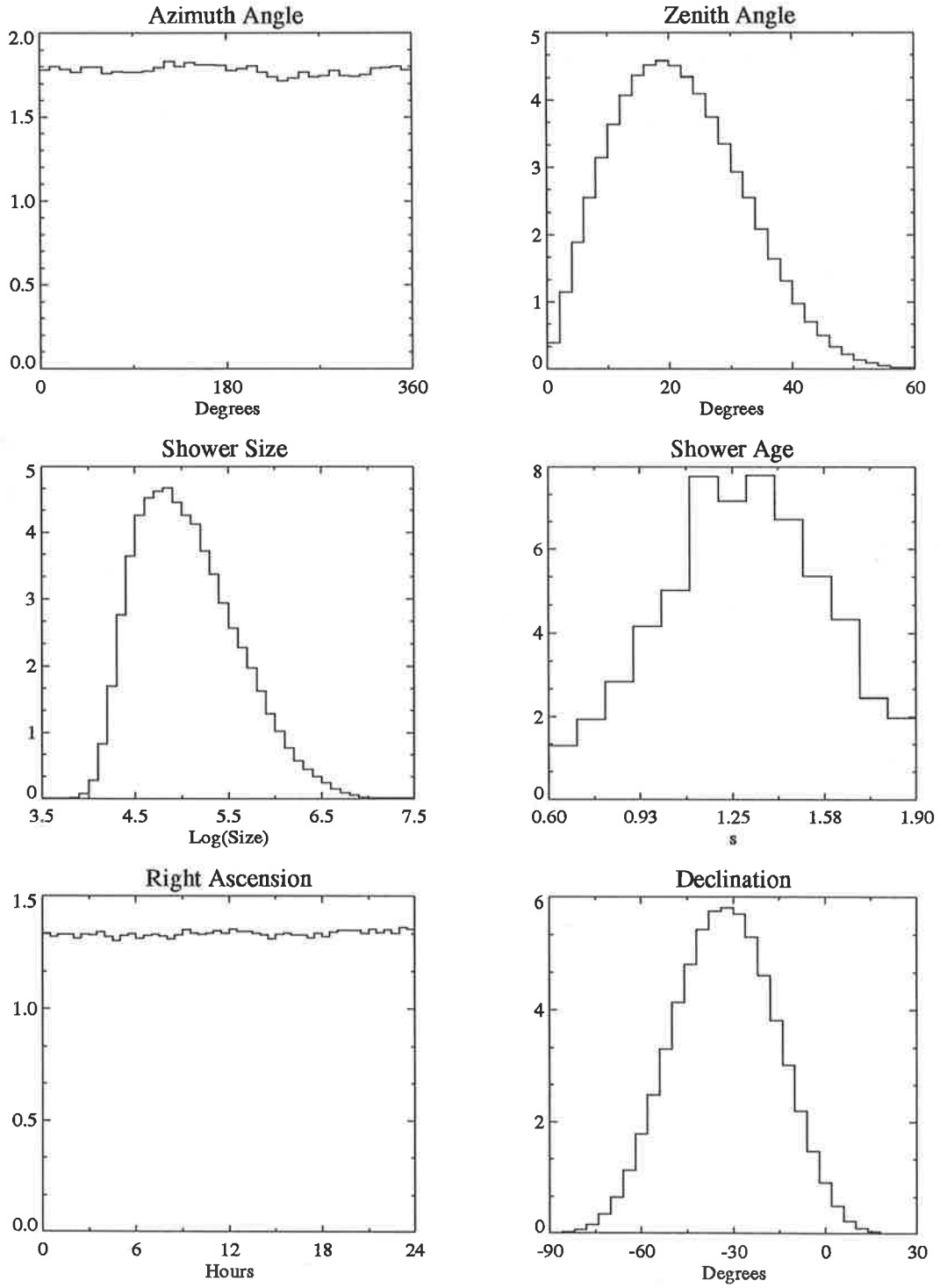

Figure 3.25: The 1990 – 1991 data distributions, the y axes values have been divided by 10^4.

3.9 Array Characteristics 1978 – 1982

The array during the period 1978 to 1982 was smaller than in its present configuration. Investigations during that time concentrated mainly on the anisotropy of cosmic rays in the region $10^{15} - 10^{16}$eV (see Gerhardy 1983). Data from 1979 to 1981 have been used in searches for UHE point sources (Protheroe, Clay & Gerhardy 1983, Protheroe & Clay 1984, Meyhandan et al. 1992). These data were reanalysed in 1983 to determine shower ages as they were not calculated in the original analysis.

Archival data from around this period (1978 & 1982) had been retrieved by the author in order to extend the data-base of this period for point source searches. Distributions for the 1978 data set are shown in Figure 3.26. These data do not contain shower age estimations. The 1979 to 1981 data are shown in Figure 3.27. The data were archived in a format which was suited to the computer of that period (CDC Cyber 173 binary). In order that the data were available for present day analysis the data were converted to ascii. It was found that during the original analysis there was an error in the assignment of the Julian Day by one day (ie the Julian Day was one day greater than it should have been). This error was corrected. The implication for UHE source searches is discussed in §5.3.6. The Right Ascension & declination values were therefore recalculated.

The data for 1982 were not stored on tape, however there were printed copies of all the events available. These data were manually entered onto computer, and are shown in Figure 3.28. These data were checked for inconsistencies, and again the Right Ascension & Declination values calculated, as they were not included in the original analysis.

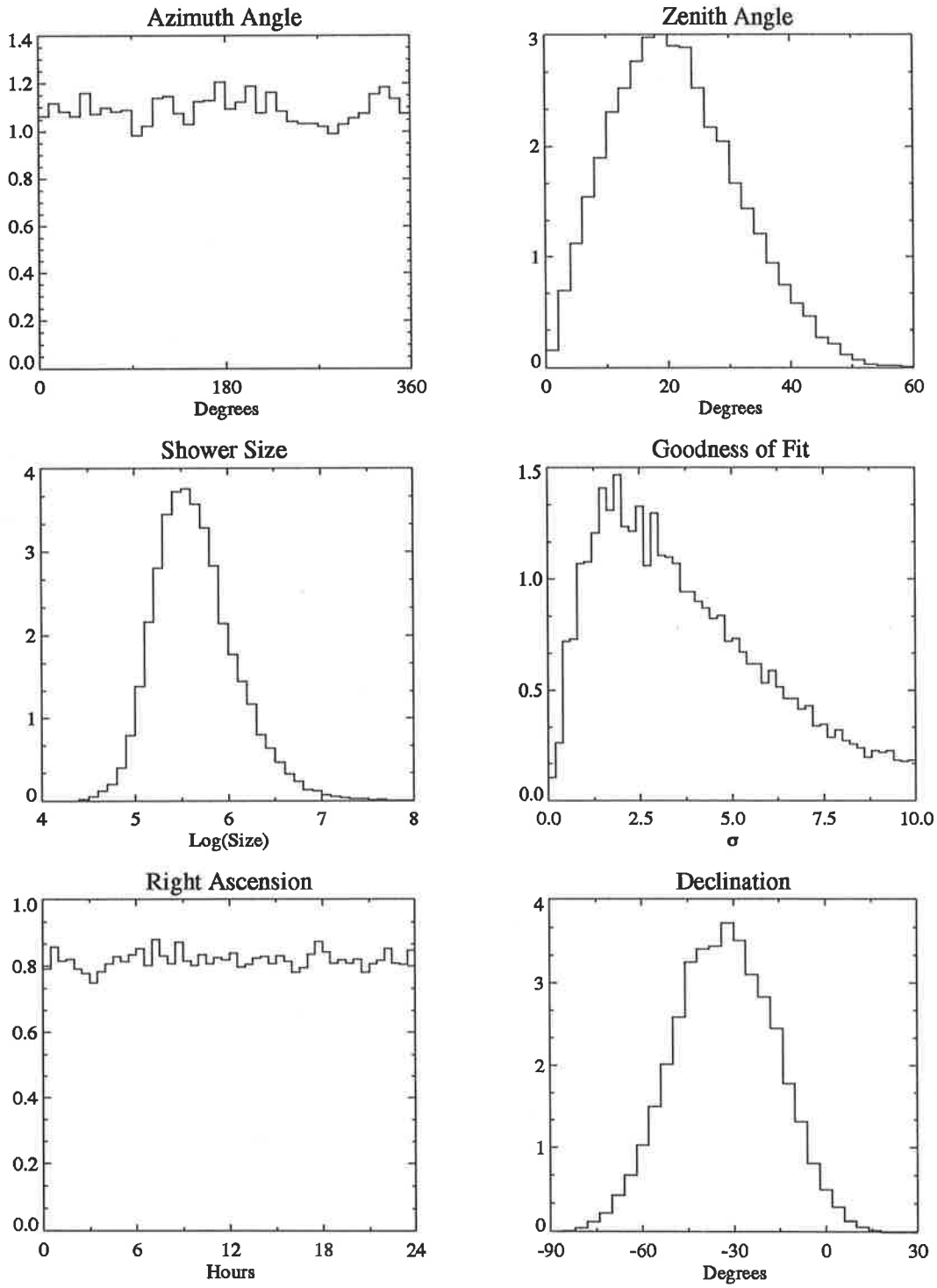

Figure 3.26: Distributions for the 1978 data set, the y-axis has been divided by 10^3. There is a total of 3.9×10^4 events. The Goodness of Fit distribution σ is described by eqn. 3.5.

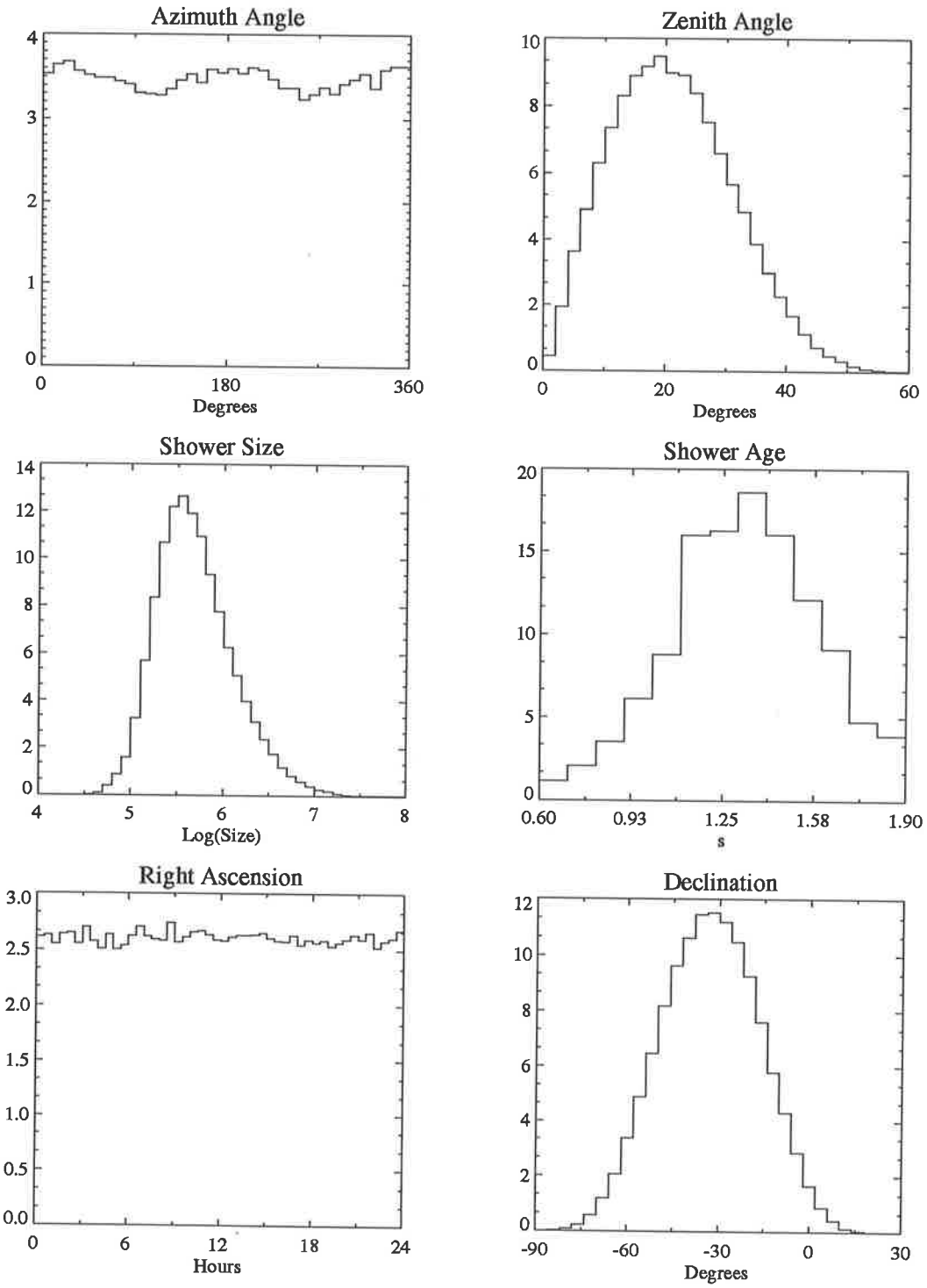

Figure 3.27: Distributions for the 1979–1981 data set, the y-axis has been divided by 10^3. There is a total of 1.25×10^5 events. The Goodness of Fit distribution σ is described by eqn. 3.5.

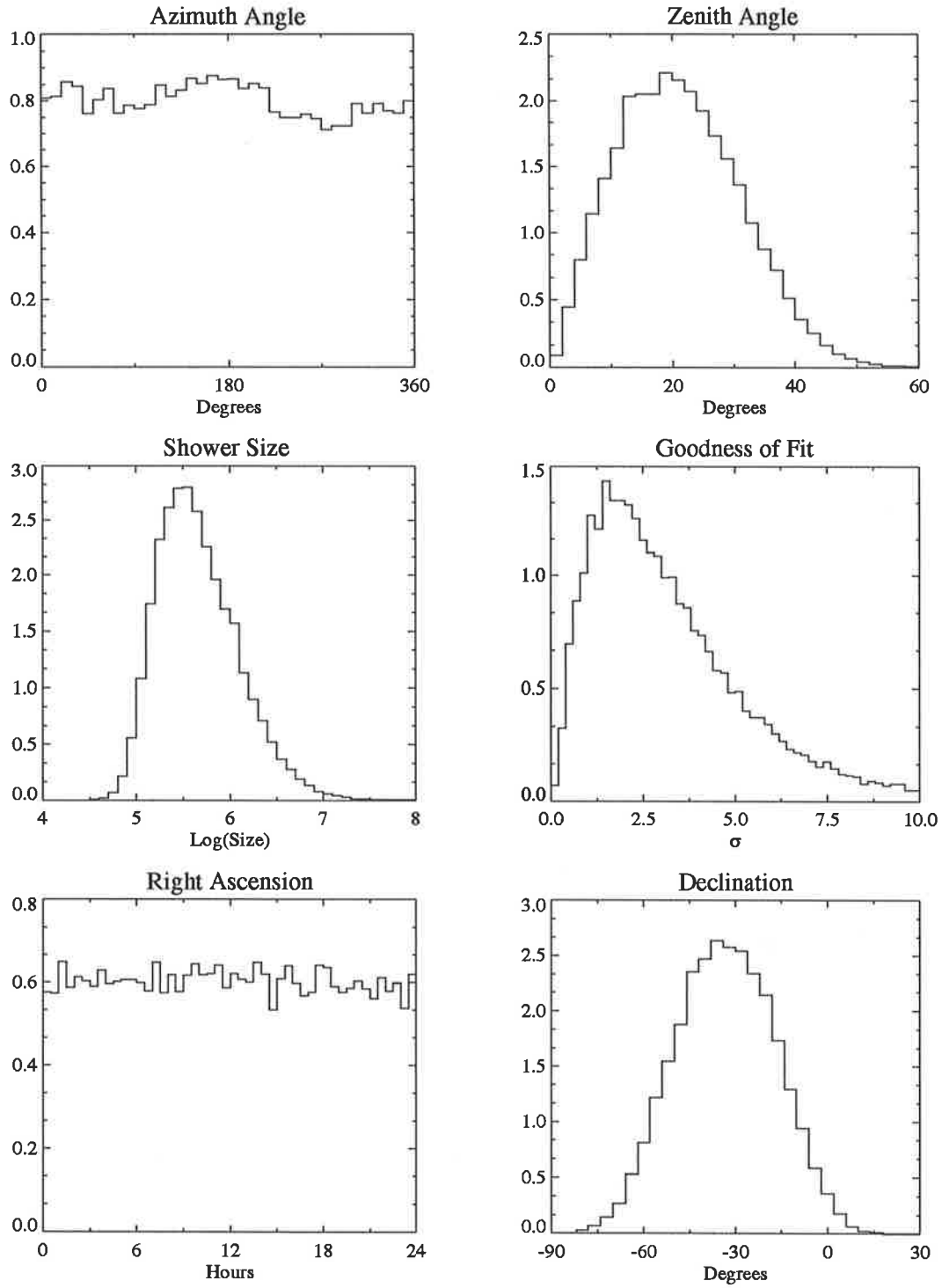

Figure 3.28: Distributions for the 1982 data set, the y-axis has been divided by 10^3. There is a total of 2.9×10^4 events. The Goodness of Fit distribution σ is described by eqn. 3.5.

3.10 Angular Resolution

The resolution for determining arrival directions depends on both the array characteristics and the data analysis procedure. Given that it is difficult to detect UHE γ-ray sources with great confidence, improving the angular uncertainty in arrival directions would increase the signal to noise rapidly. A reduction in the angular resolution by a factor of two results in a reduction in background by a factor of four.

For a planar front the angular resolution can be approximated by

$$\omega = \frac{\delta t \times c}{d}$$

where

δt: the uncertainty in relative time between detectors

d: the distance between detectors

c: velocity of light

For an array, the angular resolution will depend on a number of factors. The resolution of the detector itself and its size, the spacing of detectors, and the number of detectors triggered.

Detector Arrangement

The rise-time of the 'fast' photomultiplier is of the order $\sim$ 2ns. Discriminators are triggered with a 'jitter' due in part to photomultiplier rise-time and the variations in pulse size and shape. This effect can be minimised with the use of double discriminators (see §3.1.1). The distance between the photomultiplier and the scintillator it views produces a similar 'light collection' rise-time of $2-3$ ns. This is due to geometry of the detector and how photons from the scintillator are seen by the photomultiplioer, either directly or indirectly. Some of the detectors in the Buckland Park array (A1,B1,D1,E1 & C) use baffles between the scintillator and the photomultiplier to maintain uniformity of response across the scintillator, but unfortunately this is not optimal for angular resolution as it precludes direct

detection of light.

It is desirable to trigger off the leading particle, larger detectors would increase this probability, however, it was found that in general the 'light collection' rise-time also increases resulting in no net gain (Ciampa et al 1988).

Detector Spacing and Number

Increasing the distance between detectors improves the angular resolution. However there is a competing effect from shower front curvature. At large core distances the number of particles drops off rapidly and the probability of triggering off the leading particle is smaller. An increase in the array threshold to larger sea-level sizes ($\sim 10^5$ particles) would increase this probability and therefore improve the angular resolution.

A greater number of triggered detectors together with a greater detector baseline provides the greatest improvement in the angular resolution. Smaller showers trigger fewer detectors, and have fewer leading particles. It was expected that the increase in threshold of the Buckland Park array would improve its angular resolution.

The effect of refinements made to the array and analysis discussed in §3.4 & §3.7 are now considered. The angular resolution has been determined in two ways. For the data (1984 – 1989) it was estimated from simulations. The resolution for the new (1992) array was determined by simulations and by sub-array analysis.
The angular resolution function for an array can be approximated by

$$\frac{dN}{d\Omega} = \frac{1}{2\pi\sigma_o^2} \exp^{-\frac{\psi^2}{2\sigma_o^2}}$$

(Protheroe & Clay 1984)

where ψ is the space angle between the true and apparent arrival directions, σ_o is the width of the Gaussian, N is the number of events and Ω is the solid angle.

3.10.1 Sub-Array Analysis 1992

For an array with many fast timing detectors, 2N say, the array can be divided into two interleaved independent sub-arrays of N detectors each. The distribution of the difference in arrival directions determined by the sub-arrays allows the angular resolution to be estimated.

For the purpose of this analysis there were 30 detectors providing timing information. They were divided equally into two arrays as follows:

Array 1: B1, 5, 7, A1, 1, 4, R, S, N, T1, X, C, B, L and BFD

Array 2: D1, 8, 6, E1, 2, 3, T, Q, D, P, W, S1, E, M and A

The arrival directions determined by the sub-arrays for a sample of $\sim 3.2 \times 10^4$ events were compared for a plane shower front fit, and a curved fit, where the arrival times are corrected for curvature as discussed in §3.5.2.

The difference in space angle between the two determined arrival directions was calculated. This difference (corrected for solid angle effects) should be distributed as a Gaussian. The angular resolution is then

Triggered Detectors	Plane Fit σ_{res}	Number of events	Curve Fit σ_{res}	Number of events
3	2.22	696	2.41	625
4	1.67	2576	1.88	2539
5	1.36	4158	1.40	4132
6	1.16	3187	1.28	3211
7	1.02	1636	1.10	1658
8	0.87	912	1.03	933
9	0.89	373	1.04	375
10	0.78	148	0.96	159
11	0.56	65	0.51	59
12	0.66	25	0.54	37

Table 3.3: The results from the 1992 sub-array analysis for various numbers of triggered detectors. As can be seen the angular resolution improves as the number of triggered detectors increases.

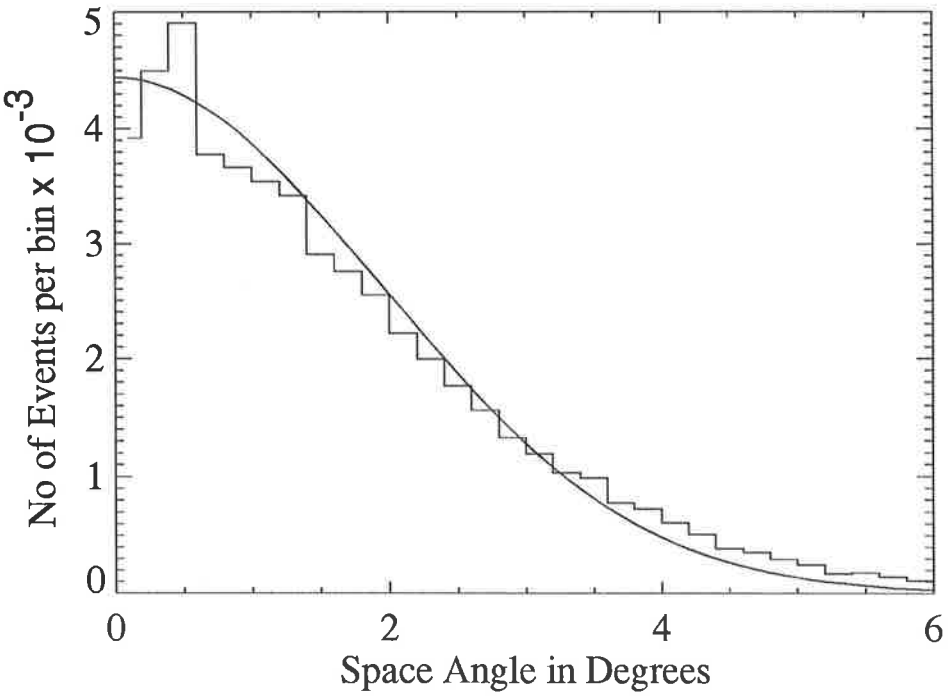

Figure 3.29: The distribution of differences in space angle for 5 triggered detectors in each sub-array corrected for solid angle effects, ie $\frac{dN}{d\Omega}$ vs ψ for the 1992 array. The smooth curve is a Gaussian with a standard deviation $\sigma_o = 1.93°$

$$\sigma_{res} = \frac{\sigma_o}{\sqrt{2}}$$

where σ_o is the standard deviation of the Gaussian. Figure 3.29 shows a plot of the distribution of differences in space angle for an equal number of triggered detectors in each sub array so that the error in determining the direction is the same for each sub-array. The results are compiled in Table 3.3, and will be discussed below.

3.10.2 Simulated Angular Resolution

A simulation was performed to determine the angular resolution for earlier epochs of the array as well as another check of the 1992 angular resolution The procedure adopted was similar to that discussed in §3.4.1. Many of the individual timing channel delays were not available to be used in the simulation, so in order to get a realistic response, the simulated goodness of fit (equation 3.5) was matched to that

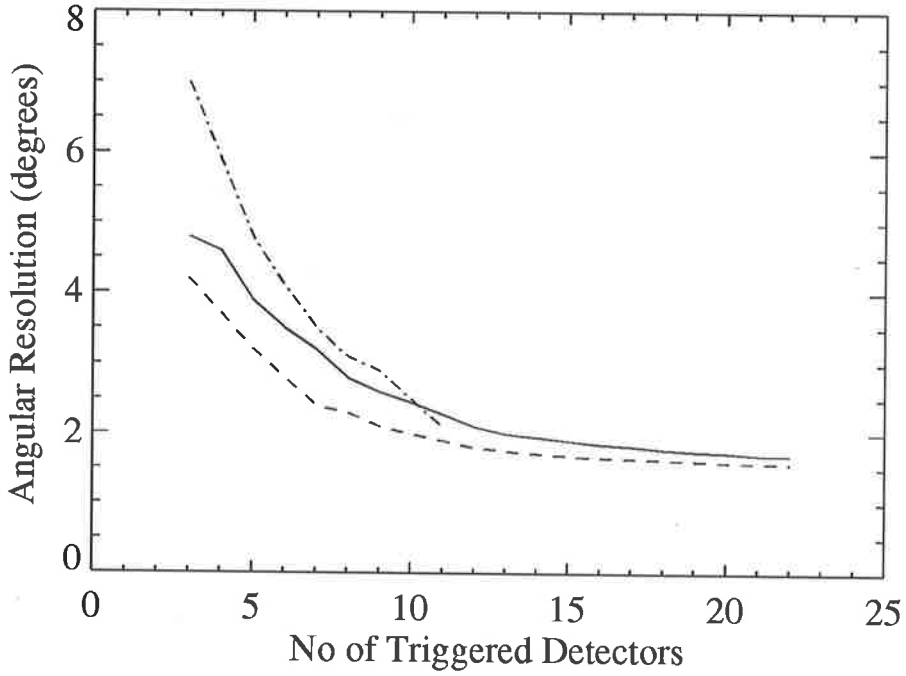

Figure 3.30: Simulated angular resolution curves for the array from 1984 to 1989. The dot dash line is the curve for the epoch 1984 – 1986. The solid line is for the epoch 1986 – 1987 before double discriminators were introduced & the dashed line is for 1987 – 1989, after double discriminators were introduced

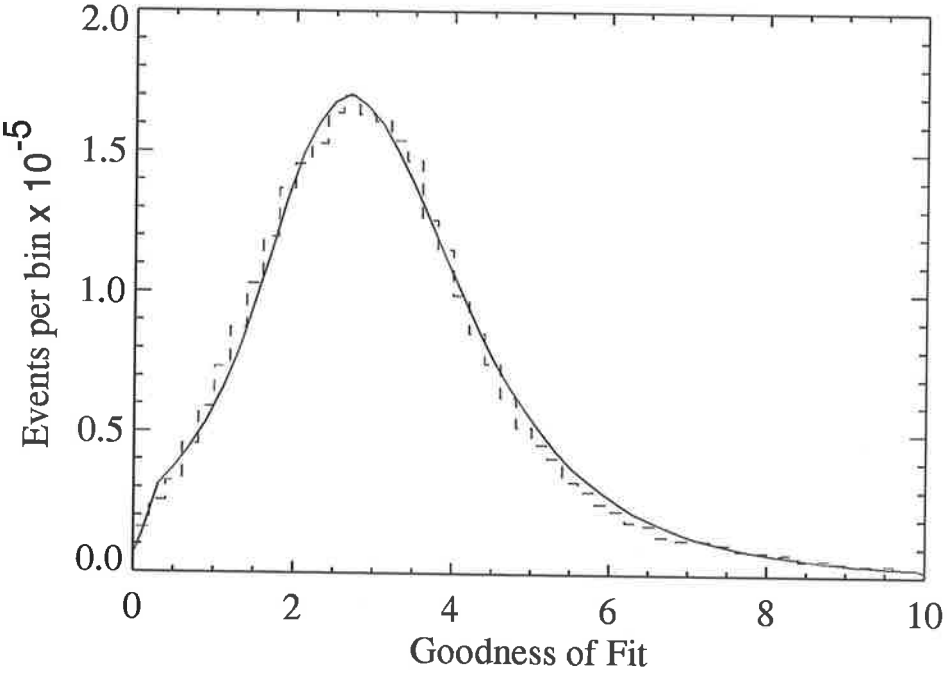

Figure 3.31: Comparison of the Goodness of Fit for the array during the period 1986 – 1989 after double discriminators had been installed (solid line) and the simulated data for the same period (dashed line).

obtained from the data analysis. Figure 3.31 shows a comparison of the 'simulated' and 'real' goodness of fit distributions for the 1986 – 1989 data. The angular resolution for a particular number of triggered detectors was then the standard deviation of the gaussian obtained from the distribution of space angle of true and reconstructed directions.

3.10.3 Discussion of Results

The resolution as a function of the number of triggered detectors for the 1992 array is shown in Figure 3.32 below. Comparing the simulated data with that obtained from the sub-array analysis, it is clear that there is a break at about 5 triggered detectors. The simulation provides a flatter curve after this point whereas the sub-array analysis shows a much steeper curve.

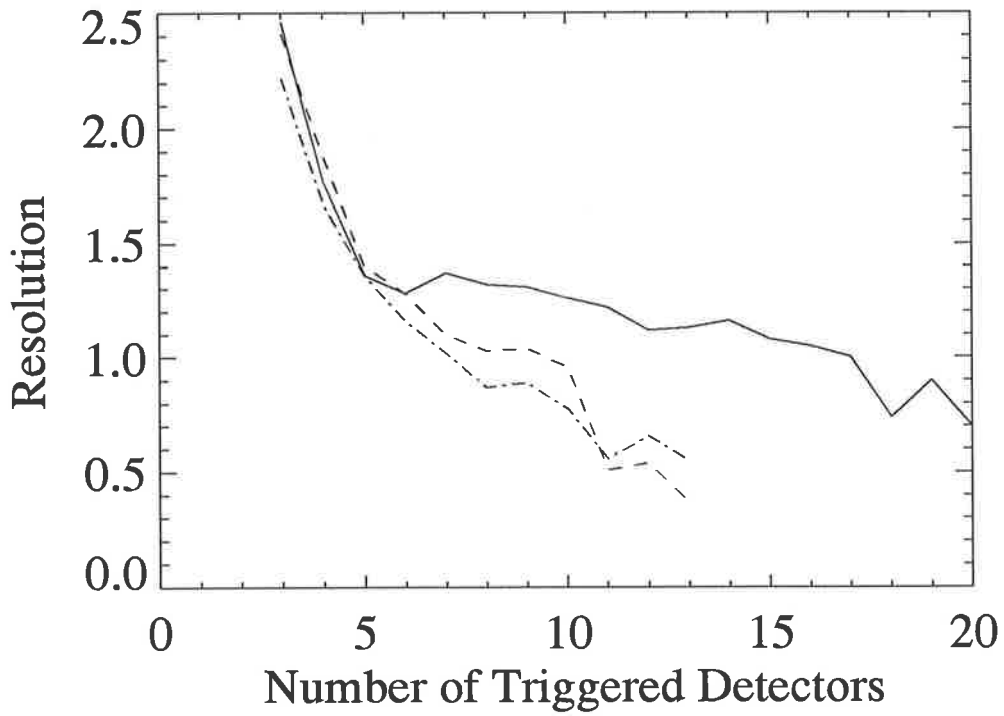

Figure 3.32: Comparison of the sub-array analysis and simulation results for arrival direction fits (1992 array). The solid line shows the data from simulations (see §3.10.2), the dashed line is the curve fit, and the dot dashed line is the plane fit from the sub-array analysis (see text for details).

This may be explained by the way in which the sub-array data were complied. It was required that each sub-array triggered with the same number of timing detectors. Consequently the total number in the 'full' array is twice as large. So by making this requirement it is possible that there is also an implicit requirement for larger showers, which would give better sampling of the shower front and consequently smaller fluctuations leading to an overall better direction fit.

It is interesting to note that the angular resolution results for the plane fit are slightly better overall than for the curve fit. The value of curvature obtained in §3.5.1 of $(0.1 \pm 0.05\text{ns/m})$ was found using the array as a whole, hence using this value for curvature correction for the two sub-arrays may not be appropriate. It should be noted however, that the curvature correction for the array as a whole shows an improvement in the average timing residuals (see Table 3.2).

The angular resolution curve shown in Figure 3.30 is similar to that obtained by Ciampa (1988) for the same period of data, giving confidence in the values obtained. These curves were used to represent events by a two dimensional gaussian probability distribution in the construction of contour maps for the analysis of Centaurus A §5.2.1. Also they were used to determine the optimal search region for each epoch (see below) in the UHE analysis of 2A1822 -371 and LMC X-4, using Buckland Park data (see §5.2.4 & 5.2.5).

3.10.4 Search Region

The search region is an area which maximizes the signal to noise ratio for a given array configuration. Using the simulated angular resolution curves for each epoch of the array (Figures 3.30 & 3.32) it is possible to determine an optimum search region for the purpose of UHE γ-ray astronomy (see Chapter 5). The technique is outlined in Appendix C. The search regions for each epoch are shown below. A simulation was not performed for the earliest epoch, however, an estimate was made from earlier calculations (Protheroe & Clay 1984).

Epoch	Half Angle Search Region	Shower Front Curvature Correction
1978 - 1982	3.0^o	No Correction
1984 - 1986	5.10^o	As in §3.5.2
1986 - 1987	3.49^o	//
1987 - 1989	2.69^o	//
1992	1.82^o	//

Table 3.4: The five epochs of the Buckland Park data set and their corresponding search regions (determined in Appendix C) used in Chapter 5 §5.2.4 & §5.2.5. The last column indicates whether the data has been corrected for shower front curvature.

Chapter 4

Sydney University Giant Air-shower Recorder

4.1 Introduction

The SUGAR array was located in the Pilliga State Forest in New South Wales (array latitude -30.53^o , longitude -149.60^o) and was operated between 1968 and 1979. It enclosed an area of up to 70 km^2, and was designed to detect showers produced by the highest energy cosmic rays (see Winn et al. 1986a). The array had an energy threshold of about 1.8×10^{17}eV, and in its final configuration consisted of 47 independent stations. Each station contained two buried detectors, and hence it was sensitive to the penetrating muon component of extensive air showers. A total of 15237 showers were detected of which 13729 were analysable.

4.2 Array Detectors and Trigger

The individual stations were located on a regular grid of 5 by 8 miles with each station one mile apart (see Figure 4.1). The centre the array was infilled with detectors, so that it would be sensitive to lower energy showers. Each station was autonomous and contained two buried liquid scintillator counters (tanks) separated

by a distance of 50m, in a north-south direction. The shielding over each detector was (1.5 ± 0.3)m of earth. The effective area of each detector was 6m^2, and was viewed by a single EMI 9623B Photomultiplier. The threshold energy for detected muons was $0.75\sec\theta$ GeV, where θ is the zenith angle.

The shape of the tank was designed so that a particle traversing any part of the scintillator at a given angle would produce the same light flux on the photomultiplier. An individual detector triggered if the signal was greater than or equal to 3 coincident vertical muons passing through the scintillator. The individual detector rate was $\sim 30\ \text{sec}^{-1}$.

If both detectors at a station triggered within 350ns, a master trigger was generated and the time of the event together with the station particle density was recorded by a local tape recorder. These 'local' events occurred at $\sim$ 12 per hour. The stations were fed with a continuously transmitting timing signal. The arrival times of showers were recorded relative to this timing signal with a resolution of 50ns (Bell et. al. 1974). These data were retrieved periodically to be analysed on computer.

Event Analysis

Directions were obtained using the fast timing method. Coincidences within 80μs between 3 or more stations were considered an 'array event'. Events were later rejected from further analysis if the stations were collinear or if the event was unphysical. For 3 triggered stations the direction was uniquely determined, however for greater multiplicities a plane disc fit by a weighted least-squares method was used.

It is difficult to accurately determine the angular resolution of the array in situations where only a few stations have triggered. Unfortunately this is the case for the majority of events in the data (See Figure 4.2 Multiplicity). In situations where greater than 3 stations have triggered it was found that the uncertainty in the least-squares fit was about $3°\sec\theta$. However this assumes a plane shower front and does not include the effects of curvature in the estimate of uncertainty.

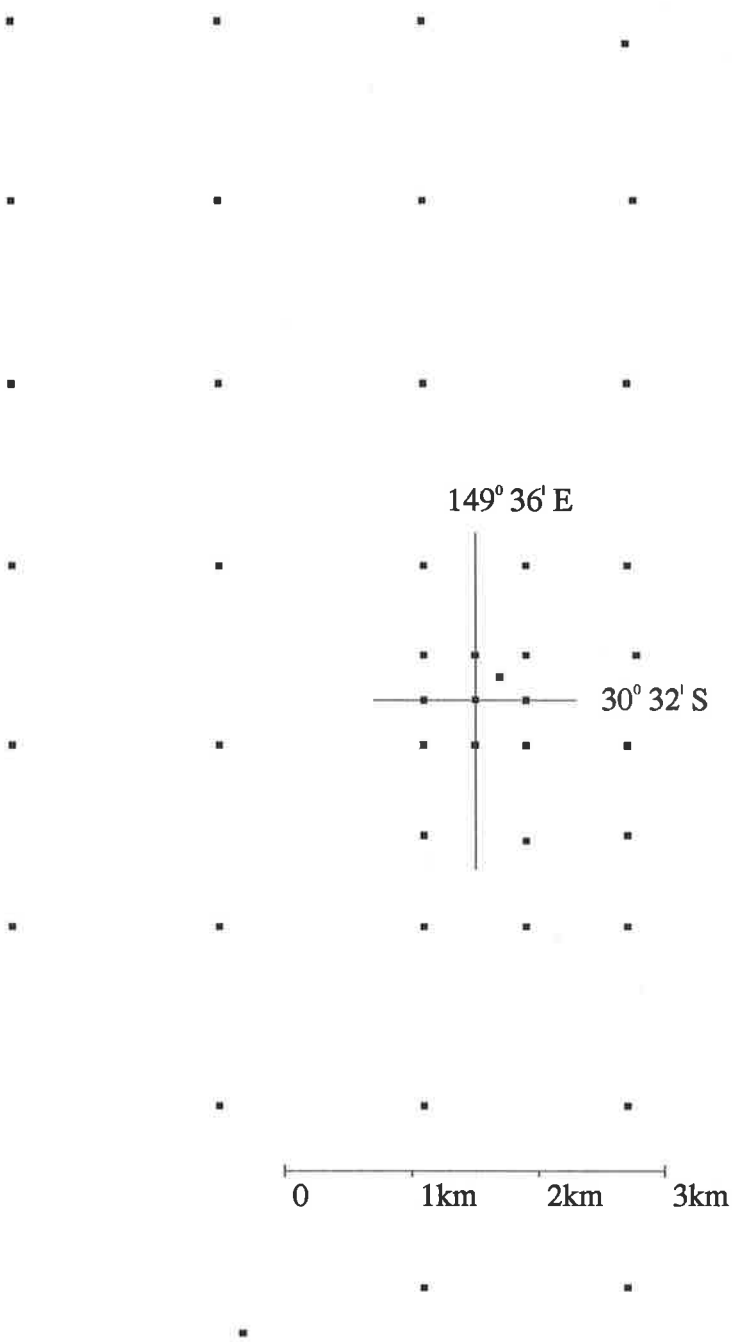

Figure 4.1: Map of the SUGAR array showing the places where stations were operated at some time during the life of the experiment. Adapted from Winn et al. (1986).

Clay et al. (1991) have made an estimate of the angular uncertainty by optimising the angular search region & orbital period for the X-ray binary 2A 1822-37.1 (see §5.2.3). The optimum search region radius was 9^o which suggests that the angular resolution for the array, averaged over all events, is of the order $\sim 6^o$ (a circular region of 1.59 times the angular resolution maximizes the signal to noise, see §5.1.1).

The location of the core and size (total number of muons) was estimated using the maximum likelihood method (Winn et al. 1986a), fitted to a muon lateral distribution function (see §2.3).

The equivalent vertical muon number N_v was converted to a primary energy using the Hillas model E (Hillas et al. 1971).

$$E = 1.64 \times 10^{18}(N_v \times 10^{-7})^{1.075}\text{eV}$$

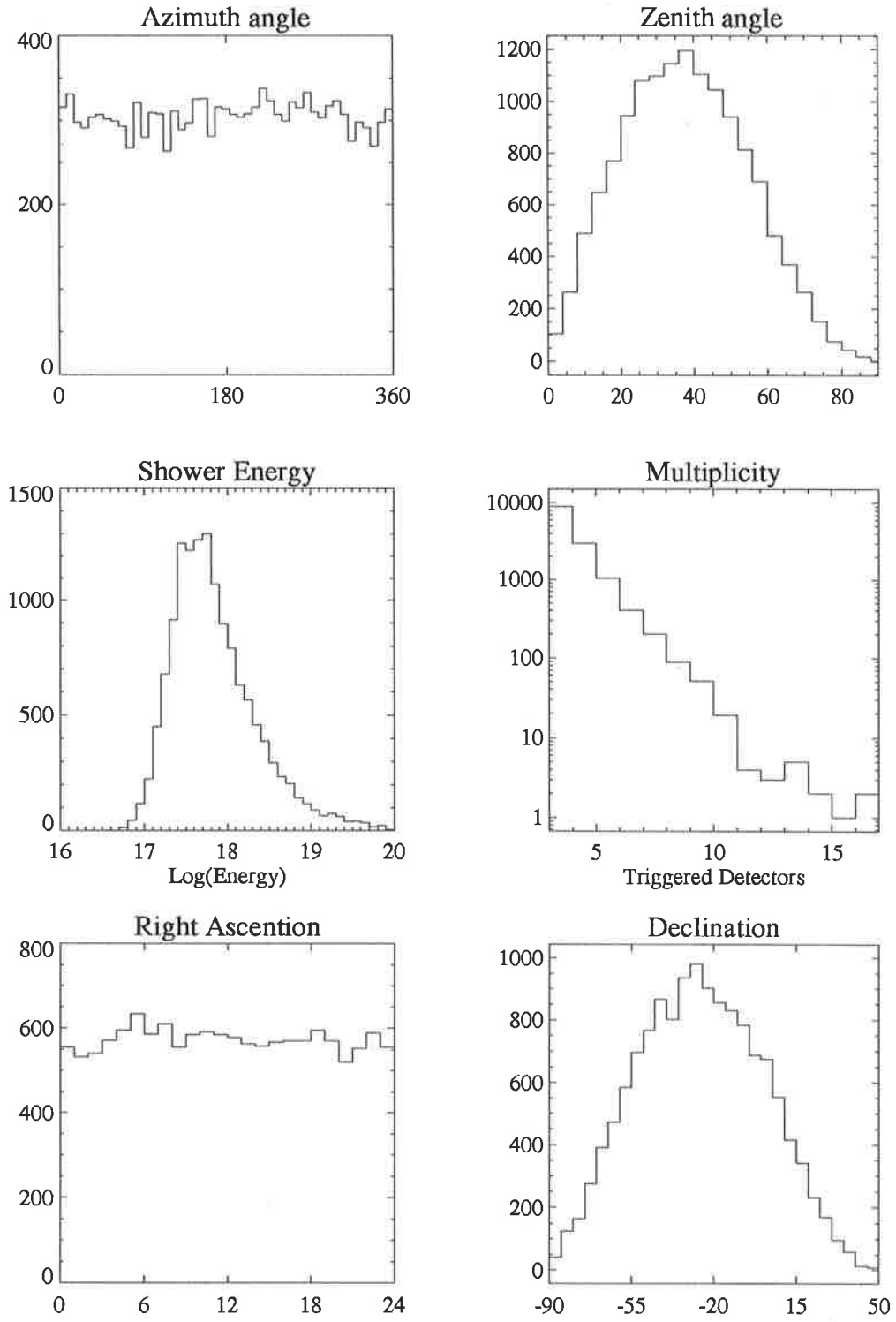

Figure 4.2: The analysed data distributions for SUGAR. The zenith angle and Declination distributions have a broader range than those of Buckland Park due to the higher penetrability of muons. The Multiplicity distribution shows the number of showers that trigged stations, as can be seen the majority of the 13729 showers triggered only 3 or 4 stations.

Chapter 5

Searches for UHE Emission

5.1 Introduction

The results from a search of potential UHE sources in the southern hemisphere observed by the Buckland Park and SUGAR arrays are presented. Most of the sources which have been studied are binary systems (see §1.5.1 for possible acceleration mechanisms). In addition, the active galaxy Centaurus A was also examined. Techniques for analysing air-shower data are presented in this section, together with statistical tests for the presence of DC and periodic signals, and methods for estimating the γ-ray flux & upper limits.

5.1.1 Search for a DC Excess

Before a search for an excess of events can begin, it is vital that the angular resolution of the array is determined, and a region that maximizes the signal to noise ratio chosen. The angular resolution of the Buckland Park array has been discussed in §3.10. Showers are selected from within a solid angle chosen to give the highest ratio of signal events to the square root of the number of background events. For the manner in which the angular resolution σ_o was defined in §3.10, a circular region of $1.59\sigma_o$ maximizes the signal to noise (Protheroe & Clay 1984, Appendix C).

Once this circular region has been defined then it is possible to begin a search. To

obtain a reliable background estimate, an identical analysis is performed on a number of other regions of the sky in the same declination band as the source. These 'false sources' are chosen so that they have the same exposure in right ascension, and do not overlap at any declination at which data are taken. Therefore the declination band in question is broken into $\mathcal{K}$ circular regions, one for the on-source region and ($\mathcal{K}$ - 1) for the background regions. If an event lies within a circular region centered on the source or one of the background regions, it contributes to the on-source count N_{ON} or the off-source count N_{OFF} respectively.

When testing the significance of a DC excess it is important to take account of the uncertainty in the background estimate. In practice, provided the array down-time is uniformly distributed in sidereal time, the ratio of on-source to off-source exposures can be defined as

$$\mathcal{E} \simeq 1/(\mathcal{K}-1)$$

The best estimate of the background during the on-source observation is

$$\hat{B} = \mathcal{E}\, N_{\mathrm{OFF}}$$

and the best estimate of the source count is

$$\hat{N_{\mathrm{S}}} = N_{\mathrm{ON}} - \hat{B}$$

The source count $\hat{N_{\mathrm{S}}}$ and the background estimate $\hat{B}$ are the maximum-likelihood estimates. The significance of any excess can be tested using the maximum-likelihood statistic, λ which allows for the uncertainty in the background estimate, defined by Li & Ma (1983)

$$\lambda = \left[\left(\frac{\mathcal{E}}{1+\mathcal{E}}\right)\left(\frac{N_{ON}+N_{OFF}}{N_{ON}}\right)\right]^{N_{ON}} \left[\left(\frac{1}{1+\mathcal{E}}\right)\left(\frac{N_{ON}+N_{OFF}}{N_{OFF}}\right)\right]^{N_{OFF}} \qquad (5.1)$$

The quantity -2lnλ is distributed as χ^2(1 d.o.f.) and the significance of an excess is equivalent to $\sqrt{-2ln\lambda}$ standard deviations.

5.1.2 Periodic analysis

Apart from searching for a excess of events from a particular source, it is sometimes more sensitive to perform a periodic test. Sources which have well known pulsar or orbital periods, from radio or X-ray data, can have their event arrival times t_i converted to phases ϕ_i. This requires a knowledge of the period P_o, eclipse epoch T_o and the rate of change of period $\dot{P}$ of the binary system or pulsar. For periods which are short it is necessary to correct the event times for the motion of the earth around the sun (see Appendix D). These times are then converted to an orbital phase by

$$\Phi = \frac{t_i - T_o}{P_o} - \frac{\dot{P}(t_i - T_o)^2}{2P_o^2} \tag{5.2}$$

This number gives the total number of revolutions since epoch T_o. The oribital phase ϕ_i is then the fractional part of Φ. These phases can be binned to produce a phase histogram or 'phaseogram'. The approach for the background events is similar except that the eclipse epoch is shifted to

$$T_o(i) = T_o + \left(\frac{24i}{\mathcal{K}}\right) \times 0.0415529^d \tag{5.3}$$

for each background region, where $T_o(i)$ is the eclipse epoch of the i^{th} background region and, $\mathcal{K}$ is the number of circular regions. The shift is equal to one twenty-fourth of a sidereal day for each hour of right ascension, so that any zenith angle effects affect the background regions at the same phase (see Nagle, Gaisser & Protheroe 1988).

The conventional approach is to then test the on-source phase bins against the background using the χ^2 test. However this approach has the usual problem with binned data, that is the choice of bin origin and bin width.

UHE γ-ray emission from X-ray binary systems has typically been in a narrow range of orbital phases ~ 0.05 (Lloyd-Evans et al. 1983, Protheroe et al. 1984). For this reason the test statistic used here for searches of UHE emission is one sensitive to narrow duty cycles, namely the Z^2_{10} test, from the family of Z^2_n statistics based on

the generalisations of the Rayleigh test to include 2nd and higher harmonics (Buccheri & Sacco 1985). The statistic is defined by

$$Z_n^2 = \frac{2}{N}\sum_{k=1}^{n}\left[\left(\sum_{j=1}^{N}\cos 2\pi k\phi_j\right)^2 + \left(\sum_{j=1}^{N}\sin 2\pi k\phi_j\right)^2\right] \tag{5.4}$$

where N is the total number of on-source events. The Z_{10}^2 test is sensitive to power in all harmonics up to the tenth, and is therefore useful in searches for narrow phase features. The Z_n^2 tests have a well-known probability level, it is distributed as $\chi^2(2n)$, for N sufficiently large. For the Z_{10}^2 test this condition is met for $N \geq 100$.

Another test, which is extremely powerful for finding narrow-peaked light curves, as well as broader duty cycles, is one suggested by Protheroe (1985). However the Protheroe test statistic Υ_N has the disadvantage that it is unsuitable for dealing with large numbers of events (> 200) because of the large computing time required to calculate Υ_N and its critical values. It is useful in data sets where there would typically be a small number of events in the on-source count. This test was used by Protheroe & Clay (1985) in the search for UHE γ-ray sources using the $1979 - 1981$ data set, as well as in the present analysis of the SUGAR data (§5.2.4 & §5.2.5). The statistic is defined by

$$\Upsilon_N = \frac{2}{n(n-1)}\sum_{i=1}^{n-1}\sum_{j=i+1}^{n}(\Delta_{ij} + 1/n)^{-1} \tag{5.5}$$

where the distance between two phase observations ϕ_i & ϕ_j is defined by $\Delta_{ij} = 0.5 - |\{|\phi_i - \phi_j| - 0.5\}|$ and n is the total number of events.

5.1.3 Estimation of Flux

Once an observation has been made it is then possible to either estimate the flux of γ-rays or neutral particles from the source in the case of a positive detection, or set an upper limit to the neutral emission. The flux estimation used in the present analysis is the method described by Nagle, Gaisser & Protheroe (1988). The flux above an effective energy threshold is estimated by the ratio of excess events

attributed to γ-rays to the expected cosmic ray background events (calculated using the cosmic ray integral intensity $I_{CR}(>E)$). It is defined by

$$F_\gamma(>E_t^{eff}) \simeq \frac{a_\gamma(E_t^{eff},\delta_o)\, a_\Omega^{-1}\, \Omega_{ON}\, I_{CR}(>E_t^{eff})(\hat{N}_S \pm \sqrt{N_{ON}})}{\hat{B}} \tag{5.6}$$

where

- a_γ is a factor which takes account of the differences in the response of an array to a γ-ray and cosmic ray shower, at the effective energy threshold of the array E_t^{eff} and declination of the source δ_o.
- a_Ω is the fraction of γ-ray showers which will appear to fall within the search region ($\sim$ 72% for the circular region defined above).
- Ω_{ON} is the solid angle about the source direction used in the search.

The cosmic ray intensity is obtained from the spectrum of Hillas (1983), which is represented by

$$I_{CR}(>E) \simeq 10^{-10}\left(\frac{E}{2PeV}\right)^{-\Gamma} cm^{-2}s^{-1}sr^{-1}$$

Γ is $\sim$ 1.55 for (E < 2PeV) and $\sim$ 2.1 for (E > 2PeV), which gives a reasonable fit to the spectrum over the range 1 TeV to 1 EeV (Nagle, Gaisser & Protheroe 1988).

5.1.4 Upper limit to DC Flux

An upper limit to the DC flux above the effective energy threshold may be obtained for cases where no significant excess is found. The upper limit at the 95% confidence level (CL) is given by

$$F_\gamma(>E_t^{eff}) < a_\gamma\, a_\Omega^{-1}\, \Omega_{ON}\, I_{CR}(>E_t^{eff})\, \beta_{95} \tag{5.7}$$

(Nagle, Gaisser & Protheroe 1988)

The value of β_{95} may be obtained from Protheroe (1984) for relevant on-source counts, background counts and the number of background regions ($\mathcal{K}$ - 1).

5.1.5 Background Estimation by Shuffling

During the analyses of data, situations have occurred when it was not possible to obtain a statistically accurate estimate of the background or when a better estimate was necessary. In these cases a shuffling technique (Cassiday et al. 1990) was employed.

A simulated data set is created by assigning to every real shower's local arrival coordinates (zenith & azimuth angle) a new arrival time chosen at random from another event in the real data set. In this way the simulated data set is endowed with the same zenith angle, azimuth angle and live-time distributions as the real data set, and naturally takes care of problems such as slight non-uniformities in right ascension exposure.

This method was used to obtain statistically solid backgrounds in the analyses of Centaurus A, Sco X-1 & Vela X-1, and was performed by Dawson (1993).

5.1.6 Combining Probabilities

At first it may be thought that combining independent probabilities such as those from an observation of a DC (p_1) and a periodic or burst (p_2) signal is a simple matter of multiplying the two probabilities together p_1p_2 to obtain the final significance. However this overestimates the final significance since there are many combinations of p_1 & p_2, which can give the final significance.

The method discussed in Eadie et al. (1971) is used where the combined significance is defined by

$$P = p_1p_2\,(1 - \ln(p_1p_2)) \tag{5.8}$$

where P is the final combined significance.

5.2 Sources

As mentioned earlier most of the objects searched for UHE γ-ray emission are X-ray binary systems. The objects are Scorpius X-1, 2A1822 -371, LMC X-4, Vela X-1, and the active galaxy Centaurus A. The data used in these searches are from both the Buckland Park and SUGAR arrays. Only three objects were searched using the SUGAR data, Vela X-1, LMC X-4 and 2A1822 -371.

Data from the Buckland Park array were divided into 5 epochs relating to the different array configurations and thresholds (see §3.10.4). Of these five epochs four comprised data which had been corrected for shower front curvature (see §3.5.2). With the exception of Scorpius X-1 & Vela X-1, searches for UHE emission made use of these corrected data. The analysis for Scorpius X-1 made use of an earlier slightly less sophisticated method of shower front curvature correction (Meyhandan et al. 1991 & 1993). Vela X-1 was only analysed with the 1979 – 1981 Buckland Park data and SUGAR data. A table of the relevant characteristics is shown below.

The results of some of these observations have been published, see Clay et al. (1992) for SUGAR observations of 2A1822 -371, Meyhandan et al. (1992) for SUGAR and Buckland Park observations of Vela X-1 & LMC X-4, Meyhandan et al. (1993) for Buckland Park observations of Scorpius X-1 and Clay et al. (1994) for Buckland Park observations of Centaurus A.

Object	Right Ascension	Declination	Orbital Period	Estimated Distance	Data Analysed
Centaurus A	13^h22^m	$-42°45'$	——	5 Mpc	BP
Scorpius X-1	16^h17^m	$-15°$	0.787^d	(0.3 - 2)kpc	BP^S
2A 1822-37.1	18^h22^m	$-37°6'$	0.2321^d	(2 - 3)kpc	BP & SUGAR
LMC X-4	5^h32^m	$-66°24'$	1.40^d	50kpc	BP & SUGAR
Vela X-1	9^h	$-40°18'$	8.96^d	(1.4 - 2)kpc	BP^V & SUGAR

Table 5.1: Characteristics of the objects searched for UHE γ-ray emission. BP refers to all 5 epochs defined in Table 3.4, S refers to the SUGAR data, BP^S refers to an 8 week period begining on the 12/4/86 see §5.2.2 and BP^V refers to the 1979 – 1981 Buckland Park data.

5.2.1 Centaurus A

Centaurus A ($\alpha = 13^h22^m, \delta = -42°45'$) is the nearest active galaxy at a distance of $\sim$ 5Mpc. It was the first extra-galactic X-ray source detected (Boyer et al. 1970) and it has been observed in all spectral ranges from radio to very high energy gamma-rays (Baity et al. 1981). Cen A has a flat spectrum (differential index about -1.6) in the X-ray and low energy gamma-ray regime (Gehrels et al. 1984) but no steady high energy gamma-ray emission was found by either SAS-II or COS B. However, it was observed in 1972 to 1974 at TeV energies using a ground based Cerenkov telescope (Grindley et al. 1975) and a 2.7σ excess was reported from the direction of the object using the Buckland Park air shower array (Clay et al. 1984) at PeV energies.

The nuclei of active galaxies are the most powerful emitters of radiation. It is thought that active galaxies like Cen A may contain supermassive black holes at their centres in which power is derived from matter falling towards the black hole.

The type of regions which may accelerate cosmic rays are found in extreme forms in the nuclei of active galaxies and it would seem natural to expect such nuclei to be copious sources of cosmic ray particles (Protheroe & Szabo 1992). Any particles which interact near the source are likely to produce a flux of gamma-rays with energies approaching those of the highest energy particles. There is therefore considerable interest in searching for a gamma-ray flux from the nuclei of active galaxies.

At energies above about 200 TeV, the interaction of intergalactic gamma-rays with the cosmic microwave background is expected to result in strong absorption and an end to the gamma-ray spectrum for at least three orders of magnitude in energy (Protheroe 1986, §1.5.2). The expectation is that a nearby active galaxy such as Cen A should have a gamma-ray spectrum which may well be observable to very high energies but then should exhibit this characteristic cut-off. The distance to Cen A is estimated to be in the region of 5Mpc and at 10^{15}eV the attenuation factor is expected to be $\sim 10^3$ (see Figure 1.6c).

Apart from Grindley et al. (1975), previous VHE observations of Cen A have

failed to produce any significant excess of events, JANZOS (Bond et al. 1990), Narrabri (Brazier et al. 1990), Woomera (Gregory et al. 1990). However, recently, the JANZOS group (Allen et al. 1993) has reported a search for gamma-ray emission from Cen A using their air shower array over the period October 1987 to January 1992. No evidence was found for a steady flux but a period of 48 days in 1990 showed a flux excess (2% chance probability) and a shower size distribution consistent with the expected absorption. Objects such as this are commonly variable at high energies (Hartman et al. 1992) and Cen A has a long history of variability (Baity et al. 1981, Gehrels et al. 1984). In particular, there was an extended high X-ray emission period between 1973 and 1977 with evidence for outbursts lasting of the order of 50 days (Terrell 1986). Radio observations (de Mello Rabaça & Abraham 1990) suggest that the nucleus of Cen A exhibits large changes in luminosity over period of only a few days. Indeed the observation of Grindley et al. (1975) is thought to have coincided with an active period at X-ray energies.

Present Observations

A contour map of the region around Cen A was produced using data from all 5 epochs (1978 – 1992), Figure 5.1. This map was obtained by representing all events by a two dimensional gaussian probability distribution (Cassiday et al. 1990b) with the width determined by the angular resolution for that event (see §3.10.3 & Figures 3.30 & 3.32 for the angular resolution of an event as a function of triggered detectors). The probability distribution for an event is described by,

$$\mathrm{P(r)} = \frac{1}{2\pi\sigma_o^2} \exp\left(\frac{-\mathrm{r}^2}{2\sigma_o^2}\right) \tag{5.9}$$

where r is the angular distance from the nominal direction of the event and σ_o is the width of the gaussian. The source region was represented by an array of 25 × 25 grid points each half a degree apart. Each event contributed a fraction of an event to a grid point depending on the distance and the angular resolution for that event. In

this way a sky map or contour map representing the density of events was built up.

Events were rejected if they had poorly fitted directions (events were accepted if the Goodness of Fit (eqn. 3.5) $\sigma \leq 10$) or if there was no timing redundancy. The data in the non-source region of the declination band provided estimates of the background in the source region. The distributions of shower direction densities along lines of constant declination were used to obtain the standard deviation contour maps for three shower size intervals. It is evident that the map for the size interval $N_e < 3 \times 10^4$ (Figure 5.1) shows an excess suggestive of a point source and that this point source is compatible in direction with Centaurus A. Maps for size ranges $N_e > 10^5$ and $3 \times 10^4 < N_e < 10^5$ showed no source feature (Figures 5.2 & 5.3). The significance of the $N_e < 3 \times 10^4$ excess has been evaluated in three ways described below.

The contour map excess of 3.7σ implies a pre-trial chance probability of 1×10^{-4}, assuming that the contour map shower densities are normally distributed and the background is statistically solid. Given the uncertainty in these assumptions, a test of significance was performed using a more traditional method. The number of showers with error circles containing the source direction was determined to be 25333, where the error circle has a variable radius of $1.6\sigma_o$ for each event, where σ_o is the angular resolution. This number was compared with 10 equivalent non-overlapping background regions, spaced uniformly around the source declination band. The mean background was found to be 24677 showers, giving a source region excess of 4.0σ (calculated using the method of Li and Ma §5.1.1) with pre-trial chance probability of 3×10^{-5}.

A third method using a shuffling technique (Cassiday et al. 1990b) was employed as a final check by Dawson (1993) §5.1.5. An ensemble of these simulated data sets were used to determine how often an excess equal to or greater than the real excess is observed in the direction of Cen A.

Only events belonging to the source declination band were shuffled. To belong to this band, an event arrival direction had to be within $1.6\sigma_o$ of the source declination.

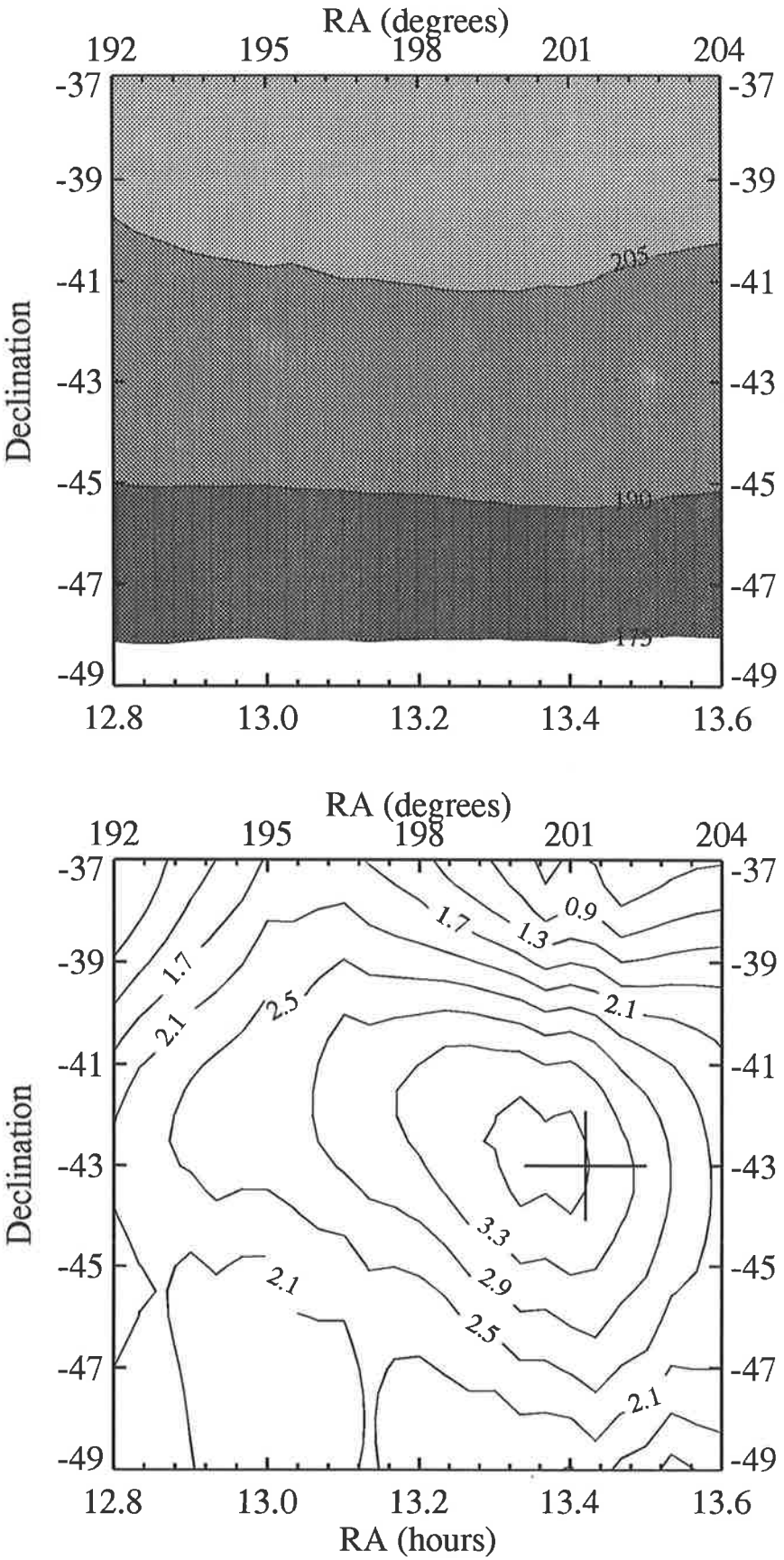

Figure 5.1: Contour for shower sizes less than 3×10^4 particles. The top figure is the density of events per square degree. The bottom figure are the contours of standard deviations based on the off-source regions in the same declination band. The source position is represented by a cross.

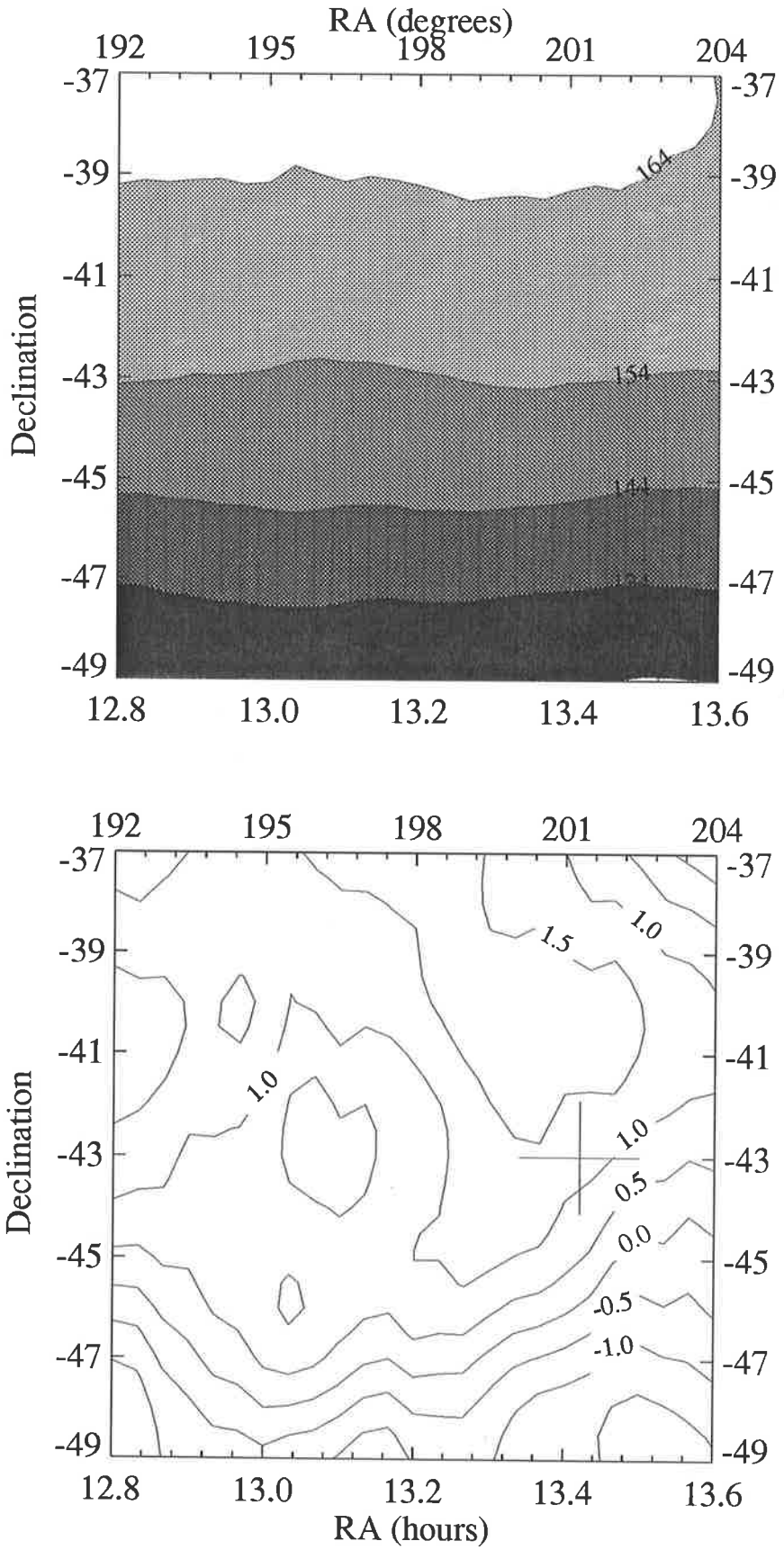

Figure 5.2: Contour map for shower sizes between 3×10^4 and 10^5 particles. The top figure is the density of events per square degree and the bottom figure are the contours of standard deviations based on the off-source regions in the same declination band. The source position is represented by a cross.

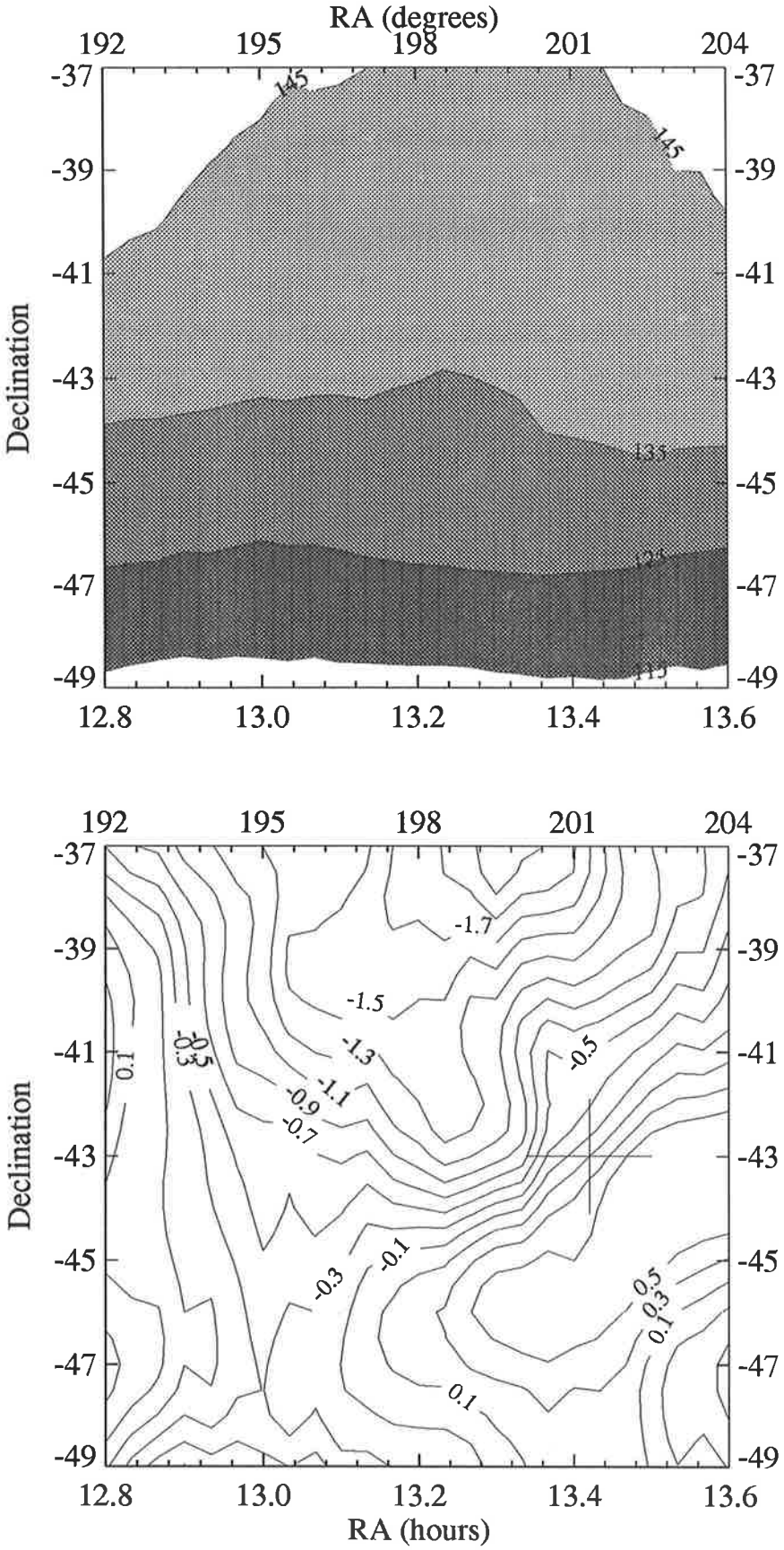

Figure 5.3: Contour map for showers sizes greater than 10^5 particles. The top figure is the density of events per square degree and the bottom figure are the contours of standard deviations based on the off-source regions in the same declination band. The source position is represented by a cross.

Local coordinates of events from this band were matched with arrival times from real events from outside this band, so that arrival times of real 'signal' events did not contaminate any background estimate. The impracticality of producing contour maps for every simulated data set led to the use of the more standard error circle method described earlier. As mentioned above the number of such events in the real data set with $N_e < 3 \times 10^4$ was 25333. From 20000 simulated data sets, the mean number of 'source' showers observed was 24875 with a standard deviation of 155.5 and a distribution which was a very good approximation to a Gaussian. This mean value is a little above the background number indicated previously because of a slight non-uniformity in the right-ascension distribution of the Buckland Park events. If this value is taken as a statistically solid background value then the observed value of 25333 represents an excess of 2.90 standard deviations. This is an upper limit to the significance level because of the residual uncertainty in the background and represents a pre-trial chance probability of 2×10^{-3}. The probability derived from the shuffling technique was consistent with this number. The source region count of 25333 was equaled or exceeded in 33 out of the 20000 data sets, or a probability of $(1.65 \pm 0.3) \times 10^{-3}$. This final probability estimate is probably the most reliable and conservative. Taking into account the three shower size trials into account the chance probability of this observation is 6×10^{-3}.

Evidence of Spectral Cut-off

If the source of the observed events is Centaurus A and they result from primary photons, a spectral cut-off is expected at $\sim$ 200 TeV (Protheroe 1986, Figure 1.6c) and a shower size spectrum which falls rapidly above a few times 10^4 particles. Given the result above derived from three shower size regions, the excesses were examined in finer size ranges (see Table 5.2). Here, excesses were evaluated using the second method described above, by using a source region and 10 equivalent background regions in the same declination band. The most significant signal excesses are confined to shower sizes below 3×10^4 particles.

A Monte Carlo simulation was performed by Dawson (1993), which confirms that this behaviour would be expected for a source such as Cen A. It was assumed that the source emits γ-rays with an energy spectrum identical in slope to the cosmic ray spectrum, but with a sharp cut-off at 200 TeV. Atmospheric γ-ray showers were simulated using the MOCCA simulation package (Hillas 1993). The reconstructed sea level shower size distribution, which takes into account Buckland Park triggering efficiencies and reconstruction over a range of zenith angles, is shown in Figure 5.4. The background cosmic ray distribution (taken from real data) is also shown. This simulation, which had not been optimized in any way, clearly shows that a signal would be detected only at shower sizes smaller than 3×10^4 particles.

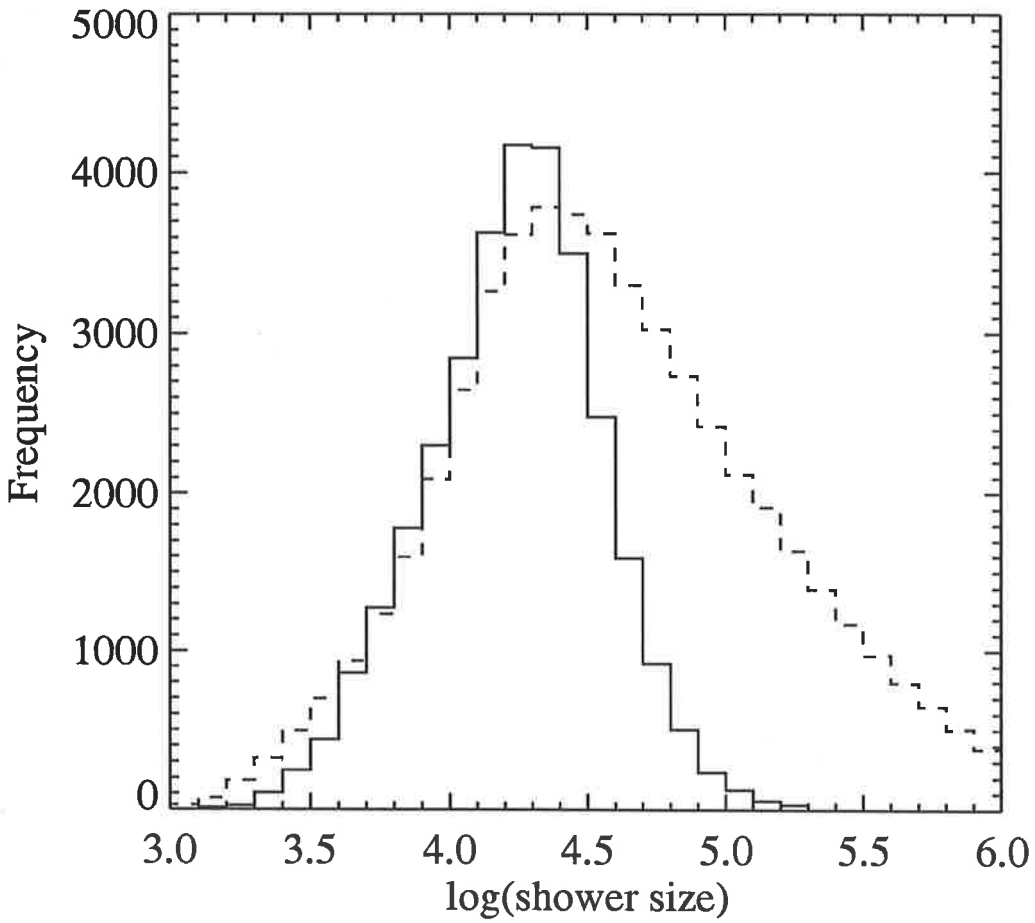

Figure 5.4: The expected shower size distribution for a γ-ray signal with a spectral cut-off at 200 TeV (solid line) compared with the background cosmic ray distribution (dashed line). The normalization is arbitrary.

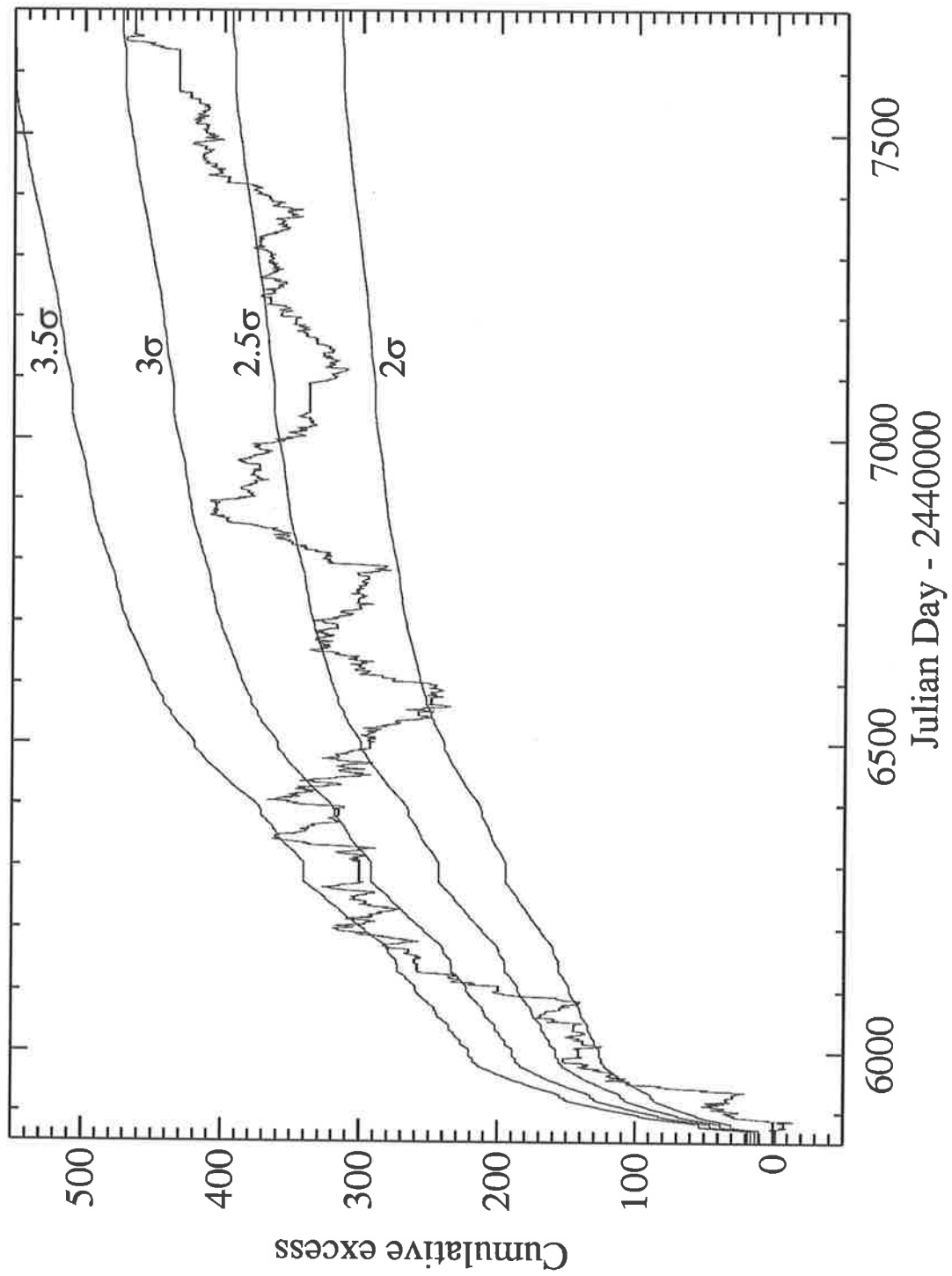

Figure 5.5: The cumulative excess of events from the direction of Cen A for shower sizes below 3×10^4 particles. The background count used here was generated using 1000 shuffled data sets. The time period shown, July 1984 to May 1989, is the period during which the array was sensitive to this shower size range.

Search for Burst Activity

The JANZOS group found no evidence for constant emission from Cen A but did find a burst period lasting about 50 days in 1990. This may be compared with earlier low energy data (Terell 1986) which showed a three year on-state within which there were enhanced periods lasting about 50 days. Figure 5.5 shows the progressive accumulation of the excess counts for Buckland Park showers with sizes below 3×10^4 particles. (The background rate used to produce this plot was derived from 1000 shuffled data sets, Dawson (1993)). It appears that the excess accumulated rapidly over the period from July 1984 to May 1985 (JD 2445900 - JD 2446200) but after that period the accumulation rate reduced. However, the significance of this behaviour is not compelling. Using the Kolmogorov-Smirnov test (Press et al. 1986) a 16% chance probability is found that the arrival time distributions of the signal and background are drawn from the same parent distribution. Therefore there is no evidence for burst-like behaviour.

To estimate the flux, the exposure of the array to cosmic rays was calculated using the background rate between the array size threshold of $\sim 10^4$ particles and 3×10^4 particles giving a value of $8.7 \times 10^{13}\mathrm{cm}^{-2}\mathrm{s}^{-1}$. The shuffling analysis gives an excess shower count of 458 showers, or a time averaged flux of $(7.3 \pm 2.4) \times 10^{-12}$ cm^{-2} s^{-1} between γ-ray energies of approximately 100 and 200 TeV. (The flux includes a factor of 1/0.72 since the optimal search region will only contain 72% of the signal events.) This flux is well below the extension of the low energy X-ray spectrum but is consistent with the flux reported by the JANZOS experiment during the fifty day high-state episode in 1990.

Conclusions

Data have been presented which support the observation of an excess of events at air shower energies from the direction of Centaurus A with a confidence level of 99.4% and an average flux over the period July 1984 to May 1989 of $(7.3 \pm 2.4) \times 10^{-12}$

Size N_e	On	Off	N_s (On - Off)	Excess σ	Excess %
$< 1.5 \times 10^4$	13811	13462	349	2.9	2.6 ± 0.9
$1.5 \times 10^4 - 3 \times 10^4$	11522	11215	307	2.8	2.7 ± 1.0
$< 3 \times 10^4$	25333	24677	656	4.0	2.6 ± 0.6
$3 \times 10^4 - 10^5$	13376	13221	155	1.3	1.2 ± 0.9
$10^5 - 3 \times 10^5$	5734	5911	-177	-2.2	-3.0 ± 1.5
$3 \times 10^5 - 10^6$	2886	2984	-98	-1.7	-3.3 ± 1.9
$10^6 - 3 \times 10^6$	817	811	6	0.2	0.7±3.5

Table 5.2: Numbers of showers observed in the direction of Cen A as a function of shower size. The off-source results were derived using ten equivalent background regions in the source declination band. The resulting excess σ values were calculated using the method of Li and Ma §5.1.1. Data from the additional size ranges were examined only after the significance of the signal was evaluated for the original choice of three size regions.

cm^{-2} s^{-1}. The spectrum exhibits a cut-off consistent with photon absorption by microwave photons in the intergalactic medium. No compelling evidence for flux variability is found in the data.

This average flux is close to the figure of $(5.5 \pm 1.5) \times 10^{-12}$ cm^{-2} s^{-1} found by the JANZOS experiment in a similar energy range within the burst lasting 48 days in 1990. That experiment reported a generally quiet state, apart from the burst, over the period from October 1987 to January 1992. An interpretation compatible with both experiments (including Figure 5.5) would be that the Buckland Park array observed emission mainly prior to October 1987, possibly in the period July 1984 to May 1985, and that the source then continued in a low state until the JANZOS burst of 1990. The average high-state flux in 1984/85 would then have been about 2.9×10^{-11} cm^{-2} s^{-1}. Such variability is found in other energy ranges (Jourdain et al. 1993).

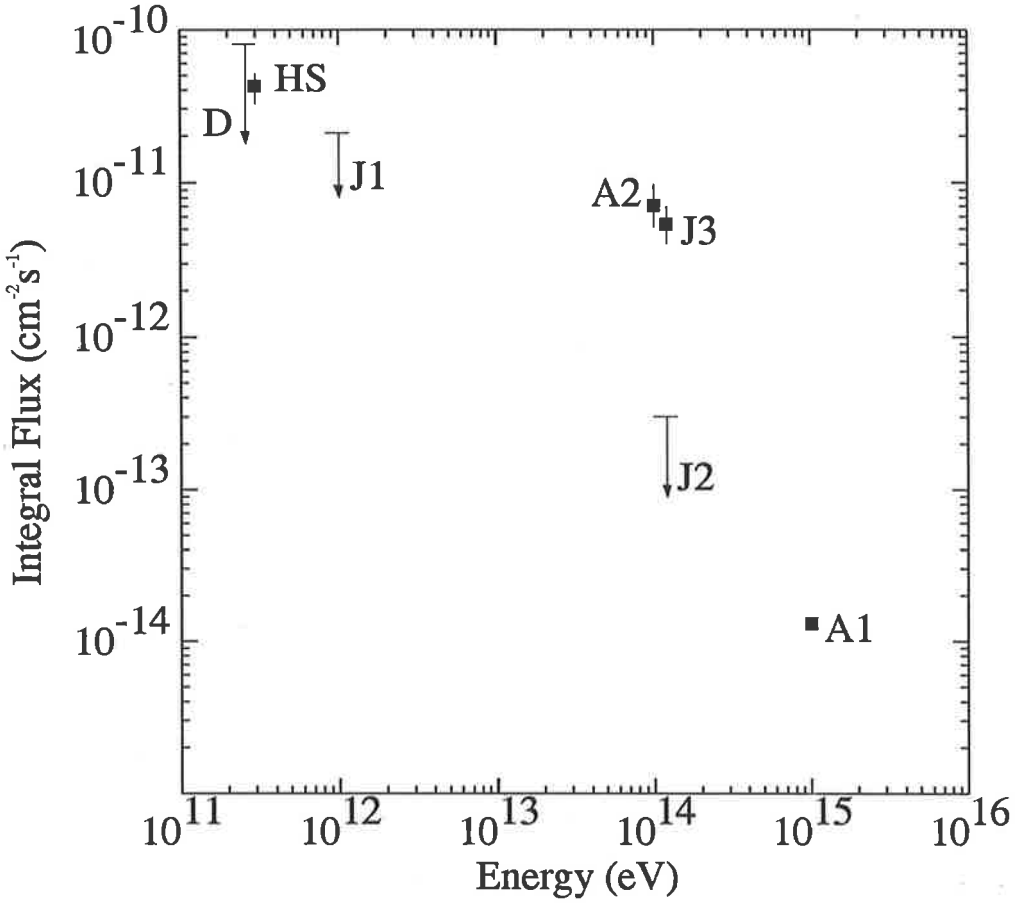

Figure 5.6: Centaurus A observations by a number of experiments (after Allen et al. 1993). References: Harvard-Sydney (HS) Grindley et al. (1975), Durham (D) Bowden et al. (1993), JANZOS results: J1, J2 (steady) and J3 (burst) Allen et al. (1993). Early Buckland Park result (A1) Clay et al. (1984), present steady flux estimate A2. Care must be exercised in the interpretation of this figure, given the variable length and non-overlapping observation times of the experiments.

5.2.2 Scorpius X-1

Scorpius X-1 ($\alpha = 244.8°, \delta = -15.6°$) was the first non-solar X-ray source discovered (Giacconi 1962) but models for the X-ray production mechanism have been hampered by the lack of any pulsations or orbital periodicity (see Middleditch & Priedhorsky (1986) for a summary of the source characteristics). A weak orbital modulation has been observed at optical wavelengths with a period of $0^d.787$ (Gottlieb et al. 1975), but less than 1% modulation is seen in X-rays at this period (Holt et al. 1976), and there has also been a suggestion of a 62 hour period in hard X-rays (Kudryavtsev et al. 1989). The source distance is uncertain, with estimates ranging from 300 pc to 2 kpc (Middleditch & Priedhorsky 1986).

Sco X-1 has been observed to have quiescent and active states in both the optical and X-ray regions. The active periods have time scales of a few hours to a few days and represent flux increases of 2-3 times Middleditch & Priedhorsky (1986). A summary of observations of the source in VHE γ rays is given by Chadwick et al. (1990), and some possibilities for the γ-ray production mechanism have been outlined by Mitra (1989).

The BASJE group (Kaneko et al. 1991) have set a steady state 90% (CL) upper limit of $1.4 \times 10^{-13}\mathrm{cm}^{-2}\mathrm{s}^{-1}$ above 2×10^{14}eV on their data from September 1987 to December 1990 for a signal from Sco X-1.

Tonwar et al. (1991) have recently reported the observation of Sco X-1 at ultra-high-energies by the Ooty array (latitude 11.4°N, altitude 2200 m a.s.l.). This observation followed an apparent signal observed by Inoue et al. (1991) (The BASJE group) at Mt. Chacaltaya (latitude 16.4°S, altitude 5200 m a.s.l.) during May 1986. The Ooty group searched their data from June 1984 to May 1987 and found an eight week period between 4 March and 2 May 1986 which showed a significant excess, and argued that this represented an active period of the source and that Inoue et al. may have observed a second such period rather close by in time. This coincidence of results was suggestive but the statistical significance of the Mt. Chacaltaya result was poor.

The Buckland Park array completes the trio of air shower arrays that were operational and were able to view Sco X-1 during the time of its reported activity. The array in 1986 consisted of 24 scintillation detectors, 11 of which were used for fast timing (Edwards 1988). The array had an effective enclosed area of $\sim 10^4 m^2$ and was sensitive to sea level sizes above about 10^4 particles.

A test of the Ooty result was made in the Buckland Park data set by following a procedure as close as possible to the method described in Tonwar et al. (1991). Initially a search was made for a net 'DC' excess over the eight week period in question, and then a test for burst activity, by comparing the on-source daily count over the period with the variation expected for a Poisson distribution. (A periodicity search was not performed at the supposed orbital period of $0^d.787$, since this has been seen only at optical wavelengths and not in the high energy regime).

The Buckland Park array was operational for 40 full Julian days (beginning 12^h 12 March 1986 UT) during the eight week period specified by the Ooty group. Only data from these 40 days were used. Events arriving on days interrupted by array maintenance or failure were discarded. Several cuts were made on the data to enhance a possible signal. Only showers within 40° of zenith were accepted, shower cores were restricted to within 50m of the array centre and 7 or more fast-timing detectors were required to trigger. In order to maximize the signal to background ratio under these cuts, a circular bin of fixed radius 1.75° centered on the source direction was used to select possible signal events. (The size of the bin was chosen *a priori* using earlier less sophisticated Monte Carlo calculations than those discussed in §3.10.2).

The background was estimated using the shuffling technique described in §5.1.5 by Dawson (1993) to produce an ensemble of simulated data sets. Such a method is especially appropriate for studies such as this where the period of interest is only eight weeks long. It has been noted that there is a diurnal variation in the overall array event rate (amplitude $\leq 5\%$ at this time of year) probably caused by detector temperature variations. For observations spanning years, this variation is of minor

importance, but here it was necessary to take account of these small event rate variations.

For each of the thirty simulated data sets the number of events arriving from within 1.75° of the source direction was recorded, giving a mean background expectation of 38.73 events (daily rate of 0.97 showers/day). The true source bin contained 52 events (1.30 showers/day). This excess corresponds to a 2.0σ excess (using the method of Li and Ma §5.2.2).

Search for Burst Activity

Evidence for burst activity was obtained by testing whether the distribution of daily event count in the source bin over the 40 days was consistent with that expected from a Poisson (random) distribution by using the dispersion test of Fisher (Santer & Duffy 1989). The statistic is defined

$$\sum_{i=1}^{40} \frac{(y_i - \overline{y})^2}{\overline{y}} \geq \chi^2_{39} \tag{5.10}$$

where here y_i is the daily event count and $\overline{y} = \sum_{i=1}^{40} y_i/40$. The statistic approximates the χ^2 distribution with 39 degrees of freedom. [1]

The probability estimates were tested with a Monte Carlo program by simulating 10^5 forty day periods and assuming that the mean event rate in the source error circle was the same for every daily transit of the source. The total number of events in the error circle in a given 40 day period was sampled from a Poisson distribution with a mean of 38.73, and these events were then randomly distributed over the 40 days. The dispersion statistic was calculated and the probability assigned from the χ^2_{39} distribution. The correctness of the resultant probability distribution was tested as shown in Figure 5.7. A true distribution of probabilities should have the property that the fraction of trials with probability less than x should be x. It can be seen that the test statistic underestimates the probability at low probabilities. This is a limitation of the Fisher dispersion test, and is not related to this application. A

[1] Note that this statistic is used to test the dispersion of the data around their mean, and is not intended to also test differences from a parent distribution with a different mean.

Monte Carlo simulation is required to assign reliable probabilities.

Given that the local time of source transit varied by 3.7 hours over the eight week period, a more realistic simulation than the one already described was performed which included the small diurnal array event rate variations (Dawson 1993). Shuffled data sets were again used, where real event arrival times were assigned to real local arrival direction (zenith θ, and azimuth ϕ angles) from other events. Arrival times were used from 21500 well analysed events arriving during parts of the 40 days when the source was within 40° of the zenith. These times were randomly assigned to the 1101 events with (θ, ϕ) coordinates capable of being "shuffled" into the source circle. An ensemble of 10000 simulated data sets was produced, and for each set the daily

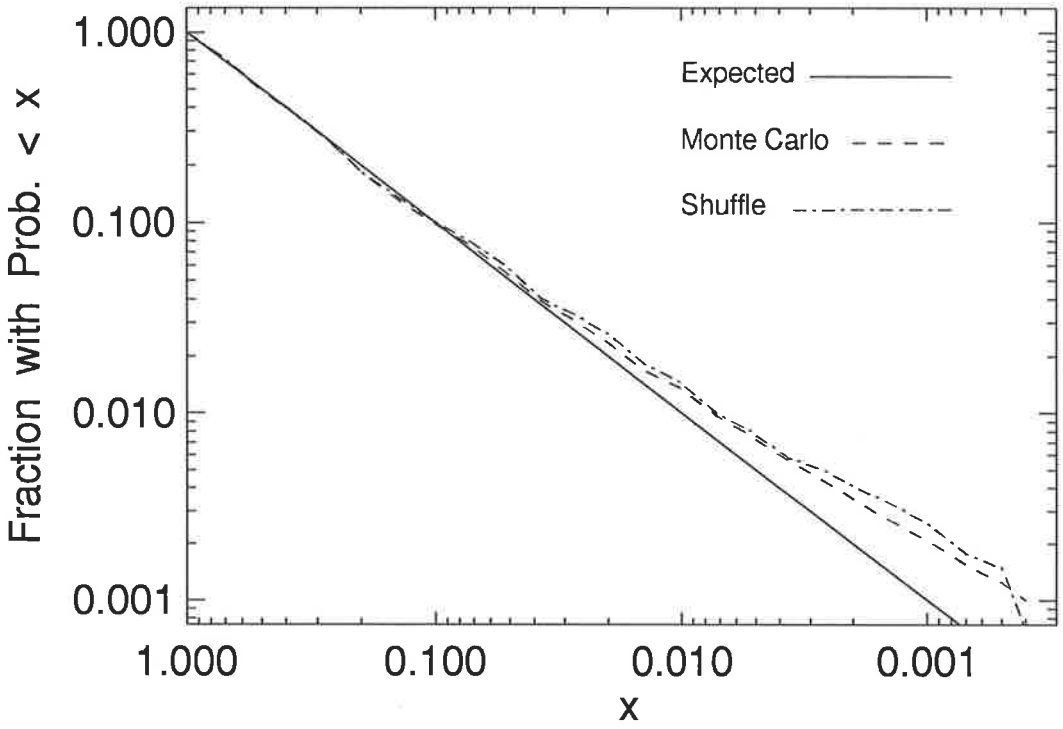

Figure 5.7: Distribution of assigned probabilities from the Fisher dispersion test for 10^5 Monte Carlo generated samples (dashline) and 10^4 "shuffled" samples (dot-dash line). The distribution expected for a correct probability estimator is shown by the solid line. The assumption that the Fisher dispersion statistic follows the χ^2_{39} distribution fails for low probabilities.

event count for the source circle was found, and the Fisher dispersion probability calculated using the χ^2_{39} distribution. The distribution of probabilities is also shown in Figure 5.7, showing reasonable agreement with the more simple simulation.

The source bin gives a dispersion statistic of 69.0. This value was exceeded in 46 of the 10000 shuffled data sets, giving a chance probability of this dispersion of 4.6×10^{-3}. The most significant error circle of the 98 tested in the same declination band as the source had a value of 62.1. The relatively low probability in the source bin comes in part from a day (JD2446524, beginning 12^h 3 April 1986 UT) when 6 events were recorded from the source direction, and 1.30 (the mean daily source bin rate) were expected. The overall array event rate was checked during that part of JD2446524 when Sco X-1 was within 40° of the zenith and no unexpected variations

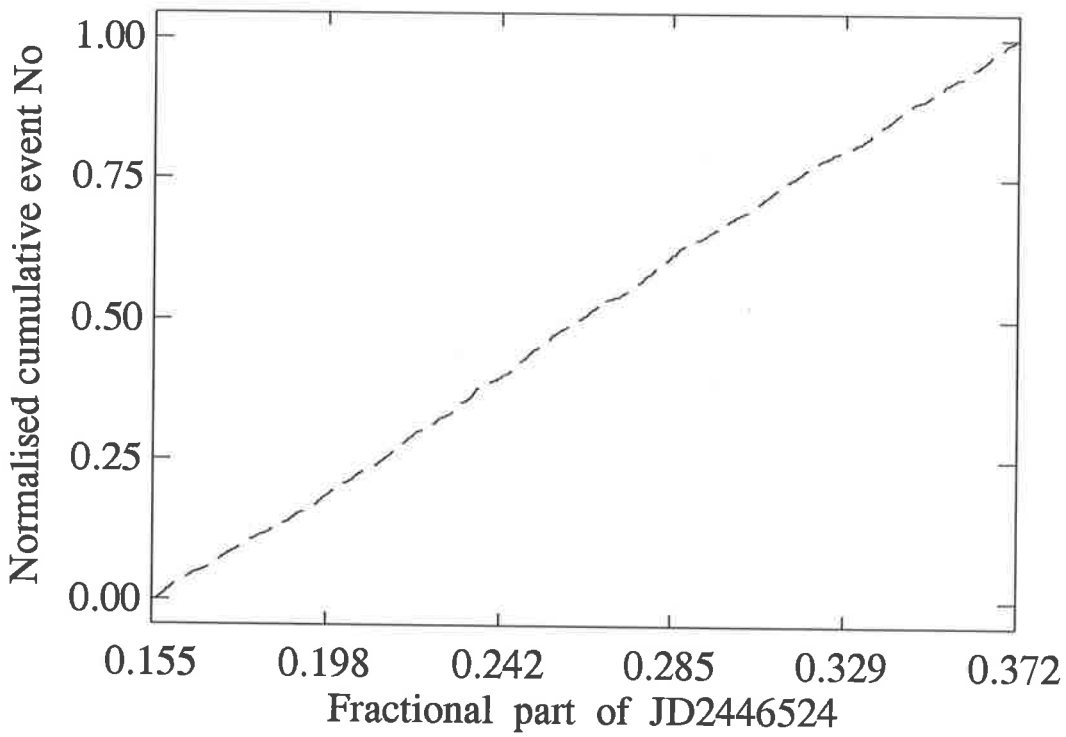

Figure 5.8: The cumulative event rate for the array (all arrival directions) during the transit of Sco X-1 on JD2446524. The period is defined as the time that the source was within 40° of the zenith. There are no episodes of unusual array behaviour evident.

in rate were found (Figure 5.8). Note that the dispersion test involves just a single trial, and tests the deviation of the entire daily count distribution over the 40 days from the expected Poisson distribution.

The total probability of the DC excess and burst probability is then 1.1×10^{-3}, using the method described in §5.1.6. This is the total chance probability of the observation of Sco X-1 for the 2 month period.

Using the method described in §5.1.3, and assuming that γ-ray showers trigger the Buckland Park array as efficiently as hadronic showers at these energies ($\sim 2 \times 10^{14}$ eV), the apparent average flux from the direction of Sco X-1 during the 40 days in question is $(1.3 \pm 0.7) \times 10^{-11}\mathrm{cm}^{-2}\mathrm{s}^{-1}$ above an estimated energy threshold of 2×10^{14}eV. For consistency the Ooty flux was recalculated using the method described in §5.1.3. and the signal & background event numbers given, giving a flux of $(1.0 \pm 0.2) \times 10^{-11}\mathrm{cm}^{-2}\mathrm{s}^{-1}$ above 2.5×10^{14}eV.

In conclusion, the result of Tonwar et al. (1991) was confirmed with a confidence level of 99.89%. This episodic activity in Sco X-1 may be typical of similar X-ray binary systems (especially at UHE energies).

5.2.3 Vela X-1

The first observation of Vela X-1 at PeV energies was reported by Protheroe et al. (1984) using data from the Buckland Park array collected from 1979 to 1981. The data from within 4 degrees of the source direction and with shower ages greater than 1.3 were folded at the orbital period into 50 bins, and showed an excess of events in the bin centred at phase 0.63. The total confidence level of this observation was 99.99%, and the time averaged flux was estimated at $(9.3 \pm 3.4) \times 10^{-15}$ cm^{-2} s^{-1} above 3×10^{15}eV.

As mentioned in §3.9, the assignment of the Julian date in this data set was in error by one day. This does not change the intrinsic shape of the orbital phaseogram, but it does displace the curve by a phase-shift of (orbital period *in days*)$^{-1}$ backwards. These data have been re-analysed using the same ephemeris (Nagase et al. 1981, (quoted by Hayakawa 1981)), namely $P = 8^d.96411$, $\dot{P} = (3.6 \pm 9.4) \times 10^{-8}$ at epoch T_0= 2 441 446.533 JD (eclipse centre). The light curve (Figure 5.9) now shows the peak between phase $0.50 - 0.54$.

This phase is now in better agreement with the result from the BASJE group (Suga et al. 1985), using data collected from 1964 to 1966. In their analysis, cuts on shower age and muon content were used to enhance the signal. Using the same ephemeris as above they find an excess of events at phase 0.5 - 0.525, and quote a significance of 99.9%.

The Potchefstroom group (van der Walt et al. 1987) searched for a signal from Vela X-1 in data collected between 1979 and 1981, the period of the Buckland Park observation. Again using the same ephemeris they reported an excess centered at phase 0.13 after selecting showers with ages greater than 1.3. The data were tested using the Z^2_{10} statistic, and the resulting significance was 4.8% after trials were taken into account.

Other groups have recently searched for emission from Vela X-1. The upper limits are: BASJE 90% CL 1.3×10^{-13}cm^{-2}s^{-1} above 2.4×10^{14} eV (Kaneko et al. 1991), JANZOS 95% CL 2.8×10^{-11}cm^{-2}s^{-1} above 10^{12} eV (Allen et al. 1993) and SPASE

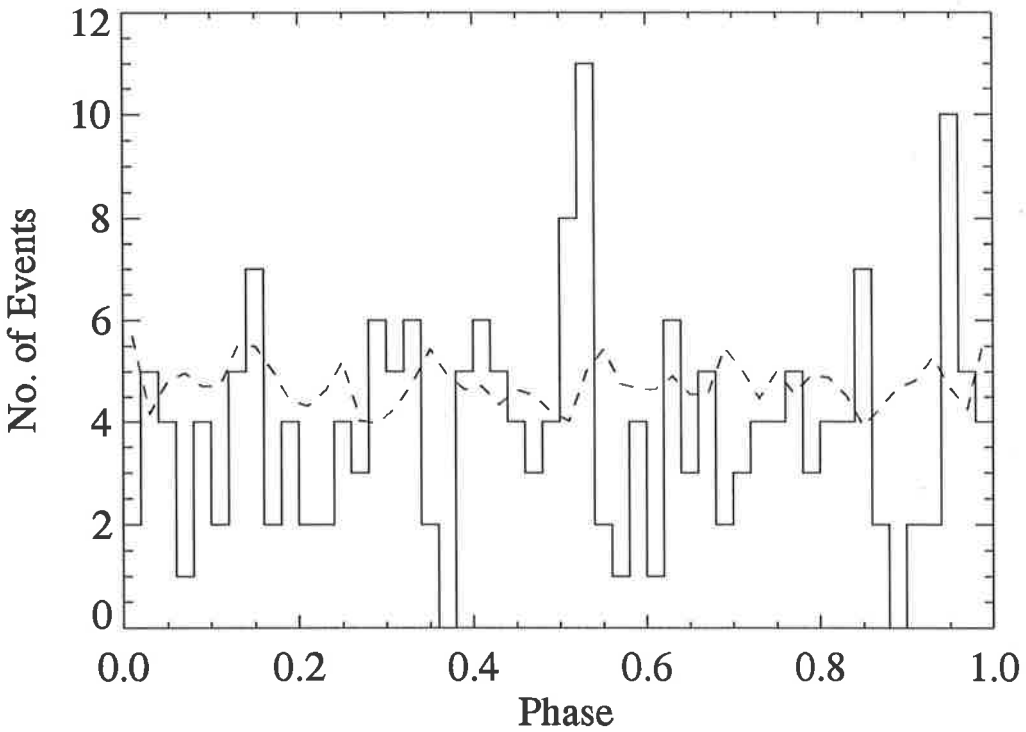

Figure 5.9: Reanalysed phaseogram of Vela X-1 from the Buckland Park data set of 1979-81. Using the ephemeris of Nagase et al. 1981, (quoted by Hayakawa 1981), the phase excess is now centered between 0.50-0.54 after the error in Julian day is corrected.

95% CL $6 \times 10^{-14}\text{cm}^{-2}\text{s}^{-1}$ above 2×10^{14} eV (van Stekelenborg et al. 1993).

The closeness of the orbital period of Vela X-1 to nine sidereal days (8.975 solar days) causes the background to be non-uniform as a function of phase. In light of this, van der Walt et al. investigated the distribution of the Z^2_{10} statistic with thirty six 10° by 10° background bins in the declination band of the source. The mean and standard deviation were 25.2 and 7.26 respectively, and the value of Z^2_{10} test in a 10° by 10° box centered on Vela X-1 was 37.9.

EHE Observations

Turning to the SUGAR data, events within a 10° radius error circle were used around the source direction and 12 equivalent independent positions at the same declination as the source were used to estimate the background. A 9° error circle was determined by Clay et al. (1992 & §5.2.4) as the optimum search region in the

analysis of 2A1822 -371 using the SUGAR data, but the slightly larger value of 10° was used for Vela X-1 given its lower maximum elevation.

As mentioned earlier the orbital period of Vela X-1 is close to nine sidereal days, hence artificially large values of Z^2_{10} are possible because of the non-uniformity of the exposure in phase. Given this problem, a method was adopted which determined the significance of the source phaseogram against a flat background. Shuffled data sets (§5.1.5), were used to obtain a statistically solid background by Dawson (1993). A total of 37 were produced, Figure 5.10. This background was then used to modify the source phaseogram by re-assigning phases to the events,

$$\varphi = \int_0^{\phi} P(\phi_b) d\phi_b \; / \; \int_0^1 P(\phi_b) d\phi_b$$

where ϕ is the old phase, φ is the new phase, and $P(\phi_b)$ is the background

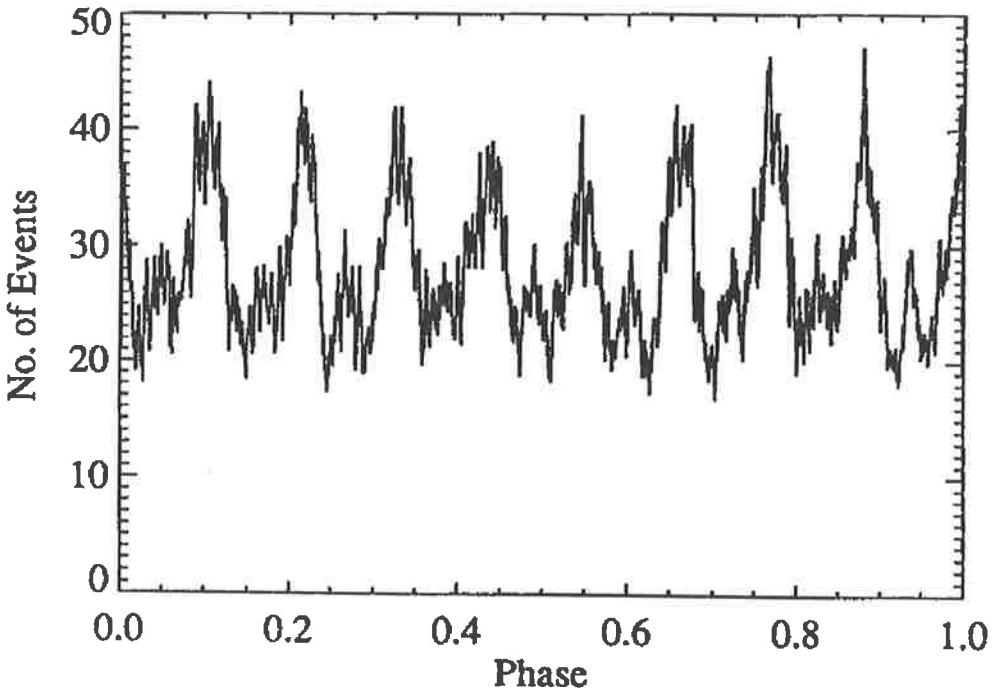

Figure 5.10: Phaseogram of the summed 37 randomised data sets which is used to reassign phases as a means of providing a flat background. The ordinate is the number of events per bin (2160 bins used). The closeness of the orbital period to 9 sidereal days is evident here.

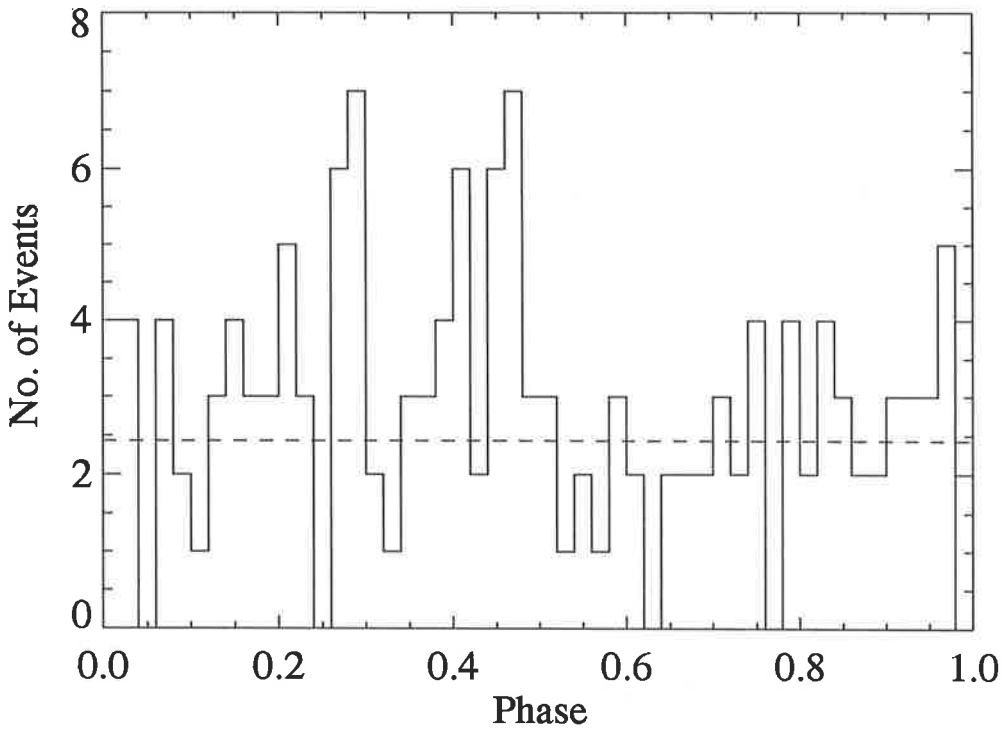

Figure 5.11: Phaseogram of events from direction of Vela X-1 with SUGAR data after correcting for non-uniformity in phase. The ephemeris used in Figure 5.9 is also used here.

phaseogram. The new phaseogram (Figure 5.11) now effectively has a flat background. The Z^2_{10} test gives a value of 26, corresponding to a probability of 17% that the source phaseogram is a chance fluctuation of a flat background. There is a DC excess of 1.1σ in the source circle. When this is combined with the Z^2_{10} test value using the method described in §5.1.6, the total significance is 2.5%, which is not statistically significant.

The method described in §5.1.4 was used to set an upper limit on the flux of particles from Vela X-1. The effective energy threshold for this source is 2×10^{17}eV and the upper limit is estimated to be 1.5×10^{-16} cm^{-2} s^{-1} above this energy at the 95% C.L. This figure assumes that the SUGAR array has the same triggering efficiency for the neutral radiation as for cosmic rays. This would be true for primary neutrons, while the efficiency for γ-ray primaries may be lower. A discussion of the response to γ-ray showers follows later (§5.3).

5.2.4 2A1822 -371

The low mass X-ray binary 2A1822-371 was first observed by the Uhuru satellite in the early 1970s. Later in 1978 a 5.57 hour orbital periodicity was observed at optical wavelengths and subsequently discovered in the X-ray, ultraviolet and infrared emissions. Observations in both the optical and X-ray regions exhibit a broad dip in intensity occuring at the eclipse of the 5.57 hour orbit (ie phase 0).

A model had been developed by White & Holt (1982) to describe the X-ray light curve of the system. In this model (the accretion-disc corona (ADC) model) the broad dip in intensity is caused by occultation of the corona by a bulge (see Figure below). Subsequently Mason & Cordova (1982) had found that this model also provides good fit to the infrared, optical and ultraviolet light curves.

The parameters from these models infer an inclination of the binary system of between $76° - 84°$, and a distance of 2 to 3 kpc.

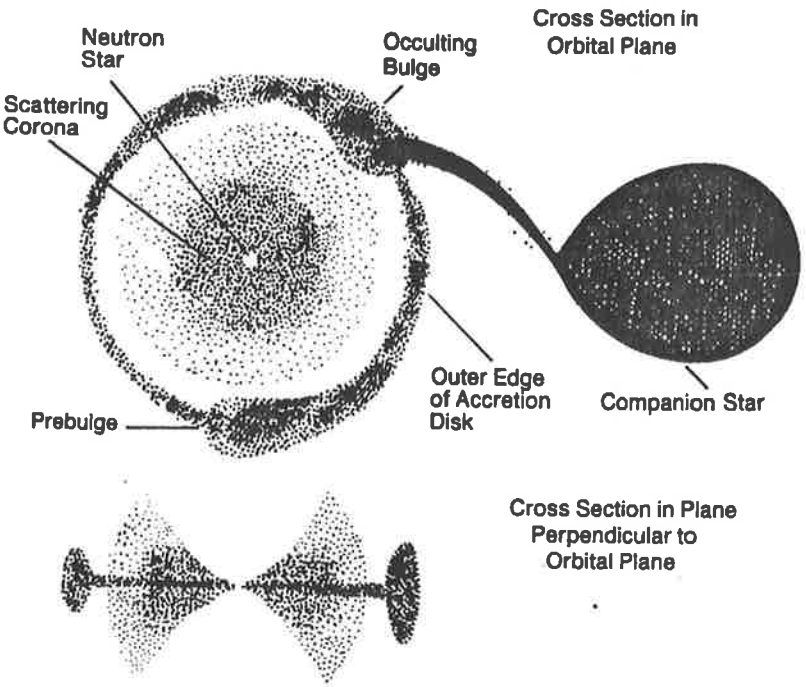

Figure 5.12: The accretion-disc corona model for 2A1822 -371 showing the corona & occulting buldge on the outer rim (from Cordova 1986).

UHE observations of 2A1822 -371 in the past by the Buckland Park array had not shown a significant DC excesses. However there appeared to be excesses predominately around phases 0 & 0.6 (Ciampa et al. 1989, Meyhandan et al. 1991, Clay et al. 1992). These excesses coincide with the bulges on the outer edge of the accretion disc proposed by White & Holt (1982). If this is the case then it is entirely possible that these bulges provide target material for the conversion of accelerated protons or ions into γ-rays from the decay of neutral pions.

The BASJE group have searched their September 1987 to December 1990 data set. No signal was found from 2A1822 -371 and they set an upper limit of $7.9 \times 10^{-14}\mathrm{cm}^{-2}\mathrm{s}^{-1}$ above 2.4×10^{14}eV (Kaneko et al. 1991).

UHE Observations of 2A 1822 -371

All five epochs (Table 3.4) of the Buckland Park data set were searched for evidence of UHE emission from 2A1822 -371. For each epoch and its corresponding angular resolution (see Table 3.4) a test for a DC excess was performed. The results are shown in Table 5.3. The background was estimated by using events from equivalent search regions in the same declination band as the source. The total number of regions for each epoch is different to accomodate the changing angular resolution for each epoch. Also the two circles neighbouring the source bin were eliminated from the analysis, and the number for each epoch is shown in Table 5.3, column $\mathcal{K}$ - 3. No evidence was found in any of the epochs for a significant DC excess of events.

The data were also tested for modulation by the source orbital periodicity. The Z^2_{10} test statistic was used (§5.1.2) and the epoch of Mason et al. (1982), with a period of $0.^d232108$ and a T_o= 2444105.674JD, after the data were corrected for the earth's motion around the sun. As in the DC search none of the epochs show a significant result. The phaseograms for each epoch are shown in Figure 5.13.

It is therefore concluded that there is no evidence for UHE emission from 2A1822 -371 in the five epochs of the Buckland Park data set. The upper limits for each epoch are calculated using the method described in §5.1.4, and are shown in the last

Epoch	S	B	$\mathcal{K}$ - 3	Li & Ma σ's	Z^2_{10} Value	$\chi^2(20)$	DC Upper Limit $cm^{-2}\ s^{-1}$
78-82	458	16470	36	0.023	24.45	0.210	$5.0 \times 10^{-13} > 10^{15}$eV
84-86	18412	405958	22	-0.293	21.49	0.370	$4.8 \times 10^{-12} > 10^{14}$eV
86-87	3064	111379	36	-0.530	29.83	0.073	$5.1 \times 10^{-12} > 10^{14}$eV
87-89	4600	222774	48	-0.598	30.26	0.066	$2.5 \times 10^{-12} > 10^{14}$eV
92	84	5925	73	0.311	33.48	0.030	$5.4 \times 10^{-13} > 10^{15}$eV

Table 5.3: The results of the search for UHE emission from 2A1822 -371 using the Buckland Park data set. S & B refer to the on-source and background counts, $\mathcal{K}$ - 3 is the number of background search regions used. The DC significance using the method of Li & Ma is defined in §5.1.1 eqn. 5.1, negative numbers indicate a deficit in the source bin. $\chi^2(20)$ indicates the probability that the phaseogram is a random fluctuatuation of a uniform background using the Z^2_{10} test. The DC upper limits were calculated using the method described in §5.1.4. The search regions used for each epoch is shown in Table 3.4.

column of Table 5.3. These upper limits are higher than those set by the BASJE group which is perhaps understandable given the poor angular resolution (see Table 3.4) of the Buckland Park array in the past .

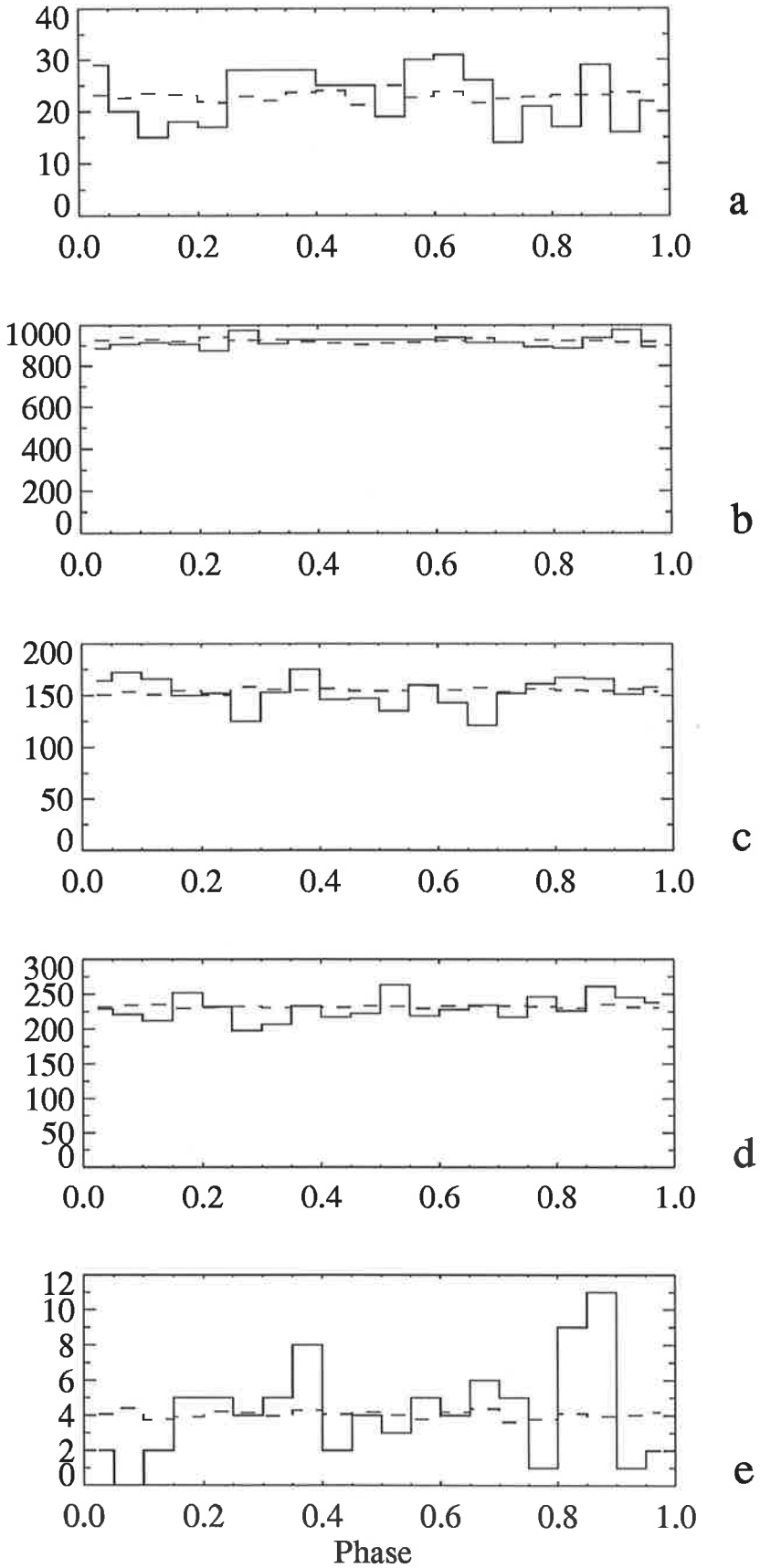

Figure 5.13: Phaseograms for the Buckland Park data set. The dashed lines are the expected background. (a) 1978-1982, (b) 1984-1986, (c) 1986-1987, (d) 1987-1989, (e) 1992.

EHE Observations of 2A 1822 -371

Data from the SUGAR array were used in this analysis. Figure 5.14 shows the heliocentered phaseogram for events within 10 degrees of 2A 1822-37.1 using the ephemeris of Mason et al. (1982). The background level is shown, based on an average of 12 off-source directions in the same declination band.

When tested using the Z^2_{10} test statistic, this distribution has a 1% probability of being derived from a uniform distribution. There also exists a DC excess of 1.87σ. The combined significance is given by the expression $p_1 p_2(1 - \ln(p_1 p_2/0.02))$ (§5.1.6), where p_1 and p_2 are the individual test significances. The expression takes into account the *a priori* requirement of a Z^2_{10} result better than 2%. The resulting significance is 1.6×10^{-3}.

Using the excess of events between phases 0 to 0.05, the flux is estimated, using the method described in §5.1.3, at $2 \times 10^{-15} cm^{-2} s^{-1}$ above 1.8×10^{17}eV, and a corresponding luminosity of $2.6 \times 10^{36} ergs^{-1}$ at a distance of 2.5kpc[2]

The result of a period/angular uncertainty search based on SUGAR data is shown in Figure 5.15. It can be seen that the result is compatible with the X-ray period of $0^d.23210(8)\pm(1)$, but that an improved period is $0^d.232107(4)\pm(8)$ with a corresponding oversampled Z^2_{10} statistic at the 0.4% level. Using the Protheroe statistic, a compatible period was found, $0^d.232106(6)\pm(6)$ significant at the 0.1% level.

The SUGAR data were predominately recorded in the early 1970's, and one may regard this source period as corresponding to that time. Hellier and Mason (1989) quote an X-ray period of $0^d.232108(93)\pm(13)$ for the period 1983-1985, together with an ephemeris which is quadratic in the number of cycles, so that a progresive increase in the period is found. The quadratic ephemeris of Hellier and Mason also gives a good fit both in sense and numerical value for the combined X-ray and EHE data. The family of curves shown in Figure 5.15 peaks for an angular uncertainty of

[2]This assumes isotropic emission of γ-rays which may not be the case if it is assumed the buldges on the rim of the accretion disc provide the target material for the production of γ-rays.

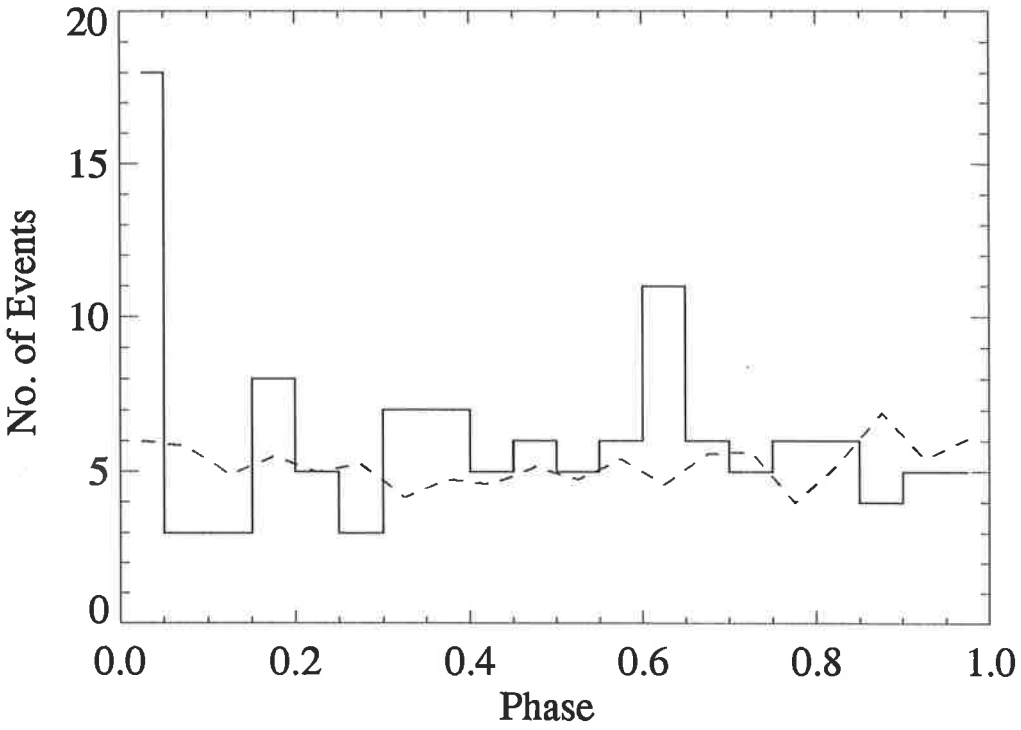

Figure 5.14: Phaseogram of events from within 10° of the direction of 2A1822 -371 using the ephemiris of Mason et al. (1982) using SUGAR data. The dashed line shows the expected level based on 12 equivalent background directions.

9° half angle and the improved period discussed above. A discussion of the EHE observations of 1822-371 is combined with the EHE observations of LMC X-4 at the end of this chapter.

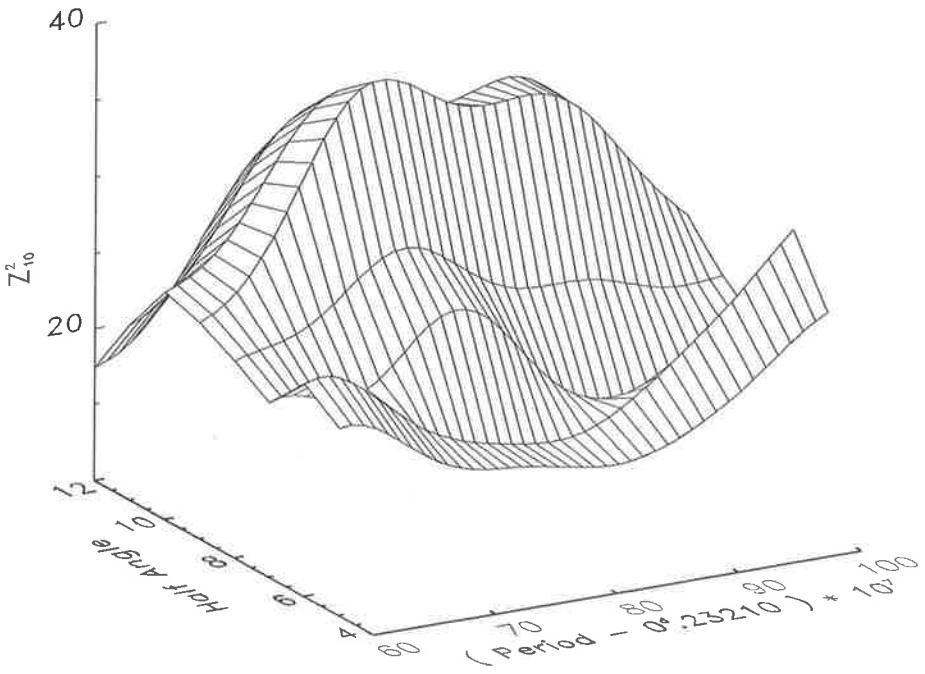

Figure 5.15: Three dimensional plot showing period, and angular search as a function of the Z^2_{10} test for events from the direction of 2A 1822-37.1 using SUGAR data.

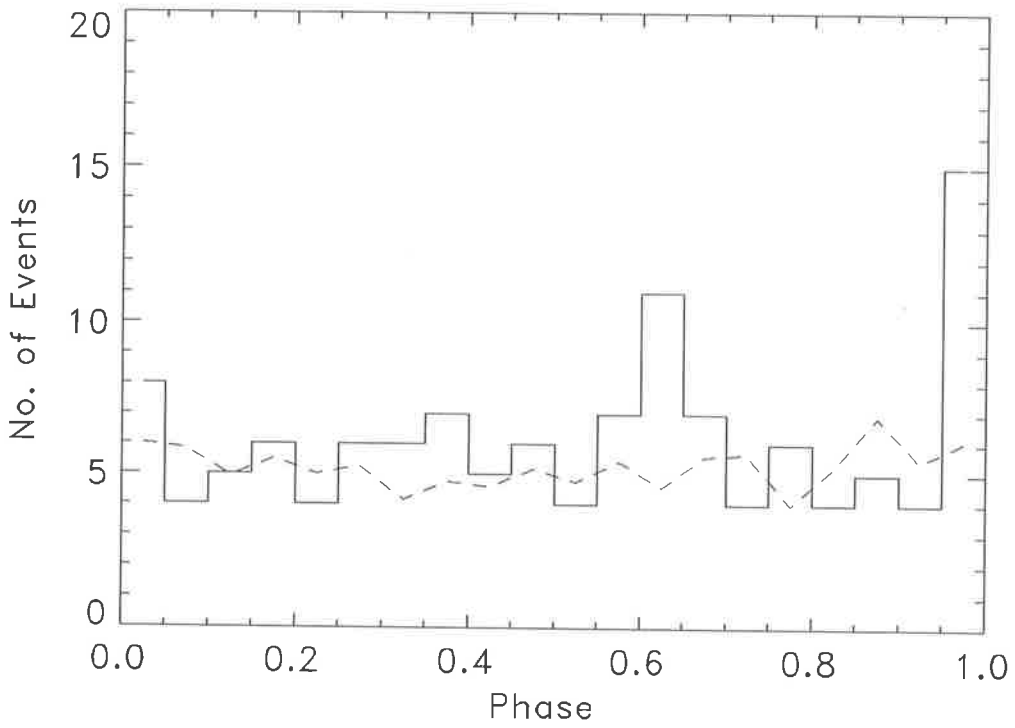

Figure 5.16: Phaseogram of events form 2A1822 -371 for the optimum period and search region for the SUGAR data. The dashed line shows the expected level based on 12 equivalent background directions.

5.2.5 LMC X-4

The extragalactic object LMC X-4 is a massive X-ray binary system which exhibits occasional flaring episodes (Kelly et al. 1983). It was discovered by the UHURU satellite (Giacconi et al. 1972). Photometric observations of the optical counter part led to the discovery of a 1.4 day periodic modulation (Chevalier & Ilovaisky 1977), which was subsequently confirmed in the X-ray data (White et al. 1978).

As a powerful extragalactic object, LMC X-4 is an important candidate source of high energy radiation. It has been first observed at UHE energies by Protheroe and Clay (1985) using Buckland Park data from 1979 – 1981. Given the error in Julian date in this data set mentioned earlier (see §3.9) the Buckland Park data for these years were reanalysed using the same ephemeris of Kelley et al. (1983), P=$1^d.40832$, T_0= JD 2442829.994. The light curve will be displaced by a phase shift of (orbital period *in days*)$^{-1}$ backwards. The new phaseogram, plotted in 20 bins (as it was originally) is shown in Figure 5.18a. The phase peak that was centred at 0.925 has shifted to approximately 0.17. The original claim was based on the Protheroe statistic and hence the significance of the result is not affected by this coherent shift in phase.

Subsequent observations by Edwards (1988) and Ciampa (1988) did not show any significant DC or periodic signals. Observations by other groups have not shown a significant signal either. The upper limits are JANZOS 95% CL
$3.5 \times 10^{-13}\text{cm}^{-2}\text{s}^{-1}$ above 1.4×10^{14}eV (Allen et al. 1993) and SPASE 95% CL
$2 \times 10^{-13}\text{cm}^{-2}\text{s}^{-1}$ above 5×10^{13}eV (van Stekelenborg et al. 1993).

UHE Observations of LMC X-4

The present Buckland Park data base was searched for a DC or periodic signal. None of the epochs show significant signals. The signal and background events are shown in Table 5.4, as well as the Li & Ma DC standard deviations (see §5.1.1). The background was estimated by using equivalent search regions in the same declination band as the source, and eliminating those two neighbouring the source bin, ($\mathcal{K}$ - 3)

Epoch	S	B	$\mathcal{K}$ - 3	Li & Ma σ's	Z^2_{10} Value	$\chi^2(20)$	DC Upper Limit $cm^{-2}\ s^{-1}$
78-82	111	1635	14	-0.522	21.83	0.350	$1.9 \times 10^{-13} > 2 \times 10^{15}$eV
84-86	5619	45221	8	-0.422	29.82	0.073	$2.6 \times 10^{-12} > 2 \times 10^{14}$eV
86-87	750	11124	14	-1.543	19.09	0.520	$2.8 \times 10^{-12} > 2 \times 10^{14}$eV
87-89	1199	23427	20	0.785	31.18	0.053	$2.6 \times 10^{-12} > 2 \times 10^{14}$eV
92	20	660	33	0.000	33.96	0.026	$2.5 \times 10^{-13} > 2 \times 10^{15}$eV

Table 5.4: The results of the search for UHE emission from 2A1822 -371 using the Buckland Park data set. S & B refer to the on-source and background counts, $\mathcal{K}$ - 3 is the number of background search regions used. The DC significance using the method of Li & Ma is defined in §5.1.1 eqn. 5.1, negative numbers indicate a deficit in the source bin. $\chi^2(20)$ indicates the probability that the phaseogram is a random fluctuatuation of a uniform background using the Z^2_{10} test. The DC upper limits were calculated using the method described in §5.1.4. The search region used for each epoch is shown in Table 3.4.

indicates the number of background regions used for each epoch.

Also shown are the periodic tests for each epoch using the Z^2_{10} test statistic (§5.1.2) and folded at the epoch of Kelly et al. (1983). The test does not indicate enhancement at any orbital phase. Figure 5.17 show the phaseograms for each of the 5 epochs. No broad scale features are evident in the light curves.

It is therefore concluded that no evidence for γ-ray emission from LMC X-4 is observed at UHE energies with the Buckland Park data base. The upper limits were calculated using the method described in §5.1.4 and are show in Table 5.4. They are generally higher than those set by the SPASE or JANZOS arrays, however this is not surprising given the poor angular resolution (see Table 3.4) of the Buckland Park array in the past .

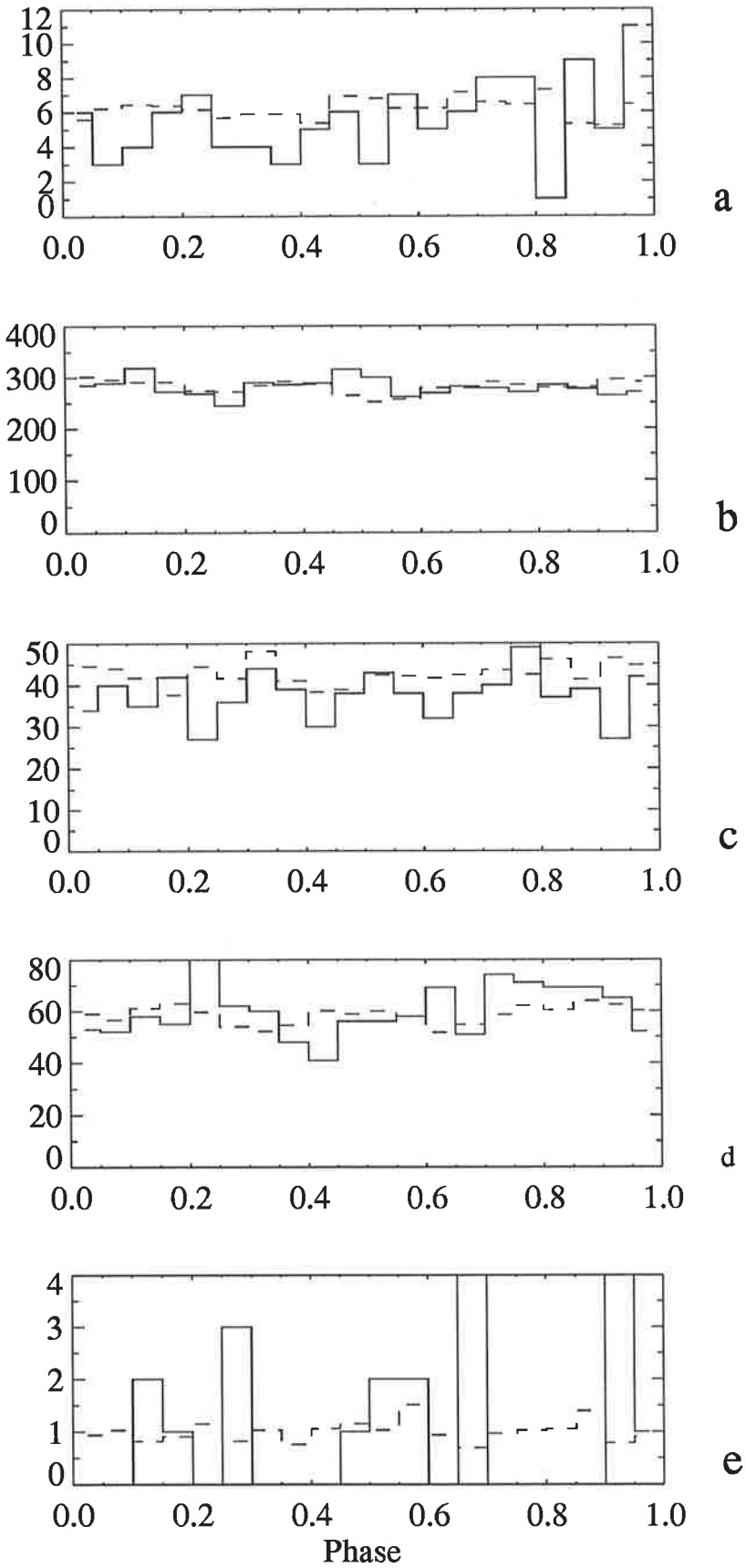

Figure 5.17: Phaseograms for the Buckland Park data set. The dashed lines are the expected background. (a) 1978-1982, (b) 1984-1986, (c) 1986-1987, (d) 1987-1989, (e) 1992.

EHE Observations of LMC X-4

In the analysis of 2A 1822 -37.1 (Clay et al. 1991 & §5.2.4) an optimum source error circle of 9° was found for the SUGAR data. However for LMC X-4 it was decided that an error circle of 10° would be used given its lower maximum elevation in the sky.

A 10° radius error circle was used around the source direction with six equivalent background circles in the same declination band. The Z^2_{10} test statistic (§5.1.2) was applied to the phase data, resulting in a value of 35.7, corresponding to a chance probability of the data coming from a flat phase distribution of 1.4%. The Protheroe test (§5.1.2) gives a similar chance probability (1.3%) for the source bin. The phaseogram is shown in Figure 5.18b. A D.C. excess of 1.5σ is present in the source circle, giving a total chance probability of the source sample being different from the background (phase information and D.C. excess) of 0.09 %.

To check the validity of the Z^2_{10} test statistic as a probability estimator in this context, 69 independent 10° circles on the sky were evaluated for this statistic using the LMC X-4 ephemeris. The resultant chance probabilities of the 69 phaseograms being different to a flat distribution are shown in Figure 5.19. This distribution of probabilities follows the expected form for random events (shown by the dashed line), giving confidence in the probability assignment above.

The number of events above background in the phase regions 0.1-0.2 and 0.6-0.7 is consistent with the measured D.C. excess of 26 events. The arrival times of the events in those phase regions were examined for clustering in arrival times. The Kolmogorov-Smirnov test (eg Press et al. 1986) has been used to compare the cumulative arrival time distribution of the data in these two phase bins to that of the entire data set. The test showed no evidence of burst activity giving a 98% probability that the two cumulative data sets are drawn from the same distribution.

A longer period of approximately 30.4 days is present in the optical and X-ray emissions of LMC X-4 (e.g. Lang et al. 1981). It is thought to be associated with precession of the neutron star accretion disk in the binary system (Ilovaisky et al.

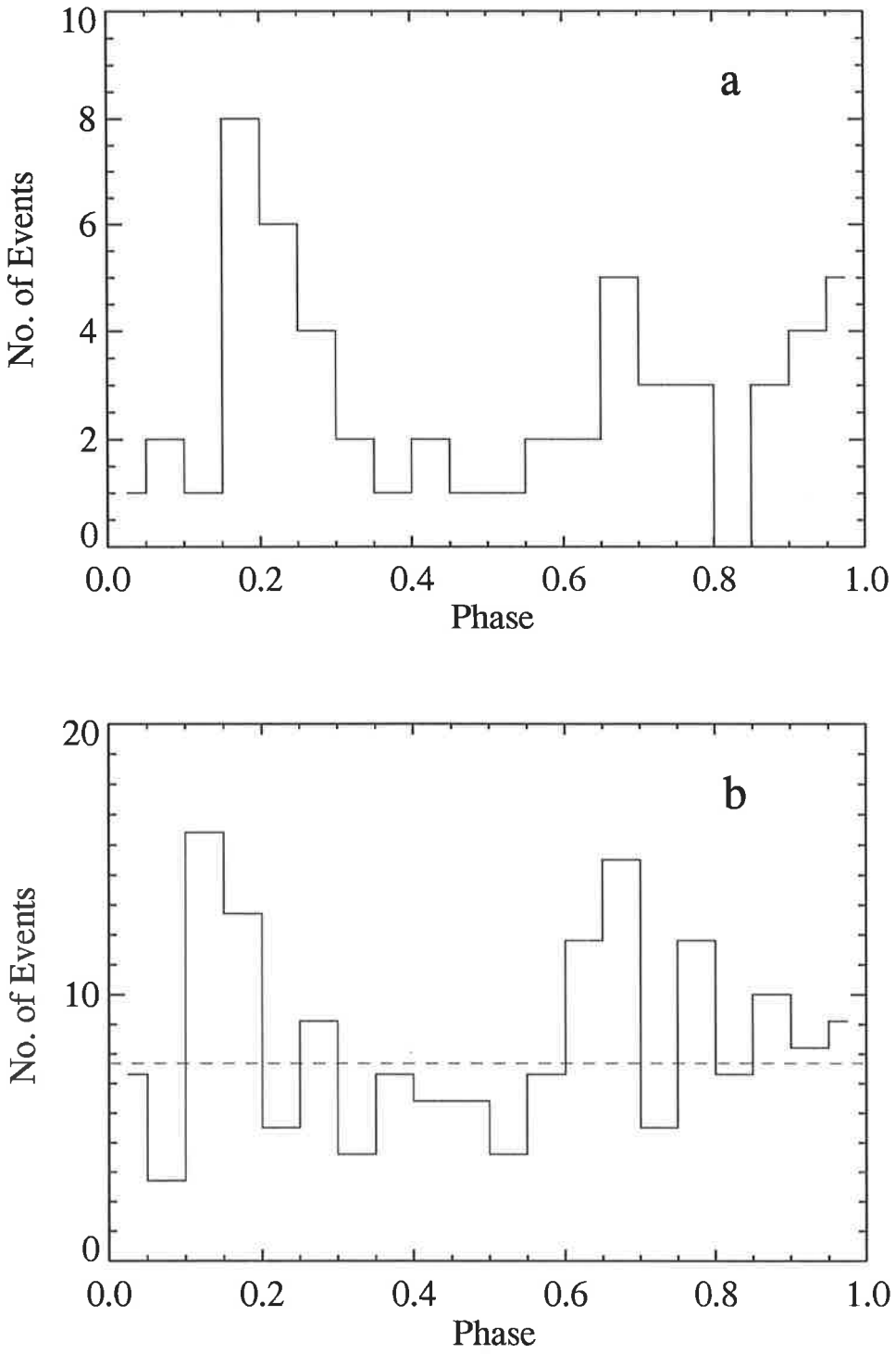

Figure 5.18: (a) Reanalysed phaseogram of LMC X-4 from the Buckland Park data set of 1979-81, after correcting for the error in Julian day. (b)Phaseogram of events within 10^0 from the direction of LMC X-4 using SUGAR data. The dashed line is the the expected level based on 6 equivalent background directions. There is an excess of 26 events between phases (0.1-0.2) & (0.6-0.7) above the background which is consistent with the DC level excess.

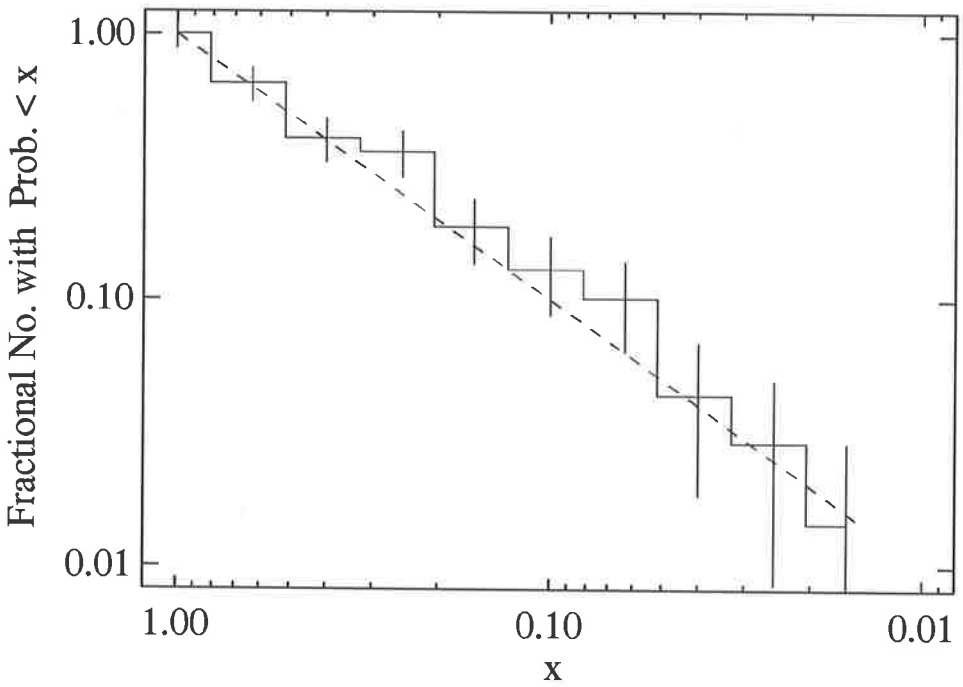

Figure 5.19: The integral probability distribution for 69 independent 10^0 radius sky regions, based on the Z^2_{10} test statistic for phaseogram non-uniformity. The expected form of the distribution is shown by the dashed line. The sky region containing LMC X-4 has the most significant chance probability, 1.4%.

1984). The current best estimates of the period appear to be P=$30^d.36 \pm 0^d.2$ from optical data (Heemskerk and van Paradijs 1989) and P=$30^d.42 \pm 0^d.3$ from X-ray observations (Pakull et al. 1985). A period search was performed on the SUGAR data, using the Z^2_2 statistic as the indicator of significance. (Z^2_2 was chosen because of the broad nature of the 30.4 day phase peaks in the optical and X-ray regions). The result of this search over one independent Fourier period is P=$30^d.43$ was a significance of only 14%. The resulting light curve is shown in Figure 5.20, using an epoch of JD 2443392.52 for the X-ray off state (phase=0) (Heemskerk and van Paradijs 1989). As can be seen there is a peak centered at phase 0.175, which is sharper than any present in the optical and X-ray data, and is therefore not necessarily identifiable as the result of the same type of process.

A comparison of the orbital phaseograms from the Buckland Park (1979 – 1981) and SUGAR (1968 – 1979) data sets (Figure 5.18 a & b) is interesting. While there

is a qualitative similarity between the two figures, a chi-squared test indicates that there is a probability of only 10% that the two distributions come from the same parent distribution. The two phase peaks centered at 0.15 and 0.65 match to within one phase bin, which might suggest a period time derivative. However a period derivative search on the SUGAR data resulted in the most significant Z^2_{10} value occurred for $\dot{P} = 0$. Also, a recent analysis of X-ray data (Levine et al. 1991) found no conclusive evidence for a period derivative.

Assuming that the signal arrives in the orbital phase regions $0.1 - 0.2$ and $0.6 - 0.7$, the signal events are 26 ± 7.5 from LMC X-4. This corresponds to a time-averaged integral flux of $(5.2 \pm 1.5) \times 10^{-16}$ cm^{-2} s^{-1} above 2×10^{17}eV, again using the method of Nagle et al.(1988). The assumption in this figure is that the signal is carried by quanta producing showers that trigger the SUGAR array with same efficiency as cosmic-ray showers.

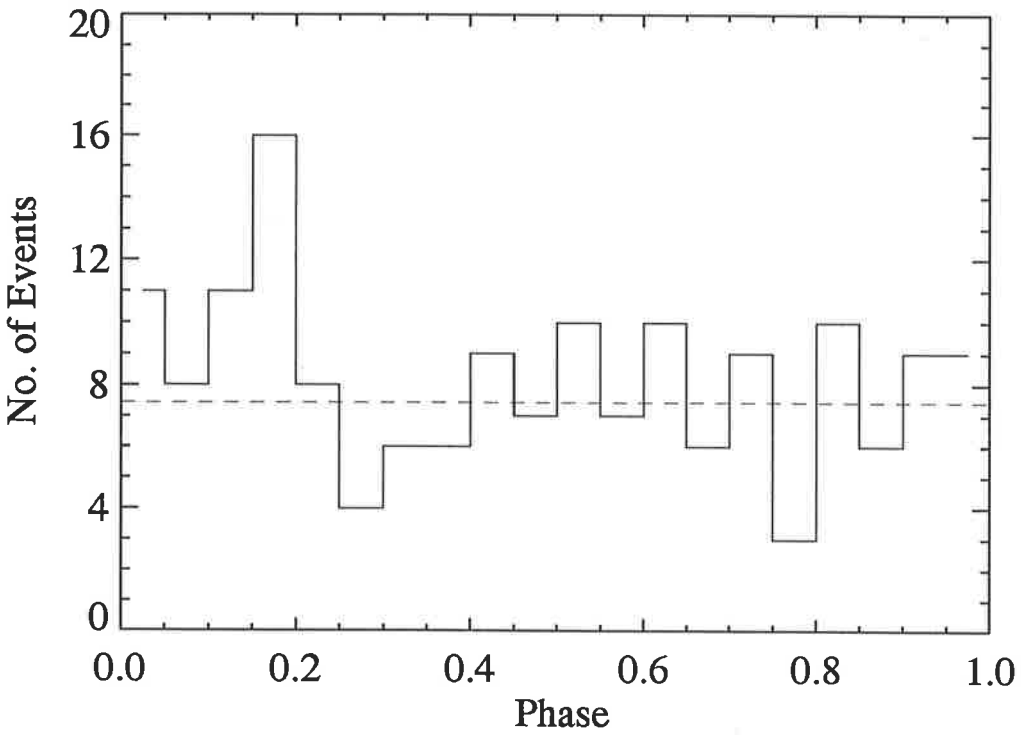

Figure 5.20: Phaseogram of events from LMC X-4 folded at the most significant precession period 30.43 days. The significance of this phaseogram using the Z^2_2 test statistic is 14%.

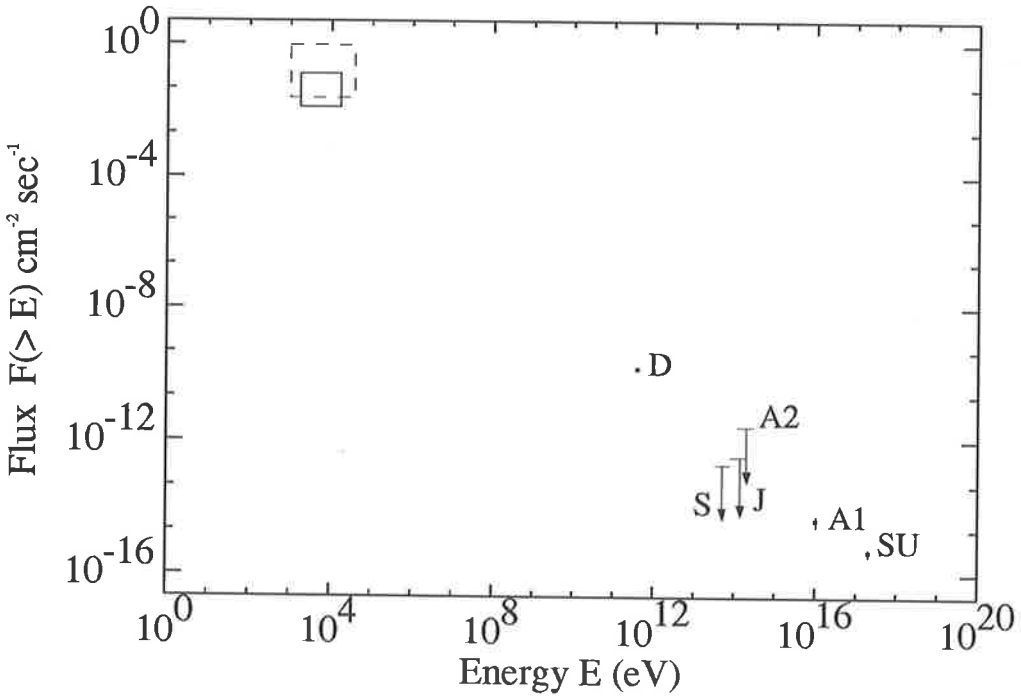

Figure 5.21: The integral spectrum of LMC X-4. The solid box (1.7-17)keV is X-ray data (White 1978); the dashed box (1-37)keV. is X-ray data (Levine et al. 1991). The pulsed flux from Durham (D) (Brazier et al. 1990); upper limit from JANZOS (J) Allen et al. 1993); upper limit from SPASE (S) (van Stenkelenborg et al. 1993); upper limit from the present analysis of Buckland Park data (A2); Original detection of LMC X-4 (A1) (Protheroe et al. 1985); Present analysis of SUGAR data (SU) (Meyhandan et al. 1992).

5.3 Nature of EHE Observations

There is some difficulty in attributing the signals from 1822 -37.1 & LMC X-4 to gamma-rays. As a detector sensitive to the muon component of air showers, SUGAR is biased against detecting showers initiated by γ-rays, assuming that gamma-rays at these energies behave in a familiar way and produce showers with only 10% of the muon numbers present in the proton cascades (Edwards et al. 1985, Stanev et al. 1985, Dumora et al. 1992; see §2.5.1). On the other hand, recent calculations by Aharonian et al. (1990) suggest that these standard shower models predicting low muon numbers at PeV energies come to quite different conclusions at 10^{18}eV because of the different energy dependences of the γ-ray and hadronic EAS muon multiplicities. In fact, they predict that γ-ray and hadronic showers have the same number of sub-GeV muons at 10^{18}eV at sea level (see §2.5.2). This model would go some way to giving the SUGAR array raised sensitivity to γ-ray signals.

The other possibility is high energy neutrons, which are capable of producing the EeV signals. They have been suggested to come from Cygnus X-3 (Jones 1988, Cassiday et al. 1989, Teshima et al. 1990). With an estimated distance of 2 - 3 kpc to 1822 -371 it is possible for neutrons to be observed at these energies. Figure 5.22 shows the expected differential flux of neutrons from 1822 -37.1.

However neutrons pose problems for LMC X-4 since it is a distant source (50kpc). At this distance, the survival probability for a 10^{18}eV neutron is only 2%. Unfortunately, the energy of the particles are too high and the period of the orbit too long to use phase coherency arguments to put a limit on the mass of the signal carrier.

Given this uncertainty, the source luminosity for LMC X-4 is calculated for two possibilities. Firstly it is assumed that the signal carriers are γ-rays which act to produce showers with the same triggering efficiency as cosmic-rays showers of the same energy. The luminosity was calculated per decade of energy, and assume an E^{-1} integral signal spectrum. Also assuming that the source radiates isotropically

and that the γ-rays suffer attenuation through interaction with the 3K blackbody photons (an attenuation factor of only 1.8 at these energies, Protheroe 1986, §1.5.3) the luminosity was estimated at 2×10^{38} erg s^{-1} per decade above 2×10^{17}eV.

This is roughly 800 times the luminosity quoted for Cygnus X-3 in this energy range (Cassiday et al. 1989), and 200 times more luminous than 2A 1822-371 (Clay et al. 1992 & 5.2.4), assuming all these sources radiate isotropically.

This figure is comparable with the power output of LMC X-4 in the X-ray region (1.7 - 17)keV of 10^{38} erg s^{-1} (White 1978) and from the Buckland Park observation, 10^{38} erg s^{-1} per decade above 10^{16}eV. This constant value of the luminosity across many decades of energy appears to imply a flux of gamma-rays with an integral spectrum falling as E^{-1}, as shown in Figure 5.21 (compared with E^{-2} for the cosmic-ray spectrum). Such a flat spectrum has probably made the detection by the

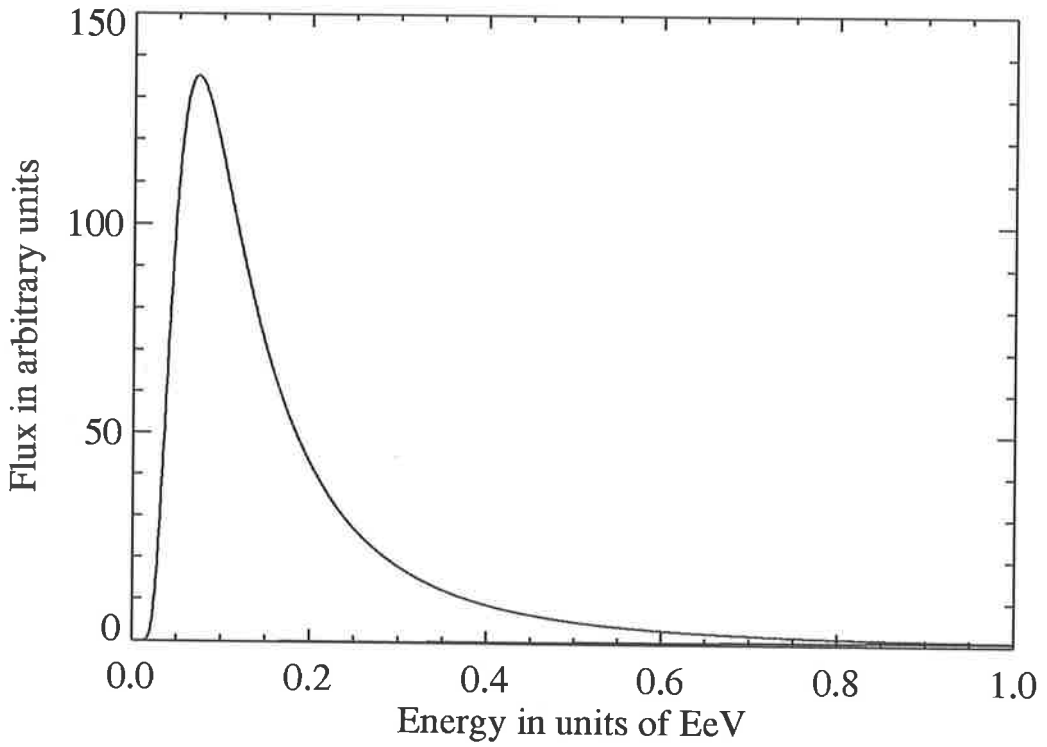

Figure 5.22: The shape of the neutron spectrum reaching Earth from 1822 -37.1 (assuming a distance of 2.5kpc), calculated for neutrons produced by a proton flux with a differential spectrum proportional to E^{-3} (Jones 1988)

SUGAR array possible. The relatively poor angular resolution of the array would have precluded a positive signal if it had not been for the increase in the signal to background ratio caused by the flatter signal spectrum.

As discussed in Chapter 1 §1.5.1, calculations have been made regarding the muon content of what might be called 'normal' γ-ray showers, where it is assumed that the photoproduction cross section in air increases only very slowly with photon energy (eg., McComb et al. 1979, Edwards et al. 1985, Stanev et al. 1985 & Dumora et al. 1992). It is assumed that these showers have only 10% of the normal proton cascade muon content above 1GeV (the detector threshold appropriate for the declination for LMC X-4). This difference in lateral distribution of the photoproduced muons published by McComb et al. 1979 has a very similar shape to the standard muon lateral distribution used in the SUGAR analysis Winn et al. (1986). Therefore it was assumed that a γ-ray with primary energy E will appear like a hadron shower with energy E/10. The result is that the flux estimate remains the same but the energy threshold increases by an order of magnitude to 2×10^{18}eV, correspondingly, the source luminosity increases by a factor of 10 to 2×10^{39} erg s^{-1} per decade above 2×10^{18} eV, again assuming the source radiates isotropically.

Chapter 6

Conclusions

Summary

The field of UHE γ-ray astronomy has been in existance for 10 years. Early observations in the northern and southern hemisphere were full of promise indicating the possibility of many sources. New arrays, which were built with vast improvements over those observations made with earlier arrays, did not confirm those early expectations.

The discipline of UHE γ-ray astronomy was pursued with the idea that, objects associated with γ-ray production (eg binary systems, active galaxies) may also be associated with cosmic ray production at Ultra High Energies.

This thesis has described changes made to the Buckland Park array and data set to improve factors such as angular resolution (as discussed in Chapter 3). Searches have been made for evidence of UHE & EHE emission from several candidate sources using both the Buckland Park and SUGAR data sets. Those objects searched using the SUGAR data set (Vela X-1, 2A 1822 -371 & LMC X-4) did not show strong evidence for a DC or periodic signal, although this is perhaps not surprising given the poor angular resolution of the SUGAR array. There were however, similarities between the SUGAR data light curves and those obtained at lower energies with the Buckland Park data set.

The results from the analysis of the Buckland Park data set were slightly better.

The objects searched were Centaurus A, Scorpius X-1, LMC X-4 & 2A1822 -371. The first two objects were studied after other groups (JANZOS & Ooty respectively) claimed to have observed bursts from these objects. The analysis for UHE emission from Centaurus A showed evidence of a signal below 3×10^4 particles which is consistent with photon absorption in the microwave background. The burst analysis of Scorpius X-1 was not highly significant, but was consistent with the result obtained by the Ooty group in the same period.

The latter two objects 2A1822 -371 and LMC X-4 had revealed evidence of UHE γ-ray emission with data taken with early Buckland Park data (1979 – 1981). However no compelling evidence was observed with the data set as a whole. Other arrays such as BASJE, JANZOS & SPASE have not shown evidence of UHE emission from these two objects either. The upper limits for 2A1822 -371 and LMC X-4 determined from the Buckland Park data were higher than those set by other groups mentioned above, caused mainly by the poor angular resolution of the Buckland Park array.

Future Work

It is evident that UHE γ-ray astronomy is not a well established field as far as significant ($> 3\sigma$) detections are concerned. The Buckland Park array has contributed partial evidence for the existence of UHE γ-ray point sources even though the angular resolution in the past was poor.

There is a need for further observations to continue especially now that improvements have been made to the Buckland Park array in the area of angular resolution, which will hopefully yield better results.

References

Acharya, B. S. and Rao, M. V. S.: 1991, Is the Centauro-1 event due to heavy primary nuclear break-up, *J. Phys. G:* **17**, 759 – 768.

Aharonian, F. A., Kanevsky, B. and Sahakian, V. A.: 1991, On some peculiarities of EAS initiated by gamma rays of extremely high energies, *J Phys. G:* **17**, 1909 – 1924.

Alexandreas, D. E. et al.: 1991, A search of the northern sky for UHE point sources, *Ap.J* **383**, L53 – L56.

Alexandreas, D. E. et al.: 1992, The CYGNUS extensive air-showers experiment, *Nucl Inst & Meth* **A311**, 350 – 367.

Allan, H. R.: 1971, *Proc. Elem. Particles and Cosmic Ray Physics* **10**, 170.

Allen, W. H.: 1993, Possible observation of 100 TeV gamma rays from the active galaxy Centaurus A, *Astro. Part.* **1**(3), 269 – 276.

Amenomori, M. et al.: 1993, Direct evidence of the interplanetry magnetic field effect on the cosmic-ray shadow by the sun, *Ap. J.* **415**, L147 – L150.

Baity, W. A. et al.: 1981, Cenaturus A at 2keV - 2.3 MeV: HEAO 1 Observations and Implications , *Ap. J.* **244**, 429 – 435.

Baltrusaitis, R. M.: 1985, The Utah Fly's Eye Detector, *Nucl Instrum & Methods* **A240**, 410 – 428.

Bell, C. J.: 1974, The upper end of the observed cosmic ray energy spectrum, *J. Phys. G:* **7**(8), 990 – 1009.

Bird, D. et al.: 1993a, The Fly's Eye etremely high energy cosmic ray spectrum, *23rd International Cosmic Ray Conference Calgary.*

Bird, D. et al.: 1993b, The Cosmic ray Composition above 0.1EeV., *23rd International Cosmic Ray Conference Calgary.*

Bird, D. J.: 1991, PhD thesis, University of Adelaide.

Bird, D. J. et al.: 1993c, Evidence for Correlated Changes in the Spectrum and Composition of Cosmic Rays at Extremely High Energies, *Phys. Rev. Lett.* **71**(21), 3401 – 3404.

Bond, I. A.: 1988, Search for TeV γ rays form SN 1987A during december 1987 and january 1988, *Phys. Rev. Lett.* **61**(20), 2292 – 2295.

Bond, I. A.: 1990, *Proc* 21^{st} *ICRC Adelaide* **2**, 198.

Bourilkov, D., Petrov, S. and Vankov, H.: 1991, Low-energy threshold calculations of EAS with primary energy $10^{13} - 10^{15}$ eV, *J Phys. G:* **17**, 1925 – 1932.

Boyer, C. S. et al.: 1970, *Ap. J Lett* **161**, 21.

Braizer, K. S. et al.: 1990, *Proc.* 21^{st} *ICRC Adelaide* **2**, 288.

Buccheri, R. and editor L. Scarsi, B. S.: 1985, *Data Analysis in Astronomy*, Vol. 15, New York: Pleum.

Cassiday, G. L. et al.: 1989, *Phys. Rev. Lett.* **62**, 383.

Cassiday, G. L. et al.: 1990a, A Coarse-Grain Search for Anisotropy in the Arrival Directions of Cosmic Rays above 10^{17}eV, *Ap. J.* **351**, 454 – 458.

Cassiday, G. L. et al.: 1990b, Mapping the UHE sky in search of point sources, *Nucl. Phys. B* **14A**, 291 – 298.

Cassiday, G. L. et al.: 1990c, The Ultra High Energy Cosmic Ray Spectrum, *Proc.* 21^{st} *International Cosmic Ray Conference, Adelaide, Australia* **3**, 163 – 164.

Chadwick, P. M., McComb, T. J. L. and Turver, T.: 1990, TOPICAL REVIEW, *J. Phys. G:* **16**, 1773 – 1802.

Chanmugam, G. and Brecher, K.: 1985, Ultra-high energy γ rays and cosmic rays from acceting degenerate stars, *Nature* **313**, 767 – 768.

Châtelet, E., Procureur, J. and Stamenov, J. N.: 1991, About the selection efficiency of EAS initiated by different cosmic primaries, *J. Phys. G:* **17**, 93 – 102.

Châtelet, E., Procureur, J. and Stamenov, J. N.: 1992, Hadrons in EAS initiated by cosmic gamma-rays with UHE, *J. Phys. G:* **18**, 951 – 960.

Chatelet, E., Procureur, J., Stamenov, J. N. and Ushev, S. Z.: 1990, Muons in EAS generated by cosmic gamma-rays with UHE, *J. Phys. G:* **16**, 317 – 325.

Chevalier, C. and Ilovaisky, S.: 1977, *Astro. Astrophy.* **59**, L9.

Chudakov, A. E.: 1991, Primary mass composition at energies $10^{13} - 10^{15}$ev from the analysis of multiple muon events, *Proceedings 22nd International Cosmic Ray Conference, Dublin* **2**, 5.

Ciampa, D.: 1988, *A southern hemisphere search for UHE gamma ray sources*, PhD thesis, University of Adelaide, North Tce. Adelaide GPO 498.

Ciampa, D. et al.: 1986, Development of the buckland park cosmic ray air shower array for ultra high energy gamma ray astronomy, *Proc. Astro. Soc Aust.*

Ciampa, D. et al.: 1989, *Ap. J.* **346**, 151.

Clay, R. W.: 1984, *Aust J. Phys.* **37**, 97.

Clay, R. W.: 1985, Extensive Air Showers, *Proc.* 19^{th} *International Cosmic Ray Conference, La Jolla, U.S.A* **9**, 357 – 382.

Clay, R. W.: 1987, *Aust. J. Phys.* **40**, 423.

Clay, R. W.: 1993, Private Communication.

Clay, R. W. and Gregory, A. G.: 1978, Light collection from $1m^2$ scintillator for cosmic ray work, *Nucl. Inst. & Meth.* **153**, 467.

Clay, R. W., Dawson, B. R. and Meyhandan, R.: 1994, Evidence for the Detection of Gamma-Rays up to 200 TeV from the Active Galaxy Centaurus A, *In The Press (Astroparticle Physics).*

Clay, R. W. et al.: 1984, Observation of an Excess of Cosmic Ray Showers from the Direction of Centaurus A, *Aust. J. Phys.* **37**, 91 – 95.

Clay, R. W. et al.: 1992a, Prospects for 10^{19} eV cosmic ray studies in South Australia, *Nulc. Phys. B.*

Clay, R. W., Meyhandan, R., Horton, L., Ulrichs, J. and Winn., M. M.: 1992b, Neutral particle emission from the X-ray binary 2A 1822-37 at energies above 10^{17} eV., *Astro. Astrophys.* **255**, 167 – 170.

Cocconi, G.: 1959, *Proc ICRC; Moscow* **2**, 327.

Cocconi, G.: 1961, *Encyclopedia of Physics*, Vol. XLVI, Springer - Verlag, Berlin, 215 - 271, ed S. Flügge. Cosmic Rays I.

Cooper, R. et al.: 1990, *Fly's Eye observations in: Astrophysical Aspects of the Most Energetic Cosmic Rays, Proc ICRR Int. Symposium Kofu, Japan; ed M. Nagano & F. Takahara* p. 34.

Cordova, F.: 1986, X1822 -371 and the Accretion-Disk Corona Model, *Los Alamos Science.*

Crewther, I. Y. and Protheroe, R. J.: 1992, Fluctuations in gamma-ray initiated air showers: lateral distribution, *J Phys. G:* **18**, 205 – 220.

Cronin, J. W. et al.: 1992, Search for discrete sources of 100 TeV gamma radiation, *Phys. Rev. D.* **45**(12), 4385 – 4391.

Cunningham, G. et al.: 1977, The energy spectrum of cosmic ray particles above 10^{17}ev, *Proc.* 15^{th} *ICRC Plovdiv* **2**, 303 – 308.

Dawson, B. R.: 1985, PhD thesis, University of Adelaide.

Dawson, B. R.: 1993, *Private Communication.*

Dawson, B. R. et al.: 1989, The lateral distribution of Cerenkov light from extensive air showers, *J. Phys. G.* **15**, 893 – 908.

de. Jager, O. C., Swanepoel, J. W. H. and Raubenheimer, B. C.: 1986, Kernel density estimators applied to gamma ray light curves, *Astron. Astrophys.* **170**, 187 – 196.

de Mello Rabaça, D. F. and Abraham, Z.: 1990, Study of the Variability of the Nucleus of Cenaturus A, *Rev. Mexicana Astron. Astrof* **21**, 155 – 157.

Dedenko, L. and Kolomatsky: 1987, The primary particle energy and cross section estimates from EAS data in the $10^{18} - 10^{21}$ energy range, *Proc.* 20^{th} *ICRC Moscow* **6**, 154 – 157.

Dicke, R. H.: 1965, Cosmic Black-Body Radiation, *Ap. J.* **142**, 414 – 419.

Dingus, B. L. et al.: 1988, *Phys. Rev. Lett.* **61**(18), 1906.

Dumora, D., Procureur, J. and Stamenov, J. N.: 1992, Evidence for the behaviour of the photoproduction cross section at UHE, *J. Phys. G:* **18**, 1839 – 1847.

Eadie, W. T.: 1971, *Statistical Methods in Experimental Physics*, Amsterdam: North-Holland.

Eames, P.: 1987, The angular resolution of the Haverah Park gamma ray telescope, *Proc* 20^{th} *ICRC (Moscow)* **2**, 449.

Edwards, P. G.: 1988, *A search for UHE gamma ray emission from binary X-ray systems*, PhD thesis, University of Adelaide, North Tce. Adelaide.

Edwards, P. G., Ciampa, D., Clay, R. W. and Patterson, J. R.: 1989, Search for uhe gamma-ray emission from X-ray systems, *Aust. J. Phys.* **42**, 581 – 589.

Edwards, P. G., Protheroe, R. J. and Rawinski, E.: 1985, The muon component of gamma-ray-initiated air showers, *J. Phys. G:* **11**, L101 – L107.

Efimov, N. et al.: 1987, Cosmic ray anisotropy with $E_o > 10^{17}$ eV, *Proc.* 20^{th} *ICRC Moscow* **2**, 41 – 44.

Eichler, D. and Vestrand, W.: 1985, Implications of ultra-high-energy emission from Hercules X-1, *Nature* **318**, 345 – 347.

Fenyves, E.: 1985, Can age parameter be used to distinguish between nucleon and gamma initiated air showers, *Techniques in UHE gamma ray astronomy, ed R. J. Protheroe and S. A. Stephens (University of Adelaide)* p. 124.

Firkowski et al.: 1961, *J. Phys. Soc.* **17A**, 122.

Gaisser, T. K.: 1990, *Cosmic Rays and Particle Physics*, University Press, Cambridge.

Gehrels, N.: 1984, The Gamma-Ray Spectrum of Centaurus A: A High-Resolution Observation between 70 keV and 8 MeV, *Ap. J.* **278**, 112 – 118.

Giacconi, R. et al.: 1962, Evidence for X-rays from Sources outside the solar system, *Phys. Rev. Lett.* **9**, 439.

Giacconi, R. et al.: 1972, *Ap. J.* **178**, 281.

Gottlieb, E. W. et al.: 1975, *Ap. J. Lett.* **195**, L33.

Green, K.: 1993, Private Communication.

Gregory, A. G. et al.: 1990, *Proc.* 21^{st} *ICRC Adelaide* **2**, 586.

Greisen, K.: 1960, Cosmic Ray Showers, *Ann. Rev. Nucl. Sci.* **10**, 63 – 108.

Greisen, K.: 1966, End to the Cosmic-Ray Spectrum ?, *Phys. Rev. Lett.* **16**(17), 748 – 750.

Grindley, J. E. et al.: 1975, Evidence for the Detection of Gamma Rays from Cenaturus A at E_γ *geq*3×10^{11}eV, *Ap. J.* **197**, L9 – L12.

Gunn, J. and Ostriker, P.: 1969, Acceleration of high-energy cosmic rays by pulsars, *Phys Rev Lett* **22**(14), 728 – 731.

Halzen, F.: 1988, *Preprint MAD/PH/459 University of Wisconsin-Madison.*

Hartman, R. C.: 1992, Detection of High-Energy Gamma Radiation from Quasar 3C 279 by the EGRET Telescope on the CGRO , *Ap. J.* **385**, L1 – L4.

Hayakawa, S.: 1969, *Cosmic Ray Physics.*

Hayakawa, S.: 1981, *Space Sci. Rev.* **29**, 221.

Hayashida, N. et al.: 1991, A search for point sources above 10^{17}ev using data from the agasa, *Proc* 22^{nd} *ICRC Dublin* **1**, 309 – 312.

Heemskerk, M. and van Paradijs, J.: 1989, Analysis of the optical light curve of the massive X-ray binary LMC X-4, *Astro. Astrophys.* **223**, 154 – 164.

Hellier, C. and Mason, K.: 1989, *MNRAS* **239**, 715.

Hill, C. T. and Schramm, D. N.: 1985, UHE cosmic-ray spectrum, *Physical Rev. D* **31**, 564 – 580.

Hill, C. T., Schramm, D. N. and Walker, T. P.: 1986, Implications of the UHE cosmic-ray spectrum observed by the Fly's Eye detector, *Physical Rev. D* **34**, 1622 – 1625.

Hillas, A. M.: 1971, *Proc.* 12^{th} *ICRC, Hobart, Australia* **3**, 1007 – 1012.

Hillas, A. M.: 1979, Does Scaling Remain a Good Approximation at EAS Energies ?, *Proc. 16 International Cosmic Ray Conference, Kyoto, Japan.* **9**, 13 – 18.

Hillas, A. M.: 1983, A Note on Various Versions of the Primary Energy Spectrum, *Proc. Cosmic Ray workshop, University of Utah, (ed: T. K. Gaisser, Newark Del. Bartol Res. Fdn.)* pp. 16–24.

Hillas, A. M.: 1984, Is Cygnus X-3 a monoenegetic 10^{17} accelerator, *Nature* **312**, 50 – 51.

Hillas, A. M.: 1987, Calculated time structure of air shower fronts, and fluctuation in triggering delay, *Proc 20^{th} ICRC (Moscow)* **6**, 432.

Hillas, A. M.: 1987b, Anomalous features of showers produced by radiation from Cygnus X-3 and other point sources, *Proc 20^{th} ICRC (Moscow)* **2**, 362.

Hillas, A. M.: 1987c, Source mechananisms (accretion objects), *Very High Energy Gamma Ray Astronomy NATO ASI Series; ed K. E. Turver, Durham* **199**, 71 – 80.

Hillas, A. M.: 1993, *Private Communication.*

Holt, S. S. et al.: 1976, *Ap. J. Lett.* **205**, L27.

Horton, L. et al.: 1983, *Proc. 18^{th} ICRC, Bangalore.*

Ikhsanov, N. R.: 1991, Particle acceleration and main parameters of UHE gamma-rays binaries, *Astro. & Space Sci.* **184**, 297 – 311.

Ilovaisky, S. A. et al.: 1984, LMC X-4: the optical 30 day cycle and its implications, *Astro. Astrophys.* **140**, 251 – 258.

Inoue, N.: 1990, VHE Gamma rays with energies above 10^{14} eV Observed at Mt Chacaltaya, *Nucl. Phys. B (Proc Suppl)* **14**, 121.

Jones, L. W.: 1985, High Energy Interactions of Cosmic Ray Particles, *Proc. 19^{th} Intervational Cosmic Ray Conference, La Jolla, U.S.A* **9**, 323 – 336.

Jones, L. W.: 1988, The Possible Observation of PeV Neutrons from Pulsar Gamma Ray Sources, *Workshop on Frontier Objects in Astrophysics and Particle Physics, Vulcano, Italy.*

Jourdain, E. et al.: 1993, *Ap. J.* **412**, 586.

Kalmykov, N. et al.: 1973, Extensive air showers and characteristics of nuclear interactions at superhigh energies, *Proc. 13^{th} ICRC Denver* **4**, 2633 – 2638.

Kamata, K.: 1968, *Can. J. Phys.* **46**, S72.

Kaneko, T. et al.: 1991, Search for point sources of gamma rays with energies above 30 TeV in the southern hemisphere, *Proc 22^{nd} ICRC, Dublin* **1**, 372 – 375.

Karakula, S., Osborne, J. L. and Wdowczyk, J.: 1974, Origin of energetic cosmic rays II. The possibility of a contribution from pulsars, *J. Phys. A: Math., Nucl. Gen.* **7**(3), 437 – 443.

Kazanas, D. and Ellison, D.: 1986, Origin of ultra-high-energy γ-rays from Cygnus X-3 and related sources, *Nature* **319**, 380.

Kelly, R. et al.: 1983, *Ap. J.* **264**, 568.

Kirov, I. N.: 1992, Search for EAS excess from the direction of compact galactic X-ray sources Cygnus X-3, Herculus X-1, Cygnus X-1 and others, *J. Phys. G:* **18**, 2027 – 2035.

Krasilnikov, D. D.: 1983, Anisotropy of Intensity of Cosmic Rays with $E_o > 10^{17}$eV, *Proc. 18th International Cosmic Ray Conference, Bangalore, India.* **9**, 223 – 226.

Krys, A., Krys, E. and Wasilewski, A.: 1991, High-energy photoproduction in air showers, *J. Phys. G:* **17**, 1261 – 1269.

Kudryavtsev, M. I. et al.: 1989, *Sov. Astro. Lett.* **15**, 466.

Lagutin, A. et al.: 1979, The radial distribution of electromagnetic cascade particles in the air, *Proc.* 16th *ICRC Kyoto* **7**, 18 – 23.

Lamb, R. C. et al.: 1988, *Ap. J.* **328**, L13.

Lang, F. L. et al.: 1981, Discovery of a 30.5 day Periodicity in LMC X-4, *Ap. J.* **246**, L21.

Lawrence, M. A. and Watson, A. A.: 1992, Are the arrival directions of the highest-energy cosmic rays clustered?, *J. Phys. G:* **18**, 1827 – 1832.

Lawrence, M. A. et al.: 1989, *Phys. Rev. Lett.* **63**, 1121.

Lawrence, M. A., Reid, R. J. O. and Watson, A. A.: 1991, The cosmic ray energy spectrum above 4×10^{17} eV as measured by the Havarah Park array, *J. Phys. G:* **17**, 733 – 757.

Lawrence, M. et al.: 1990, A reassement of the Havarah Park energy spectrum above 3×10^{17} ev, *Proc* 21st *ICRC Adelaide* **3**, 159 – 162.

Lawrence, M. et al.: 1990b, The arrival direction distribution of ultra-high energy cosmic rays measured at Havarah Park, *Proc* 21st *ICRC Adelaide* **3**, 200.

Levine, A. M. et al.: 1991, *Ap. J.* **381**, 101.

Li, T.-P. and Ma, Y.-Q.: 1983, Analysis methods for results in gamma-ray astronomy, *Ap. J* **272**, 317 – 324.

Linsley, J.: 1985, Aplications of UHE γ-ray relescopes to the study of cherged cosmic rats, *Techniques in UHE gamma ray astronomy, ed R. J. Protheroe and S. A. Stephens (University of Adelaide)* p. 138.

Linsley, J. and Watson, A.: 1977, Review of data on cosmic ray anisotropy, 1951-65 energy $10^{14} - 3 \times 10^{17}$ ev, *Proc* 15th *ICRC Plovdiv* **12**, 203 – 208.

Linsley, J. and Watson, A. A.: 1981, Validity of Scaling to 10^{20}eV and High-Energy Cosmic-Ray Composition, *Phys. Rev. Lett.* **46**(7), 459 – 463.

Lloyd-Evans, J.: 1982, *The Arrival Direction Distribution of Primary Cosmic Rays above* $10^{15} eV$, PhD thesis, University of Leeds.

Lloyd-Evans, J.: 1991, Cosmic ray origins above 10^{15}eV, *Proc.* 22^{nd} *ICRC Dublin, Rapporteur Talks* **5**, 215.

Lloyd-Evans, J. et al.: 1983, Observation of γ rays $> 10^{15}$ eV from Cygnus X-3, *Nature* **305**, 784 – 787.

Mason, K. and Cordova, F.: 1982, Infrared Photometry of the X-ray binary 2A1822 -371: A model for the ultraviolet, optical and infrared light curve, *Ap. J.* **262**, 253.

Mason, K. et al.: 1982, *M.N.R.A.S.* **200**, 793.

Matsubara, Y. et al.: 1990, Arrival direction of Cosmic Rays in the energy region between 10^{18}eV and $10^{19.5}$eV, 21^{st} *International Cosmic Ray Conference, Adelaide, Australia* **3**, 201 – 204.

Maze, R. and Zawadzki, A.: 1960, On an attempt of detection of primary cosmic photons of very high energy, *IL Nuovo Cimento* **17**, 625 – 633.

Maze, R. et al.: 1969, Origin of muon-poor extensive air showers, *Phys Rev Lett* **22**(17), 899 – 901.

McComb, T. J. L., Protheroe, R. J. and Turver, K. E.: 1979, Photoproduction in large cosmic-ray showers, *J. Phys. G:* **5**(11), 1613 – 1620.

Meyer, J.-P.: 1985, The Baseline Composition of Solar ,Energetic Particles, *Ap. J* **57**, 151.

Meyhandan, R., Clay, R. W., Dawson, B. R. and Edwards, P. G.: 1993, Evidence of UHE radiation from Scorpius X-1, *J. Phys. G:* **19**(1), L1 – L5.

Meyhandan, R., Dawson, B. R. and Clay, R. W.: 1991, EAS direction re-analysis with shower front curvature, *in* M. Cawley (ed.), *Volume 2: 22nd ICRC*, Dublin Institute for Advance Studies, pp. 712 – 715.

Meyhandan, R., Dawson, B. R., Clay, R. W., Horton, L., Ulrichs, J. and Winn, M. M.: 1992, Evidence for neutral emission above 10^{17} eV from LMC X-4, *Ap.J* **391**, 236 – 241.

Michalak, W., Wdowczzk, J. and Wolfendale, A. W.: 1990, Cosmic gamma rays and neutrinos of energy near 10^{20} eV, *J. Phys. G:* **16**, 1917 – 1924.

Middleditch, J. and Priedhorsky, W.: 1986, *Ap. J.* **306**, 230.

Mitra, A. K.: 1989, *Astro. Astrophys* **219**, L1.

Nagano, M. et al.: 1992, Energy spectrum of primary cosmic rays above 10^{17}eV determined from extensive air shower experiments at Akeno, *J. Phys. G:* **18**, 423 – 442.

Nagle, D. E., Gaisser, T. K. and Protheroe, R. J.: 1988, Extensive air showers associated with discrete astrophysical sources, *Ann. Rev. Nucl. Part. Sci.* **38**, 609 – 657.

Pakull, M.: 1985, LMC X-4, A0538-66 and surrounding X-ray sources observed with EXOSAT, *Space. Sci. Rev.* **40**, 379 – 382.

Penzias, A. and Wilson, R.: 1965, *Ap. J.* **142**, 419.

Peters, B.: 1961, Primary Cosmic Radiation and Extensive Air Showers, *IL Nuovo Cimento* **22**(4), 800.

Press, W. H. et al.: 1986, Numerical Recipes: the art of scientific computing Cambridge, *Cambridge University Press* p. 472.

Procureur, J. and Stamenov, J. N.: 1987, Extensive air showers initiated by primary gamma quanta with energies $10^2 - 10^3$TeV, *J. Phys. G.* **13**, 1579 – 1584.

Protheroe, R. J.: 1984, Statistical analysis in gamma-ray astronomy: The upper limit, *Astron. Exprs.* **1**, 33 – 38.

Protheroe, R. J.: 1984b, Clues from the photonuclear time scale on the nature of particle accelerators in Cygnus X-3 and Vela X-1, *Nature* **310**, 296–298.

Protheroe, R. J.: 1985, A new statistic for the analysis of circular data with applications in UHE gamma-ray astronomy, *Astron. Express* **4-6**(1), 137 – 142.

Protheroe, R. J.: 1987, Gamma Ray Astronomy at Energies above 0.3 TeV, *Proc. 20^{th} ICRC: Moscow* **8**, 21 – 44.

Protheroe, R. J.: 1993, Status of UHE Observations, *In the Press Ap. J. Suppl.*

Protheroe, R. J. and Clay, R.: 1984, Ultra-high energy γ-ray astronomy using an EAS array: Search for Emission from 100 MeV sources, *Proc. Astro Soc. Aust.* **5**(4), 586 – 589.

Protheroe, R. J. and Clay, R.: 1985, *Nature* **315**, 205.

Protheroe, R. J. and Stanev, T.: 1987, Possible explanation of the γ-ray light curve and time variability in Cygnus X-3, *Nature* **328**, 136–139.

Protheroe, R. J. and Szabo, A. P.: 1992, High Energy Cosmic Rays from Active Galactic Nuclei, *Phy. Rev. Lett.* **69**(20), 2885 – 2888.

Protheroe, R. J., Clay, R. W. and Gerhardy, P. R.: 1984, First Observation of Gamma-Rays from Vela X-1 at Energies Greater than 3×10^{15}eV., *Ap. J.* **280**, L47 – L50.

Protheroe, R. J. et al.: 1984c, *Ap. J.* **280**, L47.

Punch, M.: 1992, Detection of TeV photons from the active galaxy Markarian 421, *Nature* **358**, 477 – 478.

Resvanis, L. et al.: 1988, *Ap. J.* **328**, L9.

Rossi, B.: 1952, *High Energy Particles*, Prentice-Hall, New York.

Rossi, B.: 1964, *Cosmic Rays*, McGraw-Hill, New York.

Rossi, B. and Greisen, K.: 1941, Cosmic-Ray Theory, *Rev. Mod. Phy.* **13**, 240 – 309.

Samorski, M. and Stamm, W.: 1983, *Ap. J.* **268**, L17.

Santer, T. J. and Duffy, D. E.: 1989, *The statistical Analysis of Discrete Data*, Berlin: Springer p94.

Simpson, J. A.: 1983, *Ann. Rev. Nucl. Part. Sci.* **33**, 323.

Sokolsky, P.: 1987, High Energy Cosmic Ray Extensive Air Showers, *Proc.* 20^{th} *ICRC Moscow, Rapporteur Talks* **8**, 318 – 328.

Sokolsky, P., Sommers, P. and Dawson, B. R.: 1992, Extremely High Energy Cosmic Rays, *Physics Reports* **217**(5), 225 – 277.

Stanev, T. and Vankov, H. P.: 1992, Air shower detection and the energy flow in electromagnetic cascades, *J. Phys. G:* **18**, L49 – L54.

Stanev, T., Gaisser, T. and Halzen, F.: 1985, Muons in gamma showers from Cygnus X-3?, *Phys Rev D* **32**(5), 1244 – 1247.

Stavrev, P., Gavritova-Stavreva, N. and Petrov, S.: 1992, Mass composition of cosmic rays with primary energies in the region $10^{15} - 10^{16}$ eV: New treatment of Tien-Shan and Akeno data, *J. Phys. G:* **18**, 1833 – 1838.

Suga, K.: 1985, *Proc Workshop on Techniques in UHE γ-ray Astronomy, La Jolla ed: R. J. Protheroe (University of Adelaide)* p. 48.

Terrell, J.: 1986, *Ap. J.* **300**, 669.

Teshima, M. et al.: 1990, Energy spectrum of primary cosmic rays above 10^{17}ev obtained using the AKENO 20Km^2 array, *Proc* 21^{st} *ICRC Adelaide* **3**, 158.

Thornton, G. J. and Clay, R. W.: 1979; and 1980, Development of Atmospheric Cosmic-Ray Showers, *Phys. Rev. Lett. ; and Errata* **43; and 45**, 1622 – 1625; and 1463.

Tonwar, S. C. et al.: 1991, Detection of UHE radiation from Scorpius X-1: Ooty observations during 1984-1987, *Phys. Rev. Lett.* **67**(17), 2248 – 2251.

van. der. Walt, D. J.: 1988, The lateral distribution of electrons in EAS, *J. Phys. G:* **14**, 105 – 113.

van der Walt, D. J. et al.: 1987, *Proc.* 20^{th} *ICRC (Moscow)* **1**, 303.

van Stekelenborg, J. et al.: 1993, Search for point sources of ultrahigh energy γ rays in the southern hemisphere with the South Pole Air Shower Array, *Phys. Rev. D* **48**, 4504 – 4517.

Vestrand, W. T. and Eichler, D.: 1982, On the Ultra High Energy Gamma Rays from Cygnus X-3, *Ap. J.* **261**, 251 – 258.

Wdowczyk, J. and Wolfendale, A.: 1990, Consequences for EAS phenomena of adopting a very large photonuclear cross section, *Proc* 21^{st} *ICRC Adelaide* **9**, 25.

Wdowczyk, J. and Wolfendale, A. W.: 1983a, Cosmic γ rays and cosmic-ray particles, *Nature* **305**, 609 – 610.

Wdowczyk, J. and Wolfendale, A. W.: 1983b, Mass composition of high-energy cosmic rays and scaling violation in their interactions, *Nature* **306**, 347 – 349.

Weeks, T. C.: 1988, Very High Energy Gamma-Ray Astronomy, *Physics Reports* **160**(1 & 2), 1 – 121.

White, N. E.: 1978, *Nature* **271**, 38.

White, N. E. and Holt, S. S.: 1982, Accretion Disk Corona, *Ap. J.* **257**, 318.

Winn, M. M., Ulrichs, J., Peak, L. S., McCusker, C. B. A. and Horton, L.: 1986a, The cosmic-ray energy spectrum above 10^{17} eV, *J. Phys. G:* **12**, 653 – 674.

Winn, M. M., Ulrichs, J., Peak, L. S., McCusker, C. B. A. and Horton, L.: 1986b, The arrival directions of cosmic rays above 10^{17}eV, *J. Phys. G:* **12**, 675 – 686.

Yodh, G. B.: 1984, Composition of primary cosmic rays at energies $\sim 10^{15}$eV from data on high-energy muons in extensive air showers, *Phys. Rev. D.* **29**, 892.

Zatsepin, G. and Kuz'min, V.: 1966, Upper limit of the spectrum of cosmic rays, *Sov Phys JETP lett* **4**, 78 – 80.

Appendix A

Direction Fits

The initial direction of an air shower is obtained from a least-squares fit of a plane to the shower front.

The fit is made by minimizing the function:

$$\Psi^2 = \sum_{i=1}^{30} \omega_i \left(lx_i + my_i + (t_i - to)\right)^2$$

Where

- x_i = x co-ordinate of the i^{th} detector.
- y_i = y co-ordinate of the i^{th} detector.
- t_i = relative observed time at the i^{th} detector.
- t_0 = timing offset.
- ω_i = weight for detector, 1 if triggered, 0 otherwise.
- l, m = x and y direction cosines respectively.

Differentiating the above equation gives

$$\frac{\partial \Psi^2}{\partial l} = 2 \sum_{i=1}^{N} \omega_i x_i [lx_i + my_i + (t_i - t_o)]$$

$$\frac{\partial \Psi^2}{\partial m} = 2\sum_{i=1}^{N} \omega_i y_i [l x_i + m y_i + (t_i - t_o)]$$
$$\frac{\partial \Psi^2}{\partial t_o} = -2\sum_{i=1}^{N} \omega_i [l x_i + m y_i + (t_i - t_o)]$$

Now setting these partial differentials to zero to find the minimum, and representing the equations in matrix form gives:

$$\begin{pmatrix} XX & XY & X \\ XY & YY & Y \\ X & Y & N \end{pmatrix} \begin{pmatrix} l \\ m \\ t_o \end{pmatrix} = \begin{pmatrix} XT \\ YT \\ T \end{pmatrix}$$

Where

$XX = \sum \omega_i x_i^2$ $\quad XY = \sum \omega_i x_i y_i$ $\quad XT = \sum \omega_i x_i t_i$

$X = \sum \omega_i x_i$ $\quad YY = \sum \omega_i y_i^2$ $\quad YT = \sum \omega_i y_i t_i$

$Y = \sum \omega_i y_i$ $\quad T = \sum \omega_i t_i$ $\quad N = \sum \omega_i$

Simple matrix manipulation gives:

$$determinant = XX[Y^2 - (N \cdot YY)] + XY[(N \cdot XY) - (X \cdot Y)] + X[(X \cdot YY) - (Y \cdot XY)]$$

$$l = \frac{XT[(N \cdot YY) - (Y \cdot Y)] + YT[(X \cdot Y) - (N \cdot XY)] + T[(XY \cdot Y) - (X \cdot YY)]}{determinant}$$

$$m = \frac{XT[(X \cdot Y) - (XY \cdot N)] + YT[(XX \cdot N) - (X \cdot X)] + T[(XY \cdot X) - (Y \cdot XX)]}{determinant}$$

$$t_o = \frac{XT[(X \cdot YY) - (Y \cdot XY)] + YT[(XX \cdot Y) - (XY \cdot X)] + T[(XY)^2 - (XX \cdot YY)]}{determinant}$$

The third directional cosine is then

$$n = \sqrt{1 - (l^2 + m^2)}$$

The direction in local coordinates is found by

$$\theta = tan^{-1}\left(\frac{\sqrt{1 - n^2}}{n}\right) \tag{A.1}$$

$$\phi = \frac{\pi}{2} - tan^{-1}\left(\frac{m}{l}\right) \tag{A.2}$$

Appendix B

Phillips 7186 TDC

Channel Number	Detector	Calibration ($ns/count$)	Range (ns)	Maximum Reading	Pedestal (ns)
1	DB1	0.871	(0—3665)	4079	113
2	DB2	0.881	(0—3695)	4079	102
3	DB3	0.881	(0—3700)	4079	106
4	DB4	0.872	(0—3660)	4079	102
5	DB5	0.871	(0—3657)	4079	101
6	DB6	0.875	(0—3660)	4079	93
7	DB7	0.886	(0—3707)	4079	95
8	DB8	0.883	(0—3691)	4079	88
9	A1	0.875	(0—3658)	4079	88
10	B1	0.883	(0—3696)	4079	95
11	D1	0.888	(0—3712)	4079	89
12	E1	0.880	(0—3692)	4079	104

The new Phillips TDC calibrations used for the outer 12 detectors.

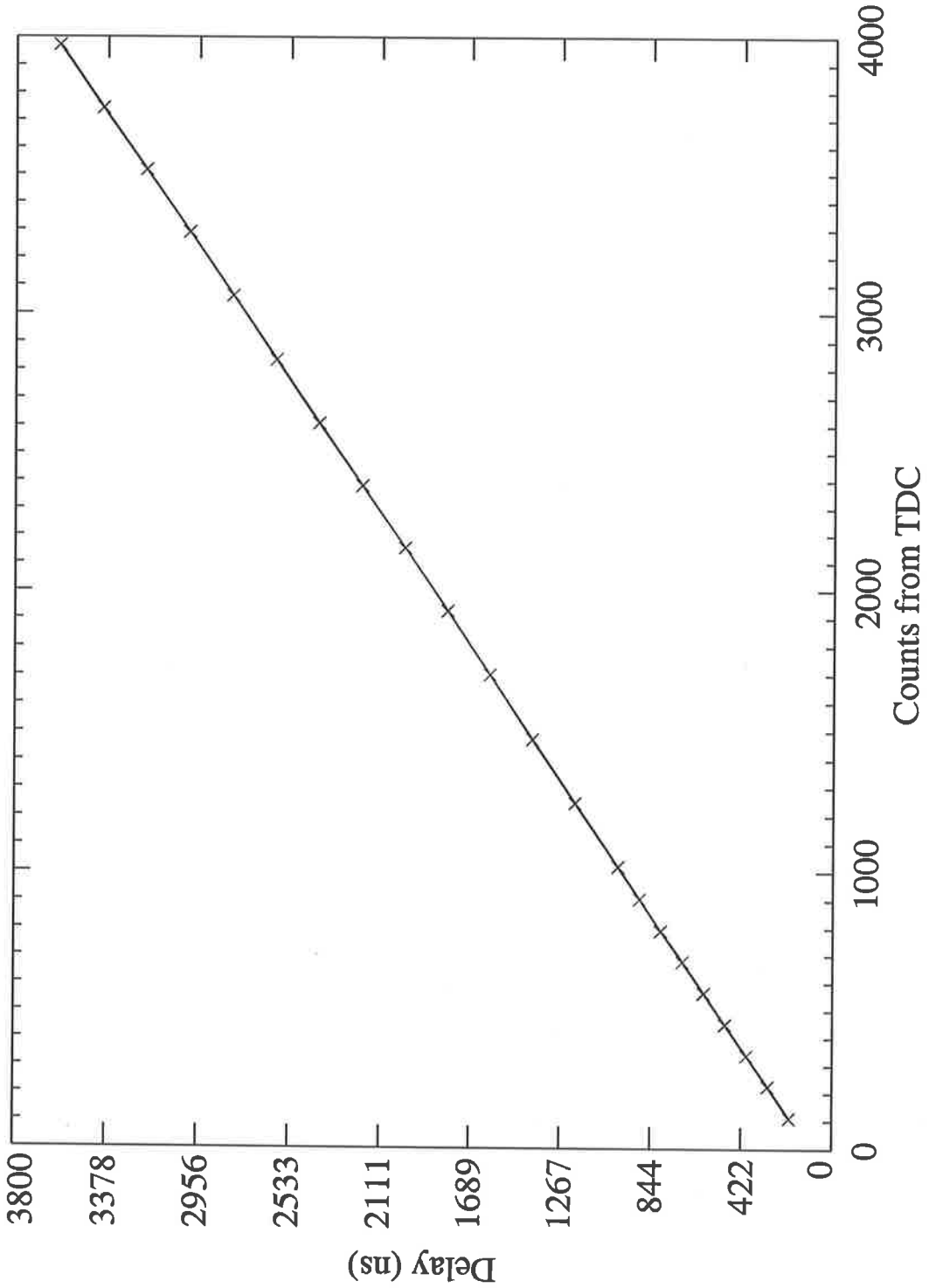

Figure B.1: Graph of delay in nanoseconds versus TDC count. The conversion from TDC count to time in nanoseconds is very close to linear across the range of the TDC. The conversion is 0.881 ns per TDC count for the second channel of the TDC.

Appendix C

Search Region

To optimize the search region radius given the angular resolution of the array, the calculation is performed as follows;

The signal (S) is equal to the area of the gaussian defined in §3.10, and the noise (N) is propotional to the square of the search region ψ^2. The noise (N) is equal to the squareroot of the background, therefore $\mathrm{N} \propto \sqrt{B} \propto \psi$, that is

$$\mathrm{S} = \frac{1}{\sigma^2} \int_0^{\psi} \exp^{(-\theta^2/2\sigma^2)} \theta \mathrm{d}\theta$$

Integrating the above equation gives

$$\mathrm{S} = \left[1 - \exp^{-(\psi^2/2\sigma^2)}\right]$$

So the ratio of signal to background is

$$\frac{\mathrm{S}}{\mathrm{N}} \propto \left[\frac{1 - \exp^{-(\psi^2/2\sigma^2)}}{\psi}\right]$$

Differentiating $\frac{S}{N}$ with respect to ψ and setting the resulting equation to zero gives

$$\exp^{-(\beta^2/2)} \left(1 + \beta^2\right) = 1$$

where $\beta = \psi/\sigma$

This equation is solved for 1.59 times the angular resolution of the array, ie $\psi = 1.59\sigma$

To accommodate the varying angular resolution with number of triggered detectors (see Figures 3.30 & 3.31), the previous equation can be modified by weighting each angular resolution (σ_i) with a probability and performing a sum over the number of triggered detectors (N_t). This probability was determined by the number of events and the corresponding angular resolution (see Figures 3.31 & 3.32) for a particular number of triggered detectors.

The signal to background ratio can then be described by

$$\frac{S}{N} \propto \sum_{i=1}^{N_t} \left[\frac{1 - \exp^{-(\psi^2/2\sigma_i^2)}}{\psi} \right] P(\sigma_i)$$

Again differentiating this equation with respect to ψ to find the optimum search region gives

$$\Xi(\psi) = \sum_{i=1}^{N_t} \left[P(\sigma_i) \left(\alpha^2 \exp^{-(\alpha^2/2)} + \exp^{-(\alpha^2/2)} - 1 \right) \right]$$

where $\alpha = \psi/\sigma_i$

Plotting this function $\Xi(\psi)$ against ψ will provide the optimum search region where $\Xi(\psi)$ equals zero. These plots are shown for the various array configurations in the following pages.

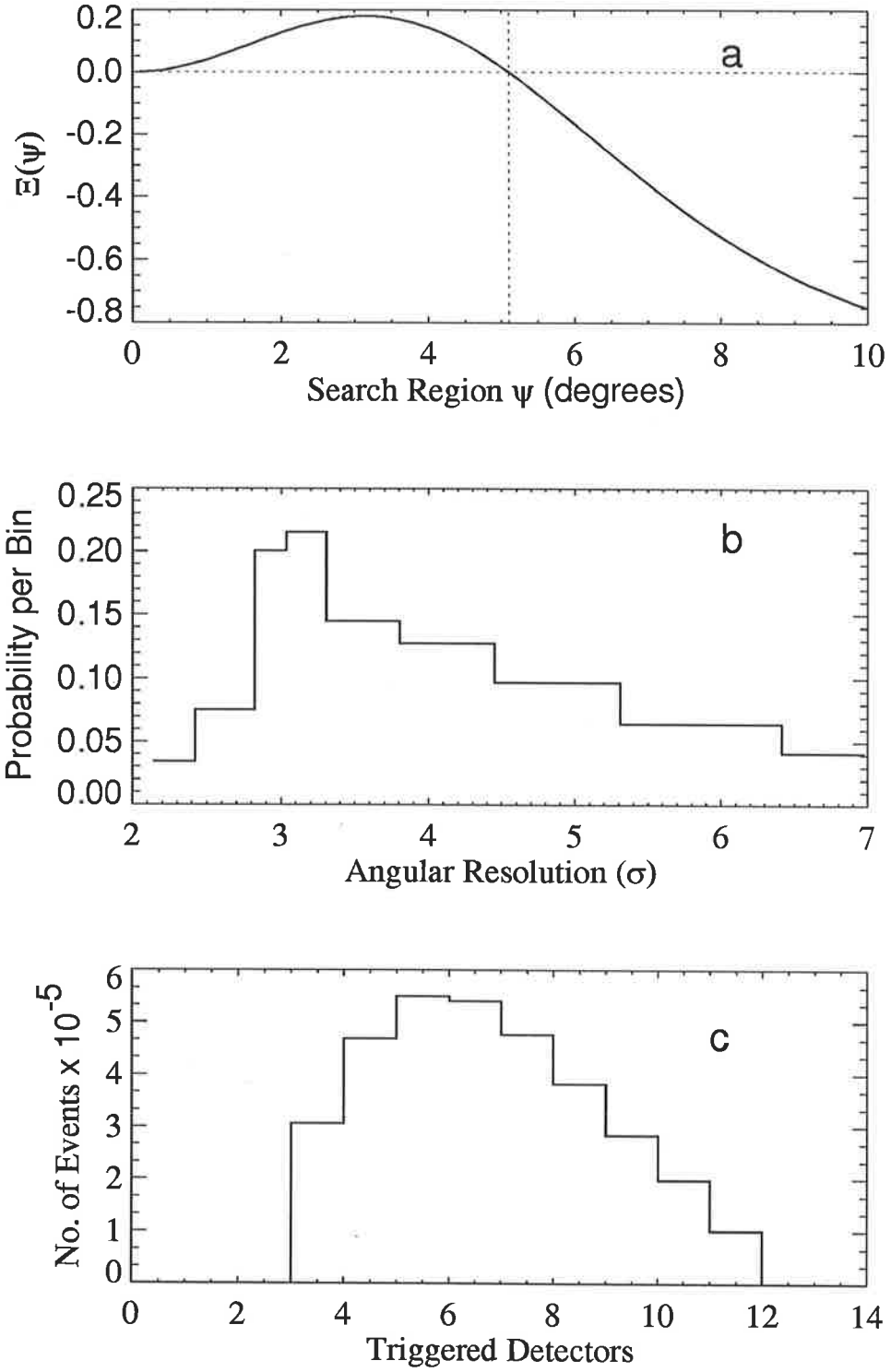

Figure C.1: The 1984-1986 data set. The optimum search region is 5.10°, plot (a) shows the curve of the function $\Xi(\psi)$. Plot (b) is the probability weight for each of the number of triggered detectors and corresponding angular resolution (determined from simulations §3.10.2)

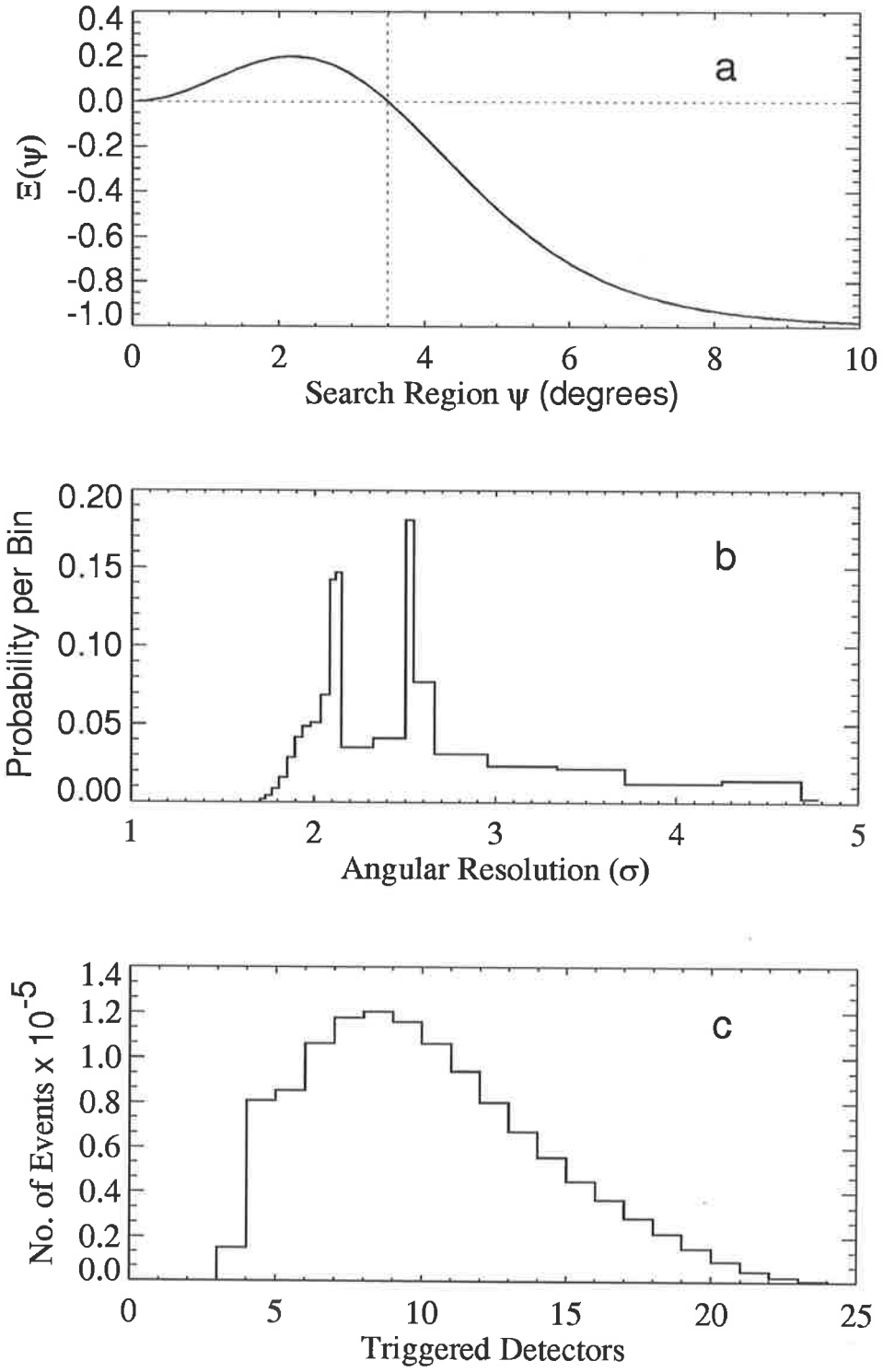

Figure C.2: The 1986-1987 data set. The optimum search region is 3.49°, plot (a) shows the curve of the function $\Xi(\psi)$. Plot (b) is the probability weight for each of the number of triggered detectors and corresponding angular resolution (determined from simulations §3.10.2)

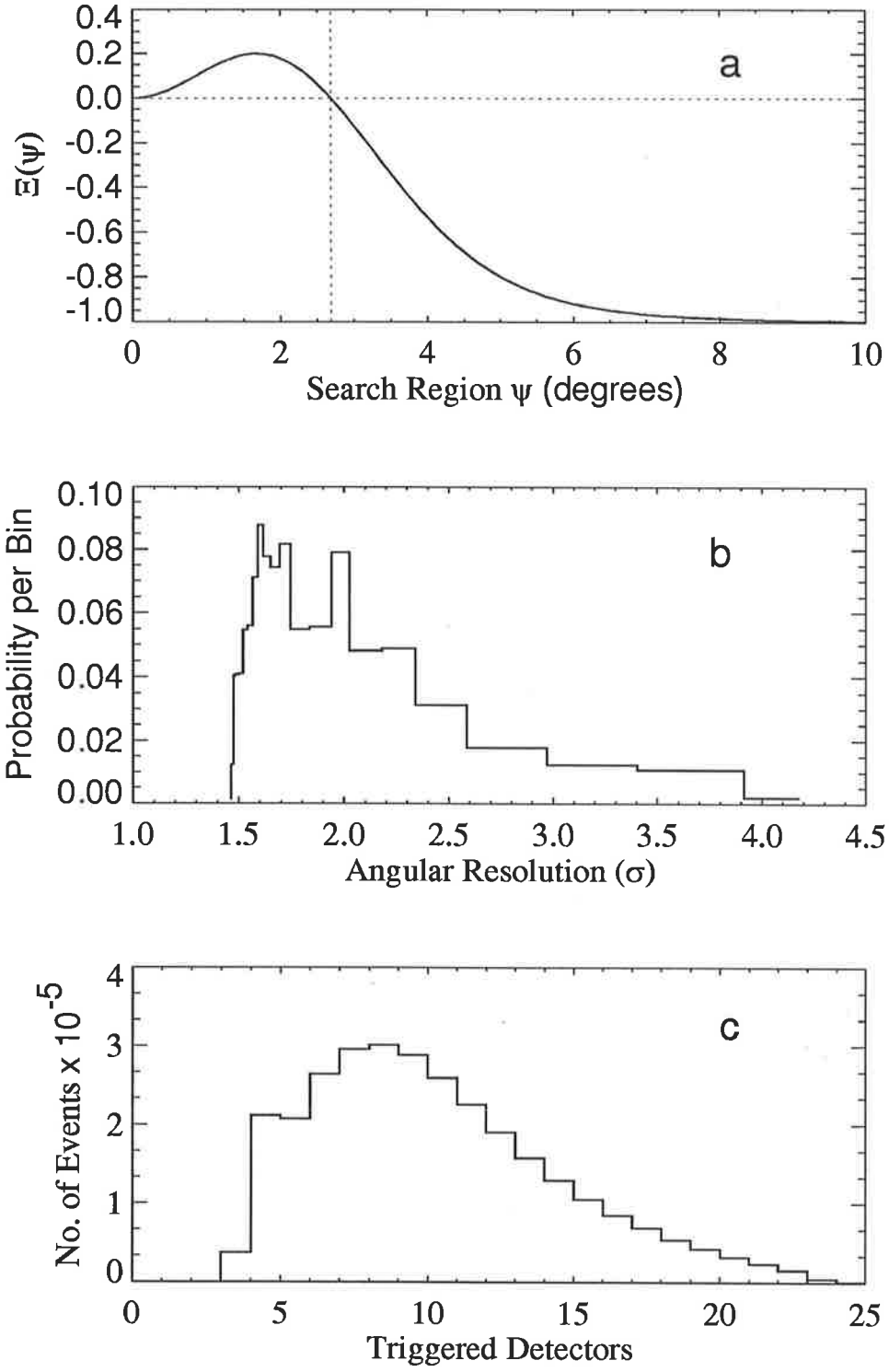

Figure C.3: The 1987-1989 data set. The optimum search region is 2.69°, plot (a) shows the curve of the function $\Xi(\psi)$. Plot (b) is the probability weight for each of the number of triggered detectors and corresponding angular resolution (determined from simulations §3.10.2)

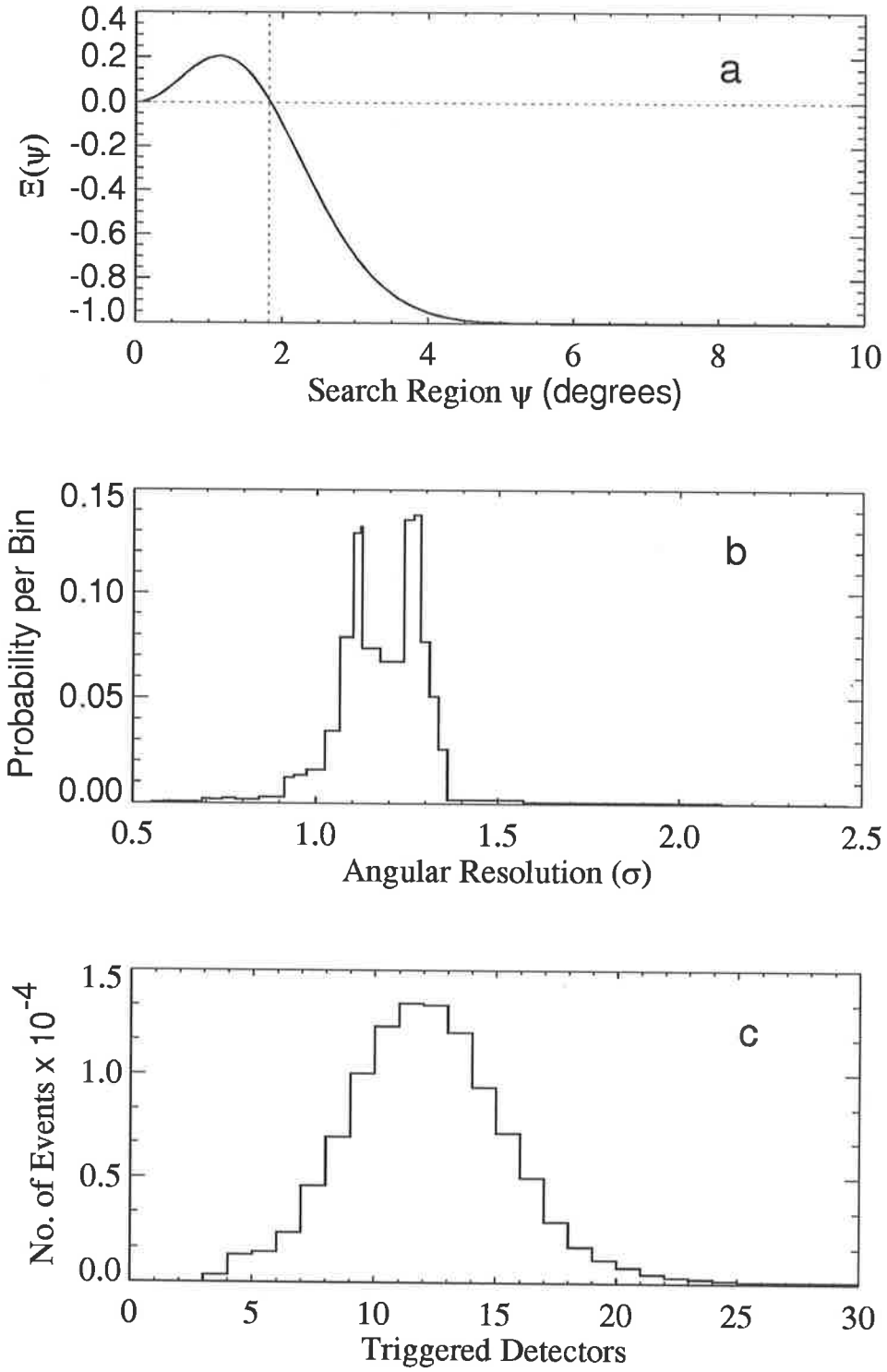

Figure C.4: The 1992 data set. The optimum search region is 1.82°, plot (a) shows the curve of the function $\Xi(\psi)$. Plot (b) is the probability weight for each of the number of triggered detectors and corresponding angular resolution (determined from simulations §3.10.2)

Appendix D

Barycentric Corrections

Variations induced in the orbital phase period of a X-ray binary system, as seen by an observer on Earth, due to the orbital motion of the Earth around the Sun will 'wash out' a periodic signal unless it is corrected. For the sources observed in this thesis it is adequate to correct arrival times as if observed at the Sun.

Given the arrival time, the right ascention & declination of the Sun is obtained. The

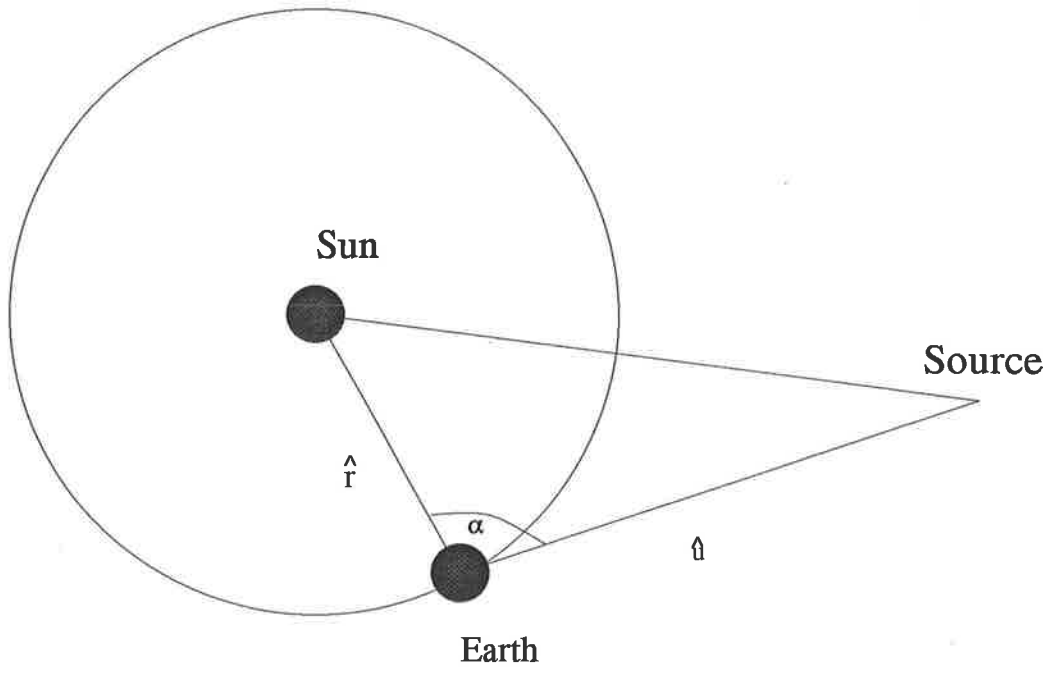

dot product of a unit vector in the direction of the Sun $\hat{r}_\odot$ with a unit vector in the direction of the source $\hat{u}$ gives the cosine of the angle α between them. The time difference D_t is obtained by multiplying the dot product by the distance to the Sun from the Earth.

$$D_t = d_\odot \times \hat{r_\odot} \cdot \hat{u}$$

This time difference is added to the arrival time to correct for the Earth's orbital motion.

Corrections

Page 6 at the end of the second paragraph add: " However the results from the JACEE balloon experiment shows that the average mass number of primary cosmic rays increases rapidly with energy at around 10^{14}eV. (M.Teshima 1994, 23^{rd} ICRC rapporteur paper p272.) "

Page 6, 4^{th} paragraph second line should read: " The elongation rate L_E which is defined as the rate of change in the average depth of shower maximum per $\log_{10}$(energy)

$$L_E = \frac{d\overline{X}_{max}}{dlnE}$$

where $\overline{X}_{max}$ is the average depth of maximum.

The way the average depth of maximum changes with energy depends on how the composition and particle interactions change. For a constant composition and slowly changing interaction parameters L_E is approximately constant. Any observed change in the rate would point to a possible change in the composition. "

Page 9, 3^{rd} paragraph 2^{nd} line Havarah should be: " Haverah "

Page 16, 2^{nd} paragraph 2^{nd} line: " This rotation is expected to give rise to large electric fields in the presence of the surface neutron star magnetic field (Cheng and Ruderman Ap.J. **300** p500 1986), which can accelerate particles in the vicinity of the neutron star. "

Page 23 last paragraph 2^{nd} line: " 50% of its energy is used for production of secondary particles in the interaction. "

Page 34, 2^{nd} paragraph 2^{nd} line should be: " 10% of the expected number of muons for a γ-ray initiated EAS at $\sim 10^{15}$eV. "

Page 39, 3^{rd} line should be: " for a 10^{18}eV "

Page 44, 2^{nd} paragraph 3^{rd} line: " size threshold to a shower size of 10^5 particles."

Page 53, 3^{rd} paragraph 2^{nd} line, laied should be " layed "

Page 56 second last line " Moiler should be: " Moliere "

Page 67, 2^{nd} paragraph, convential should be: " conventional "

Page 70, 2^{nd} paragraph, Ciampa and Clay reference: " J.Phys G **14** p787 1988 "

Page 80 Last paragraph, Figure 3.24 should be: " Figure 3.20 "